Topochemical Fluorination of Some Ruddlesden-Popper Phases

Ronghuan Zhang

Somerville College
Jan. 2017



A thesis submitted to the Board of the Faculty of
Physical Sciences in partial fulfilment of the requirements
for the degree of Doctor of Philosophy

Dedicated to my dear parents

and my brother

Declaration

The work described in this thesis was carried out at the Inorganic Chemistry Laboratory at the University of Oxford between October 2013 and January 2017 under the supervision of Prof. Michael A. Hayward. All the work presented in this thesis is my own except where I have either acknowledged help from a named person or given reference to a published source. All the work has not been submitted by the author for any degree at any other university.

Ronghuan Zhang

January 2017

Acknowledgement

First of all, I would like to thank my supervisor, Prof. Michael Hayward, for his extraordinary help in all aspects. His generous support with his wide range of knowledge is the key factor for the completion of my Dphil study. I always appreciate his patience, encouragement, and his sense of humour when explaining chemistry. His great passion in science is always inspiring. I also really appreciate his very kind help in seeking funding for my 3rd year.

I would also like to thank Prof. Shiv Halasyamani for the SHG measurements, Prof. Stephen J. Blundell for the μSR experiments, Prof. Nicole A. Benedek and her student Brian M. Abbett for DFT calculations and Dr Mark Senn for crystallography supports in the $La_3Ni_2O_{5.5}F_{3.5}$ phase. I would also like to thank staffs in ILL and ISIS facilities. I also appreciate Somerville College and the Department of Chemistry for the generous funding for my 3rd year of research.

I would also like to thank the fantastic members of the Hayward group. Midori A. Patino, it's been with great pleasure to work with you. Your kind help, your warm heart, your thoughtfulness, together with the joys we shared in this three years, will be always remembered, cherished, and appreciated for the rest of my life. Jacob Page, thanks for your world-class baking and THE most delicious salty caramel cake you baked! Thank you for acting as my 'walking-dictionary' and all the fun times we spent together. Lun Jin, a sweet and warm-hearted girl as you are, I cannot say how much I appreciate your kindness of providing me accommodation at the very last stage of my study, and all the other help. Your kind heart will always be rewarded. I would also like to thank Nijat Hasanli, Tong Zhu and other Hayward group members.

I would also like to thank Daniel Woodruff, Simon Cassidy and Jack Blandy from the Clarke group. It's been wonderful to have you guys around. Thank you for all your kind help. Apart from that, Danny, I would like to thank you for organizing those amazing parties, dinners, and of course those trips to PT. You're like a big brother taking care of me, and giving me good advices. Simon, thank you for bringing me to the glamorous and fabulous high table dinner in St. Catherine's College. Thanks for entertaining me with your 'wicked' mind. Jack, defeating you in the drinking contest is no doubt a highlight of my Dphil study. It will always be remembered, and shall be finally emphasized as a legend in my autobiography, if there will be one.

I would like to thank my dear boyfriend, Lucas Jeub, for all the happy times and sweet memories, which makes my life sparkling like a supernova. Last but not least, I would like to thank my parents and my brother for their full support during my Dphil study, and for giving me this opportunity to pursue my dream. My appreciation for them is beyond any word. I would like to dedicate this thesis to my dear parents and my brother.

Abstract

This thesis describes the synthesis and the characterization of some n = 2 Ruddlesden-Popper oxide phases ($A_3B_2O_7$; A = La, Y, Sr or Ca; B = Cr, Ni or Mn) and their topochemically fluorinated phases.

$La_2SrCr_2O_7$ adopts an *A2/a* ($a^-a^-c^-/a^-a^-c^-$) distorted structure with antiferromagnetic order below T_N ~ 260 K. DFT calculations performed on $La_2SrCr_2O_7$ suggest that this highly distorted *A2/a* ($a^-a^-c^-/a^-a^-c^-$) structure is stabilized by energy gains from the charge equalization and the improvement of chromium bonding environments associated with the unusual Sr/La distribution exhibited by this phase (the 12-coordinate A-sites are occupied by 82(2)% La^{3+} and 18(2)% Sr^{2+}).

Topochemical fluorination of $La_2SrCr_2O_7$ (Cr^{3+}) yields $La_2SrCr_2O_7F_2$ (Cr^{4+}) adopting the *A2/a* ($a^-a^-c^-/a^-a^-c^-$) distortion with antiferromagnetic order below T_N ~ 140 K. The fluorination leads a great compression of the perovskite layer within the Ruddlesden-Popper structure, enhancing the ($a^-a^-c^-/a^-a^-c^-$) distortion. As a result $La_2SrCr_2O_7F_2$ lies further from the crossover for insulating to metallic behaviour than many other Cr^{4+} oxide phases.

The A-site doping in $La_2SrCr_2O_7$ for the preparation of $La_{2-x}Sr_{1+x}Cr_2O_7$ (x = 0.2, 0.3) and $La_2Sr_{0.5}Ca_{0.5}Cr_2O_7$ leads to no obvious change in structural framework and the antiferromagnetic behaviour. $La_{2-x}Sr_{1+x}Cr_2O_7F_2$ (x = 0.2, 0.3) behaves similarly to $La_2SrCr_2O_7F_2$.

Topochemical fluorination of $La_3Ni_2O_7$ yields $La_3Ni_2O_{5.5}F_{3.5}$ with no obvious magnetic order. The fluorination leads to an enhancement of the structural distortion exhibited by the oxide starting material, driving a change from an *Amam*, $a^-a^-c^0/a^-a^-c^0$ lattice distortion to a *Pnam* $a^-a^-c^+/a^-a^-(c^+)$ lattice distortion in the fluorinated phase. The introduction of a cooperative octahedral tilt around the crystallographic *z*-axis leads to a local breaking of the inversion symmetry of the host lattice on fluorination, although the global inversion symmetry of the lattice is retained due to an alternation in the *z*-tilt direction in adjacent perovskite sheets.

The substitution of Sr^{2+} with Ca^{2+} cations in $YSr_2Mn_2O_7$ led to an increasing distortion of the metal-oxide framework, resulting in the formation of an orthorhombic symmetry in space group *Pnnm* adopted by $YSr_{0.5}Ca_{1.5}Mn_2O_7$. This novel *Pnnm* ($a^-b^-c^0/b^-a^-c^0$, $a \neq b$) distortion can be seen as an intermediate in structural change from *P4₂/mnm* ($a^-b^0c^0/b^0a^-c^0$) to *Amam* ($a^-a^-c^0/a^-a^-c^0$).

The topochemical fluorination of $YSr_2Mn_2O_7$ yields $YSr_2Mn_2O_{5.5}F_{3.5}$ with *P4₂/mnm* ($a^-b^0c^0/b^0a^-c^0$) distortion. The fluorination $YSr_2Mn_2O_7$ does not lead to a structural change as observed in that of $La_3Ni_2O_7$. This preference of retaining relatively high symmetry is driven by the A-cation ordering over the 9- and 12-coordinate A-sites in $YSr_2Mn_2O_{5.5}F_{3.5}$.

Contents

Abstract....4
Chapter 1: Introduction....9
1.1 Perovskite structure and tolerance factor....9
1.2 Basic band theory and the Mott-Hubbard model....10
1.3 Ruddlesden-Popper structure....12
1.4 Glazer notation and the symmetry analysis by Aleksandrow & Bartolome....13
1.5 Topochemical fluorine insertion into Ruddlesden-Popper structure....16
1.5.1 Manipulation of oxidation states of B-cations by topochemical fluorination....17
1.5.2 Manipulation of the cooperative tilting distortion on topochemical fluorination....18
1.6 Multiferroic materials....18
1.6.1 Difficulties and strategies in preparing multiferroic materials....18
1.6.2 Inducing ferroelectricity in phases with perovskite-like framework....19
1.6.3 Inducing ferroelectricity in n = 2 Ruddlesden-Popper phases....21
1.7 Aim of research....22
Chapter 2: Experimental methods....23
2.1 Synthetic methods....23
2.1.1 Ceramic method....23
2.1.2 Citrate gel method....23
2.2 Topochemical fluorination....24
2.3 Diffraction....25
2.3.1 X-ray diffraction....25
2.3.2 X-ray powder diffractometer....27
2.3.3 Synchrotron X-ray powder diffraction and diffractometer....28
2.3.4 Neutron diffraction....30
2.3.5 Neutron powder diffractometer....34
2.4 Rietveld refinement....39
2.4.1 Parameters to evaluate the goodness of fit....40
2.4.2 Particle size and strain broadening....41
2.5 Thermogravimetric analysis (TGA)....41
2.6 Iodometric titration....42
2.7 SQUID Magnetometery....43
2.8 Muon spin relaxation spectroscopy (μSR)....44

2.9 Bond valence sum (BVS) 45
2.10 Second harmonic generation (SHG) 46
Chapter 3: Characterization of $La_2SrCr_2O_7$ 48
3.1 Introduction 48
3.2 Experimental 49
3.3 Results 50
3.3.1 Structural refinement of $La_2SrCr_2O_7$ 50
3.3.2 Magnetic Characterization of $La_2SrCr_2O_7$ 54
3.4 Discussion 59
3.4.1 Structural refinement of $La_2SrCr_2O_7$ 59
3.4.2 Unusual A-cation distribution in $La_2SrCr_2O_7$ 62
3.4.3 Understanding of the unusual *A2/a* distortion and the A-cation distribution in $La_2SrCr_2O_7$ by first-principles Density Functional Theory 63
3.4.4 Comparison to other double layer Ruddlesden-popper phases 75
3.4.5 Magnetism of $La_2SrCr_2O_7$: the canted antiferromagnetism and spin glass behaviour of $La_2SrCr_2O_7$ 76
3.5 Conclusion 79
Chapter 4: Topochemical fluorination of $La_2SrCr_2O_7$ to $La_2SrCr_2O_7F_2$ 81
4.1 Introduction 81
4.2 Experimental 82
4.3 Results 83
4.3.1 X-ray powder diffraction data 83
4.3.2 Compositional characterization of $La_2SrCr_2O_7F_2$ 84
4.3.3 Structural refinement of $La_2SrCr_2O_7F_2$ 86
4.3.4 Magnetic Characterization of $La_2SrCr_2O_7F_2$ 89
4.4 Discussion 94
4.4.1 Anion distribution of $La_2SrCr_2O_7F_2$ 94
4.4.2 Compression of the perovskite layers by fluorine insertion 95
4.4.3 The cooperative tilting distortion in $La_2SrCr_2O_7F_2$ 96
4.4.4 Magnetism 97
4.4.5 Comparison to other phases containing Cr^{4+} centre 99
4.5 Conclusion 102
Chapter 5: $La_{2-x}Sr_{1+x}Cr_2O_7$, $La_2Sr_{0.5}Ca_{0.5}Cr_2O_7$ and $La_{2-x}Sr_{1+x}Cr_2O_7F_2$ 103
5.1 Introduction 103

5.2 Experimental....103
5.3 Results....104
5.3.1 $La_{1.8}Sr_{1.2}Cr_2O_7$ and $La_{1.8}Sr_{1.2}Cr_2O_7F_2$....104
5.3.2 $La_{1.7}Sr_{1.3}Cr_2O_7$ and $La_{1.7}Sr_{1.3}Cr_2O_7F_2$....110
5.3.3 $La_2Sr_{0.5}Ca_{0.5}Cr_2O_7$....111
5.4 Discussion....114
5.4.1 Structural comparison in $La_2SrCr_2O_7$, $La_{1.8}Sr_{1.2}Cr_2O_7$ and $La_2Sr_{0.5}Ca_{0.5}Cr_2O_7$....114
5.4.2 Magnetic comparison in $La_{2-x}Sr_{1+x}Cr_2O_7$ and $La_2Sr_{0.5}Ca_{0.5}Cr_2O_7$....116
5.4.3 $La_{1.8}Sr_{1.2}Cr_2O_7$ and $La_{1.8}Sr_{1.2}Cr_2O_7F_2$....118
5.4.3 $La_2SrCr_2O_7F_2$ and $La_{1.8}Sr_{1.2}Cr_2O_7F_2$....119
5.5 Conclusion....120
Chapter 6: Topochemical fluorination of $La_3Ni_2O_7$ to $La_3Ni_2O_{5.5}F_{3.5}$....121
6.1 Introduction....121
6.2 Experimental....122
6.3 Results....123
6.3.1 X-ray powder diffraction data of $La_3Ni_2O_xF_y$....123
6.3.2 Compositional characterization of $La_3Ni_2O_xF_y$....125
6.3.3 Structural refinement of $La_3Ni_2O_{5.5}F_{3.5}$....127
6.3.4 Magnetic Characterization of $La_3Ni_2O_{5.5}F_{3.5}$....131
6.4 Discussion....132
6.4.1 The fluorination chemistry....132
6.4.2 The anion distribution of $La_3Ni_2O_{5.5}F_{3.5}$....133
6.4.3 Structural modification by topochemical fluorination....134
6.5 Conclusion....138
Chapter 7: Characterization of $YSr_{2-x}Ca_xMn_2O_7$....139
7.1 Introduction....139
7.2 Experimental....141
7.3 Results....141
7.3.1 X-ray powder diffraction data of $YSr_{2-x}Ca_xMn_2O_7$....141
7.3.2 Structural refinement of $YSr_{0.5}Ca_{1.5}Mn_2O_7$....143
7.3.3 Structural refinement of $YSrCaMn_2O_7$....147
7.4 Discussion....151
7.4.1 A-cation substitution....151

7.4.2 The *Pnnm* distortion 154
7.5 Magnetization data of $YSr_{2-x}Ca_xMn_2O_7$ 157
7.6 Conclusion 158
Chapter 8: Topochemical fluorination of $YSr_2Mn_2O_7$ to $YSr_2Mn_2O_{5.5}F_{3.5}$ and $YSr_2Mn_2O_{6.4}F_{1.5}$ 159
8.1 Introduction 159
8.2 Experimental 159
8.3 Results 160
8.3.1 X-ray powder diffraction data of $YSr_2Mn_2O_{5.5}F_{3.5}$, $YSr_2Mn_2O_{6.4}F_{1.5}$ and $YSr_{0.5}Ca_{1.5}Mn_2O_xF_y$ 160
8.3.2 Compositional characterization of fully fluorinated product $YSr_2Mn_2O_xF_y$ ($YSr_2Mn_2O_{5.5}F_{3.5}$) by iodometric titration 162
8.3.3 Structural refinement of $YSr_2Mn_2O_{5.5}F_{3.5}$ 163
8.3.4 Compositional characterization of staged phase $YSr_2Mn_2O_{7-\delta}F_z$ ($YSr_2Mn_2O_{6.4}F_{1.5}$)..166
8.3.5 Structural refinement of $YSr_2Mn_2O_{6.4}F_{1.5}$ 166
8.4 Discussion 168
8.4.1 The fluorination chemistry and the anion distribution in $YSr_2Mn_2O_{5.5}F_{3.5}$ 168
8.4.2 Structural modification by topochemical fluorination from $YSr_2Mn_2O_7$ to $YSr_2Mn_2O_{5.5}F_{3.5}$ 170
8.5 Conclusion 173
Chapter 9: Conclusion 174
Appendix 177
References 203

Chapter 1: Introduction

1.1 Perovskite structure and tolerance factor

Complex transition metal oxides with ABO_3 perovskite-like structures have attracted enduring and intensive attention.[1] In fact, the perovskite type oxide structure is reported to incorporate stably around 90% of the metallic natural elements of the Periodic Table[2]. This gives rise to a broad diversity of electronic, magnetic and transport properties exhibited by compounds with a perovskite-like structure. These properties include ferroelectricity (e.g. $BaTiO_3$)[3], ferromagnetism (e.g $SrRuO_3$)[4], multiferroic behaviour (e.g. $TbMnO_3$)[5], superconductivity (e.g. $YBa_2Cu_3O_7$)[6], colossal magnetoresistance (e.g. $La_{1-x}Ca_xMnO_3$)[7]. Thus materials with perovskite-like structures can find applications in a wide range of technologies such as catalysis[2], information storage, fuel cells[8], etc.

A typical perovskite oxide adopts a general formula ABO_3, where A-cations can be alkaline earth metals or lanthanides and B-cations are transition metals. In this structure, the A-cations sit in the 12-fold sites, while the B-cations in the 6-fold coordinated sites forming a 3-dimensional array of apex-linked BO_6 octahedra. A perfect perovskite structure requires an ideal size of A and B cations which is defined by the Goldschmidt tolerance factor[9]. A typical example is $SrTiO_3$ with a cubic structure in space group $Pm\bar{3}m$ as shown in Figure 1.1.[10] In this ideal structure, the structural framework of perovskite can be thought of as being derived from a cubic close packed lattice, where the atoms are touching one another. Thus the B-O bond distance <B-O> is equal to $a/2$ and <A-O> is equal to $a/\sqrt{2}$ (where a is the cubic unit cell parameter), giving to the following relationship: $<A\text{-}O> = \sqrt{2}<B\text{-}O>$. The tolerance factor ($t$) is thus defined[9]:

$$t = \frac{< A - O >}{\sqrt{2} < B - O >} = \frac{r_A + r_O}{\sqrt{2}(r_B + r_O)}$$

It is obvious that for an ideal perovskite structure, its tolerance factor is equal to 1. A lower t-value, which indicates a mismatch between A- and B-cations, is also allowed. In fact, the

perovskite structure can form thermodynamically stable phases incorporating combinations of A- and B-cations with a large range of radius ratios ($0.75 < t < 1.0$).

As shown in Figure 1.1 (b), the perovskite structure adjusts to a $t < 1$ by cooperative rotations of the BO_6 octahedra. Therefore, the mismatch between A-O and B-O bond lengths could be accommodated by a tightening of the B-O-B bond angles[1] while leaving the internal coordinates of the BO_6 units largely unchanged. The tightening of the B-O-B bond angles affects the interactions between the *d*-orbitals on adjacent transition metal centres. For example, as observed in the $LnNiO_3$ (Ln = lanthanide) series, the substitution of lanthanum to smaller lanthanides (smaller t) modifies the overlapping of Ni 3*d*-orbitals, tuning the electron behaviour of $LnNiO_3$ to change from metallic to semiconducting.[11] Similarly, as observed for the $LnFeO_3$ series, a tightened Fe-O-Fe bond angles, resulted from a smaller tolerance factor when substituting lanthanum to smaller lanthanides, weakens the superexchange interactions between adjacent Fe, and thus lowered the Neel temperatures of $LnFeO_3$.[1]

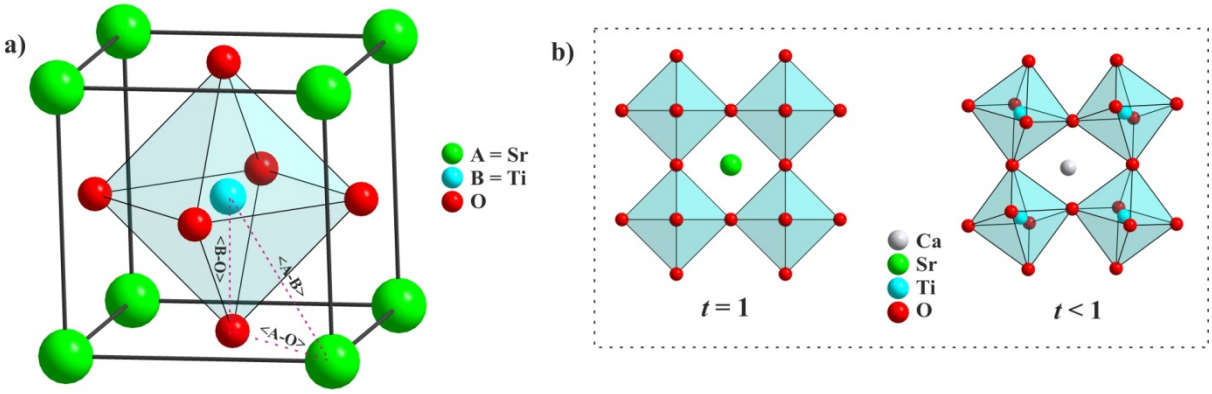


Figure 1.1. a) $SrTiO_3$ with a cubic perovskite structure[10], and b) the perovskite structure adjusts to $t < 1$ by cooperative rotations of the apex-linked BO_6 octahedra.[12]

1.2 Basic band theory and the Mott-Hubbard model

Energy bands can be seen as an extension of orbitals in molecules as shown in Figure 1.2. As the number of atoms in a molecule increases, the molecular orbitals become closer in energy, and merge together in a solid to form a continuous range of energy levels, becoming energy bands.[13]

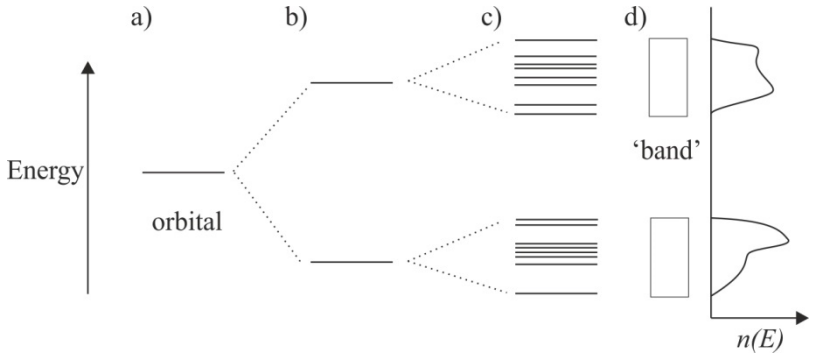


Figure 1.2. Origin of electronic energy bands in solids. Orbital of a) an atom; b) a small molecule; c) a large molecule, becoming d) the band with the density of states in solids.[13]

In a simple band approach as shown in Figure 1.3 (a), a partially filled band which allows free movement of electrons gives rise to a metallic behaviour. For example, $NaWO_3$ with partially filled *d* band (d^1) is metallic while WO_3 with d^0 is an insulator[14]. However, many compounds containing transition metal centres with partially filled *d* orbitals are observed as non-metallic solids, such as NiO. This is mainly because *d* orbitals are rather narrow such that the electron repulsion in such narrow *d* orbitals becomes significant and cannot be neglected.[14] The Hubbard model takes electron repulsion in solids into account, giving a more reliable prediction on their electronic behaviours. In the Hubbard model, transition metal *d* orbitals split into two different energy levels due to electron repulsion. The lower energy (-*I*, where *I* is the ionization energy when an electron is removed from an orbital) is the energy of the singly occupied orbitals. The upper energy (-*A*, where *A* is the electron affinity of the neutral atom) is the energy of an extra electron added to the solid to give a doubly occupied orbital. The gap in between these two energy levels is defined as the 'Hubbard U' (U = *I* - *A*), as shown in Figure 1.3 (b).[13,14]

As shown in Figure 1.3 (c), the electronic properties of a solid depend crucially on the relative magnitude of its Hubbard U and its band width W. In the NiO case, the band width arising from the overlapping of Ni 3*d* orbitals is insufficient to overcome the electron repulsion energy U (W < U), and thus NiO with partially filled *d* orbitals still behaves as an insulator. A solid behaves as a metal when W > U. A particular interesting area of intensive research lies on

the metal-insulator boundary where W ≈ U. Near this metal-insulator transition point the metallic state shows fluctuations and orderings in the spin, charge, and orbital degrees of freedom[15]. Thus small chemical or structural modifications of such systems would be sufficient to adjust the relative energies of different competing electronic ground states in such materials, enabling the properties of the materials to be tuned to potentially exhibit exotic behaviours such as superconductivity and magnetoresistance.[16]

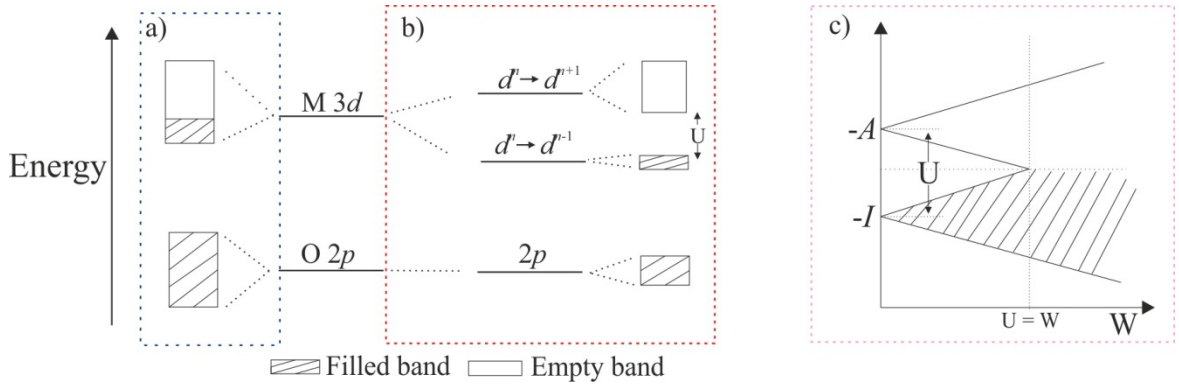


Figure 1.3. a) In a simple band approach where a partially filled band gives to a metallic behaviour; b) The Hubbard model where electron repulsion gives rise to orbital energy splitting;[13,14] c)The electronic properties of a solid depend crucially on the relative magnitude of its Hubbard U and its band width W.[13]

1.3 Ruddlesden-Popper structure

Ruddlesden-Popper structure is a layered variant of perovskite structure, which has a general formula $A_{n+1}B_nO_{3n+1}$ where A-cations can be alkali, alkaline earth metals or lanthanides and B-cations are transition metals. A Ruddlesden-Popper structure contains *n* blocks of perovskite layers (ABO_3) separated by a rock salt layer (AO) as shown in Figure 1.4. Thus the general formula of Ruddlesden-Popper could also be written as $(AO)(ABO_3)_n$.

In a typical Ruddlesden-Popper structure, the B-cations sit in the 6-fold coordinated sites forming a 2-dimensional infinite array of apex-linked BO_6 octahedra. The A-cations sit in two distinctive sites, the 12-coordinated sites residing in the perovskite blocks and the 9-coordinated sites residing in the rock salt layers as shown in Figure 1.4. These two distinctive A-sites allow the possibility of A-cation order. In many *n* = 2 Ruddlesden-Popper phases that have two or more

A-cations that differ significantly in charge and/or radius, it is observed that the larger cation will preferentially occupy the perovskite A-site (CN = 12). Thus, for example, the perovskite A-sites in $YSr_2Mn_2O_7$ are exclusively occupied by Sr^{2+},[17] and similarly the perovskite A-sites in $Nd_2BaMn_2O_7$ are preferentially occupied by Ba^{2+}.[18]

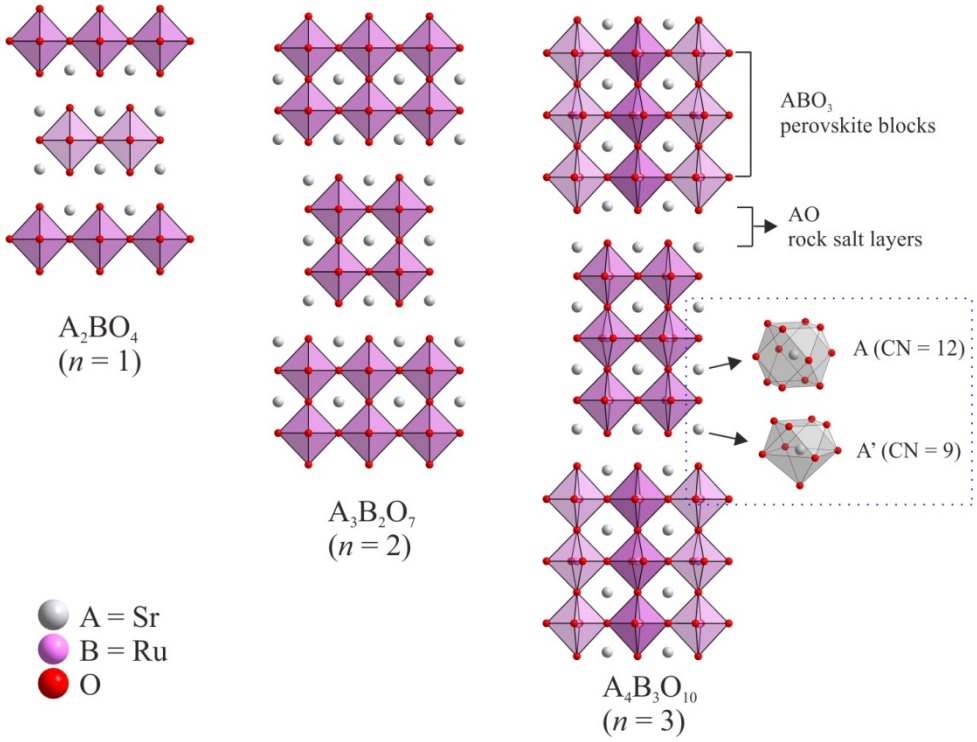


Figure 1.4. Ruddlesden-Popper phases with n = 1, 2, 3. Inset: coordination environment of two different A-cation sites.

1.4 Glazer notation and the symmetry analysis by Aleksandrow & Bartolome

Glazer notation[19] is used in this thesis to describe rotational distortions of BO_6 octahedra about each Cartesian axis in perovskite structure. Each letter in the notation specifies the magnitude of the rotational distortion about an axis while the superscript indicates the direction of adjacent octahedral rotations. Adjacent octahedra rotating in the same (opposite) direction(s) is defined as an in-phase (out-of-phase) twist, which is denoted by a positive (negative) superscript, as shown in Figure 1.5. A superscript of '0' is also used when there is no twisting rotation of the octahedra. For example, ($a^0a^0a^0$) denotes that there is no twisting rotation along any of the *x*, *y* and *z*-axes; ($a^-a^-a^-$) denotes that there is an out-of-phase twisting rotation along each axis with the

same magnitude denoted by letter 'a'; ($a^-b^-c^+$) denotes that there is an out-of-phase twisting rotation along each of the *x* and *y*-axes and an in-phase twisting rotation along the *z*-axis, all with different magnitudes denoted by letter 'a', 'b' and 'c' respectively.

For an n = 2 Ruddlesden-popper phase, since adjacent layers need not necessarily be distorted in the same way, a pair of Glazer notations separated by a slash are used to describe the twisting rotation of adjacent slabs (a slab is defined in Figure 1.5). The ($a^-b^0c^0/b^0a^-c^0$) notation, for example, indicates that one slab adopts the ($a^-b^0c^0$) twisting rotation while the adjacent slab adopts ($b^0a^-c^0$).

Aleksandrov and Bartolome (A&B) performed a symmetry analysis of the possible cooperative twisting distortions of the BO_6 octahedra in $A_3B_2O_7$ n = 2 Ruddlesden-Popper phases.[20] In their symmetry analysis, Φ (Ψ) is used to indicate out-of-phase (in-phase) twisting rotation as shown in Figure 1.5. The space groups used in this thesis and their tilt systems are selected from the symmetry analysis from A&B, and are listed in Table 1.1.

As shown in Table 1.1, there are negative signs in front of the letters when describing the tilt of *Acmm* and *Pnam*, indicating a change of rotational directions. Taking a *Pnam* ($a^-a^-c^+/ a^-a^-(-c^+)$) model as an example, the $-c^+$ indicates that the adjacent slab B adopts an in-phase twisting rotation along *c*-axis (c^+ twist) but in the opposite direction with respect to previous slab A (Figure 1.6). Similarly, the (-Φ) twist in Table 1.1 indicates an opposite rotation with respect to Φ.

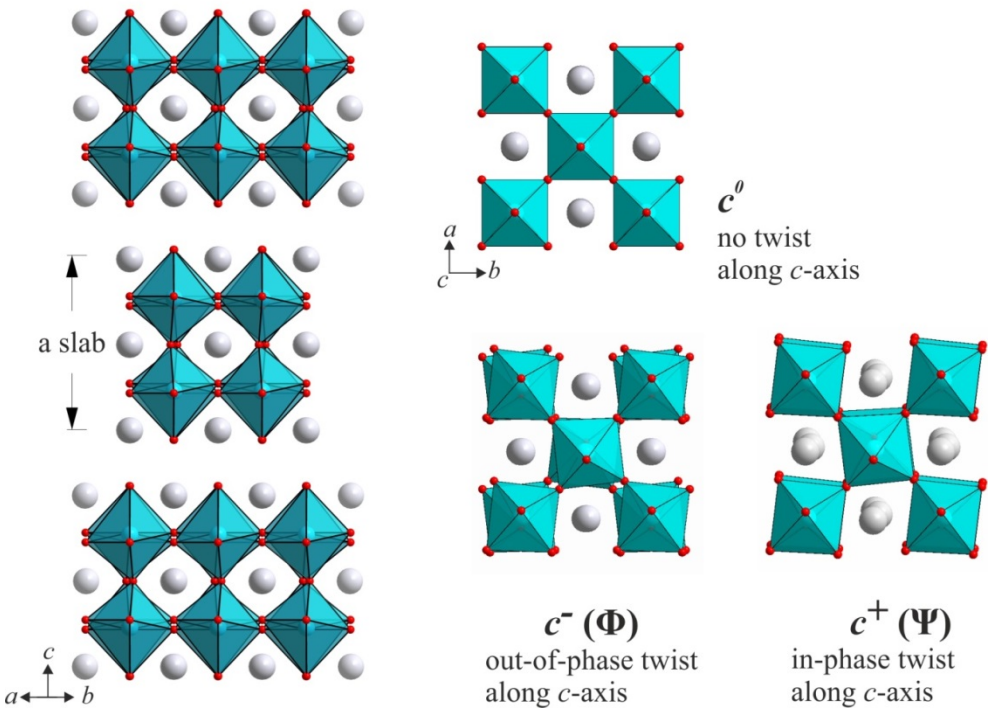


Figure 1.5. The n = 2 Ruddlesden-popper phase (left) and the clarification of the glazer notation.

Space Group	Tilt System	Glazer Tilt	Tilts	Unit cell parameters		
				a	*b*	*c*
I4/mmm	000/000	$a^0a^0a^0$/ $a^0a^0a^0$	0 tilt	a_0	a_0	c_0
P4₂/mnm	Φ00/0Φ0	$a^-b^0c^0$/$b^0a^-c^0$	1 tilt	$\sqrt{2}a_0$	$\sqrt{2}a_0$	c_0
Acam	$00\Psi_z$/$00\Psi_z$	$a^0a^0c^+$/ $a^0a^0c^+$		$\sqrt{2}a_0$	$\sqrt{2}a_0$	c_0
Acaa	$00\Phi_z$/$00\Phi_z$	$a^0a^0c^-$/ $a^0a^0c^-$		$\sqrt{2}a_0$	$\sqrt{2}a_0$	c_0
Pnnm	$\Phi_1\Phi_2$0/$\Phi_2\Phi_1$0	$a^-b^-c^0$/$b^-a^-c^0$	2 tilts	$\sqrt{2}a_0$	$\sqrt{2}a_0$	c_0
Acmm	ΦΦ0/(-Φ)(-Φ)0	$a^-a^-c^0$/$(-a^-)(-a^-)c^0$		$\sqrt{2}a_0$	$\sqrt{2}a_0$	c_0
Amam	ΦΦ0/ΦΦ0	$a^-a^-c^0$/$a^-a^-c^0$		$\sqrt{2}a_0$	$\sqrt{2}a_0$	c_0
A2₁am	$\Phi\Phi\Psi_z$ /$\Phi\Phi\Psi_z$	$a^-a^-c^+$/ $a^-a^-c^+$	3 tilts	$\sqrt{2}a_0$	$\sqrt{2}a_0$	c_0
Pnam	$\Phi\Phi\Psi_z$ /$\Phi\Phi(-\Psi_z)$	$a^-a^-c^+$/ $a^-a^-(-c^+)$		$\sqrt{2}a_0$	$\sqrt{2}a_0$	c_0
A2/a	$\Phi\Phi\Phi_z$ /$\Phi\Phi\Phi_z$	$a^-a^-c^-$/$a^-a^-c^-$		$\sqrt{2}a_0$	$\sqrt{2}a_0$	c_0

Table 1.1. The space groups used in this thesis and their tilting notations.[20]

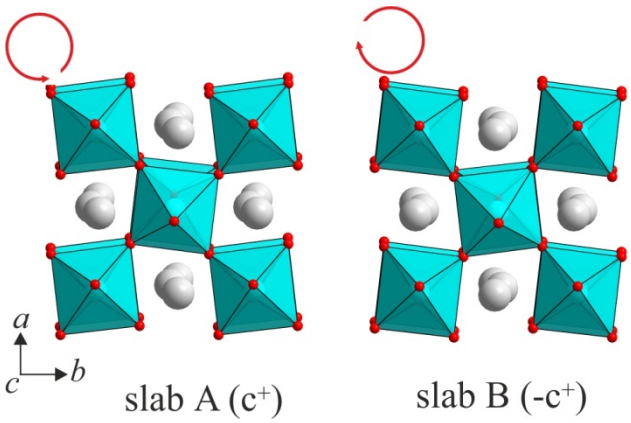


Figure 1.6. ($-c^+$) rotation in a *Pnam* ($a^-a^-c^+$/ $a^-a^-(-c^+)$) model.

1.5 Topochemical fluorine insertion into Ruddlesden-Popper structure

The layered nature of Ruddlesden-Popper structure offers an opportunity to insert anions (e.g. F^-) into the tetrahedral interstitial sites within its rock salt layers (Figure 1.7) while the cation framework stays largely unchanged. For example, topochemical fluorine insertion into $Sr_3Ru_2O_7$ yields $Sr_3Ru_2O_7F_2$ with fluoride ions in the tetrahedral interstitial sites.[21] Similar reactions with $La_{1.2}Sr_{1.8}Mn_2O_7$ and $LaSrMnO_4$ yield $La_{1.2}Sr_{1.8}Mn_2O_7F_2$ and $LaSrMnO_4F_{1.7}$ respectively (Figure 1.3).[22]

On topochemical fluorination, fluoride ions can also exchange with the existing oxide ions in the parent framework while being inserted into the interstitial sites. For example, fluorinations of $Sr_3(Fe_{0.5}Ru_{0.5})_2O_7$ and $La_2BaFe_2O_7$ yield $Sr_3(Fe_{0.5}Ru_{0.5})_2O_{5.5}F_{3.5}$ and $La_2BaFe_2O_5F_4$, respectively.[23,24] It is worth noting that as observed both in the $Sr_3(Fe_{0.5}Ru_{0.5})_2O_{5.5}F_{3.5}$ and $La_2BaFe_2O_5F_4$, the extra fluoride ions reveal a strong preference to replace the apical oxygen anions residing in the rock salt layers (Figure 1.7) rather than the remaining oxygen anions.

In addition, phases with low fluorine content in the rock salt layer can also be obtained. For example, if $LaSrMnO_4F_{1.7}$ is heated with the appropriate amount of $LaSrMnO_4$, a staged phase $LaSrMnO_4F$ with lower fluorine content can be formed via the thermal equilibration of the fluorine concentration.[25] In this case, the fluoride anions were inserted alternatively into the rock salt layers, that is, there is either full or empty layer of fluoride ions in rock salt layers. The crystal structure of this staged phase is shown in Figure 1.7.

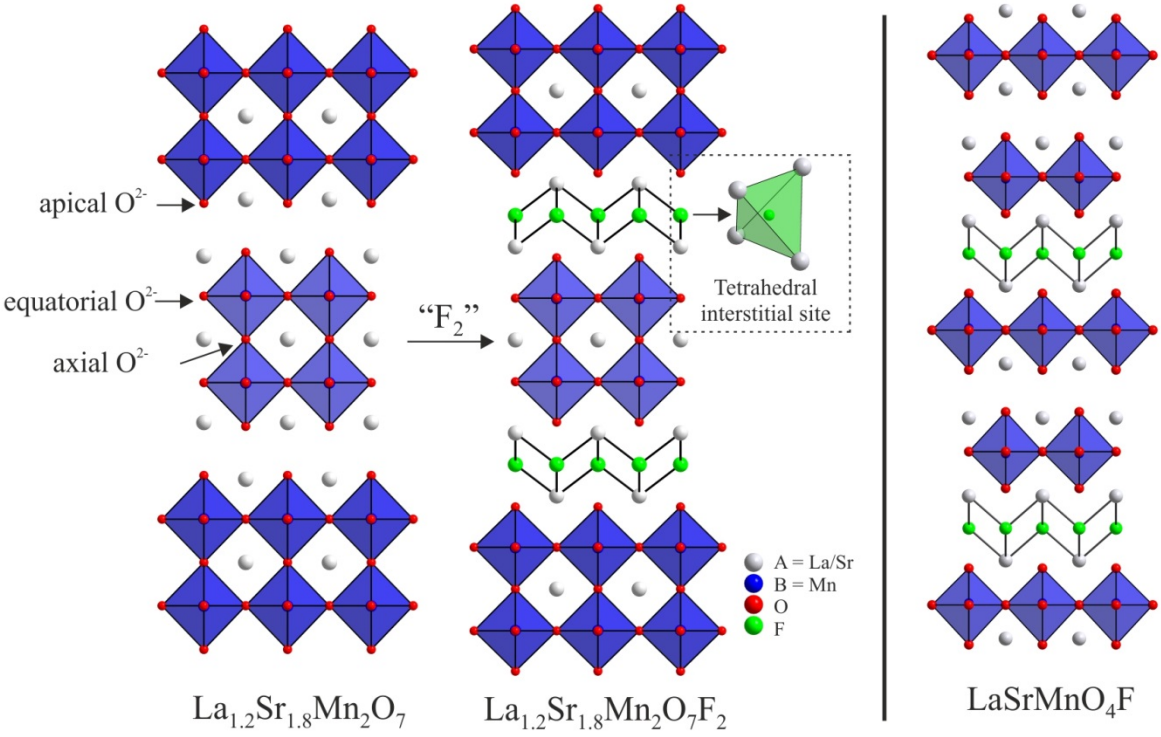


Figure 1.7. Topochemical fluorination of Ruddlesden-Popper phases[22]. Right: Structure of staged oxyfluoride.

1.5.1 Manipulation of oxidation states of B-cations by topochemical fluorination

An important feature of the topochemical oxidative insertion of anions into Ruddlesden-Popper structure is that the anions are inserted into locations within the host phase where are relatively 'remote' from the transition metal centres. As a result, in a simple case where $A_3B_2O_7$ are converted into $A_3B_2O_7F_2$, the transition metal B-cations are oxidized from B^{n+} to $B^{(n+1)+}$ while their local coordination geometry remains largely unchanged. For example, on fluorination of $Sr_3Ru_2O_7$ to $Sr_3Ru_2O_7F_2$, Ru^{4+} cations are oxidized to Ru^{5+}, while the octahedral coordination environment of Ru remains unchanged.[21] This topochemical manipulation of oxidation states of B-cations in n = 2 Ruddlesden-Popper phases offers an opportunity for the preparation of phases containing metal centres with novel oxidation states and/or sitting in novel coordination geometries, as will be discussed in Chapter 4.

1.5.2 Manipulation of the cooperative tilting distortion on topochemical fluorination

In addition to oxidizing transition metal B-cations, topochemical fluorination introduces electron repulsion and tensions to parent lattices. This could cause a dramatic change of cooperative tilting distortions of the apex-linked BO_6 octahedra in the host lattice, without disrupting its cation framework. For example, fluorination of $Sr_3Ru_2O_7$ with undistorted *I4/mmm* symmetry drives a disordered twisting of the RuO_6 octahedra around the *z*-axis to yield an $a^0a^0c^{+/-}$ $a^0a^0c^{+/-}$ distorted structure in $Sr_3Ru_2O_7F_2$.[26] Fluorination of $Sr_3(Mn_{0.5}Ru_{0.5})_2O_7$ to $Sr_3(Mn_{0.5}Ru_{0.5})_2O_7F_2$ drives a structural change from the undistorted *I4/mmm* framework to *Acaa* ($a^0a^0c^-$/ $a^0a^0c^-$)[23]. This manipulation of the cooperative tilting distortion by topochemical fluorination could be utilized to stabilize highly distorted, metastable structures (such as antiferroelectric phases), as will be discussed in Chapter 6.

1.6 Multiferroic materials

Magnetoelectric multiferroic materials are those which exhibit a combination of ferromagnetism and ferroelectricity. This type of multifunctional material could find applications in a wide range of technologies, such as sensors and data storage devices.[27] However, despite this wide variety of applications, only a few materials have been reported as multiferroic.[28] The difficulties of preparing such multifunctional materials lie in the fundamental differences between ferromagnetism and ferroelectricity.

1.6.1 Difficulties and strategies in preparing multiferroic materials

Ferromagnetism requires a material to have unpaired electrons, whose magnetic moments are coupled together to yield a collective spontaneous magnetization. Ferroelectricity requires materials to have a spontaneous electric polarization that can be reversed by the application of an external electric field. In other words, for a phase to exhibit ferroelectric behaviour, the anions and cations need to displace relative to each other to form dipole moments. This is conventionally achieved by the off-centring of transition metal cations. This off-centring is often stabilized

through second-order Jahn-Teller (SOJT) distortions of transition metal cations with d^0 electronic configuration (Ti^{4+}, Nb^{5+}, W^{6+}, etc.)[3,29]. The requirement of using d^0 transition metals for ferroelectricity is apparently contradictive to the requirement of unpaired *d*-electrons for magnetism. This contradiction accounts for the great challenge in the preparation of phases which exhibit magnetoelectric behaviour.[30,31] Two reasonable strategies to overcome this contradiction are: 1) to find an alternative mechanism for magnetism thus *d*-electron is not involved; 2) to find an alternative mechanism for ferroelectricity which is compatible with a partially filled *d*-shell.

The former strategy inspired the research of $EuTiO_3$, in which the interactions between the *f*-electrons are considered for magnetism. However, the low magnetic ordering temperature (eg. $EuTiO_3$, $T_N \approx 5$ K)[32] resulting from the tightly bound *f*-electrons limits the application of this type of materials.

The latter strategy has attracted great interest and extensive research. Recently much attention has been focused on attempts of utilizing the complex structural distortions observed in perovskite frameworks to prepare non-centrosymmetric (NCS) ferroelectric phases in the absence of SOJT cations.

1.6.2 Inducing ferroelectricity in phases with perovskite-like framework

As discussed earlier in this Chapter, section 1.1.1, the perovskite structure can accommodate combinations of A- and B-cations with a large range of radius ratios (parameterized by the tolerance factor *t*) due to the mechanical flexibility imparted into perovskite frameworks by the facile collective rotations of the constituent, apex-linked, BO_6 octahedra. The cooperative tilting of the BO_6 octahedra lowers the crystallographic symmetry of the perovskite framework, and results in associated displacements of A-cations, which potentially could be utilized to break the inversion symmetry. Unfortunately in a material in which the BO_6 units are continuously linked in all three dimensions, the reciprocal nature of the collective rotations of the apex-linked BO_6 units in perovskite frameworks results in a cancellation of the

dipole moments, thus the material adopts a centrosymmetric structure. For example, in $GdFeO_3$ perovskite framework with a distortion described as ($a^-a^-c^+$) by Glazer notation, the collective rotations of the BO_6 units drive a coupled displacement of the A-cations to the 'left' and 'right' as indicated by arrows in Figure 1a. In the lattice, the direction of the A-cation displacement inverts between adjacent layers, and thus this structure is described in the centrosymmetric space group *Pnma*.

This reciprocal feature indicates that to break the inversion symmetry, one phase should either adopt a structure with A-site/B-site cation order[33-36], or a structure with a lower dimensionality such as those layered variants of perovskite structure[34].

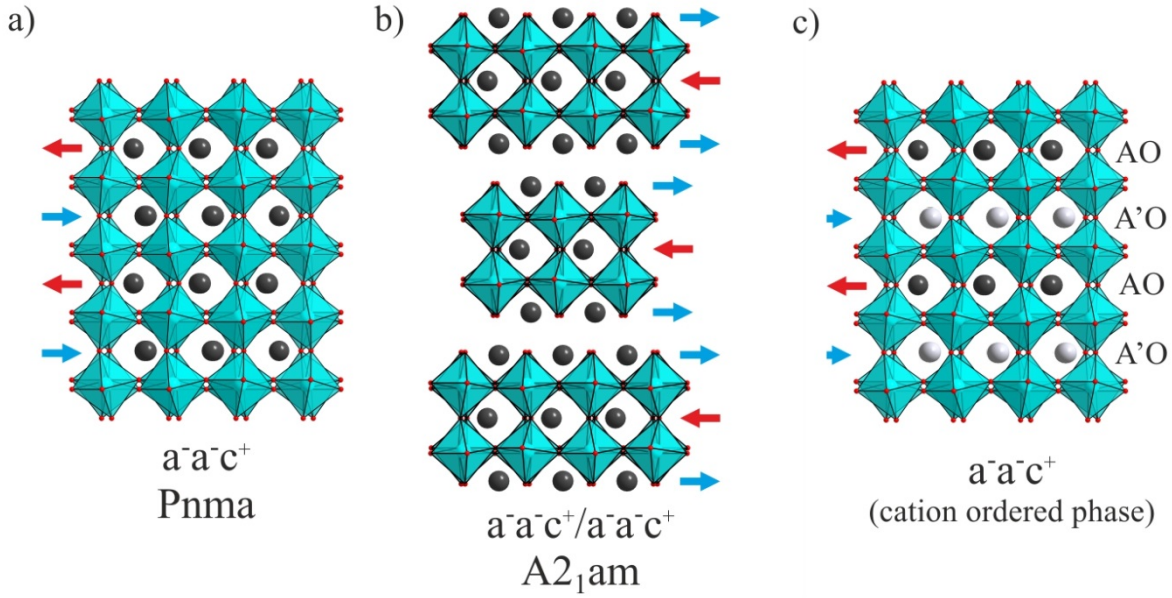


Figure 1.8. a) The $GdFeO_3$ distorted perovskite structure ($a^-a^-c^+$), b) The n = 2 Ruddlesden-Popper phase with $A2_1am$ ($a^-a^-c^+$/ $a^-a^-c^+$) distortion, and c) The ($a^-a^-c^+$) distortion in cation ordered phases.

For example, as shown in Figure 1.8, for an A-cation ordered phase (A/A')B_2O_6, the displacement of each A/A'-cation associated with the cooperative tilting of BO_6 octahedra is noted by the arrow. If A- and A'-cations are the same, their displacement with respect to the O^{2-} anions should also be the same, and thus be cancelled as discussed in $GdFeO_3$. If A- and A'-cations are different, the cancellation is not exact, thus gives a net non-zero dipole moment[34].

However, the preparation of cation ordered perovskite phases is also a significant synthetic challenge. The need to prepare cation-ordered phases can be avoided by lowering the dimensionality of the lattice.[37] For example, in those layered variants of perovskite structures, such as the n = 2 Ruddlesden-Popper phase $Ca_3Mn_2O_7$ with an acentric space group $A2_1am$, the BO_6 octahedra are not linked in all 3-dimentions, and thus the cooperative BO_6 rotations and associated A-cation displacements do not cancel and inversion symmetry is broken.

1.6.3 Inducing ferroelectricity in n = 2 Ruddlesden-Popper phases

As mentioned above, the prospect of preparing NCS phases by utilizing the tilting distortions of n = 2 Ruddlesden-Popper phases is very attractive. A recent study by Pitcher et al.[38] has investigated a case in tuning the tilting distortion of Fe^{3+} based Ruddlesden-Popper phase to induce ferroelectricity.

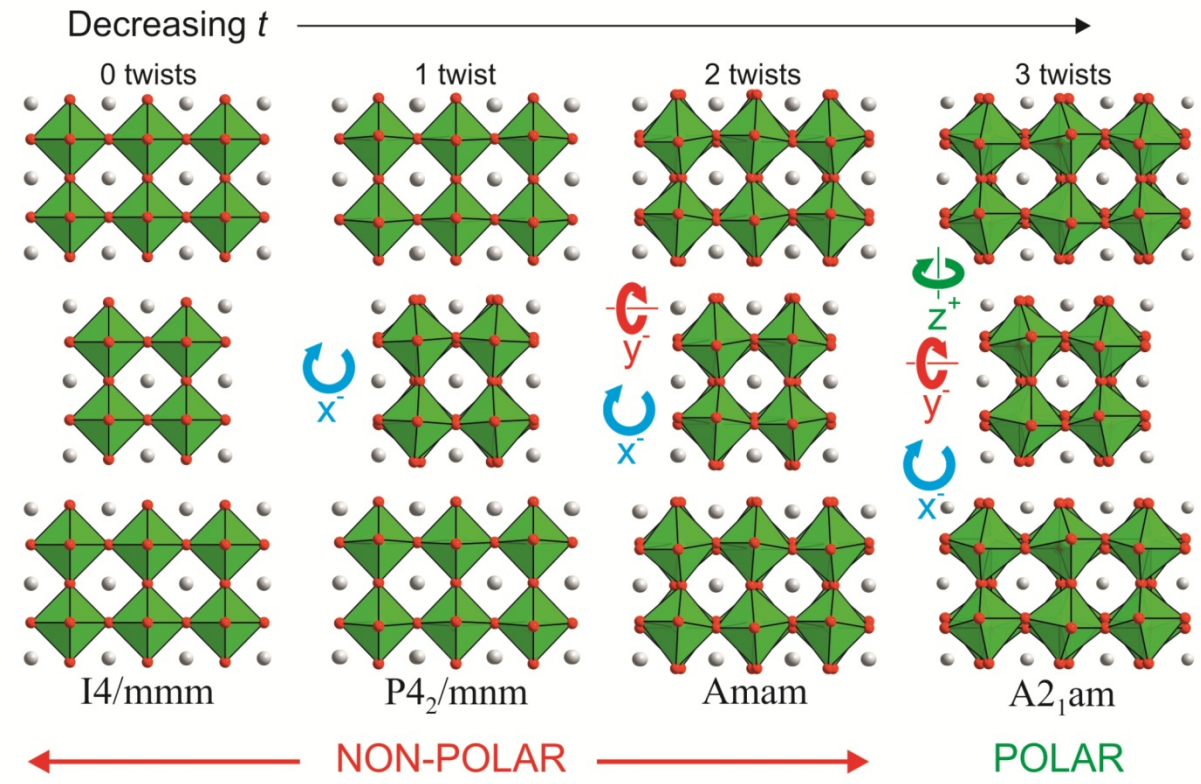


Figure 1.9. Tuning the tilting distortion in n = 2 Ruddlesden-Popper phase to induce ferroelectricity.

As shown in Figure 1.9, smaller cations were substituted onto the A-cation site to drive the framework to adopt increasingly distorted arrangement (tolerance factor t becomes smaller);

$La_2BaFe_2O_7$ adopts an undistorted *I4/mmm* structure, $Tb_2SrFe_2O_7$ *P4₂/mnm* ($a^-b^0c^0/b^0a^-c^0$), $Tb_2CaFe_2O_7$ *Amam* ($a^-a^-c^0/ a^-a^-c^0$). However it was not possible to drive the framework to adopt the desired *A2₁am* ($a^-a^-c^+/ a^-a^-c^+$) structure as the tolerance factor required to stabilize the desired polar *A2₁am* distortion is extremely small. Instead partial substitution of the B-site Fe^{3+} by Ti^{4+} (an SOJT cation) was required to achieve the *A2₁am* distortion. This suggests that the stabilization of the *A2₁am* distortion in phases containing small, paramagnetic transition metal B-cations (a necessary prerequisite for magnetoelectric behaviour) will only be possible in a few exceptional cases.

1.7 Aim of research

This research aims to investigate structures and properties of some *n* = 2 Ruddlesden-Popper oxide phases ($A_3B_2O_7$; A = La, Y, Sr or Ca; B = Cr, Ni or Mn) and their topochemically fluorinated phases. Chapter 3 aims to investigate the highly distorted structure of $La_2SrCr_2O_7$ and associated unusual Sr/La distribution over the A-sites. Chapter 4 aims to investigate physical properties of an *n* = 2 Ruddlesden-Popper phase with octahedrally coordinate Cr^{4+} centres ($La_2SrCr_2O_7F_2$) prepared via topochemical fluorination. Chapter 5 discusses the A-site doping in $La_2SrCr_2O_7$ and corresponding fluorinated phases. As discussed in Chapter 6, the structural modification observed in topochemical fluorination of $La_2SrCr_2O_7$ inspires us to investigate the fluorination of $La_3Ni_2O_7$ to examine if this could drive a structural change from *Amam* ($a^-a^-c^+/ a^-a^-c^+$) to the highly desired ferroelectric *A2₁am* ($a^-a^-c^+/ a^-a^-c^+$) structure. Chapter 7 investigates if a new *n* = 2 Ruddlesden-Popper phase with *Amam* ($a^-a^-c^0/a^-a^-c^0$) lattice distortion could be prepared by lowering the tolerance factor of the existing phase, $YSr_2Mn_2O_7$, with *P4₂/mnm* ($a^-b^0c^0/b^0a^-c^0$) lattice distortion. Chapter 8 investigates if the fluorination of $YSr_2Mn_2O_7$ could drive a structural change from *P4₂/mnm* ($a^-b^0c^0/b^0a^-c^0$) lattice distortion to the ferroelectric *P2₁nm* ($a^-b^0c^+/b^0a^-c^+$) lattice distortion.

Chapter 2: Experimental methods

2.1 Synthetic methods

2.1.1 Ceramic method

Conventional ceramic synthesis techniques were used for the preparation of some thermodynamically stable phases discussed in this thesis. This synthesis strategy involves heating mixtures of binary metal oxides and/or metal oxy-acid salts (carbonates, nitrates, chlorides, etc.) at high temperature. High reaction temperatures (T > 1000 °C) are generally required to overcome large energetic barriers to diffusion of reagents. The reaction rate of this type is largely limited by the intrinsically poor ionic diffusion in metal-oxide phases. Compressing samples into condensed pellets is used to improve grain contact of reagents, and thus increase the reaction rates. Moreover, it is of great importance to grind reagent mixtures intensively in order to form a homogenous product. During the preparation of samples discussed in this thesis, the sample reagents were ground thoroughly and then pressed into 13 mm diameter pellets under 5 tonnes of force. Multiple heating periods (~ 2 days) with regular grinding in between each heating were performed on sample pellets to reach a single phase or equilibrium. The reaction process was monitored via X-ray powder diffraction.

The use of metal carbonates as reagents requires a pre-heating at 900 °C for 12 h with a slow ramp rate of 1 °C/min before being pressed into pellets. Exact synthetic procedures for each phase are detailed in the appropriate chapters.

2.1.2 Citrate gel method

The citrate gel synthetic route allows the preparation of more homogenous reagent mixtures, and thus offers a strategy to reduce reaction times and lower reaction temperatures required by conventional ceramic methods. This method was first reported by M. Pechini.[39] It involves the use of citric acid and ethylene glycol. Citric acid is a common tridentate ligand which binds

strongly to a wide variety of metal cations. In a typical synthesis, suitable amounts of each reagent (binary metal oxides and/or metal oxy-acid salts) are dissolved in a 1:1 (v/v) solution of nitric acid in distilled water. An excess amount of citric acid is then added to form metal-citrate chelate complexes, followed by a suitable amount of ethylene glycol. On heating, the presence of metal-citrate and ethylene glycol drives an efficient condensation polymerization, resulting in the formation of a polyester network trapping a homogeneous array of coordinated metal cations[40]. A highly viscous gel is thus formed. The gel is then heated at 200 ~ 400 °C to combust the organic component. A loose black powder is obtained. The powder is ground and then heated to 1000 °C in air at a rate of 1 °C/min to remove the remaining organic components. The resulting powder is then pressed into pellets for further heating treatments.

2.2 Topochemical fluorination

As discussed in Chapter 1, fluoride ions can be inserted into a Ruddlesden-Popper structure. This type of topochemical fluorination reaction can be performed by using dilute fluorine gas or binary metal fluoride MF_2 (M = Ni, Cu, Zn, Ag)[41] as fluorine sources. The use of MF_2 as fluorine sources eases the practical difficulties associated with handing and performing reactions with fluorine gas. During the fluorination, the metal fluorides act as an *in situ* source of fluorine through reactions with atmospheric oxygen as described by Scheme (S1), and the released fluorine then reacts with the host phase (e.g. an n = 2 Ruddlesden-Popper phase $A_3B_2O_7$) to give the overall reaction as describe by Scheme (S2).

$$\mathbf{MF_2 + \frac{1}{2}O_2 = MO + F_2} \qquad \textbf{(S1)}$$

$$\mathbf{A_3B_2O_7 + CuF_2 \xrightarrow{O_2} A_3B_2O_7F_2 + CuO} \quad \textbf{(S2)}$$

Binary metal fluoride CuF_2 was used to fluorinate phases discussed in this thesis. One way to perform a fluorination reaction by using CuF_2 is to grind suitable amount of reagents ($A_3B_2O_7$ and CuF_2) together, followed by heating at an optimized reaction temperature. However,

as shown in reaction S2, samples fluorinated in this way would be inevitably contaminated with the CuO by-products, which are often hard to remove. The presence of the CuO would make structural analysis of fluorinated phases more difficult.

Another effective way to perform a fluorination reaction by using CuF_2 is to place the $A_3B_2O_7$ sample and CuF_2 separately in adjacent furnaces as shown in Figure 2.1. In a typical fluorination reaction performed in this way, the CuF_2 is heated at 500 °C under flowing oxygen to liberate fluorine. The resulting O_2/F_2 gas mixture is then passed over a sample of $A_3B_2O_7$ powder, held at optimized reaction temperature in the adjacent furnace. This avoids contamination of samples with CuO which occurs when mixing the CuF_2 with mixed directly into the sample as discussed above.

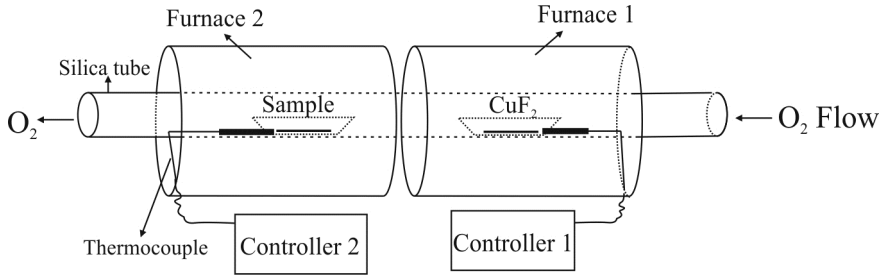


Figure 2.1. Fluorination reaction setup with placing $A_3B_2O_7$ sample and CuF_2 placed separately in adjacent furnaces

2.3 Diffraction

2.3.1 X-ray diffraction

X-rays are electromagnetic radiation of wavelength ~ 1 Å and can be scattered by electrons in an atom elastically; that is, the outgoing X-rays have the same energy and thus the same wavelength as the incoming X-rays, only with altered direction. When X-rays interact with a crystal with regularly repeating structure, a diffraction pattern is produced by interference effects. The diffraction of X-rays by a crystal can be treated in terms of reflection from sets of lattice planes. Constructive interference between reflected beams is only satisfied if their path difference is an integral number of wavelengths. As shown in Figure 2.2, given an incident beam

with incident angle θ, the path difference between reflected beams is calculated to be $2dsin\theta$, the value of which is required to be an integral number of wavelengths $n\lambda$. This selective condition is described by Bragg's law (S3):

$$\boldsymbol{2dsin\theta = n\lambda} \qquad \textbf{(S3)}$$

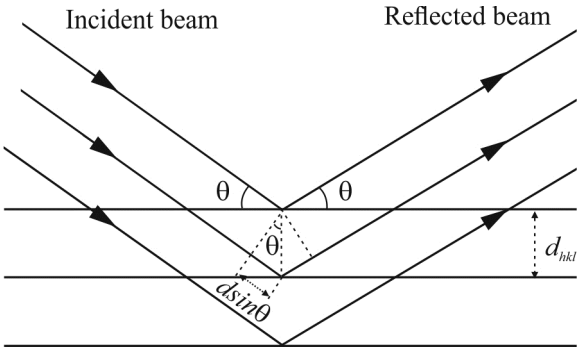


Figure 2.2. Schematic representation of X-ray diffraction by a crystal.

Braggs law gives only the geometrical condition for a reflection to occur. The observed reflection intensity depends on several factors. A major factor that affects the relative intensity of a given (*hkl*) reflection (I_{hkl}) is the structure factor F_{hkl} as described by S4 and S5:

$$\boldsymbol{I_{hkl} \propto F_{hkl}^2} \qquad \textbf{(S4)}$$

$$\boldsymbol{F_{hkl} = \sum_j f_j \exp\left[2\pi i(hx_j + ky_j + lz_j)\right]}$$

$$= \textstyle\sum_j \boldsymbol{f_j \cos\left[2\pi(hx_j + ky_j + lz_j)\right]} + \boldsymbol{i}\textstyle\sum_j \boldsymbol{f_j \sin\left[2\pi(hx_j + ky_j + lz_j)\right]} \qquad \textbf{(S5)}$$

where this is the sum is of all atoms in the unit cell; x_j, y_j, z_j are the positional coordinates of the *j*th atom; and f_j is the scattering factor (form factor) of the *j*th atom[42].

The form factor of an atom is proportional to its atomic number, Z, or, more strictly, to the number of electrons possessed by that atom. In addition, in a given atom, the reflected beams from different electrons at different positions differ in phase. This phase difference is usually rather less than one wavelength because of the short distances between electrons within an atom. As a result, only partial destructive interference occurs between diffracted beams from different

electrons. This leads to a gradual decrease in the scattering powder of a certain atom with increasing angle 2θ.[42]

For completeness, the effect of thermal motion which essentially acts to blur the position of each atom also needs to be introduced to the structure factor described in S5, by using an additional multiplicative factor $\boldsymbol{exp}(-\boldsymbol{B_j}\frac{\boldsymbol{sin^2\theta}}{\boldsymbol{\lambda^2}})$.[42] Thus taking into consideration the thermal motion, the structure factor can be described by S6:

$$\boldsymbol{F_{hkl}} = \sum_j \boldsymbol{f_j} \mathbf{exp}\left[\boldsymbol{2\pi i}(\boldsymbol{hx_j} + \boldsymbol{ky_j} + \boldsymbol{lz_j})\right]\boldsymbol{exp}(-\boldsymbol{B_j}\frac{\boldsymbol{sin^2\theta}}{\boldsymbol{\lambda^2}}) \qquad \textbf{S(6)}$$

where B_j is related to the mean square amplitude of vibration, and is found to be proportional to temperature.

Apart from the structure factor, reflection intensity also depends on other factors, some of which depend upon the experimental technique employed and some upon the composition and physical nature of crystal solids. These factors include Lorentz polarization factor, the multiplicity factor and the absorption factor.[42]

2.3.2 X-ray powder diffractometer

In a typical X-ray powder diffractometer, the X-rays are generated by firing electrons at a metal target. The electron beam provided by a heated tungsten filament is accelerated towards an anode by a potential difference of ~ 30 kV. The electrons strike the target, most commonly a piece of copper fixed to the anode, and a spectrum of X-rays is emitted. This process takes place in a chamber under vacuum which is known as the X-ray tube (Figure 2.3). Emitted X-rays leave the tube through a beam window made of beryllium. The anode needs continuous cooling to avoid overheating during the generation of X-rays. For most diffraction experiments, a monochromatic beam of X-rays is desired. For copper radiation, a sheet of nickel foil is used to filter out Cu Kβ radiation and most of the white radiation, leaving a beam of Kα radiation. A crystal monochromator can be mounted on the incident beam to screen out Kα2 radiation, giving

an array of relatively clean beam containing mostly Kα1. The incident X-ray beam passes through a series of slits to collimate the beam before spotting on the sample. The goniometer utilizes a Bragg-Brentano geometry such that reflection from the sample results in the diffracted beam being refocussed at the detector provided that the sample holder is rotated at half the speed of the detector (Figure 2.3).[42]

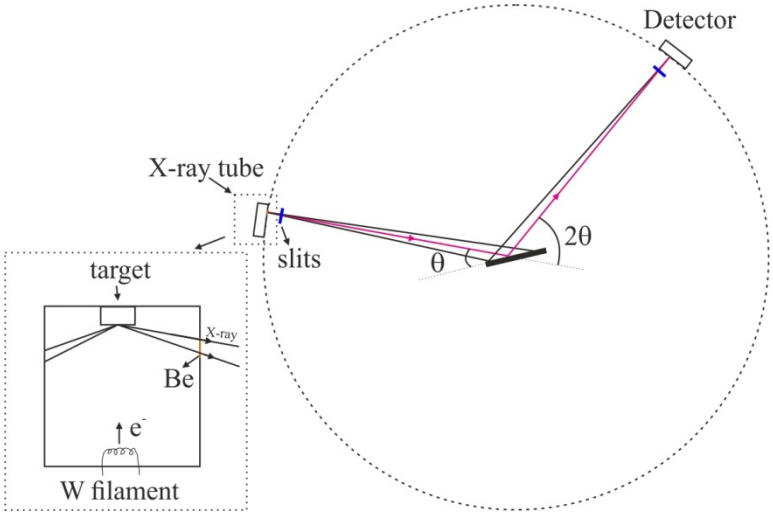


Figure 2.3. Schematic design of an X-ray tube and Bragg-Brentano diffraction geometry.

The PANalytical X'pert diffractometer used in this work is a high resolution instrument operating in Bragg-Brentano geometry. A crystal monochromator, Ge (111), is equipped on this instrument to select exclusively Kα1 radiation. A pair of 0.04 mm soller slits is used to collimate both incident and reflected beams. The PANAlytical Empyrean, similar to the PANalytical X'pert introduced above, is also used in this work.

A silicon wafer cleaved along the systematically absent (110) plane was used as a sample holder for X-ray diffraction. During the measurement, the wafer is rotated at 30 rpm to minimise contribution from a non-uniform distribution of the sample.

2.3.3 Synchrotron X-ray powder diffraction and diffractometer

Compared to a lab X-ray source, a synchrotron source provides a mechanism for generating an intense beam of high-energy photons. It is a fundamental principle of physics that charged particles give off electromagnetic radiation when accelerated. In a synchrotron, an

electron travelling in a circular orbit is constantly accelerated in a radial direction by using bending magnets (Figure 2.4), undulators and/or wigglers. Thus the circular beam continuously loses energy as photons, which is known as synchrotron radiation. There are two clear advantages of synchrotron radiation over a lab X-ray source. One is that the wavelength of the photons is completely tuneable by using suitable crystal monochromators. The other advantage is that the intensity of the photons is increased by many orders of magnitude due to the high efficiency.

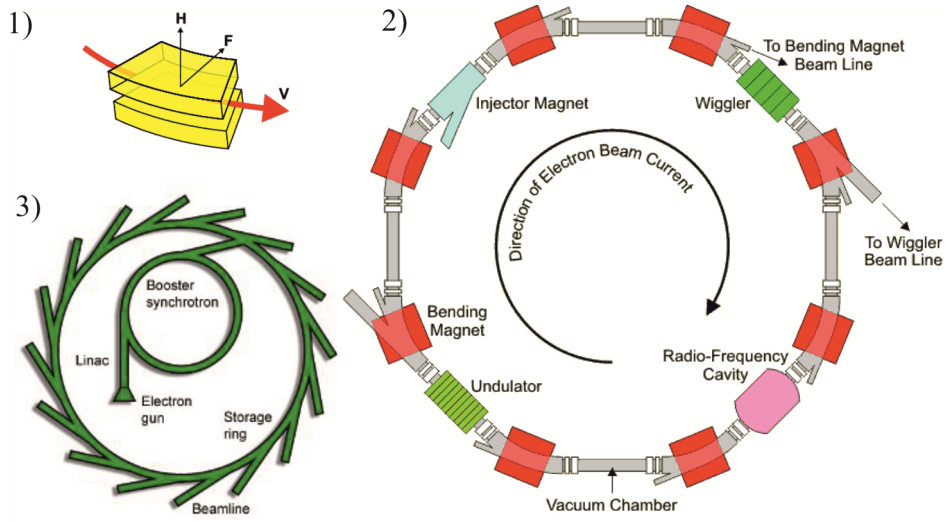


Figure 2.4. (1) Bending magnet[43]; (2) Schematic of a synchrotron storage ring[43]; (3) Schematic design of Diamond synchrotron source[44].

The schematic design of the Diamond synchrotron source is shown in Figure 2.4. Electrons are generated in an electron gun and then fired into a linear accelerator (*linac*) connected to a booster ring. The linac and the booster synchrotron ring work to accelerate the electrons to nearly light speed. These high speed electrons enter the storage ring. The storage ring is in fact not a true circle, but a type of polygon made of straight sections angled together with bending magnets as shown in Figure 2.4. Electron beams circulate the storage ring, and continuously loses energy as photons when its travel path is bent by the magnets.

I11 is a high resolution powder diffraction beamline at Diamond Light Source that produces X-rays ranging from 5-30 keV[45]. A double-crystal-monochromator (DCM) comprising two liquid nitrogen cooled Si(111) crystals are used in the optics hutch to select the desired beam

energy for diffraction. Samples are loaded in capillaries and mounted on the instrument. The position sensitive detector (PSD) can be used for a fast data collection (~ 1 min). The PSD uses the Microstrip system for time-resolved experiment silicon microstrip technology (MYTHEN-II), providing wide-angle powder diffraction data with high resolution. The Multi-Analyser Crystal (MAC) detector is mounted with five identical nine-crystal MAC-arms, which gives a better resolution compared to PSD[45].

2.3.4 Neutron diffraction

2.3.4.1 Nuclear neutron diffraction

Whereas the scattering process in X-ray diffraction occurs via interaction of the X-ray with the electron cloud of each atom in the material, in neutron diffraction the interaction is with the atomic nuclei. Similar to that of X-ray diffraction, the neutron scattering intensity I_{hkl} is proportional to the structure factor F^2_{hkl}. This structure factor for neutron diffraction as described in S7 is of a similar form as that of X-ray diffraction:

$$\boldsymbol{F_{hkl}} = \sum_j \boldsymbol{b_j} \exp\left[2\pi \boldsymbol{i}(\boldsymbol{hx_j} + \boldsymbol{ky_j} + \boldsymbol{lz_j})\right] \boldsymbol{exp}(-\boldsymbol{B_j}\frac{\boldsymbol{sin^2\theta}}{\boldsymbol{\lambda^2}}) \qquad \textbf{(S7)}$$

where the b_j is the neutron scattering length for the atom j, an indicator describing how strongly a certain atom scatters neutrons. In contrast to the X-ray diffraction form factor whose value is proportional to atomic number Z, the neutron scattering length is not strongly dependent on Z since the neutron interaction with nuclei over distances much shorter than the neutron wavelength. This feature offers a great chance in separating atoms with a similar X-ray diffraction form factor. The neutron scattering lengths of atoms discussed in this thesis are listed in Table 2.1.[46] In addition, unlike the X-ray diffraction form factor, the neutron scattering length for a certain atom is largely independent of the scattering angle. This can be ascribed to the small size of nuclei such that the neutron interacts with the atomic nuclei over a distance much shorter than the neutron's wavelength and thus destructive interference can be safely neglected.

Apart from the structure factor, the intensity of neutron diffraction also depends on many other factors. For example, in a time-of-flight neutron powder diffraction measurement, the integrated intensity of neutron diffraction can be affected by incident neutron flux and detector efficiency at a certain wavelength, sample volume, and reflection multiplicity.[47]

Element	Scattering length (fm)	Element	Scattering length (fm)
O	**5.803(4)**	Y	**7.75(2)**
F	**5.654(10)**	Sr	**7.02(2)**
La	**8.24(4)**	Ca	**4.80(2)**

Table 2.1. Bound coherent neutron scattering lengths for selected atoms[46].

2.3.4.2 Magnetic neutron diffraction

Another important feature of neutron diffraction arises from a fundamental property of neutron: its spin. This suggests as well as scattering from atomic nuclei, the neutron can interact with electron spins, giving an additional magnetic scattering. For an unpolarised incident neutron beam, the total scattered intensity is the pure sum of the nuclear and magnetic scattering.

$$\boldsymbol{I_{total} = I_{nuc} + I_{mag}} \qquad \textbf{(S8)}$$

$$\boldsymbol{F_{total} = F_{nuc} + F_{mag}} \qquad \textbf{(S9)}$$

$$\boldsymbol{F_{mag} = \sum_{j} \vec{q_j} p_j exp(2\pi i \vec{h} x_j)}$$

where F_{mag} is the magnetic structural factor, the summation is over all the magnetic atoms in the unit cell; x_j is the position vectors of the magnetic atoms; $\vec{h}$ is scattering vector; p is the magnitude of magnetic scattering length; and $\vec{q}$ is the magnetic interaction vector. The magnetic scattering length of a certain atom is proportional to its form factor f_m. Like the X-ray diffraction form factor, the neutron magnetic diffraction form factor decreases with decreasing d-spacing (increasing 2θ). This is because the magnetic scattering process involves an interaction with electrons in an atom over distances comparable to neutron wavelength.

Moreover, because of the complex nature of magnetic interaction, the nuclear unit cell and the magnetic unit cell are not necessary of the same dimension. Magnetic measurements are

often characterised by the appearance of magnetic scattering peaks at high *d*-spacing and/or dramatic changes in intensities of existing reflections.

2.3.4.3 Generation of neutron beam

There are two basic ways of generating neutron beams. One is though fission of ^{235}U nuclei in a nuclear reactor — a reactor source of neutrons. The other is though firing a beam of charged particles at a dense target made of a heavy element (usually uranium) — accelerator-based source of neutrons. The neutron beam generated in this way is ideally suited to the time-of-flight neutron diffraction technique.

For the reactor source of neutrons, moderators are used in the reactor to slow down the neutrons to maintain the fission reaction. The moderator normally contains large numbers of low mass nuclei (usually H or D). The neutron flux produced in a reactor is unchanging with time and covers a wide range of neutron wavelengths. During a neutron diffraction experiment, the neutron beam is monochromated to a selected narrow range of wavelengths.

For the accelerator-based source of neutron (Figure 2.5)[48], the neutrons are generated when a beam of charged and accelerated particles with a high energy is fired at a target. The charged particles (usually protons) can be accelerated by using a linear accelerator together with a synchrotron. Interactions between the proton beam and the nuclei in the target produce high energy neutrons which are then slowed down by a moderator. The accelerator-based source usually produces a pulsed neutron flux which is ideally suited to the time of flight (TOF) technique.

The TOF technique involves measuring the time taken for a neutron to travel the total flight path *L* from the moderator to the detector. The detector is fixed at a certain angle (2θ). A sample is irradiated with a pulsed neutron beam containing neutrons of many different wavelengths. As the neutron's wavelength is related to its momentum through the de Braglie

relationship, it is straightforward to calculate the *d*-spacing by combining the equation S10 and S11. The equation becomes S12 if substituting values for Planck's constant and the neutron mass.

$$\boldsymbol{\lambda = \frac{h}{mv}} \qquad \textbf{(S10)}$$

$$\boldsymbol{2dsin\theta = n\lambda} \qquad \textbf{(S11)}$$

$$\boldsymbol{d = \frac{h}{2m} \times \frac{t}{Lsin\theta} = 1.997 \times 10^{-3} \frac{t}{Lsin\theta} / \text{Å}} \qquad \textbf{(S12)}$$

The resolution function using a time-of-flight diffractometer can be defined by equation S13 while the resolution function using a reactor diffractometer (constant wavelength) can be defined by equation S 14[49].

$$\boldsymbol{\frac{\Delta d}{d} = \sqrt{(\frac{\Delta t}{t})^2 + (\frac{\Delta L}{L})^2 + (\Delta\theta cot\theta)^2}} \qquad \textbf{(S13)}$$

$$\boldsymbol{\sigma^2 = \frac{FWHM^2}{8 \ln 2} = Utan^2\theta + Vtan\theta + W} \qquad \textbf{(S14)}$$

where Δd is the width of a reflection with *d*-spacing *d*. The three terms in S13 can be considered as fixed for a given moderator and a fixed detector, thus $\Delta d/d$ is almost a constant. In contrast, for a constant wavelength diffractometer, the general expression in S14 suggests that the reflection widths increase with increasing 2θ (decreasing *d*-spacing). Therefore, a better resolution, especially at lower d-spacing (higher 2θ), can be achieved by the TOF technique.

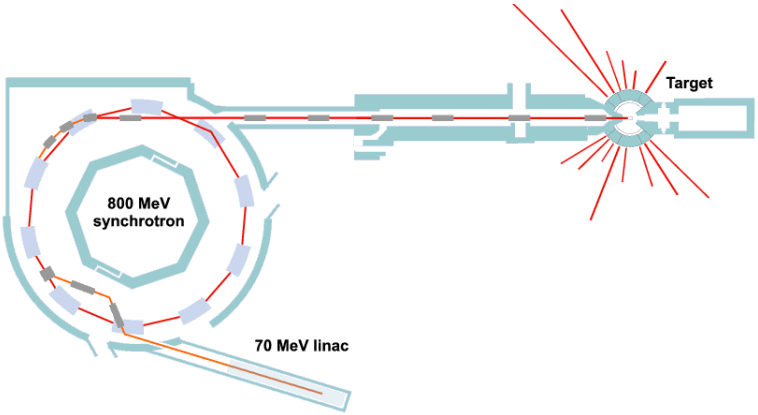


Figure 2.5. The generation of neutrons from the accelerator-based source.[48]

2.3.4.4 The advantages of neutron diffraction over X-ray diffraction

Compared to the X-ray diffraction, the neutron diffraction has the following advantages:

(1) As discussed in Section 2.3.1 and 2.3.4.1, unlike X-ray diffraction, the neutron scattering length and atomic number of a certain atom is independent. Thus some atoms that have a similar number of electrons can be better distinguished though neutron diffraction rather than X-ray diffraction. Moreover, in structures where heavy elements dominate the X-ray diffraction, the position of the lighter atoms (especially oxygen whose position is essential for the structural analysis of perovskite phases) is difficult to confirm from the X-ray diffraction data. In neutron diffraction, the scattering powers of most atoms do not differ sharply in values.

(2) The hydrogen atom which is virtually invisible to X-rays becomes recognizable through neutron diffraction since it has a negative neutron scattering length.

(3) As discussed in Section 2.3.2 and 2.3.4.1, the X-ray form factor of a certain atom decreases with increasing 2θ (low *d*-spacing) whereas its neutron scattering power is independent of the scattering angle. Hence the structure information at high angle is better achieved by the neutron diffraction.

(4) Neutrons have a magnetic spin that can interact with unpaired electrons, providing information of the magnetic structure of the sample measured, as discussed in Section 2.3.4.2.

2.3.5 Neutron powder diffractometer

2.3.5.1 ISIS Facility

The neutron source at the ISIS Facility is an accelerator-based, pulsed source of neutrons. Three diffractometers, GEM, POLARIS, HRPD, are used to determine the atomic and/or magnetic structure of phases discussed in this work. The positions of these three diffractometers are shown in Figure 2.6.

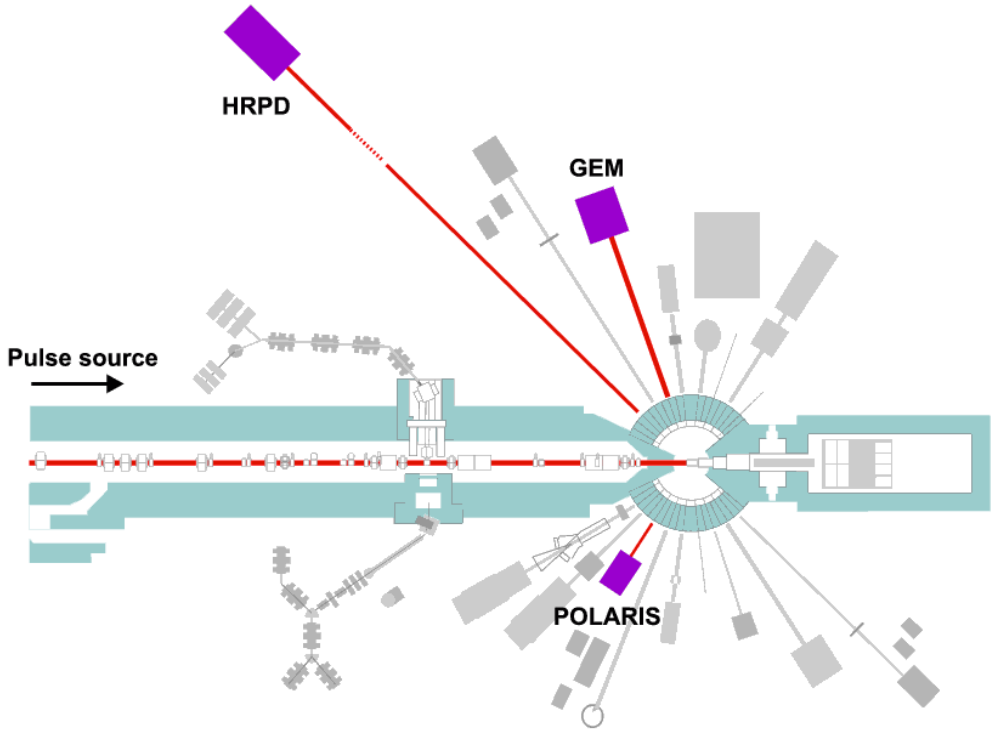


Figure 2.6. The layout of GEM, POLARIS and HRPD at ISIS Facility.[48]

2.3.5.2 GEM diffractometer

The General Materials Diffractometer (GEM) at the ISIS Facility pulsed neutron source (Figure 2.7) is a good-resolution, wide-angular-range, high-flux powder diffractometer.[50,51] The GEM detectors divided into 8 banks cover a scattering angle range from 1.1° to 169.3°, and are also extremely stable with a 0.1% variation in efficiency over a 24 *h* period[52]. The incident flight path of GEM from moderator to sample is L1 = 17 m[53]. This relatively long flight path leads to a high resolution as can be deduced from equation S13, giving an excellent resolution of $\Delta d/d \approx 0.34\%$[52]. The high resolution in high *d*-spacings offers a great opportunity for the observation and characterization of sample's magnetic scatterings as discussed in Section 2.3.4.2.

The GEM diffractometer was used to characterize $La_2SrCr_2O_7$ and $La_2SrCr_2O_7F_2$ as discussed in Chapter 3 and Chapter 4. Samples are loaded in cylindrical vanadium cans that are electron beam welded, and transparent to neutrons with a temperature range from 2K to 1273K.

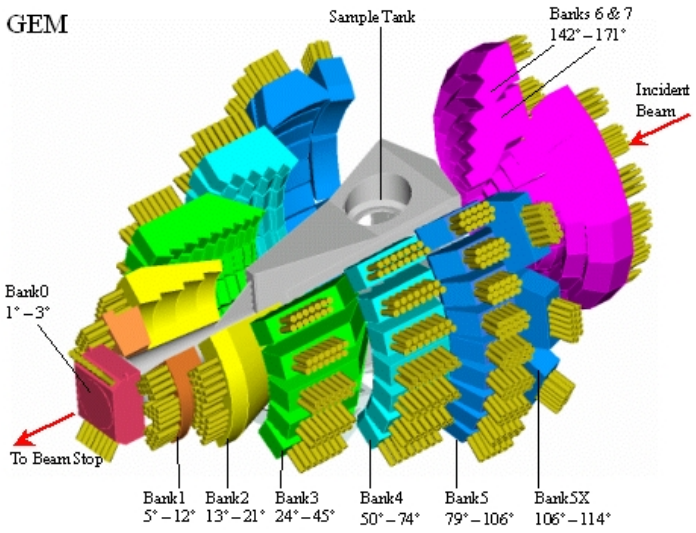


Figure 2.7. The GEM diffractometer at the ISIS Facility pulsed neutron source.[51]

2.3.5.3 POLARIS diffractometer

The POLARIS instrument at the ISIS Facility pulsed neutron source (Figure 2.8) is a high intensity, medium resolution powder diffractometer. It is optimised for the rapid characterisation of structures and the study of small amounts of materials. The incident flight path of POLARIS from moderator to sample is L1 = 12 m, shorter than that of GEM. POLARIS has a total of 434 ^{3}He gas and ZnS scintillator detectors arranged into four separate banks: two at low angles, one at 2θ~90° and one at backscattering angles. Details of these detector banks are given in Table 2.2.[54] The 90 degree bank and the back scattering bank have a resolution as high as $\Delta d/d \approx 0.7\%$ and 0.5% respectively, comparable to that of the GEM diffractomer. The POLARIS diffractometer was used to characterize $La_3Ni_2O_{5.5}F_{3.5}$ as discussed in Chapter 6.

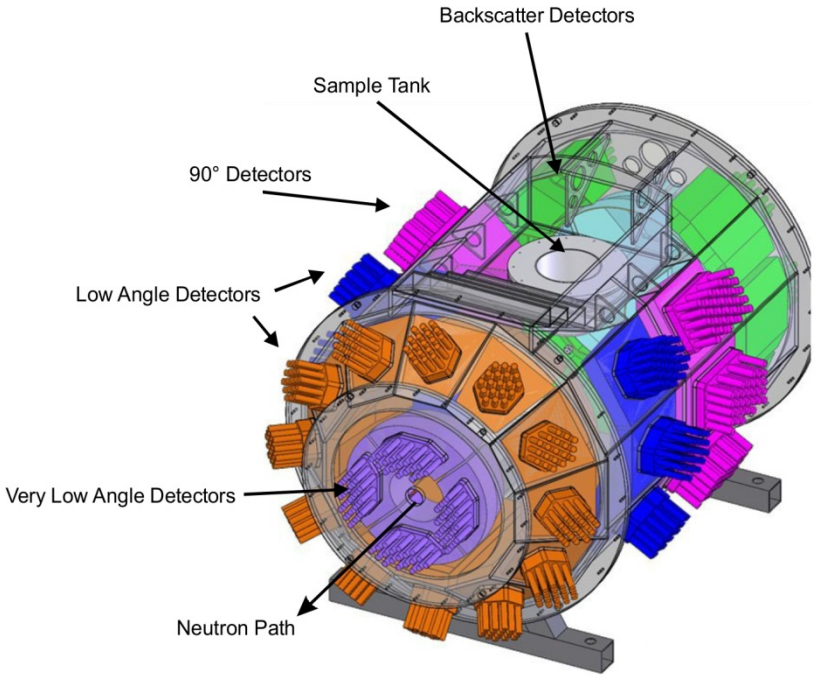


Figure 2.8. The POLARIS diffractometer at the ISIS Facility pulsed neutron source.[54]

	Very low angle	**Low angle**	**90 degrees**	**Back scattering**
Type	ZnS scintillator	^{3}He gas tubes (½")	ZnS scintillator	^{3}He gas tubes (1")
No. of detectors	80	80	216	58
2Θ range	13° - 15°	28° - 42°	85° - 95°	130° - 160°
Ω(ster)	0.009	0.046	0.48	0.29
Resolution (Δd/d)	3×10^{-2}	1×10^{-2}	7×10^{-3}	5×10^{-3}
L_2(m)	~ 2.2	1.72 - 2.65	~0.8	0.60 - 1.30
d range (Å)	0.5 - 21.0	0.5 - 8.15	0.3 - 4.1	0.2 - 3.2

Table 2.2. Parameters of the detectors mounted on POLARIS at ISIS Facility. [54]

2.3.5.4 HRPD diffractometer

HRPD is a high resolution powder diffractometer at the ISIS Facility. As shown in Table 2.3, the resolution for the back scattering bank achieve a resolution as high as ~ 0.04 % (~ 0.34 % for GEM). The high resolution arises from the long light path from moderator to sample, L1 ≈ 100 m (17 m for GEM), which thus minimizes the $\Delta L/L$ term in equation S13. This high resolution allows us to study the subtle distortions of the apex-linked octahedra in perovskite phases.

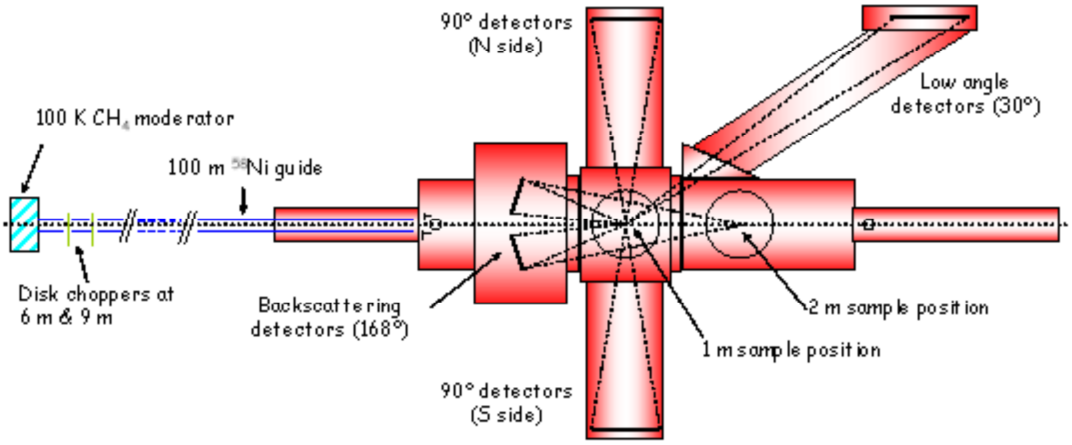


Figure 2.9. The schematic plan view of the HRPD detector configuration.[55]

Position	**Low angle**	**90 degrees**	**Back scattering**
Detector Specification	10atm ^{3}He gas tubes (½")	ZnS scintillator	ZnS scintillator
2Θ range	28° - 32°	87° - 93°	160° - 176°
Ω(ster)	0.01	0.08	0.41
Resolution (Δd/d)	~ 2×10^{-2}	~ 2×10^{-3}	~ 4-5 × 10^{-4}
d range (Å)	~ 2.2 – 16.5	~ 0.9 - 6.6	0.6 – 4.6

Table 2.3. Parameters of the detectors mounted on HRPD at the ISIS Facility.

2.3.5.5 D2B diffractometer

D2B (Figure 2.10) is a constant wavelength powder diffractometer at ILL (Grenoble), a reactor based neutron source. It was designed to achieve the ultimate resolution, limited only by powder particle size to give a $\Delta d/d \approx 0.05\%$ comparable to the resolution of the HRPD back scattering bank. In a typical experiment with the D2B diffractometer, the neutron beam is diffracted by the monochromator at a large take-off angle to obtain high resolution. Different wavelengths can be achieved by a simple rotation of the monochromator. The data are recorded by a bank of 128 moving detectors so that counts can be averaged over several detectors. $La_2Sr_{0.5}Ca_{0.5}Cr_2O_7$ discussed in Chapter 5 was characterized by using the D2B diffractometer.

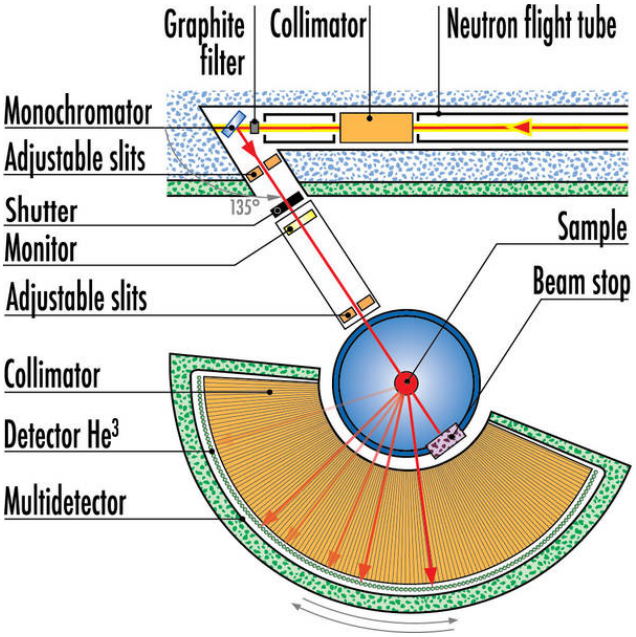


Figure 2.10. The D2B diffractometer at the ILL neutron source.[56]

2.4 Rietveld refinement

Rietveld refinement against diffraction data is a powerful technique developed by H. M. Rietveld to characterize the structure of a material. It uses a non-linear least squares algorithm to minimize the residual function (F) as define by S15:

$$\boldsymbol{F = \sum_i w_i (I_i^{obs} - I_i^{cal})^2 , w_i = \frac{1}{\sigma^2[I_i^{obs}]}} \qquad \textbf{S15}$$

where i indicates the intensity is measured at a 2θ value of $2\theta_i$; I^{obs} is the observed intensity from diffraction data; I^{cal} is the calculated intensity by computer; w_i is a weighting factor; and $\sigma[I^{obs}]$ is the stand uncertainty (s.u.) of the observed intensity. [57] The value of F is minimized only when the calculated model is, or is at least close to, the true model adopted by the material. This serves as a basis for solving the structure of a material by Rietveld refinement. The calculated intensity I^{cal} can be defined by S16:

$$\boldsymbol{I_i^{cal} = S_F \sum_j^{N(phases)} \frac{f_i}{V_j^2} \sum_{k=1}^{N(peaks)} L_k F_{k,j}^2 S_j (2\theta_i - 2\theta_{k,j}) P_{k,j} A_j + bkg_i} \qquad \textbf{S16}$$

Where bkg_i is a background term; $S_F \sum_j^{N(phases)} \frac{f_i}{V_j^2}$ is the scale factor S_j; L_k is the Lorentz-Polarization factor that depends on the instrument (e.g. geometry, monochromator, detector,

sample volume and positioning); $F_{k,j}^2$ is the structure factor (k is multiplicity of the k reflection with hkl Miller indices); $S_j(2\theta_i - 2\theta_{k,j})$ is the profile shape function (e.g. Gaussian, Voigt and Pseudo-Voigt (PV) function); $P_{k,j}$ is the preferred orientation term; A_j is the absorption factor.

2.4.1 Parameters to evaluate the goodness of fit

To indicate the goodness of fit of the calculated model to the data, several parameters have been introduced, including profile factor R_p, weighted profile factor R_{wp}, expected profile factor R_{exp} and the goodness-of-fit χ^2.[57,58] The profile factor is defined as equation S17:

$$\boldsymbol{R_p = \frac{\sum_i (I_i^{obs} - I_i^{cal})^2}{\sum_i I_i^{obs}}} \qquad \textbf{(S17)}$$

The weighted profile factor R_{wp} is defined as shown in equation S18:

$$\boldsymbol{R_{wp} = \frac{\sum_i w_i (I_i^{obs} - I_i^{cal})^2}{\sum_i w_i I_i^{obs}}} \qquad \textbf{(S18)}$$

The expected R_{exp} factor describes an ideal situation where calculated model is the exact real structural model. In this case, the standard uncertainty $\sigma^2 = (I_i^{obs} - I_i^{cal})^2$, and thus $w_i(I_i^{obs} - I_i^{cal})^2 = 1$ and $\sum_i w_i(I_i^{obs} - I_i^{cal})^2$ equals to the number of data points N. The expected R_{exp} factor can be considered as the best possible R_{wp} factor and can be defined by equation S19:

$$\boldsymbol{R_{exp} = \frac{N-P}{\sum_i w_i I_i^{obs}}} \qquad \textbf{(S19)}$$

where P is the number of parameter and can be safely neglected as it is normally sufficiently small compared to the number of data points collected from powder diffraction.

The last parameter, the goodness-of-fit χ^2 is taken as R_{wp}/R_{exp} as shown in equation S20:

$$\boldsymbol{\chi^2 = \frac{R_{wp}}{R_{exp}} = \frac{\sum_i w_i (I_i^{obs} - I_i^{cal})^2}{N-P}} \qquad \textbf{(S20)}$$

χ^2 indicates the goodness of fit of the calculated model to the data. If the model is perfect, then $R_{wp} = R_{exp}$ and thus $\chi^2 = 1$. If $\chi^2 > 1$, it suggests either the calculated model cannot describe the data satisfactorily or the calculated model is still reasonable but the standard uncertainty values are significantly underestimated. The latter case happens when data are collected to high

precision such that minor imperfections in the fit become apparent.[57] In this case the weighted profile factor R_{wp} is a better indicator to evaluate the goodness of fit.

2.4.2 Particle size and strain broadening

The broadening in diffracted peak shape normally arises from the diffractometer and/or the sample. According to the Scherrer equation as shown in S21, a smaller particle size gives a broader peak, especially when the average crystallite size is ≤ 1μm (nano particles).

$$\boldsymbol{B_L = \frac{K\lambda}{Lcos\theta}} \qquad \textbf{(S21)}$$

where B_L is the broadening caused by the particle size; L is the particle size; λ is the radiation wavelength; θ is the usual Bragg angle and K is Scherrer constant.

Another important factor for broader peak shape is the crystal strain. If the crystallite is under a compressive stress, the *d*-spacing will be smaller. Thus by Bragg's law, the value of 2θ (position of the peak) will increase. If the stress is homogeneous throughout the whole lattice shifting of diffraction peaks to higher angle will be observed. If the stress is inhomogeneous, shifting of the diffraction peaks is not consistent, resulting in peaks with different width. Normally sets of broad peaks and sharp peaks will be observed in the same diffraction data. Strain broadening has been observed commonly in a double-layer Ruddlesden-Popper phase containing stacking faults (intergrowth of single layers). Suitable coefficients and profile functions are used to account for broadening of the peaks during Rietveld refinements by using GSAS.

2.5 Thermogravimetric analysis (TGA)

Thermogravimetric analysis (TGA) is used in this work to determine the anion content and/or the oxidation state of the transition metal of a given sample. In a reductive TGA measurement, a sample is heated to a suitable temperature at a heating rate of 5 ºC/min under a flowing 10% H_2/N_2 atmosphere. The mass is continuously recorded as a function of temperature

by using a Mettler-Toledo MX1 thermogravimetric microbalance. The sample then decomposes to a mixture of simple phases confirmed by X-ray powder diffraction. The oxygen content and/or the oxidation state of the transition metal of the measured sample can then be deduced from the mass loss. The detailed procedure and data analysis are detailed in appropriate chapters.

2.6 Iodometric titration

Iodometric titration (Iodometry) is one of the most important titration methods widely used in solid state chemistry. Iodometric titration is used in this work to determine the average oxidation states of transition metals. In a typical iodometric titration experiment, sodium thiosulphate solution ($Na_2S_2O_3$) is used as a titre, and is standardized through titrating against a solution of potassium iodate (KIO_3). The reaction can be described by S22 and S23.

$$\mathbf{IO_3^- + 5I^- + 6H^+ \rightarrow 3I_2 + 3H_2O} \qquad \textbf{(S22)}$$

$$\mathbf{I_2 + 2S_2O_3^{2-} \rightarrow 2I^- + S_4O_6^{2-}} \qquad \textbf{(S23)}$$

A sample of 20 ~ 40 mg is then accurately weighed and dissolved in diluted hydrochloric acid with the presence of an access amount of potassium iodide (KI). The transition metal M(2+*x*) in the sample is thus reduced by the potassium iodide as described by S24. The liberated I_2 is then titrated against the standardized thiosulphate solution as described by S18 to give an overall reaction described by S25.

$$\mathbf{M(2+x) + H^+ + xI^- \rightarrow M(2) + \frac{x}{2} I_2} \qquad \textbf{(S24)}$$

$$\mathbf{M(2+x) + xS_2O_3^{2-} \rightarrow M(2) + \frac{x}{2} S_4O_6^{2-}} \qquad \textbf{(S25)}$$

The whole experiment is carried out under flowing Ar to avoid oxidation of I_2 with O_2 in the air. Titration experiments are repeated three times independently for better data reliability. The average oxidation state of the transition metal in the sample is calculated in the following way:

The titration results of the $YSr_2Mn_2O_{7-\delta}F_z$ phase discussed in Chapter 8 are used as an example (data shown in Table 2.2). Assuming a composition of $YSr_2Mn_2O_7F_0$ with Mn(+3.5), $YSr_2Mn_2O_7F_0$ of 25.7 mg will generate 0.1586 *mmol* of electrons, as deducted from S26 and S27. Similarly, 25.7 mg of $YSr_2Mn_2O_{5.5}F_{3.5}$ with Mn(+3.75) will generate 0.1702 *mmol* of electrons. If the value of moles of electrons gained is plotted against the oxidation state, a straight line is obtained. For 25.7 mg of $YSr_2Mn_2O_{7-\delta}F_z$ with Mn(2+*x*), the moles of electrons gained can be calculated from titration to be 0.1667 *mmol*, as shown by S28. On the plot noted above, this value corresponds to an oxidation state of Mn(3.674).

$$\mathbf{Mn(2.5) + 0.5}e^- \rightarrow \mathbf{Mn(2)} \qquad \textbf{(S26)}$$

$$\boldsymbol{moles\ of\ electron\ gained} = \frac{\boldsymbol{mass} \times \boldsymbol{number\ of\ electron\ gained}}{\boldsymbol{molar\ mass}}$$

$$= \frac{25.7\times10^{-3}\times0.5\times2}{486.03} = \mathbf{0.1586 \times 10^{-3}}/mol \qquad \textbf{(S27)}$$

$$\boldsymbol{moles\ of\ electron\ gained} = c_{Na_2S_2O_4}\times V_{Na_2S_2O_4}$$

$$= \mathbf{4.519 \times 10^{-3} \times 0.0369 = 0.1667 \times 10^{-3}}/mol \qquad \textbf{(S28)}$$

Sample	Mass (mg)	$c_{Na_2S_2O_4}$ (10^{-3} mol/L)	$V_{Na_2S_2O_4}$(mL)	Oxidation state of Mn^{n+}
$YSr_2Mn_2O_{7-\delta}F_z$	25.7	4.519	36.9	3.674

Table 2.2. Results of titrations on $YSr_2Mn_2O_{7-\delta}F_z$ from Chapter 8.

2.7 SQUID Magnetometery

The superconducting quantum interference device (SQUID) is a high-sensitivity magnetometer for characterizations of magnetic properties of materials. In a SQUID device, a closed superconductor ring is intersected equally by two thin insulating layers, forming two Josephson junctions which allow Cooper pairs of electrons to tunnel through. When the sample moves through the superconducting ring, an external magnetic field arising from the magnetic interactions of the sample in measuring is applied to the superconducting loop. A current is then induced in the ring. When this current exceeds the critical current of the Josephson junction, a

voltage appears across the junction. This voltage is proportional to the applied external magnetic field, and thus to the magnetic moment of the sample.

SQUID magnetometery was used in this work for magnetic characterizations. The magnetisation data from samples were collected as a function of temperature ranging from 5 K to 300 K in a constant applied field of 100 Oe. When a sample is cooled in the absence / presence of an applied field, the data collected at warming-up are referred as zero-field-cooling (ZFC) / field-cooling (FC). The magnetization-field isotherm data were also collected at 5 K or 300 K. In a typical SQUID experiment, a sample of ~ 30 mg is weighed accurately and loaded in a gelatine capsule. The sample capsule is fixed in a straw with four empty capsules on either side, and the straw is sealed at one end using a layer of diamagnetic tape.

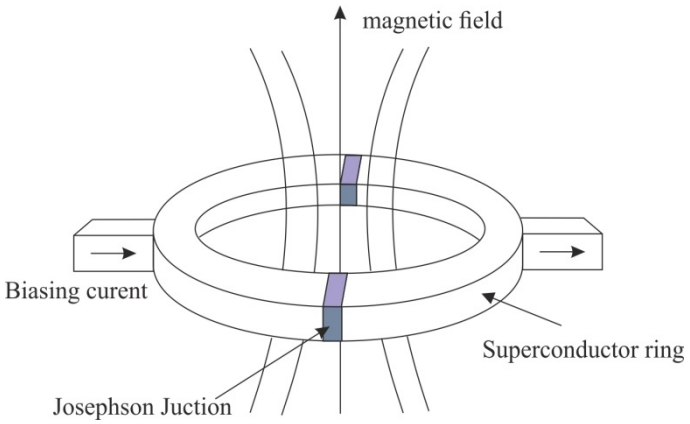


Figure 2.11. Schematic of a DC SQUID magnetometer.

2.8 Muon spin relaxation spectroscopy (μSR)

Muon spin relaxation spectroscopy (μSR) is a useful technique to probe the local magnetic environment at atomic scale inside a matter. Muons are produced by accelerated proton beams hitting a light element target, which produces pions that decay to positive muons. In a μSR experiment, a muon is implanted into the sample of interest by picking up an electron to form a so-called muonium. In an ordered magnet, the implanted muons with magnetic spin (S = ½) will undergo Larmor precession at the presence of a magnetic field before decaying away. The μSR experiments discussed in this work were carried out by Prof. Stephen J. Blundell, at the Swiss

Muon Source, PSI, in Switzerland. In a μSR experiment, spin-polarized muons were implanted in the bulk of a material and the time dependence of their polarization was monitored by recording the angular distribution of the subsequent positron decay.

2.9 Bond valence sum (BVS)

Bond valence sum provides a way to estimate the oxidation states of atoms. It is derived from the bond valence model based on Pauling's rules. In the bond valence model, the valence of an atom *i* (V_i) is defined as the number of electrons the atom uses for bonding. The valence of a bond v_{ij} between the *i*th and *j*th atom is defined as the number of electron pairs forming the bond, which is equal to the number of valence electrons that each atom contributes since each atom contributes equal number of electrons. Thus the sum of all the valences from a given atom *i* (S_i) can be described by S29, while the bond valence S_{ij} is given by an empirical expression S30.[59]

$$\boldsymbol{V_i \approx S_i = \sum_j S_{ij}} \qquad \textbf{S29}$$

$$\boldsymbol{S_{ij} = \exp\left(\frac{R_0 - R_{ij}}{B}\right)} \qquad \textbf{S30}$$

Where the R_{ij} is the actual bond length between the *i*th and *j*th atom; *B* is commonly taken as a constant of 0.37 Å; R_0 is the bond valence parameter, which is calculated by using the observed bond valences and bond lengths between pairs of atoms in selected crystal structure[59]. The bond valence parameter R_0 used in this work is listed in Table 2.3.

	O	F		O	F
Ca(II)	**1.967**	**1.842**	Mn(IV)	**1.753**	**1.71**
Cr(III)	**1.724**	**1.64**	Ni(II)	**1.654**	**1.599**
Cr(IV)	**1.794**	**1.74**	Sr(II)	**2.118**	**2.019**
La(III)	**2.172**	**2.057**	Y(III)	**2.014**	**1.904**
Mn(III)	**1.760**	**1.66**			

Table 2.3. Recommended bond valence parameters for selected atoms.[59]

The bond valence sum (BVS) gives a simple estimation of the oxidation state of a certain atom. It has been used to validate some chemical structures with localized bonds or used to predict some of their properties.[59] However, results deduced by using bond valence sum are

unreliable with metals or generally when the electrons are delocalized, as BVS is derived from the simple bond valence model. The bond valence sum (BVS) is thus only used in this work for deducing anion distribution of the oxide and fluoride anions over different anion sites in the oxyfluoride phase $A_3B_2O_7F_2$. It is difficult to distinguish the oxide and fluoride anions from X-ray or neutron diffraction data as their scattering lengths are similar. One method reported to determine the location of the fluoride ions within the structure is to use Madelung energy calculations to probe the electrostatic preferences for various ion distributions[24]. Another quick and convenient way to deduce the oxide/fluoride distributions in some oxide-fluoride phases is by detailed examination of the local bonding at anion sites using bond valence sums (BVS)[60,61]. This process is detailed in Chapter 4.

2.10 Second harmonic generation (SHG)

Second harmonic generation (SHG) is a nonlinear optical process and was first demonstrated by Peter Franken, et.al.[62] A SHG device is developed on the phenomenon that photons with the same frequency interacting with a nonlinear material results in new photons with doubled frequency. As shown in Figure 2.12, when an incident beam from a diode laser with a frequency of ω_1 is focused into a sample, a small fraction of the incident light is converted into light at a doubled frequency of $\omega_2 = 2\omega_1$. The incident laser beams normally have a wavelength in infrared range, leading to a blue/green beam observed by the detector after going through a SHG device. The SHG technique is used in this work for examining a non-centrosymmetric structure[63], and the SHG experiments were carried by Prof. Shiv Halasyamani. The absence of second harmonic light generally indicates that the structure of the measured material is centrosymmetric.

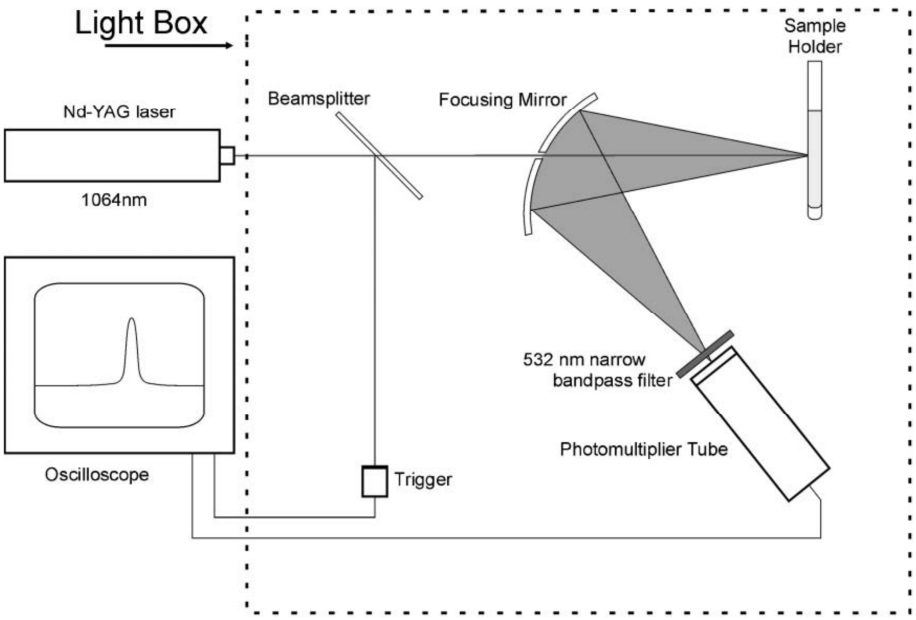


Figure 2.12. Schematic of a SHG device.[64]

Chapter 3: Characterization of $La_2SrCr_2O_7$

3.1 Introduction

As discussed in Chapter 1 Section 1.6, it is a great challenge to prepare magnetoelectric multiferroic materials that exhibit a combination of ferromagnetism and ferroelectricity. This is mainly because the conventional approach to stabilize a ferroelectric non-centrosymmetric (NCS) phase utilizes second-order Jahn-Teller (SOJT) distortions associated with octahedrally coordinated d^0 transition metal cations which are by definition diamagnetic. Therefore, an alternative mechanism for ferroelectricity that is compatible with a partially filled *d*-shell, required to induce magnetism, is needed for the preparation of multiferroic materials. Recently much attention has been focused on attempts of utilizing the complex structural distortions observed in perovskite frameworks to prepare NCS phases in the absence of SOJT cations. The cooperative tilting of the BO_6 octahedra lowers the crystallographic symmetry of perovskite framework, and results in associated displacements of A-cations, which potentially could be utilized to break the inversion symmetry of the perovskite lattice.

However, in a typical ABO_3 perovskite structure, the BO_6 units are continuously linked in all three dimensions. The reciprocal nature of the collective rotations of the apex-linked BO_6 units in the perovskite framework results in centrosymmetric structures. The inversion symmetry can only be broken if those collective rotations are combined with A-site or B-site cation order[33,35,65,66], as discussed in Chapter 1 Section 1.6.2. The requirement to control both the cation order and the collective tilting and twisting distortions of perovskite phases significantly increases the synthetic difficulty of preparing NCS materials.

Fortunately, as discussed in Chapter 1 Section 1.6.2, the need to prepare cation-ordered phases can be avoided by lowering the dimensionality of the lattice. It's been reported that the cooperative structural distortions of BO_6 octahedra in some of the layered perovskite phases, such as n =2 Ruddlesden-popper phases or Dion-Jacobson phases[67], could break the inversion

symmetry of the frameworks without the need for cation order[68]. However, of many of the different tilting and twisting schemes of the apex-linked BO_6 units can adopt, only a few yield an NCS arrangement. This provides a strong motivation to develop a better understanding of the factors that influence which of the many possible ordered tilting and twisting schemes are adopted by a particular layered perovskite phase, so that we can better direct these structural distortions to tune materials to exhibit desired properties.

The detailed structural characterization and analysis of the n = 2 Ruddlesden-Popper oxide $La_2SrCr_2O_7$ is described in this chapter. Initially this phase was prepared to act as a substrate for a topochemical fluorination study focused on synthesizing phases containing Cr^{4+} as described in Chapter 4. However detailed analysis of the structure of $La_2SrCr_2O_7$ revealed a novel interaction which couples the A-site La/Sr cation distribution to the ordered twisting distortions of the CrO_6 octahedra, offering the opportunity to tune one of these structural features by modifying the other. The bulk of this work has been published in *Inorganic Chemistry*.[69]

3.2 Experimental

Samples of $La_2SrCr_2O_7$ were prepared by grinding together suitable quantities of La_2O_3 (99.999%, dried at 900 °C), $SrCO_3$ (99.99%), Cr_2O_3 (99.97%) and then heating the mixtures in air at 1000 °C for 20 h to decompose the carbonate. The resulting material was then pressed into 13 mm diameter pellets and heated for 4 periods of 55 h at 1460 °C under flowing argon.

The preparation of $La_2SrCr_2O_7$ via this ceramic route can be described by formulae scheme S1. However, the formation of stoichiometric, phase-pure $La_2SrCr_2O_7$ is opposed by scheme S2 and S3. Scheme S2 describes an equilibrium within $La_2SrCr_2O_7$, the perovskite phase $LaCrO_3$ and the n =1 Ruddlesden-Popper phase $LaSrCrO_4$. Scheme S3 describes a partial oxidized reaction.

$$\mathbf{2La_2O_3 + SrCO_3 + 2Cr_2O_3 \rightarrow La_2SrCr_2O_7 + CO_2 + 3O_2} \qquad \mathbf{S1}$$

$$\mathbf{La_2SrCr_2O_7 \rightarrow LaSrCrO_4 + LaCrO_3} \qquad \mathbf{S2}$$

$$(1 + x)La_2SrCr_2O_7 + {}^{x}/_{4}O_2 \rightarrow La_{2-x}Sr_{1+x}Cr_2O_7 + 2xLaCrO_3 + {}^{x}/_{4}La_2O_3 \qquad \textbf{S3}$$

To oppose reaction S3 we need to lower the partial pressure of oxygen (pO_2) and/or raise the temperature (increasing TΔS) to avoid the oxidation of chromium. Oxygen buffers such as titanium strips, H_2 flowing gas or CO/CO_2 gas mixtures can be used to lower the pO_2. Reactions were performed using titanium strips as well as flowing atmosphere of 5% H_2 in N_2. The former turned out to be inefficient and difficult to control while the latter to be over-reductive as the sample was reduced to $LaCrO_3$ and amorphous phases containing strontium. As a result, raising the reaction temperature while retaining an Ar atmosphere was considered to be more efficient and effective. According to small scale sample tests, 1350 °C was a critical temperature, below which the desired $n = 2$ Ruddlesden-popper phase failed to form. However considerable amounts of impurities such as La_2O_3 and $LaCrO_3$ shown in S3 still remained in the system after several periods of heating until the temperature was raised to 1460 °C.

3.3 Results

3.3.1 Structural refinement of $La_2SrCr_2O_7$

3.3.1.1 X-ray powder diffraction data

A tetragonal unit cell with space group *I4/mmm* (the space group adopted by Ruddlesden-Popper phase $Sr_3Cr_2O_7$)[70] was initially used in a refinement against the X-ray diffraction data collected from $La_2SrCr_2O_7$. The Rietveld refinement however showed an obvious discrepancy between the observed data and that predicted by the model, shown in Figure 3.1. The splitting of peaks at 32.6 degrees/2θ indicated that a model with lower symmetry than *I4/mmm* is needed. This makes sense as the radius of La is smaller than that of Sr, resulting in a smaller tolerance factor for $La_2SrCr_2O_7$ than that of $Sr_3Cr_2O_7$. The octahedra in the perovskite layers therefore need to twist or tilt in order to accommodate the smaller A-site cations, which lowers the symmetry of the structure.

Careful inspection of the X-ray powder diffraction data indicates that $La_2SrCr_2O_7$ could be readily indexed using an orthorhombic unit cell (a = 5.492 Å, b = 5.479 Å, c = 20.182 Å) consistent with a distorted n = 2 Ruddlesden-Popper type structure. The extinction conditions of the diffraction data indicate an A-centring of the unit cell, with the stated setting of the lattice parameters. An orthorhombic unit cell with space group *Acaa* was thus constructed and refined against the X-ray diffraction data as a comparison to the *I4/mmm* model. However, as the positions of the anions are difficult to determine by X-ray powder diffraction, neutron diffraction data are required for the structural analysis on $La_2SrCr_2O_7$.

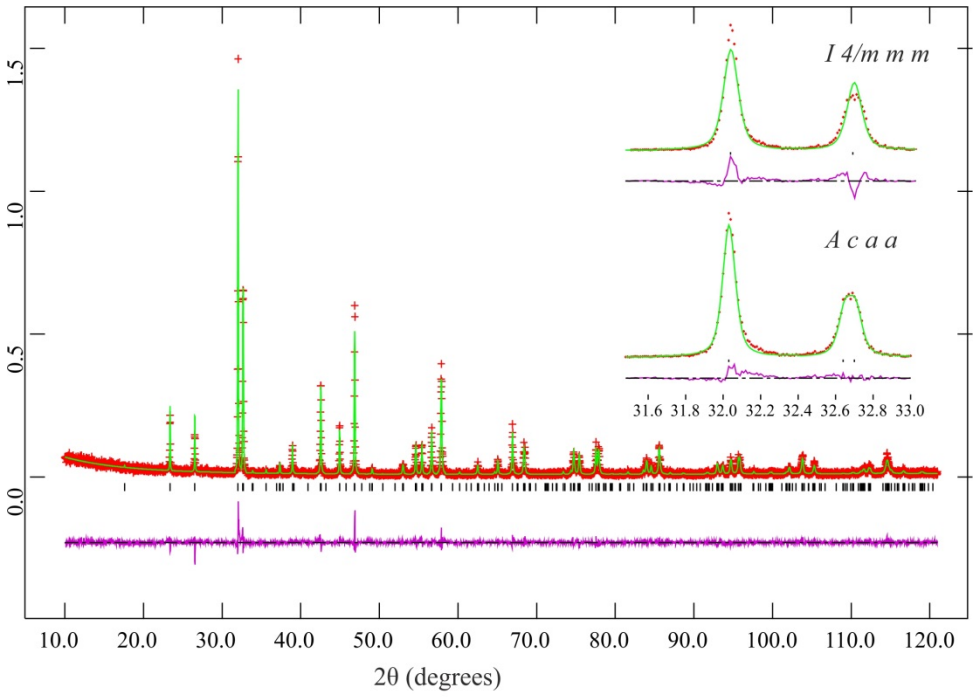


Figure 3.1. Observed calculated and difference plots from the refinement of $La_2SrCr_2O_7$, using *Acaa* model against X-ray powder diffraction data collected by using the PANalytical X'pert diffractometer. Insert: expanded region from refinement by *I4/mmm* model and *Acaa* model.

3.3.1.2 Neutron powder diffraction data (300 K)

As discussed above, the extinction conditions of the X-ray diffraction data collected from $La_2SrCr_2O_7$ indicate an A-centring of the unit cell, with lattice parameters a = 5.492 Å, b = 5.479 Å and c = 20.182 Å. Aleksandrov and Bartolome (A&B) performed a symmetry analysis of the possible cooperative twisting distortions of the BO_6 octahedra in $A_3B_2O_7$ n = 2 Ruddlesden-

Popper phases.[20] The extinction conditions observed in the diffraction data collected from $La_2SrCr_2O_7$ are compatible with the symmetry of 6 of the cooperative distortions described by A&B or by Glazer tilt notation (introduction of both the A&B tilt system and Glazer notation could be found in Chapter 1 Section 1.4). These 6 cooperative distortions are listed in Table 3.1. Crystallographic models were constructed to describe $La_2SrCr_2O_7$ with each of these cooperative distortions, and these models were refined against the neutron powder diffraction data. An additional model in which the twisting of the octahedra around the z-axis is disordered (space group *Amam*) was also considered and refined against the data. The fitting statistics from these 7 models are listed in Table 3.1. During the refinement, all atomic positional and displacement parameters were allowed to refine freely, and the Sr/La distribution over the 9-cordinate and 12-cordinate A-cation sites was allowed to refine within the constraints of the total sample composition and that each cation site must remain fully occupied. Close inspection of the neutron diffraction data revealed a set of weak additional diffraction peaks consistent with the presence of small amount of $LaCrO_3$, and so this was added to the model as a second phase. The diffraction data collected from $La_2SrCr_2O_7$ exhibited weak *hkl* dependent peak broadening, so an anisotropic broadening axis (001) was added to the peak shape description to allow crystal microstrain perpendicular and parallel to this axis to be refined independently.

It is worth noting that in addition to the $A2_1am$ and $A2/a$ models there is a further '3-twist' cooperative distortion described in space group *Pnam* ($\Phi\Phi\Psi_z$ /$\Phi\Phi$-Ψ_z) which should be considered as it can be thought of as a hybrid of the $A2_1am$ and $A2/a$ distortions (as noted earlier in Chapter 1, Section 1.4). Attempts to refine this model against the data were unsuccessful as strong diffraction features predicted by this model were not observed in the data ($\chi^2 \sim 8.5$).

It can clearly be seen from Table 3.1 that the ($\Phi\Phi\Phi_z$ /$\Phi\Phi\Phi_z$) distortion model in space group *A2/a* gives the best fit to the data. Further examination of the reasonable models suggests that only the *A2/a* model gives a chemically and physically reasonable structure as will be

discussed in Section 3.4.1. Plots of the observed and calculated data of 35° bank are shown in Figure 3.2, and that of other banks are in Figure A3.1 in Appendix. The detailed structural parameters of the refined model are given in Table 3.2.

Space Group	**A&B Tilt System**	**Glazer Tilt**	χ^2	**wRp**	**Rp**
Acam	$00\Psi_z/00\Psi_z$	$a^0a^0c^+/ a^0a^0c^+$	7.20	5.16	4.10
Acaa	$00\Phi_z/00\Phi_z$	$a^0a^0c^-/ a^0a^0c^-$	6.68	4.98	3.98
Acmm	ΦΦ0/-Φ-Φ0	$a^-a^-c^0/a^-a^-c^0$	6.83	5.02	4.01
Amam	ΦΦ0/ΦΦ0	$a^-a^-c^0/a^-a^-c^0$	6.26	4.81	3.80
Amam	ΦΦdis/ΦΦdis	$a^-a^-c^{dis}/ a^-a^-c^{dis}$	6.19	4.78	3.77
$A2_1am$	$\Phi\Phi\Psi_z /\Phi\Phi\Psi_z$	$a^-a^-c^+/ a^-a^-c^+$	6.08	4.73	3.72
A2/a	$\Phi\Phi\Phi_z /\Phi\Phi\Phi_z$	$a^-a^-c^-/a^-a^-c^-$	5.75	4.60	3.64

Table 3.1. Fitting statistics from the structural refinement of $La_2SrCr_2O_7$ using models based on the distortions of n = 2 Ruddlesden-Popper phases. Φ indicates an out of phase rotation, Ψ indicates an in-phase rotation, dis indicates a disordered rotation.

Atom	site	*x*	*y*	*z*	Fraction	U_{iso} (Å^2)
La/Sr(1)	4e	¼	0.7416(9)	0	82(2)/17(2)	0.0069(1)
La/Sr(2)	8f	0.2449(8)	0.7485(6)	0.1818(1)	58(1)/42(1)	0.0056(2)
Cr(1)	8f	0.2509(16)	0.2491(14)	0.0974(1)	1	0.0013(1)
O(1)	4e	¼	0.2205(12)	0	1	0.0096(3)
O(2)	8f	0.9869(10)	0.9981(25)	0.1008(1)	1	0.0098(1)
O(3)	8f	0.5055(9)	0.5025(21)	0.0921(1)	1	0.0106(2)
O(4)	8f	0.2412(13)	0.2649(8)	0.1982(1)	1	0.0091(3)
$La_2SrCr_2O_7$ – space group: *A*2/*a* *a* = 5.4917(3) Å, *b* = 5.4798(3) Å, *c* = 20.181(1) Å, β = 89.87(1)º volume = 607.35(9) Å^3 phase fraction = 96.3(1) % weight percent						
$LaCrO_3$ – space group: *Pnma* *a* = 5.469(2) Å, *b* = 7.762(5) Å, *c* = 5.512(2) Å phase fraction = 3.7(1) % weight percent						
χ^2 = 5.75, wRp = 4.60%, Rp = 3.64%						

Table 3.2. Structural parameters refined against neutron powder diffraction data collected at 298K from $La_2SrCr_2O_7$.

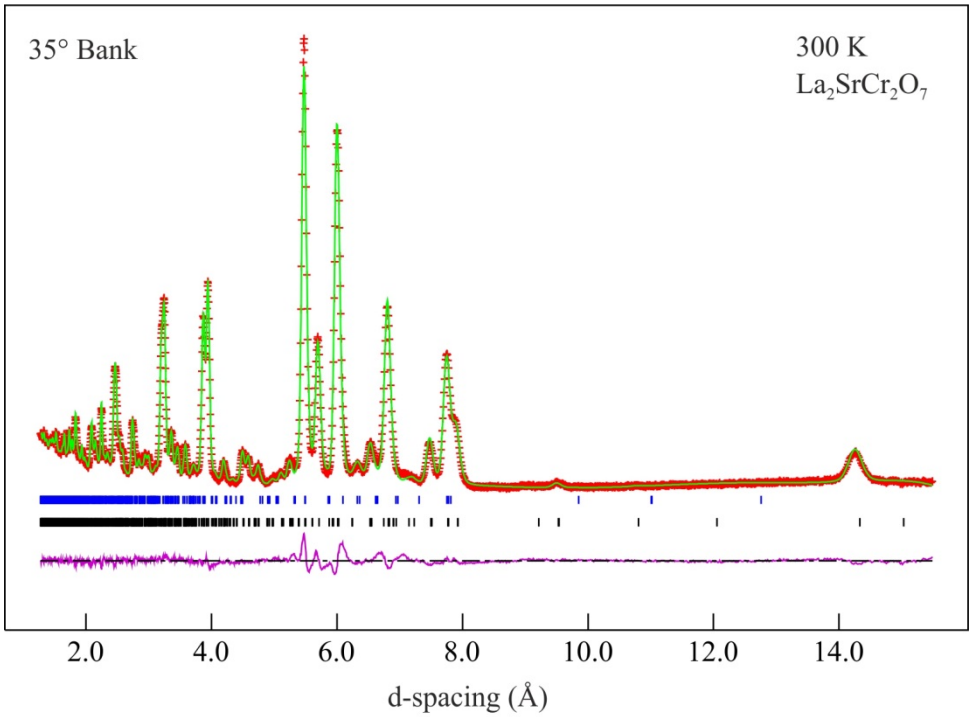


Figure 3.2. Observed, calculated and difference plots from the structural refinement of $La_2SrCr_2O_7$ by using *A2/a* model against neutron powder diffraction data collected at room temperature by using GEM diffractometer (ISIS, UK). Lower tick marks indicate peak positions for the majority phase, upper tick marks for the $LaCrO_3$ secondary phase.

3.3.2 Magnetic Characterization of $La_2SrCr_2O_7$

3.3.2.1 Magnetization data

The magnetization data collected from $La_2SrCr_2O_7$ in an applied field of 100 Oe are shown in Figure 3.3. The divergence between zero-field cooled and field cooled data indicates a weak ferromagnetism below 260 K. In the temperature range 260 < T/K < 285, there is still a small mismatch between zero-field cooled and field cooled data, which could be ascribed to the existence of small amount of $LaCrO_3$ impurities ($LaCrO_3$ has a canted antiferromagnetic ordering temperature of 285 K[71]). The magnetization-field isotherm data collected at 5 K shows weak spin-glass behaviour as the centre of the hysteresis loop shifted slightly away from the origin (Figure 3.4).

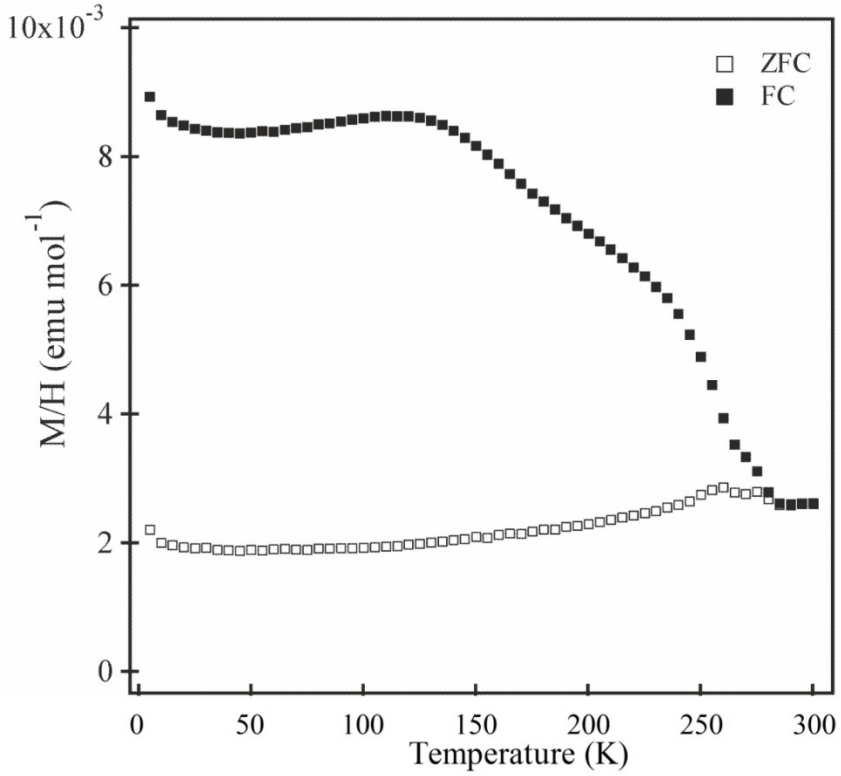


Figure 3.3. Plots of zero-field cooled and field cooled magnetization collected as a function of temperature from $La_2SrCr_2O_7$.

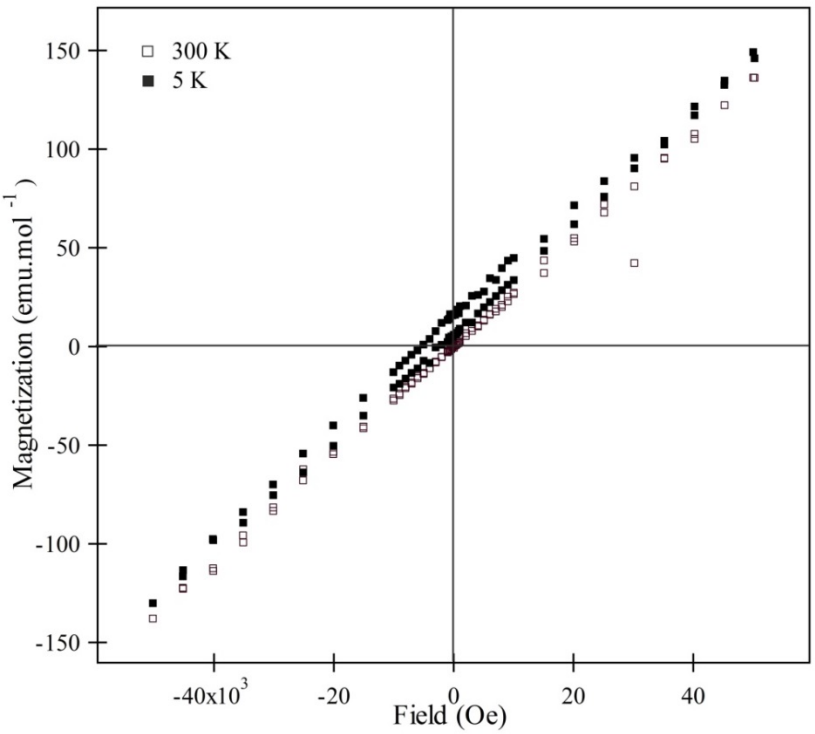


Figure 3.4. The magnetization-field isotherms collected at 300 K and 5 K from $La_2SrCr_2O_7$.

3.3.2.2 Neutron powder diffraction data (5 K)

Neutron powder diffraction data collected from $La_2SrCr_2O_7$ at 5 K show additional diffraction features compared to analogous data collected at 300 K (Figure 3.5). Given the magnetic ordering behaviour shown in the magnetization data as discussed in Section 3.3.2.1, these additional diffraction features were considered to be magnetic scattering peaks. The additional diffraction features can be indexed using the crystallographic unit cell indicating a magnetic ordering vector **k** = 0. A magnetic symmetry analysis using the Sarah code[72] was performed on $La_2SrCr_2O_7$ (space group *A*2/*a*) to yield 4 irreducible representations each consisting of 3 basis vectors, as described in the Appendix (Table 3.1). These symmetry compatible magnetic models were refined against the low-temperature neutron diffraction data and it was observed that the magnetic diffraction intensity was best accounted for using the irreducible representation corresponding to Shubnikov group *A*2/*a* which is a G-type antiferromagnetic model with spins aligned parallel to the crystallographic *b*-axis as shown in Figure 3.6. This irreducible representation allows weak ferromagnetism along both the crystallographic *a*- and *c*-axes (consistent with the weak ferromagnetism observed in the magnetization data). However these components of the magnetic lattice were too small to extract from the diffraction data, so were set to zero. Plots of the observed and calculated data of 35° bank are shown in Figure 3.5, and that of other banks are in Figure A3.3 in Appendix. The detailed nuclear and magnetic structural parameters are shown in Table A3.2 in Appendix. The ordered moment of $La_2SrCr_2O_7$ at 5 K was refined to be 2.51(3) μ_B per Cr centre, suggesting an unquenched orbital contribution to the moment.

.

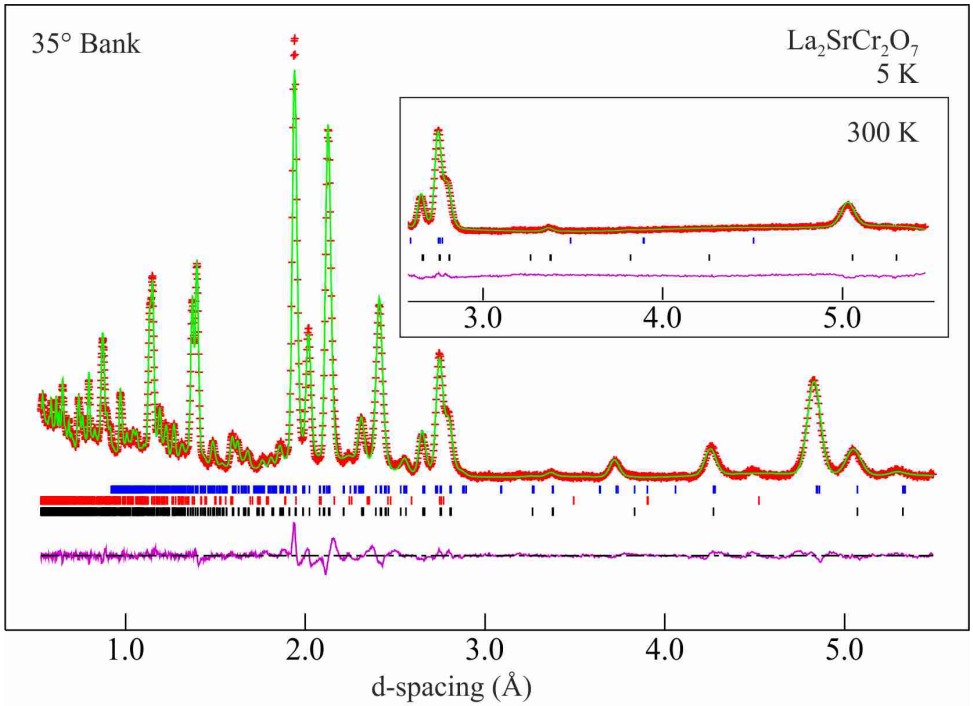


Figure 3.5. Observed, calculated and difference plots from the structural refinement of $La_2SrCr_2O_7$ against neutron powder diffraction data collected at 5 K by using GEM diffractometer. Tick marks indicate peak positions of magnetic model of $La_2SrCr_2O_7$ (blue) and $LaCrO_3$ secondary phase (red), $La_2SrCr_2O_7$ nuclear model (black). Insert: neutron diffraction data collected from $La_2SrCr_2O_7$ at 300 K.

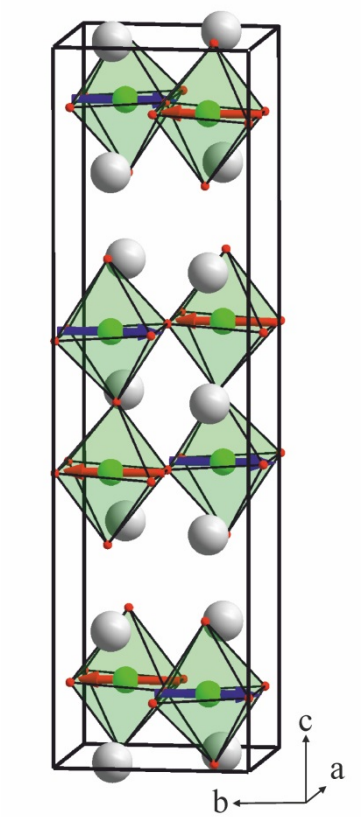


Figure 3.6. The magnetic structure of $La_2SrCr_2O_7$ refined from neutron diffraction data at 5K. Ordered moment = 2.51(3) μ_B per Cr centre.

3.3.2.3 Variable temperature neutron powder diffraction data

Neutron powder diffraction data were collected from $La_2SrCr_2O_7$ in temperature range from 5 K to 260 K. All these diffraction patterns are similar to each other apart from a decrease in values of the refined ordered magnetic moment, indicating no obvious phase transition. The ordered moment was refined to zero at 260 K (Figure 3.7), in good agreement with the magnetization data shown in Figure 3.5.

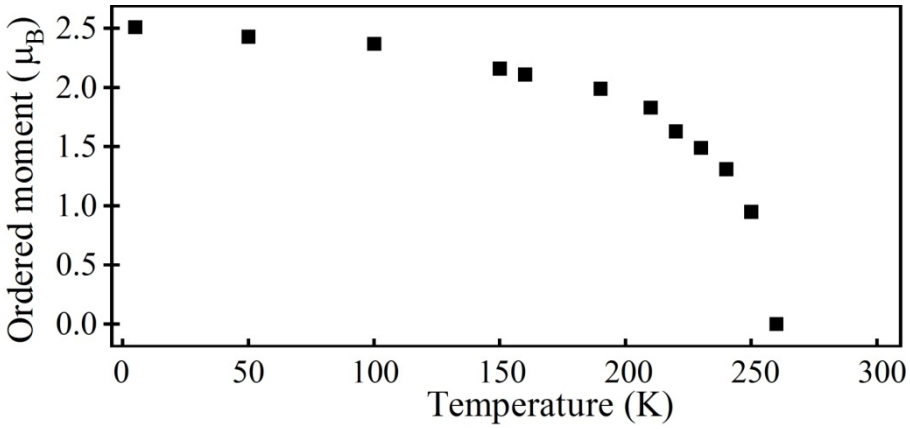


Figure 3.7. Ordered magnetic moment extracted from fits to neutron powder diffraction data of $La_2SrCr_2O_7$.

3.3.2.4 Zero-field μ^+SR data

Zero-field μ^+SR data were collected from $La_2SrCr_2O_7$ as a function of temperature. As shown in Figure 3.8, strong persistent oscillations were observed in data collected at 5 K, consistent with long range antiferromagnetic order. These oscillations declined in frequency with increasing temperature and ultimately disappeared from the signal at T ~ 260 K (Figure 3.8 and 3.9), in agreement with the antiferromagnetic ordering temperatures observed in the magnetization and neutron diffraction data.

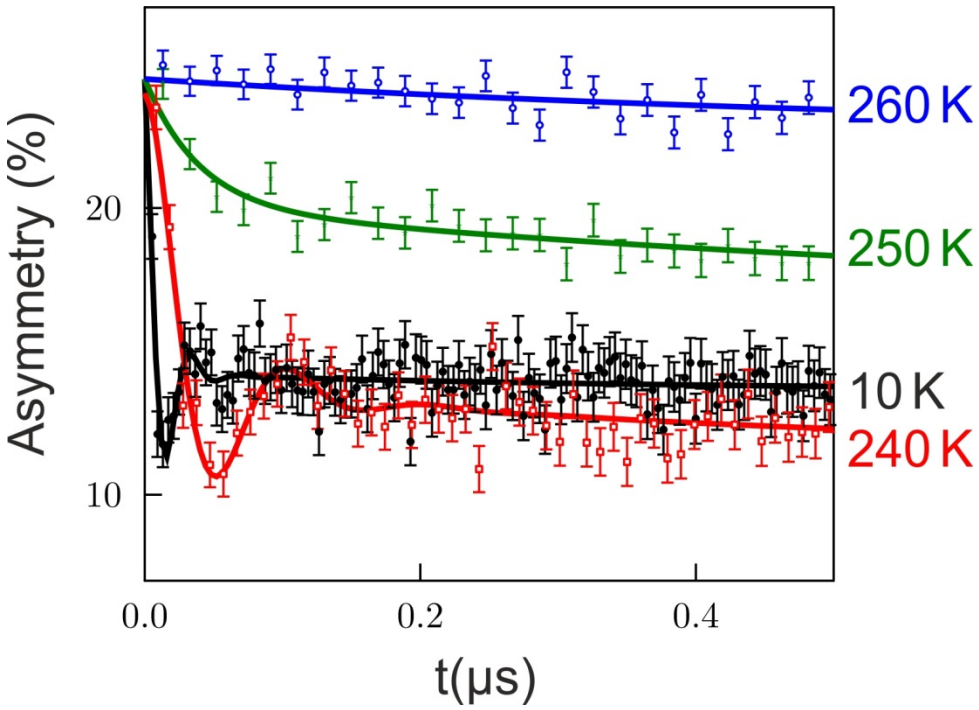


Figure 3.8. Oscillations in the asymmetry of μ^+SR data collected from $La_2SrCr_2O_7$ at low temperature indicate long range magnetic order, consistent with the observation of antiferromagnetic order in the phase via neutron powder diffraction.

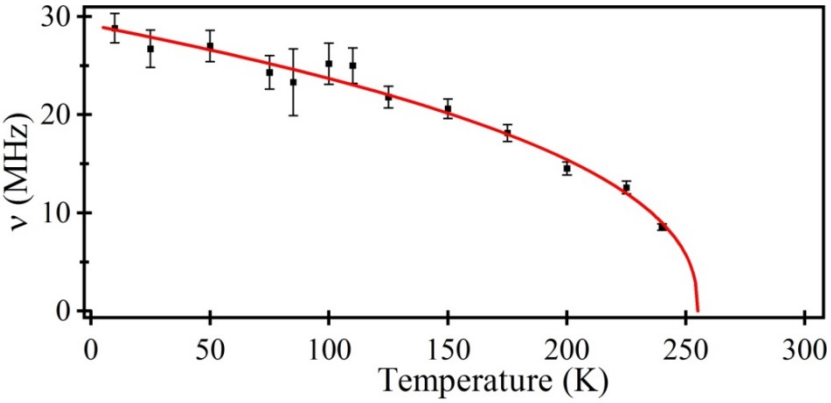


Figure 3.9. The muon oscillation frequency data collected as a function of temperature from $La_2SrCr_2O_7$.

3.4 Discussion

3.4.1 Structural refinement of $La_2SrCr_2O_7$

As discussed in Section 3.3.1.2, crystallographic models (Table 3.1) based on the distortions of n = 2 Ruddlesden-Popper phases were constructed and refined against the neutron diffraction data collected at 300 K. According to table 3.1, there are 3 models that give the best statistical fits to the diffraction data, the *Amam*, $A2_1am$ and $A2/a$ models. Careful comparisons in

three aspects (SHG activity, magnetism and A-cation displacements) were carried out on these 3 models to determine the symmetry of $La_2SrCr_2O_7$.

i. SHG inactivity of $La_2SrCr_2O_7$: SHG measurements were performed on $La_2SrCr_2O_7$ (mechanism of SHG measurement is detailed in Chapter 2 Section 2.10). No SHG signal could be observed, within the sensitivity of the apparatus, strongly suggesting that $La_2SrCr_2O_7$ adopts a centrosymmetric crystal structure. The non-centrosymmetric *$A2_1am$* model is thus eliminated.

ii. Canted antiferromagnetism of $La_2SrCr_2O_7$: The neutron diffraction data, magnetization data, and the μ^+SR data reveal that $La_2SrCr_2O_7$ adopts a canted G-type antiferromagnetic state below 260 K. According to the magnetic symmetry analysis using the Sarah code (see Section 3.3.2.2), the *A2/a* model could generate irreducible representations that allow a weak ferromagnetism along both the crystallographic *a*- and *c*-axes. Whereas this canted antiferromagnetism (weak ferromagnetism) is incompatible with the *Amam* symmetry. The *Amam* model is thus eliminated from consideration. This in combination with the previous discussion that SHG inactivity ruled out the *$A2_1am$* model, leads to a conclusion that the *A2/a* model is the only reasonable candidate structure.

iii. The A-cation displacements of $A2_1am$ and A2/a models: The cooperative twisting of the CrO_6 octahedra is driven by the need to satisfy the local bonding requirements of the relatively small Sr/La A-cation site. The cooperative rotations of the CrO_6 octahedra make the 9- and 12-coordinate A-cations sites 'smaller' and in the process lower the point symmetry of the A-sites, driving the A-cations to move from the original high-symmetry positions to better satisfy their bonding requirements. To further check the *$A2_1am$* and *A2/a* models, these A-cation displacements in the structures refined for $La_2SrCr_2O_7$ in these two space groups were investigated (Figure 3.10).

$A2_1am$ model: It can be seen in Figure 3.10 that both the 12-coordinate Sr/La(1) A-site and the 9-coordinate Sr/La(2) A-site cations are displaced in the same direction, predominantly

along the a-axis. This displacement of the Sr/La(1) and Sr/La(2) sites is not chemically realistic – we would expect the two sites to be displaced in opposite directions to maximize the bonding requirements of the A-cations. This can most easily be seen by observing that the ($\Phi\Phi\Psi_z$ /$\Phi\Phi\Psi_z$) twisting distortion of the *A2₁am* model is the same as that of the $GdFeO_3$ perovskite structure (space group *Pnma*) in which alternate sheets of 12-coordinate A-cations are displaced in alternate directions. Thus we can see that the refined structure of $La_2SrCr_2O_7$ is not chemically realistic and should be rejected.

A2/a model: As well as giving the best statistical fit to the data, the model in space group *A2/a* is the only one of the 'three twist' distortion models to refine to give a chemically and physically reasonable structure, with the combination of A-cation displacements expected for the observed octahedral rotation pattern.

In conclusion, the *A2/a* model is the only remaining structure that is compatible with the physical properties observed for $La_2SrCr_2O_7$ (see arguments i and ii, and Table 3.3). It also gives a reasonable A-cation displacement within the structure (Figure 3.10). These combined with the fact that *A2/a* model also fits best statistically (Table 3.1) to the neutron diffraction data, confirm us that the structure of $La_2SrCr_2O_7$ is best described by the *A2/a* model.

Symmetry test	*Amam*	*A2₁am*	*Pnam*	*A2/a*
χ^2	6.19	6.08	8.50	5.75
SHG inactivity	√	X	√	√
Weak Ferromagnetism	X	√	X	√
Realistic atom displacements	√	X	X	√

Table 3.3. The compatibility of different distorted *n* = 2 Ruddlesden-Popper structures with different symmetry tests.

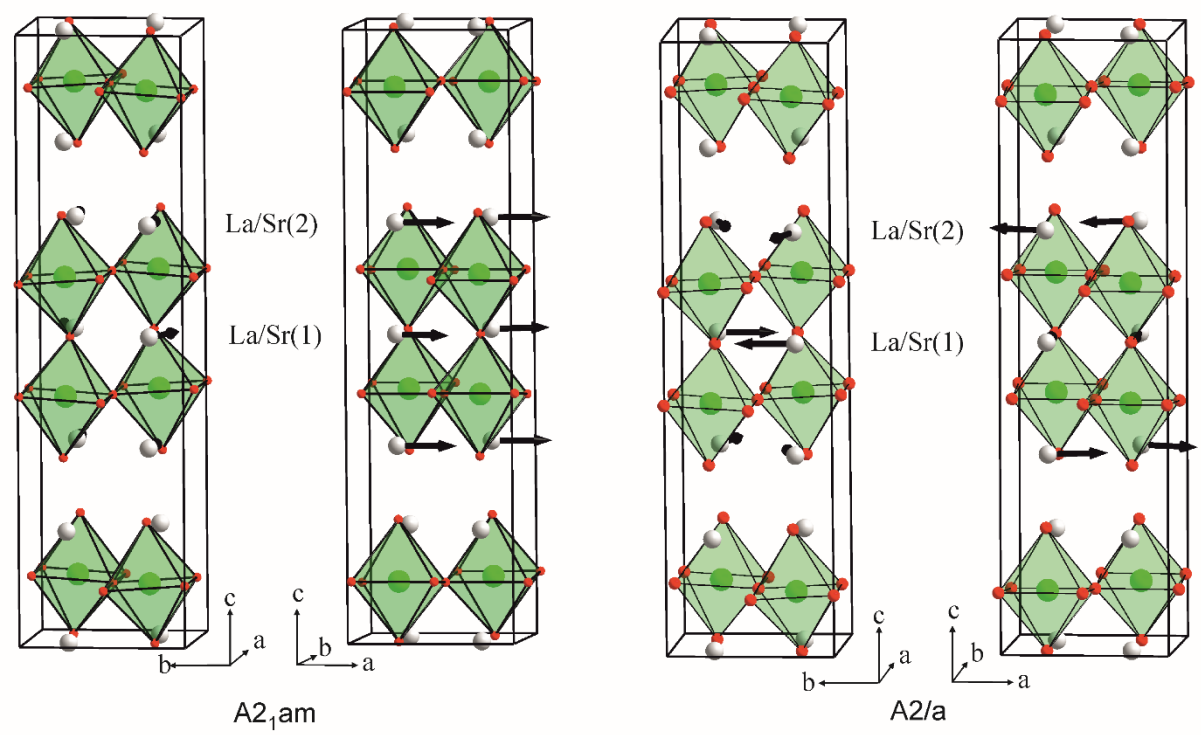


Figure 3.10. Structures of $La_2SrCr_2O_7$ refined in space groups *A2₁am* and *A2/a*. Arrows indicate the displacement of the (Sr/La) A-cation sites from the high symmetry positions.

3.4.2 Unusual A-cation distribution in $La_2SrCr_2O_7$

As discussed in Section 3.4.1, $La_2SrCr_2O_7$ adopts an *A2/a* structure. This is the first report of an n = 2 Ruddlesden-Popper phase adopting an *A2/a* ($\Phi\Phi\Phi_z$ /$\Phi\Phi\Phi_z$) distorted structure. Given that the major driving force for the distortion of $A_3B_2O_7$, n = 2 Ruddlesden-Popper phases is thought to be the mismatch in A- and B-cation radii, it is rather unexpected that $La_2SrCr_2O_7$ adopts a novel structural distortion because the ratio of A- to B-cation radii (as measured by the tolerance factor t = <A-O>/$\sqrt{2}$×<B-O>) is similar to that of many other n = 2 RP phases which adopt more common structural distortions. For example, by using Shannon ionic radii[73] to estimate the tolerance factor of phases, it was observed that the value calculated for $La_2SrCr_2O_7$ (t = 0.977) lies between those of $La_2SrFe_2O_7$ (t = 0.963) and $La_2BaFe_2O_7$ (t = 0.983) both of which crystallize with undistorted structures (space group *I4/mmm*)[5], leading to the expectation that $La_2SrCr_2O_7$ would do likewise.

An explanation of the unusual distorted structure adopted by $La_2SrCr_2O_7$ can be provided by observing that the phase also exhibits a highly unusual distribution of A-cations over the 9- and 12-coordinate A-sites. In many n = 2 RP phases which have two or more A-cations which differ significantly in charge and/or radius, it is observed that the larger cation will preferentially occupy the 12-coordinate A-site. Thus for example the 12-coordinate A-site in $YSr_2Mn_2O_7$ is exclusively occupied by Sr^{2+},[74] while the 12-coordinate A-sites in $Nd_2BaMn_2O_7$ are preferentially occupied by Ba^{2+}.[75] However, as shown in Table 3.2, the 12-coordinate A-sites of $La_2SrCr_2O_7$ are occupied by 82(2)% La^{3+} and 18(2)% Sr^{2+}, while the 9-coordinate A-sites are occupied by 58(1)% La and 42(1)% Sr. As a result the average radius of the cations on the 12-coordinate A-site is smaller than those on the 9-coordinate A-site and this highly unusual situation could be the origin of the usual structural distortion observed for $La_2SrCr_2O_7$.

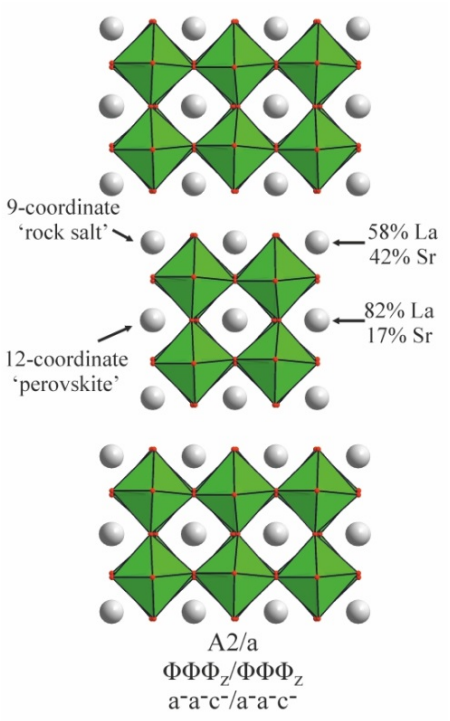


Figure 3.11. The unusual A-cation distribution in $La_2SrCr_2O_7$.

3.4.3 Understanding of the unusual *A2/a* distortion and the A-cation distribution in $La_2SrCr_2O_7$ by first-principles Density Functional Theory

A series of first-principles Density Functional Theory calculations were performed by our collaborators, Nicole A. Benedek and Brian M. Abbett. These calculations help us further

understand the unusual *A2/a* ($\Phi\Phi\Phi_z$ /$\Phi\Phi\Phi_z$) tilting distortion and the unexpected A-cation distribution in $La_2SrCr_2O_7$.

At first, two sets of structural relaxations were carried out to explore the relationship between the structural distortions (octahedral tilts) and the A-cation distributions.

i. Investigation of the structural distortion with normal Sr/La distributions: Full structural relaxations starting from the space groups listed in Table 3.1 were performed with the A-cations placed on their expected sites (Sr on the 12-coordinate perovskite A-site while La on the 9-coordinate rocksalt A-site as shown in Figure 3.11). This is to investigate whether octahedral tilts along the *c*-axis are energetically favourable with normal Sr/La distributions.

The outcome shows that the *Acmm* ($00\Psi_z/00\Psi_z$) and *Acaa* ($00\Phi_z/00\Phi_z$) structures both relaxed into *I4/mmm* (000/000) whereas the $A2_1am$ ($\Phi\Phi\Psi_z$ /$\Phi\Phi\Psi_z$), *A2/a* ($\Phi\Phi\Phi_z$ /$\Phi\Phi\Phi_z$) and *Pnam* ($\Phi\Phi\Psi_z$ /$\Phi\Phi(-\Psi_z)$) structures relaxed to *Amam* ($\Phi\Phi0/\Phi\Phi0$). In other words, tilts around the *c*-axis either Ψ_z or Φ_z relaxed out for each structure. This indicates that octahedral tilts around the *c*-axis are energetically unfavourable if the A-cations sit on their expected sites.

ii. Investigation of the effects of Sr/La distributions with no octahedral tilts: The effects of Sr/La distributions were explored by starting from a fully relaxed *I4/mmm* structure and systematically generating a series of symmetry-unique structures (for a 24-atom simulation cell) with different Sr/La distributions. Within this unit cell, any A-site disorder breaks the *I4/mmm* symmetry with the resulting space group depending on the exact distribution of Sr and La cations. It turns out that without any structural relaxation, the energy increases when any Sr cation in a 12-coordinate site is traded with any La cation in a 9-coordinate site. After full structural relaxation, the *I4/mmm* structure with Sr and La cations on their expected sites remains the lowest in energy by approximately 20 meV/formula unit (f.u.). This suggests that without octahedral tilts the La cations prefer the 9-coordinate rock salt A-site while Sr cations the 12-coordinate perovskite A-site.

From these two sets of analysis, one can learn that the unusual distribution of Sr/La cations in A-sites seems to be coupled with octahedral tilts along *c*-axis. To further understand this coupling effect, a series of structures with different Sr/La distributions and arrangements was constructed, and structural relaxations were performed on each subsequently.

3.4.3.1 Construction and selection of the structures

On construction of the structures, a 48-atom simulation cell (four formula units), a unit cell size suggested by the structural refinement against the diffraction data (see Section 3.3.1), was used. As our computational framework does not allow for fractional occupancies, 5 specific distributions of Sr/La were then selected: 100/0 in perovskite (0/100 in rock salt), 75/25 in perovskite (12.5/87.5 in rock salt), 50/50 in perovskite (25/75 in rock salt), 25/75 in perovskite (37.5/62.5 in rock salt) and 0/100 in perovskite (50/50 in rock salt). The distribution of Sr/La cations observed from $La_2SrCr_2O_7$ (18/82 in perovskite, 42/58 in rock salt layer approximately) is accommodated in this range of distribution. We then used these models to explore structural and energetic trends across this range of different Sr/La distributions to further understand the observed unusual A-cation distribution and octahedral tilts in $La_2SrCr_2O_7$.

Despite the simplifications described above, it is still extremely computationally intensive to investigate every possible arrangement of Sr/La cations for each distribution due to the large number of possibilities. Therefore, 36 arrangements with a mix of the Sr/La distributions listed above were then selected to make this investigation computationally less expensive. This selection process is based on our observations and understanding of the structure of $La_2SrCr_2O_7$. It was noticed from our calculations in a 24-atom simulation cell, that structures with multiple adjacent Sr cations tended to have higher energies. This tendency prompted us to select arrangements with the Sr cations spread out in a 48-atom simulation cell, which were expected to be lower in energy. Several arrangements with clusters of Sr cations that were expected to be high in energy were also included for comparison.

For each of these 36 arrangements of Sr/La, a relaxation was performed starting from the experimental coordinates for $La_2SrCr_2O_7$ in *A2/a*, *Pnam* and *A2₁am*; this produced 36 × 3 = 108 structures with varying Sr/La distributions. It is expected that this set of structures is sufficient to study structural and energetic trends relevant to the experimental data. The full list of structures considered and the symmetry of each is listed in Table A3.3 in the Appendix.

3.4.3.2 Results and discussion from DFT calculations on the constructed structures

Figure 3.12 shows the results of DFT calculations on the 108 structures mentioned above. A structural relaxation starting from the experimental coordinates for $La_2SrCr_2O_7$ in the *Amam* structure with the Sr and La ions in their expected positions was performed and this relaxed energy has been taken as a reference (the zero of energy). The *Amam* structure, with the (ΦΦ0/ΦΦ0) rotation distortion, could be used as a suitable reference because it differs from *A2₁am* ($\Phi\Phi\Psi_z$ /$\Phi\Phi\Psi_z$), *A2/a* ($\Phi\Phi\Phi_z$ /$\Phi\Phi\Phi_z$) and *Pnam* ($\Phi\Phi\Psi_z$ /$\Phi\Phi(-\Psi_z)$) only on the *c*-tilts; *Amam* doesn't have a rotation distortion along the *z*-axis.

There are two features that could be observed from Figure 3.12:

(1) For any of the 36 Sr/La arrangement, the relaxations starting from either *A2/a*, *Pnam* or *A2₁am* structures always result in a similar, sometimes identical, relaxed energies. In other words, the marks denoting the relaxed energies of *A2/a*, *Pnam* or *A2₁am* appear at a similar *y*-value at a given *x*. This makes it difficult to judge which of these three structures are more energetically stable.

(2) Some Sr/La arrangements have relaxed energies lower than that of *Amam* structure with the Sr and La ions in their expected positions. In other words, there are marks below the zero energy line in Figure 3.12. This indicates that some Sr/La arrangements are more energetically favourable. Moreover, these energetically favourable Sr/La arrangements are those with 25/75 in perovskite (37.5/62.5 in rock salt) and 0/100 in perovskite (50/50 in rock salt). The

experimentally observed one, 18/82 in perovskite, 42/58 in rock salt layer approximately, falls right in these categories.

The relaxed energies were also plotted against the mean Sr-Sr distance in Figure A3.5 in Appendix. This Sr-Sr distance is the mean distance between Sr cations in our relaxed *Amam* structure after swapping Sr/La positions, but before any further relaxation. From Figure A3.5, we can observe that A-site arrangements with Sr cations spread out (longer mean Sr-Sr distance) are lower in energy. This is consistent with the observation from Figure 3.12.

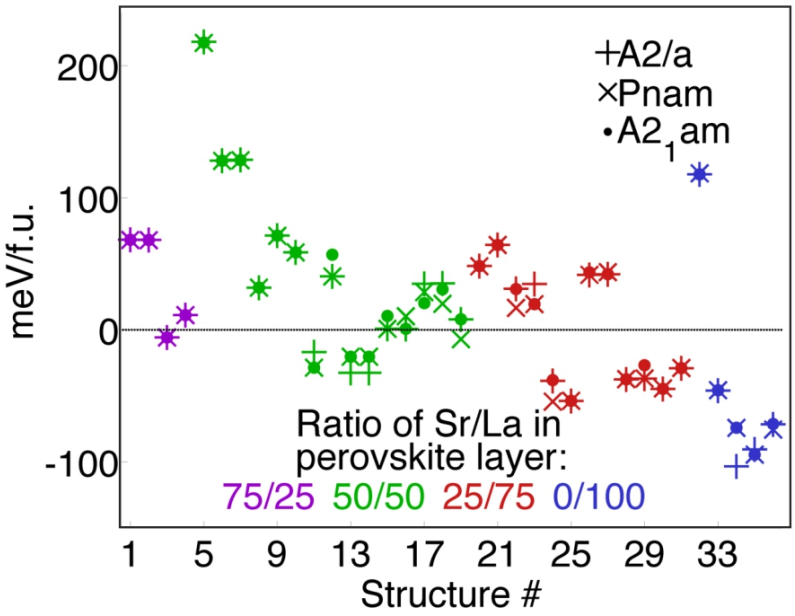


Figure 3.12. Relaxed energies per formula unit (f.u.) of our 108 structures with varying Sr/La distributions with respect to the energy of the *Amam* reference structure with Sr/La cations on their expected sites (we take the energy of this structure to be the zero of energy, indicated by the horizontal dashed line). Color and shape of points indicate the ratio of Sr/La distribution and initial ionic positions respectively. The horizontal axis is labeled by arbitrary structure numbers corresponding to Table A3.3. The structures are sorted by the Sr/La ratio and the mean distance between Sr cations in our relaxed *Amam* structure after swapping Sr/La positions, but before any further relaxation. A general tendency for energy to be lowered as the Sr cations spread out is evident.

In summary, it seems that the unusual A-cation distribution (Sr in perovskite site) combined with octahedral c-tilts could lower the ground state energy, giving a relatively more stable structure compared to the *Amam* structure with A-cations in their expected sites. However, as mentioned above, the energy difference among *A2/a*, *Pnam* and *A2$_1$am* is too subtle to draw a

clear conclusion as to which structure is more energetically favourable. Careful examination of all the low energy relaxed structures in Figure 3.12 revealed that one *A2/a*-like structure has the lowest energy. This combined with the discussion in Section 3.4.1 that *A2/a* structure is the most reasonable one for our $La_2SrCr_2O_7$ phase drives us to use *A2/a*-like structures for further analysis.

3.4.3.3 Results and discussion from DFT calculations on *A2/a*-like structures

As mentioned above, the 36 *A2/a*-like structures were selected for further analysis. This structural trend analysis among these 36 *A2/a*-like structures was expected to help us further understand the relationship between A-site disorder and octahedral tilts (mainly *c*-tilts, the rotation distortion along *z*-axis).

To start this structural trend analysis, the first challenge was to determine how to quantify the magnitude of tilting along the *c*-axis. Normally, a rigorous symmetry-adapted mode analysis would be performed to obtain such information, but in this case A-site disorder makes such an approach extremely challenging. Bond valence discrepancy factors[*76] were thus used as an alternative to quantify the average bonding environment of the equatorial oxygen atoms O_{eq} (that is, the oxygen atoms that reside in the CrO_2 layers). These equatorial oxygen atoms (O_{eq}) were chosen because they will be directly affected by octahedral rotation distortion along *c*.

This quantification problem being solved, values of 47 different structural features for each of our relaxed materials were then calculated, and a linear correlation analysis was performed to guide the search for trends between these features and the bonding environment of the equatorial oxygens. The structural features included, for example, Cr-O-Cr bond angles, CrO_6 volumes and distortion indices[**77], and bond valence discrepancy factors for each atom. The full list of these 47 structural features, along with details of our linear correlation analysis, can be found in the Appendix (Table 3.3).

The linear correlation analysis revealed strong correlations between the bonding environment of the O_{eq} anions and the average maximum Cr-O bond length, the Cr-O-Cr “in-

plane" angle[***], the ratio of Sr to La in the perovskite layer, the average CrO_6 distortion index and the average discrepancy factor of La cations in the rock salt layers (La_{rs}) (averages for certain quantities were taken because there is more than one unique atomic environment for the atoms of interest). Following after, the chemical and physical meanings of the correlation in each of them were explored individually as detailed in Section 3.4.3.3.1 and Section 3.4.3.3.2.

**The discrepancy factor* (d_i)[76]: defined as the difference between the formal valence of a particular ion, and the calculated bond valence sum for the same ion in the structure of interest:

$$d_i = V_i - \sum_j S_{ij} \qquad S_{ij} = \exp(\frac{R_0 - R_{ij}}{B})$$

Where d_i is the discrepancy factor; S_{ij} is the calculated bond valence; R_0 is the length of a bond of unit valence; R_{ij} is the actual bond length and $B = 0.37$.

Thus a positive discrepancy factor indicates underbonding (the cation-anion bonds are too long compared to the ideal, strain-free coordination environment in the bond valence model), whereas a negative discrepancy factor indicates overbonding (cation-anion bonds are too short).

***The distortion index* (DI)[77]: defined as the average fractional deviation of Cr-O bond lengths from the average Cr-O bond length in a CrO_6 octahedron:

$$\text{DI(Cr-O)} = \frac{1}{6\bar{L}} \sum_{i=1}^{6} |L_i - \bar{L}|$$

Where DI is the distortion index; L_i is the actual Cr-O bond length and $\bar{L}$ is the average Cr-O bond length in a CrO_6 octahedron.

****The Cr-O-Cr "in-plane" angle*: defined as the Cr-O-Cr angle assuming the three ions lie in the same plane as shown in Figure 3.13. This angle emphasizes octahedral rotations about *c* rather than the in plane axes that dominate the Cr-O-Cr.

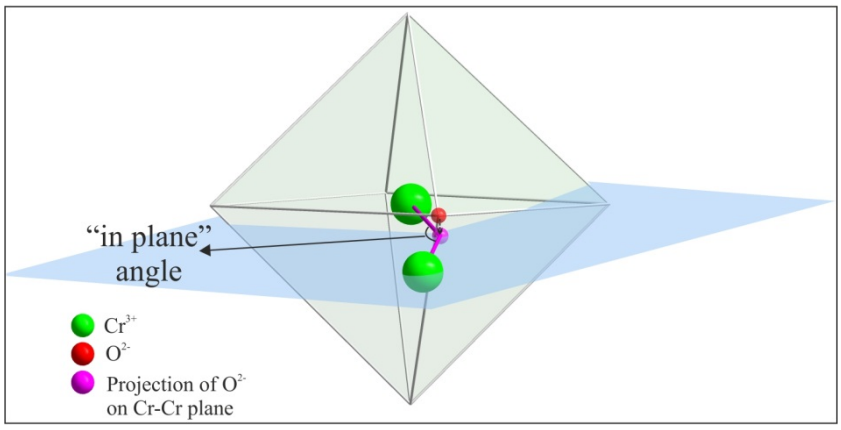


Figure 3.13. The Cr-O-Cr "in-plane" angle; the green and pink spheres are on the same plane, while the red sphere is above the plane.

3.4.3.3.1 The average CrO_6 distortion index

Two plots related to the average CrO_6 distortion are shown in Figure 3.14 and Figure 3.15. Figure 3.14 shows a plot of the average CrO_6 distortion index against the discrepancy factors of both the O_{eq} anions, and the La_{rs} cations, for *A2/a* energy minimized structures with a range of Sr/La cation distributions. Figure 3.15 shows a plot of the average CrO_6 distortion index against the mean maximum Cr-O bond length. The analogous discrepancy factors and the mean maximum Cr-O bond length calculated from the *Amam* reference structure mentioned in Section 3.4.3.1 are also plotted in Figure 3.14 and Figure 3.15 (light blue marks), respectively.

From Figure 3.14 and Figure 3.15, one can gain the following four observations about the CrO_6 distortion index:

(1) The CrO_6 distortion index in the *Amam* reference structure (0.02578) is much larger than typically observed experimentally in other Cr^{3+} oxides. For comparison the distortion indices of $Cr^{3+}O_6$ octahedra in the experimentally determined structures for $BiCrO_3$, $LaCrO_3$, $PrCrO_3$, $GdCrO_3$, $TbCrO_3$, $YCrO_3$, $HoCrO_3$, $TmCrO_3$, $YbCrO_3$, $LuCrO_3$, $InCrO_3$ and $ScCrO_3$ are respectively 0.00268,[78] 0.01143,[79] 0.00488,[79] 0.00181,[79] 0.00423,[79] 0.0044,[79] 0.00347,[79] 0.00083,[79] 0.00455,[79] 0.00445,[79] 0.01032,[80] and 0.00651.[80]

(2) As the ratio of Sr/La in the perovskite layer drops (that is, more Sr is moved into the rock salt layer), the CrO_6 distortion index decreases dramatically.

(3) The mean maximum Cr-O bond length of the *Amam* reference structure (light blue marks) is of the highest value as shown in Figure 3.15.

(4) There is an almost linear relation between the CrO_6 distortion index and the average maximum Cr-O bond length as shown in Figure 3.15.

Based on these observations, it is reasonable to propose that the relatively large CrO_6 distortion index observed for the cation-ordered *Amam* reference structure can be attributed to a single long bond between the chromium and the apical oxide ion residing within the rock salt layer. As more Sr is moved into the rock salt layers, this apical Cr-O bond length decreases, and thus the CrO_6 distortion index decreases.

This coupling between the Sr/La distribution and the Cr-O axial bond length could be explained by a simple electrostatic interaction. When the La and Sr cations are ordered within the *Amam* reference structure, there are negatively charged CrO_2 layers sandwiched between a positively charged LaO rock salt layer and a charge neutral SrO perovskite layer. In this situation the positively charged Cr atoms displace towards the neutral SrO layer, leading to a single long bond between Cr and an apical oxygen in the LaO layer. As more Sr is moved into the rock salt layers, the charges of the rock salt and perovskite AO layers become more even and the tendency for Cr to undergo this distortion decreases, leading to a more uniform set of Cr-O bond lengths (strengthening the Cr-O bonds). Therefore one of the drivers for the disordering of the La and Sr cations is to decrease the asymmetry of the CrO_6 units and thus strengthen the Cr-O bonding. However, as discussed in the beginning of Section 3.4.3 (*Investigation on the effects of Sr/La distributions with no octahedral tilts*), in the absence of octahedral tilts along the *c*-axis, Sr/La disorder is energetically unfavourable, so the strengthening of the Cr-O bonds alone is not sufficient to disorder the A-cations.

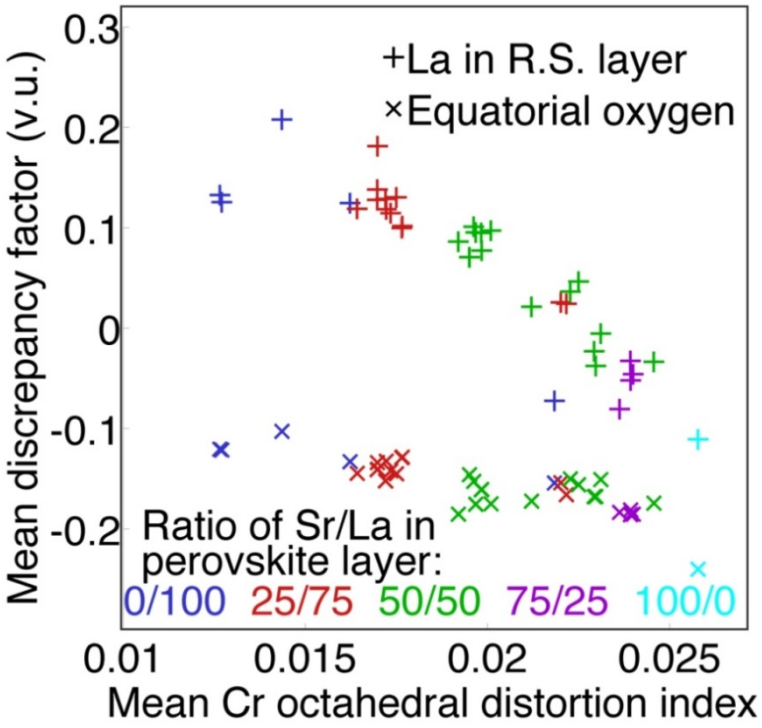


Figure 3.14. The average discrepancy factor, in valence units (v.u.) of La cations in the rock salt layer and equatorial oxygen ions as a function of the average CrO_6 distortion index with various A-site distributions. Light blue points correspond to the reference *Amam* structure with the expected A-site cation ordering.

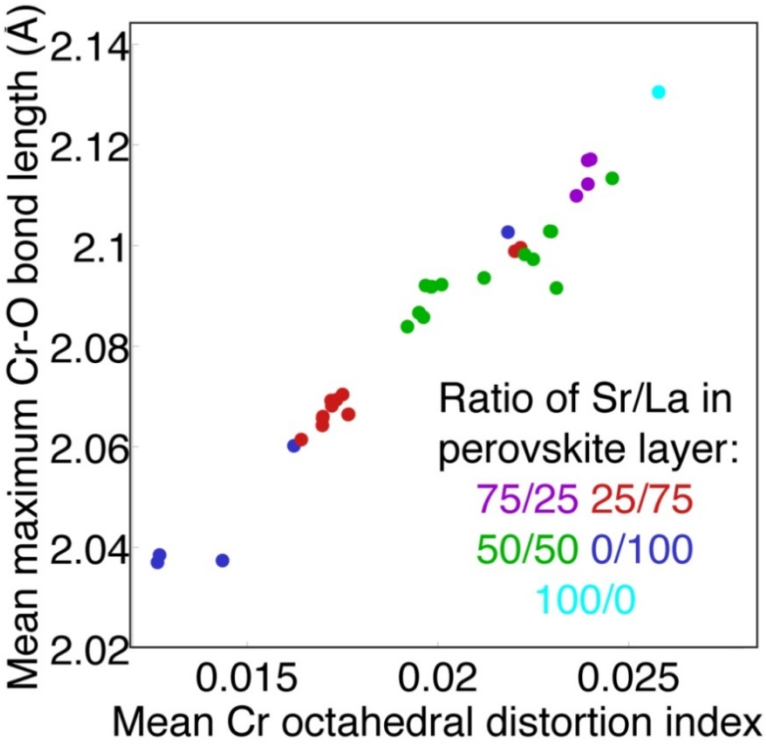


Figure 3.15. The average maximum Cr-O bond length as a function of the average CrO_6 distortion index with various A-site distributions. Light blue points correspond to the reference *Amam* structure with the expected A-site cation ordering. As the mean maximum Cr-O bond length increases, the mean CrO_6 distortion index increases linearly. The maximum of each is reached in the *Amam* structure with La and Sr cations on their expected sites.

3.4.3.3.2 The discrepancy factor (bonding environment)

Two plots related to the mean discrepancy factor of both the O_{eq} anions, and the La_{rs} cations are shown in Figure 3.14 and Figure 3.16. The mean discrepancy factor was plotted against the mean Cr octahedral distortion index in Figure 3.14 while it was against the mean "in plane" angle.

One can observe from Figure 3.14:

(1) In *Amam* reference structure with Sr/La in their expected sites, the equatorial oxygen ions O_{eq} (residing in the CrO_2 layers) are significantly overbonded which is indicated by a negative mean discrepancy factor.

(2) As ratio of Sr/La in perovskite layer decreases (that is, more Sr are moved into the rock salt layer), this overbonding mentioned in (1) is relieved (that is, the discrepancy factor becomes less negative). Meanwhile, the bonding environment of La_{rs} (in rock salt layer) gets worse (the discrepancy factor becomes bigger, indicating a more underbonding environment).

As discussed in the beginning of Section 3.4.3.3, the average bonding environment of the equatorial oxygen atoms O_{eq} is directly affected by the octahedral tilts along *c*-axis and thus is used as an indicator of quantifying the magnitude of octahedral *c*-tilts. The improvement of the overbonding environments of O_{eq} when Sr spreads out, as discussed in observation (2), supports the hypothesis that the octahedral distortion rotations play a role in stabilizing the observed structure of $La_2SrCr_2O_7$. However, this improvement of overbonding environments of O_{eq} comes at the expense of deterioration in the La_{rs} bonding environment.

Similar trends could also be observed in Figure 3.16: as the concentration of Sr in the perovskite layers decreases, the average "in-plane" Cr-O-Cr angle decreases from 180° (indicating an increasing magnitude of tilts along *c*) with an associated improvement (deterioration) of the O_{eq} (La_{rs}) bonding environments.

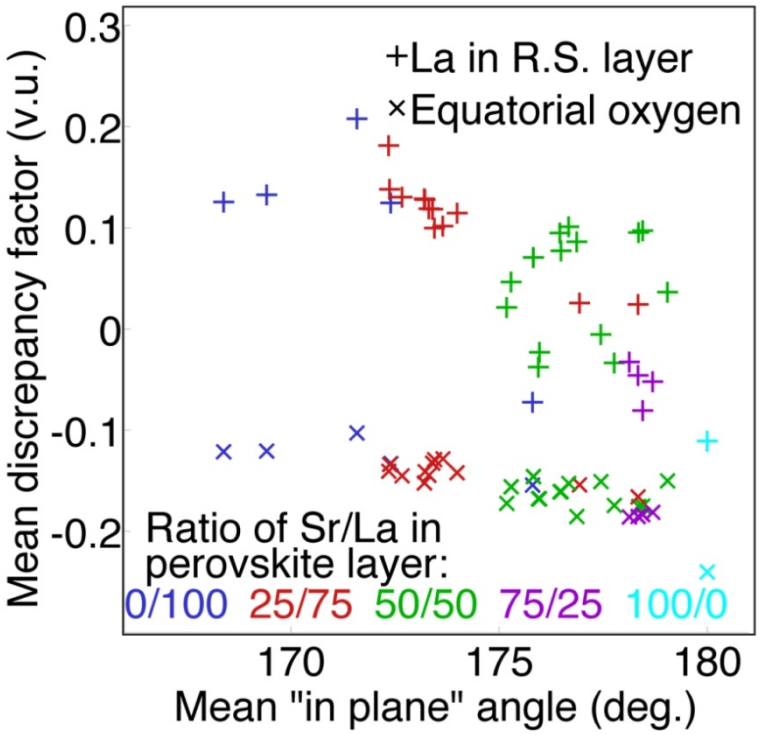


Figure 3.16. The average discrepancy factor of La cations in the rock salt layer and equatorial oxygen ions as a function of the average "in-plane" Cr-O-Cr angle with various A-site distributions. Light blue points correspond to the reference *Amam* structure with the expected A-site cation ordering.

3.4.3.4 Summary

Summarizing the arguments above, it was observed that the principal driver for the unusual distribution of the La and Sr cations is the desire to lower the charge difference between the La-O rock salt and Sr-O perovskite layers (discussed in Section 3.4.3.1), and thus make the CrO_6 units more symmetric. Though in the absence of octahedral tilts around the *c*-axis, the stabilization of the Cr-O bonding is not sufficient to overcome the inherent stability of Sr/La A-site ordered configuration, so Sr/La disorder is not observed (discussed in the beginning of Section 3.4.3 (*Investigation on the effects of Sr/La distributions with no octahedral tilts*)).

However, the unusual distribution Sr/La (Sr in rock salt, La in perovskite) equalized the charges of the rock salt and perovskite layers. Meanwhile, this unusual distribution locally breaks symmetry about the equatorial oxygens, allowing them to displace and the CrO_6 units to rotate. This promotes the O_{eq} and Cr bonding environments to be optimized (discussed in Section 3.4.3.3.2). The energy gain from the charge equalization and the improvement of bonding

environments is sufficient to make the *A2/a* ($\Phi\Phi\Phi_z$ /$\Phi\Phi\Phi_z$) distorted structure with unusual Sr/La distribution more stable than the *Amam* structure with Sr/La in their expected sites.

3.4.4 Comparison to other double layer Ruddlesden-popper phases

The importance of the optimization of the CrO_6 bonding as a driving force for the Sr/La cation disorder, and the associated *A2/a* ($\Phi\Phi\Phi_z$ /$\Phi\Phi\Phi_z$) distortion, is highlighted by comparing the $La_2SrCr_2O_7$ system to other n = 2 Ruddlesden-Popper phases, most notably the Fe^{3+} containing $Ln_2AEFe_2O_7$ (AE = Sr, Ba) series. As noted in Section 3.4.2, $La_2SrFe_2O_7$ adopts an undistorted n = 2 Ruddlesden-Popper structure (space group *I*4/*mmm*) with a 53:47 Sr:La ratio on the perovskite A-site[5]. Likewise $La_2BaFe_2O_7$ adopts an undistorted structure with a 73:37 Ba:La ratio on the perovskite A-site[5]. Thus both phases favour locating the large AE^{2+} cation on the perovskite A-site (compared to the 33:66 AE^{2+}:La^{3+} ratio expected statistically) and neither exhibit any collective rotations of their FeO_6 octahedra, in strong contrast to $La_2SrCr_2O_7$. A further contrast to the chromium system is that both $La_2SrFe_2O_7$ and $La_2BaFe_2O_7$ exhibit highly distorted FeO_6 units. As discussed above the primary distortion mode of the CrO_6 octahedra in our calculations is the lengthening of the bond between chromium and the apical oxide ion in the rock salt layer. If we define a further distortion parameter, MO_6-apical-distort, ($MO_{6\text{-ad}}$), as the ratio of the M-O bonds to the apical oxide ions in the rock salt and perovskite layers ($MO_{6\text{-ad}}$ = $M\text{-}O_{rs}/M\text{-}O_p$) then we observe the FeO_6 units in $La_2SrFe_2O_7$ and $La_2BaFe_2O_7$ yield values of 1.12 and 1.14 respectively[5], compared to a value of 1.03 for $La_2SrCr_2O_7$. These observations are consistent with the idea that i) the 'normal' A-cation distribution of AE^{2+} on the perovskite A-site and La^{3+} on the rock salt A-site induces a distortion into the MO_6 octahedra and ii) the desire to accommodate the Cr^{3+} cations in highly symmetric CrO_6 units leads to the adoption of the novel A-cation-disordered, $\Phi\Phi\Phi_z$ /$\Phi\Phi\Phi_z$ distorted structure observed for $La_2SrCr_2O_7$.

The strong preference for locating Cr^{3+} centres in highly symmetric octahedral coordinations, in comparison to other transition metal cations such as Fe^{3+}, is also consistent with

similar observations made for Cr^{3+}centres in a wide variety of other chemical systems. This wider observation is justified on the basis of the maximum ligand-field stabilization energy (LFSE) associated with the $t_{2g}^3e_g^0$ local electronic configuration of Cr^{3+}, compared to the zero net LFSE for the $t_{2g}^3e_g^2$ configuration of Fe^{3+}. On lowering the symmetry of the MO_6 units M-O bonding will be compromised, however in the case of Fe^{3+} the associated lowering in energy of the occupied e_g antibonding orbitals will help to mitigate this, reducing the energy penalty for the distortion of $Fe^{3+}O_6$ units compared to $Cr^{3+}O_6$ units. This leads us to suggest that we would expect to see a similar coupling of the A-site cation order and octahedral rotations as observed in $La_2SrCr_2O_7$ in other *n* = 2 Ruddlesden-Popper phases which contain 'un-distortable' transition metal cations, such as the as yet unreported phase $La_2SrRh_2O_7$, in which the expected low-spin $t_{2g}^6e_g^0$ electronic configuration of Rh^{3+} should strongly resist distortions to the RhO_6 octahedra.

3.4.5 Magnetism of $La_2SrCr_2O_7$: the canted antiferromagnetism and spin glass behaviour of $La_2SrCr_2O_7$

The neutron diffraction data reveal that $La_2SrCr_2O_7$ adopts a canted G-type antiferromagnetic state below 260 K with spins aligned parallel to crystallographic *b*-axis, which allows a weak ferromagnetism along both the crystallographic *a*- and *c*-axes (consistent with the weak ferromagnetism observed in the magnetization data).

The observation of frustration in the magnetic interactions of $La_2SrCr_2O_7$ is unexpected given the spherical, isotropic t_{2g}^3 electronic configuration of the Cr^{3+} cations. In order to investigate this behaviour in more detail, zero-field μ^+sr data were collected. As discussed in Section 3.3.2.4, strong persistent oscillations were observed in data collected at 5 K, consistent with long range antiferromagnetic order. These oscillations declined in frequency with increasing temperature and ultimately disappeared from the signal at T ~ 260 K, in agreement with the antiferromagnetic ordering temperatures observed in the magnetisation and neutron diffraction data. Close inspection of the μ^+sr data revealed no features indicative of magnetic frustration.

Given that μ^+sr is a bulk measurement which interrogates the entire sample volume, the lack of any features attributable to frustration suggests that only a small fraction of the sample volume is magnetically frustrated. This is further confirmed by the magnetization-field isotherms collected at different temperatures (Figure 3.18) which show that this spin glass behaviour disappeared at 220 K, before the magnetic ordering temperature (260 K). We thus propose that this small spin glass behaviour arises from the intergrowth of single layer into the n = 2 Ruddlesden Popper structure.

The arrangement of n = 2 Ruddlesden Popper structure could be interrupted by the intergrowth of single layer as noted by the arrow in Figure 3.17.[81] That is, in a block of hundreds of double layered perovskite slabs, there might be a few 'mistake' slabs which only contain a single layered perovskite block. This intergrowth is supported by two observations from the data collected from $La_2SrCr_2O_7$:

(1) Only a small amount of the $LaCrO_3$ impurities were observed in the diffraction data of $La_2SrCr_2O_7$. According to reaction scheme $La_2SrCr_2O_7 \rightarrow LaSrCrO_4 + LaCrO_3$, one can deduce that the presence $LaCrO_3$ impurities should result in the observation of $LaSrCrO_4$ impurities. The lack of the latter, in combination with the fact that there are no other obvious impurities observed from the diffraction data, indicates that the $LaSrCrO_4$ "grows" into the $La_2SrCr_2O_7$ structure.

(2) A weak *hkl* dependent peak broadening in the diffraction data was observed in the diffraction data as mentioned in Section 3.3.1.2. This peak broadening could be accounted for by the overlap of the diffraction peaks between $La_2SrCr_2O_7$ and $LaSrCrO_4$. As Ruddleden-Popper phase $A_{n+1}B_nO_{3n+1}$ has a general feature of n block of perovskite layer, their diffraction patterns resemble to each other. A tiny amount of $LaSrCrO_4$ growing into $La_2SrCr_2O_7$ would slightly broaden some of the diffraction peaks as observed in our $La_2SrCr_2O_7$ phase.

This intergrowth could interrupt the antiferromagnetic order, resulting in weak spin glass behaviour. As shown in Figure 3.17, the magnetic interaction between adjacent layers was

defined as J_1, and the interaction between next adjacent layers (where the octahedral directly sit on top of each other) J_2. This J_2 interaction is antiferromagnetic as confirmed by the magnetic analysis from neutron diffraction data. These J_1 and J_2 interactions repeat themselves in our $La_2SrCr_2O_7$ structure if there is no intergrowth of single layer. However, when a single layer of $LaSrCrO_4$ grows into $La_2SrCr_2O_7$, this J_2 magnetic interaction would be interrupted. As shown in Figure 3.17, with the presence of the "mistake" layer C, the lower pink A/B layer is caught in a dilemma. It should adopt the magnetic arrangement same as that of the layer A as required by the symmetry of $La_2SrCr_2O_7$. In this case, the J_2 interaction between the next adjacent layers adopts a normal antiferromagnetic arrangement. However, the lower pink A/B layer should also adopt the same arrangement as that of the layer B, required by the J_1 interaction as well as the symmetry requirement of $LaSrCrO_4$. In this case, this J_2' interaction becomes ferromagnetic. Thus the intergrowth of single layer leads to a small scale of magnetic disorder and frustration, resulting in the spin glass behaviour observed in $La_2SrCr_2O_7$.

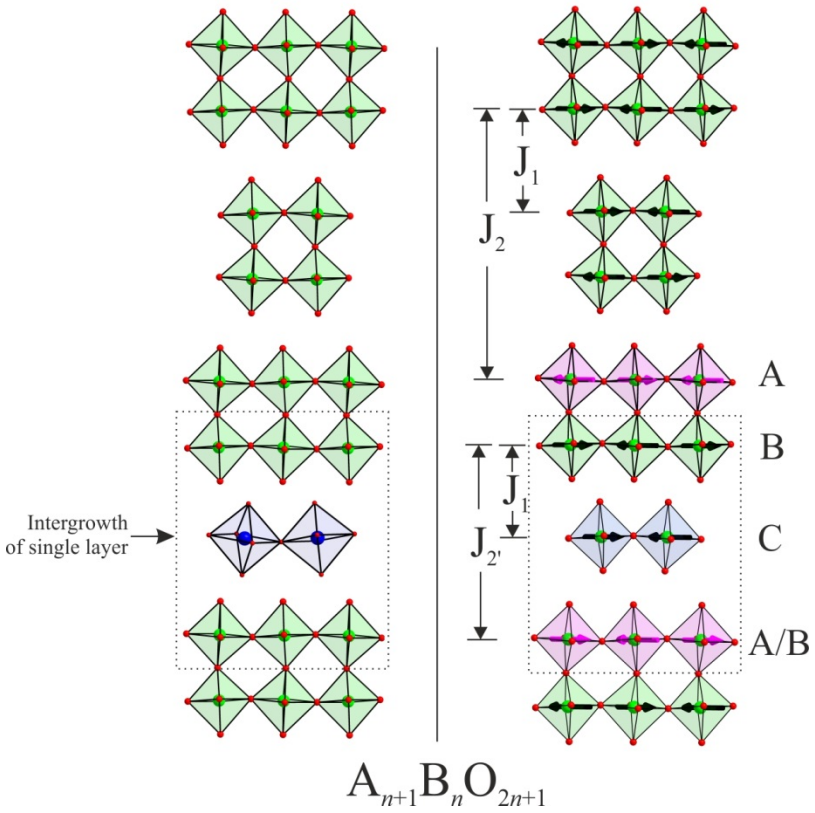


Figure 3.17. The intergrowth of single layer into the n = 2 Ruddlesden Popper structure (noted by the arrow) and magnetic disorder caused by the intergrowth. The A cations were neglected to simplify the model.

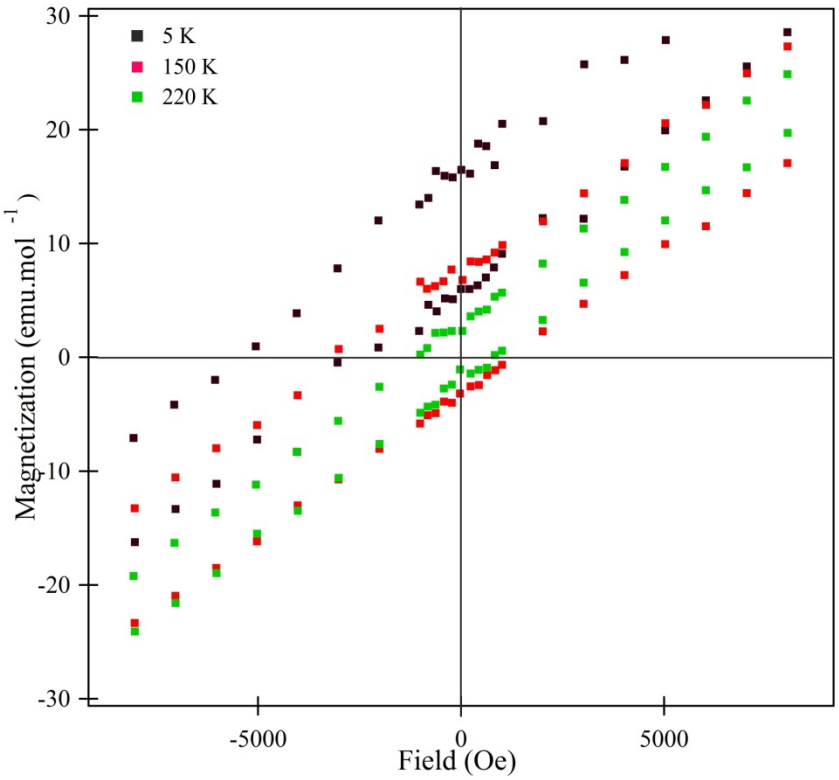


Figure 3.18. The magnetization-field isotherms collected at 5 K, 150 K and 220 K from $La_2SrCr_2O_7$.

3.5 Conclusion

The *n* = 2 Ruddlesden-popper phase $La_2SrCr_2O_7$ adopts an *A2/a* ($\Phi\Phi\Phi_z$ /$\Phi\Phi\Phi_z$) distorted structure with an unusual A-cation distribution (the 12-coordinate A-sites of $La_2SrCr_2O_7$ are occupied by 82(2)% La^{3+} and 18(2)% Sr^{2+}, while the 9-coordinate A-sites are occupied by 58(1)% La and 42(1)% Sr), and a robust antiferromagnetic order below T_N ~ 260 K.

The complex coupling between the rotations of the CrO_6 octahedra and the La/Sr A-site distribution of $La_2SrCr_2O_7$ clearly demonstrates that the cooperative, symmetry-lowering distortions of *n* = 2 Ruddlesden-Popper phases are not solely directed by the structural tolerance factor. Instead it appears that the structures adopted by these phases are determined by a number of different parameters in combination. This multiplicity of factors influencing the distorted structures of *n* = 2 Ruddlesden-Popper phases provides many opportunities to direct the tilting arrangements in layered perovskite phases, to tune both the magnitude of the B-O-B angles and the symmetry of the cooperatively distorted network.

In the specific case of $La_2SrCr_2O_7$ one can see that the apparent energy penalty associated with distorting the CrO_6 octahedra couples together the A-cation distribution and the octahedral rotations. This suggests that if isovalent A-cation substitutions are made to $La_2SrCr_2O_7$ (e.g. Ca^{2+} for Sr^{2+} or a smaller lanthanide for La^{3+}) which lead to changes in the distribution of the AE^{2+} and Ln^{3+} cations between the A-sites in the perovskite and rock salt layers, there will be resulting changes to the cooperative rotations of the CrO_6 octahedra over and above those expected on the grounds of the changing tolerance factor. Thus this new coupling between A-site distribution and octahedral rotation could provide a route to realizing as-yet unseen structural configurations and facilitate the preparation of phases with desired polar distortions. In addition there is an intriguing possibility that the coupling could be used 'in reverse' to generate novel A-cation ordering schemes in Ruddlesden-Popper phases by utilizing the inflexibility of certain octahedrally coordinated B-cations.

Chapter 4: Topochemical fluorination of $La_2SrCr_2O_7$ to $La_2SrCr_2O_7F_2$

4.1 Introduction

As discussed in Chapter 1 Section 1.2, phases that lie close to metal-insulator 'equilibrium' point where W (band width) ≈ U (electron repulsion) can potentially exhibit novel physical behaviours such as superconductivity or magnetoresistance[16]. Perovskite-like phases containing octahedrally coordinated Cr^{4+} centres fall into this category of materials because the values of the bandwidth, W, arising from the overlap of chromium *d*-orbitals, and the Hubbard U, arising from electron-electron interactions, are approximately equal, so small structural changes, such as adjusting the Cr-O-Cr bond angle of a phase, can be used to tune behaviours from metallic to insulating.

However, as the radius of Cr (IV) is relatively small, it tends to occupy 4-fold tetrahedral coordinate sites rather than the 6-fold octahedral sites in the perovskite structure. Thus phases containing Cr (IV) prepared at ambient pressure typically contain tetrahedrally coordinated Cr (IV). The preparation of phases containing octahedrally coordinated Cr (IV) centres generally requires high-pressure synthetic conditions[82]. Samples produced under such conditions tend to be of small scale and often contain binary chromium oxide impurities, typically CrO_2, which makes the detailed physical characterization of these Cr (IV) phases extremely challenging.

As discussed in Chapter 1 Section 1.5, the layered nature of Ruddlesden-Popper structure allows us to manipulate the oxidation state of cations by inserting fluoride ions into the tetrahedral interstitial sites residing in the rock salt layer. During the fluorination process, $A_3B_2O_7$ phases are converted into $A_3B_2O_7F_2$ phases, oxidizing the B-cations from B^{n+} to $B^{(n+1)+}$ while their local coordination geometry remains largely unchanged (Figure 4.1).[21-23] This type of topchemical fluorination reaction provides a new strategy for the preparation of extended oxide phases containing octahedrally coordinated Cr^{4+} centres, while avoiding the use of high-pressure

synthesis conditions. We would expect that the topochemical fluorination of an $A_3Cr^{3+}{}_2O_7$ phase should result in the formation of an $A_3Cr^{4+}{}_2O_7F_2$ phase containing sheets of apex-linked, octahedrally coordinated Cr^{4+} centres. Thus this chapter describes the topochemical fluorination of $La_2SrCr_2{}^{3+}O_7$, an n = 2 Ruddleden-Popper phase containing octahedrally coordinated Cr^{3+} centres, into $La_2SrCr_2{}^{4+}O_7F_2$. The bulk of this work has been published in *Inorganic Chemistry*.[61]

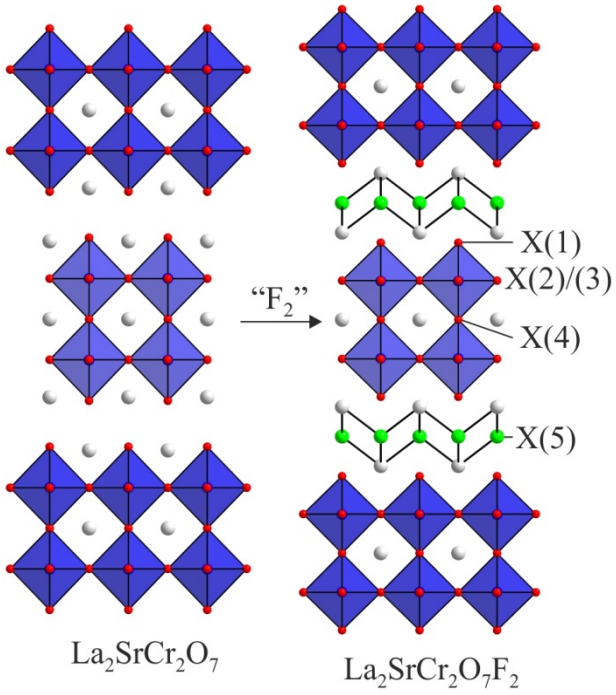


Figure 4.1. Topochemical fluorine insertion into n = 2 Ruddleden-Popper phase, $La_2SrCr_2{}^{3+}O_7$, for the preparation of $La_2SrCr_2{}^{4+}O_7F_2$.

4.2 Experimental

The synthesis of $La_2SrCr_2O_7$ is described in Chapter 3. Fluorination of $La_2SrCr_2O_7$ was performed using CuF_2 as an *in situ* fluorine source (CuF_2 + 1/2 O_2 = CuO + F_2), as discussed in Chapter 2 Section 2.2.[21] The $La_2SrCr_2O_7$ oxides and CuF_2 were ground together in a molar ratio of 1:2 and heated at 175 °C for 24 h under flowing O_2. X-ray diffraction data collected from the fluorinated sample revealed a new phase forming with a large c-lattice parameter expansion relative to the starting material, indicating the formation of $La_2SrCr_2O_7F_2$ phases. The reaction can be described according to scheme S1.

$$\mathbf{La_2SrCr_2O_7 + CuF_2 \xrightarrow{O_2} La_2SrCr_2O_xF_y + CuO} \qquad \textbf{(S1)}$$

The by-product CuO however contaminates the fluorinated phase as shown in S1. To avoid this contamination we have developed a process where CuF_2 is heated separately at 500 ºC under flowing oxygen, to liberate fluorine, and the resulting mixture of gasses is then passed over the material to be fluorinated. This fluorination reaction setup was described in detail in Chapter 2 Section 2.2 Thus $La_2SrCr_2O_7$ was fluorinated by multiple heating at 310 ºC under the O_2/F_2 gas mixture until the reaction was deemed complete by X-ray powder diffraction. Reaction in this process is far less efficient than mixing the parent oxide and CuF_2 together because most of F_2 gas formed by CuF_2 is flushed away by the flowing O_2 gas and reaction only happens on the surface of the oxide contacted with F_2 gas. The fluorinated phase, $La_2SrCr_2O_7F_2$, started to decompose into SrF_2 and $LaCrO_3$ above 310 ºC under flowing O_2/F_2 gas mixture.

4.3 Results

4.3.1 X-ray powder diffraction data

The X-ray powder diffraction data collected from the fluorinated sample at different reaction times during the fluorination process (Figure 4.2) revealed a new phase forming with a larger *c*-lattice parameter relative to the starting material as the (115) peak shifted to large *d*-spacing. The splitting of the (115) peak to (115) and (-115) indicated that the fluorinated phase adopted a monoclinic unit cell, which could be indexed with lattice parameters of a = 5.426(1) Å, b = 5.468(1) Å, c = 22.68 (1) Å, β = 90.4 (1)º.

During the fluorination process, all peaks observed in the powder x-ray diffraction patterns could be indexed to either $La_2SrCr_2O_7$ or $La_2SrCr_2O_7F_2$. No other new phases were observed. This suggests that $La_2SrCr_2O_7$ was fully converted to $La_2SrCr_2O_7F_2$ without the formation of any intermediate phases with lower fluorine content (such as $La_2SrCr_2O_7F$ phase,

analogous to the staged structure in which the fluorine ions are inserted into alternative layers as adopted by $LaSrMnO_4F$.[22]).

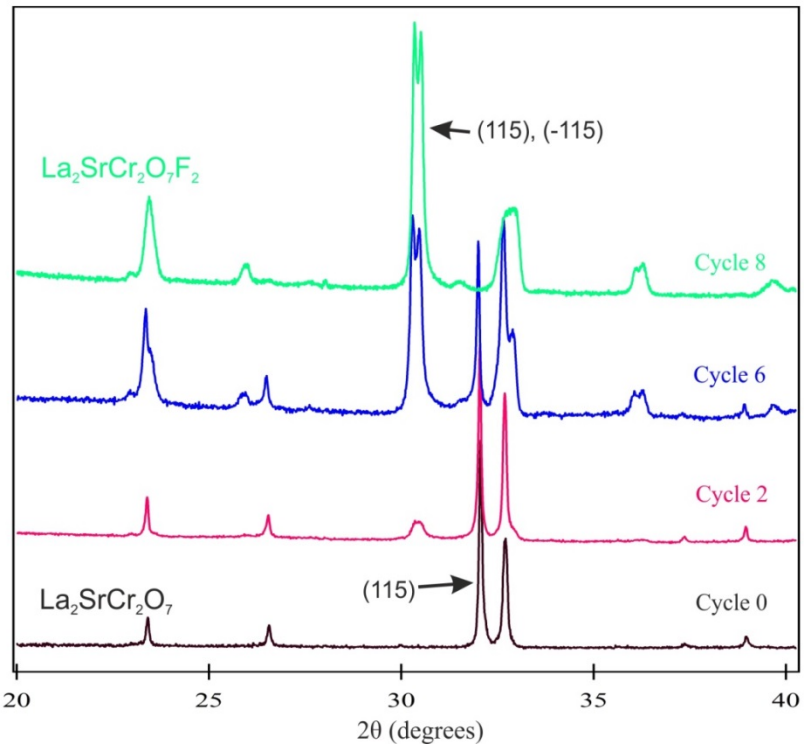


Figure 4.2. The evolution of the sample at different reaction stage during the fluorination process. Each cycle indicates a heating cycle of 2 days under the condition described in Section 4.2.

4.3.2 Compositional characterization of $La_2SrCr_2O_7F_2$

Attempts to determine the composition of the fluorinated phase by iodometric titrations failed due to sample's insolubility. Thermogravimetric analysis (TGA) was carried out by heating sample of the fluorinated phase $La_2SrCr_2O_xF_y$ to 800 ºC at a heating rate of 5 ºC/min under a flowing 10% H_2/N_2 atmosphere. X-ray powder diffraction data collected from this sample after thermogravimetric analysis process indicated the sample has been fully converted to SrF_2 and $LaCrO_3$ (Figure 4.3), and there is no sign of the formation of LaF_3. The mass loss observed from TGA was 2.46% (Figure 4.4). The expected mass loss of a $La_2SrCr_2O_7F_2$ is calculated to be 2.50 % according to scheme S2, if taking the 3.4% weight% $LaCrO_3$ impurities present in the sample (discussed in Section 4.3.2) into account.

$$\mathbf{La_2SrCr_2O_7F_2 \xrightarrow{H_2} 2LaCrO_3 + SrF_2 + \frac{1}{2}O_2} \quad \mathbf{(S2)}$$

The observed mass loss is in good agreement with that of the expected value. This confirmed a composition of $La_2SrCr_2O_7F_2$ for the fluorinated sample, which is also consistent with the structural analysis as described in this chapter, Section 4.3.3.2 and 4.4.1.

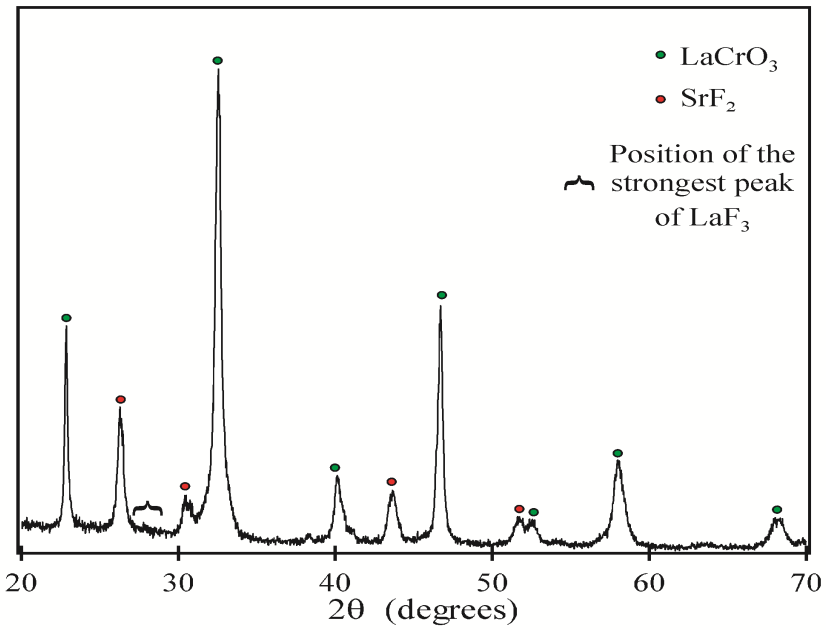


Figure 4.3. X-ray powder diffraction pattern collected from sample of $LaSr_2Cr_2O_7F_2$ after heating under 10% H_2 in N_2 on TGA.

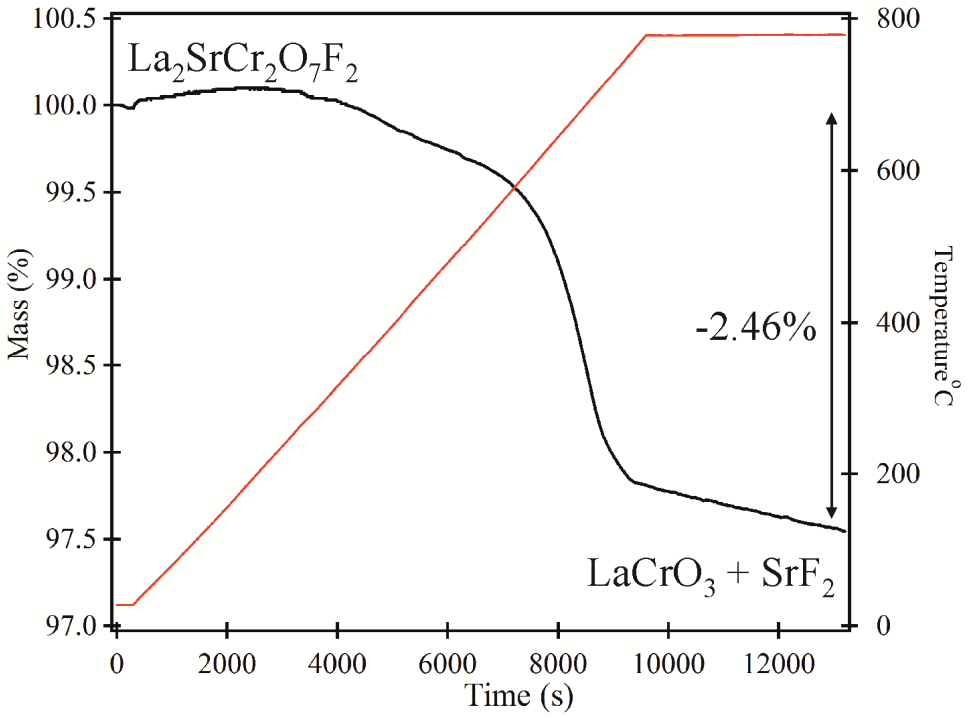


Figure 4.4. Thermogravimetric data collected by heating $La_2SrCr_2O_7F_2$ under 10% H_2 in N_2. Sample mass (black, left axis), sample temperature (red, right axis). Expected mass loss of $La_2SrCr_2O_7F_2$ when converted to $LaCrO_3$ + SrF_2 = 2.50% (N.B. sample contains 3.4 weight% $LaCrO_3$).

4.3.3 Structural refinement of $La_2SrCr_2O_7F_2$

An *A2/a* structural model constructed based on the structure of the parent oxide was refined against the neutron diffraction data collected from $La_2SrCr_2O_7F_2$ at room temperature. During the refinement, the La/Sr A-cation distribution was fixed at the values observed for the $La_2SrCr_2O_7$ parent phase (see Chapter 3 Section 3.3.1 and 3.4.2) with all other atomic positional and displacement parameters allowed to refine freely. The oxygen/fluorine anion distribution was not considered in this stage since their neutron scattering lengths are strikingly similar (O = 5.80 fm, F = 5.65 fm)[46] as discussed in Chapter 2 Section 2.3.4.1, and all the anion sites were considered to be fully occupied. In common with the all-oxide parent phase, the diffraction data collected from $La_2SrCr_2O_7F_2$ exhibited weak *hkl* dependent peak broadening, so an anisotropic broadening axis (001) was added to the peak shape description to allow crystal microstrain perpendicular and parallel to this axis to be refined independently. A small amount of $LaCrO_3$ impurity was observed and thus added as a secondary phase to the structural model.

The *A2/a* model gave a good statistical fit to the neutron diffraction data. Plots of the observed and calculated data from the 35° bank are shown in Figure 4.5, and that of other banks are in Figure A4.1 in Appendix. The detailed structural parameters of the refined model are given in Table 4.1. At the end of the refinement, the occupancy of each anion site was set to refine freely. It turned out that all anion sites were fully occupied within error. Selected bond lengths and angle from the refined structure of $La_2SrCr_2O_7$ and $La_2SrCr_2O_7F_2$ at 298K are shown in Table 4.2.

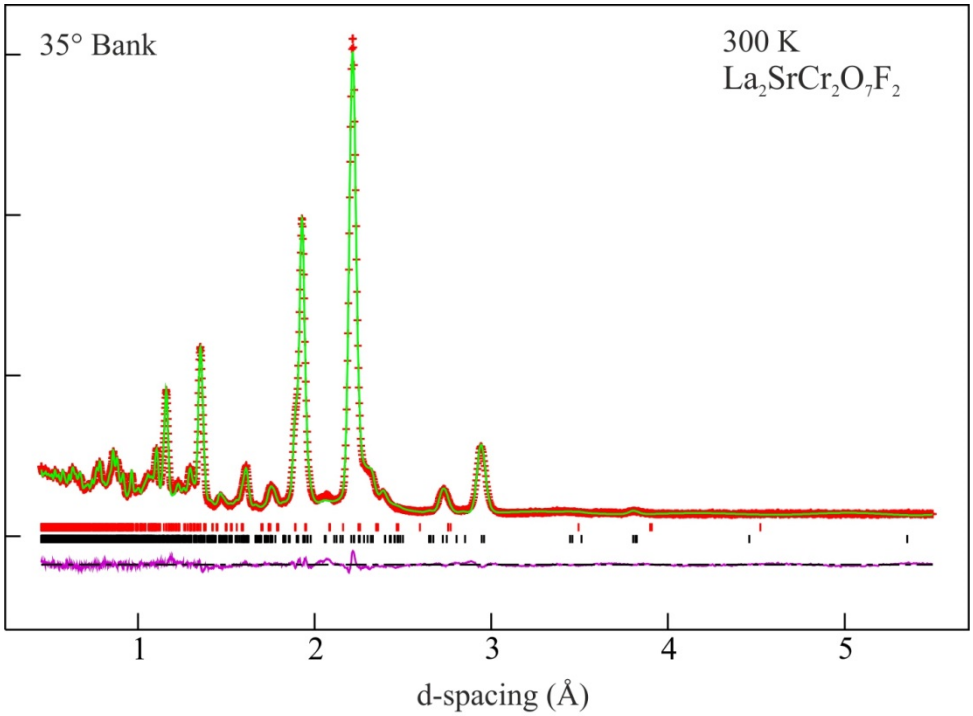


Figure 4.5. Observed, calculated and difference plots from the structural refinement of $La_2SrCr_2O_7F_2$ against neutron powder diffraction data collected at room temperature by using GEM diffractometer (ISIS, UK). Lower tick marks indicate peak positions for the majority phase, upper tick marks for the $LaCrO_3$ secondary phase.

	x	**y**	**z**	**Fraction**	**U_{iso} (Å^2)**
La/Sr(1)	¼	0.7525(10)	0	0.82/0.17	0.0045(6)
La/Sr(2)	0.2516(7)	0.7507(7)	0.1787(1)	0.58/0.42	0.0065(5)
Cr(1)	0.2474(18)	0.2501(14)	0.0848(2)	1	0.0016(5)
O(1)	0.2584(10)	0.2920(8)	0.1655(1)	1	0.0093(7)
O(2)	0.9689(8)	0.0300(10)	0.0936(1)	1	0.0062(8)
O(3)	0.5256(9)	0.4759(12)	0.0758(1)	1	0.0061(8)
O(4)	¼	0.2107(14)	0	1	0.0130(10)
F(1)	0.4957(7)	0.5004(13)	0.2517(1)	1	0.0082(5)
$La_2SrCr_2O_7F_2$ – space group: *A*2/*a* *a* = 5.4262(6) Å, *b* = 5.4681(7) Å, *c* = 22.682(2) Å, β = 90.44(1)º volume = 672.9(2)Å^3 phase fraction = 96.7(1) weight percent					
$LaCrO_3$ – space group: *Pnma* *a* = 5.467(2) Å, *b* = 7.764(5) Å, *c* = 5.513(2) Å phase fraction = 3.4(1) weight percent					
χ^2 = 5.34, wRp = 4.45%, Rp = 3.79%					

Table 4.1. Structural parameters refined against neutron powder diffraction data collected at 300 K from $La_2SrCr_2O_7F_2$. The A-cation fractions in the table were fixed at the values observed for the $La_2SrCr_2O_7$ parent phase, and thus listed without errors.

$La_2SrCr_2O_7$		**$La_2SrCr_2O_7F_2$**	
La/Sr(1)		**La/Sr(1)**	
Anion	**Bond length (Å)**	**Anion**	**Bond length (Å)**
O(2)	2.862(9) × 2	O(2)	2.701(10) × 2
O(2)	2.807(9) × 2	O(2)	3.031(12) × 2
O(3)	2.674(8) × 2	O(3)	2.456(10) × 2
O(3)	2.653(8) × 2	O(3)	2.728(11) × 2
O(4)	2.754(1) × 2	O(4)	2.505(9)
O(4)	2.856(8)	O(4)	2.721(1) × 2
O(4)	2.624(1)	O(4)	2.963(9)
La/Sr(2)		**La/Sr(2)**	
Anion	**Bond length (Å)**	**Anion**	**Bond length (Å)**
O(1)	2.786(8)	O(1)	2.526(6)
O(1)	2.849(5)	O(1)	2.701(7)
O(1)	2.747(8)	O(1)	2.778(7)
O(1)	2.671(5)	O(1)	2.975(6)
O(2)	2.562(9)	O(2)	2.567(10)
O(2)	2.522(9)	O(2)	2.892(11)
O(3)	2.671(8)	O(3)	2.906(11)
O(3)	2.629(8)	O(3)	3.157(12)
		F(1)	2.488(10) × 2
		F(1)	2.567(11)
		F(1)	2.517(10)
Cr(1)		**Cr(1)**	
Anion	**Bond length (Å)**	**Anion**	**Bond length (Å)**
O(1)	2.037(3)	O(1)	1.845(5)
O(4)	1.972(2)	O(4)	1.936(5)
O(2)	2.000(13)	O(2)	1.943(10)
O(2)	1.876(13)	O(2)	1.956(10)
O(3)	1.919(12)	O(3)	1.932(10)
O(3)	1.973(12)	O(3)	1.962(11)
			Bond Angles (°)
Cr(1)-O(2)-Cr(1)	175.08(55)	Cr(1)-O(2)-Cr(1)	162.1(4)
Cr(1)-O(3)-Cr(1)	173.68(51)	Cr(1)-O(3)-Cr(1)	163.0(4)
Cr(1)-O(4)-Cr(1)	170.88(8)	Cr(1)-O(4)-Cr(1)	167.2(1)

Table 4.2. Selected bond lengths and angles from the refined structure of $La_2SrCr_2O_7$ and $La_2SrCr_2O_7F_2$ at 298K. Labelling scheme is shown in Figure 4.1.

4.3.4 Magnetic Characterization of $La_2SrCr_2O_7F_2$

4.3.4.1 Magnetization data

The magnetization data collected from $La_2SrCr_2O_7F_2$ in an applied field of 100 Oe are shown in Figure 4.6. The divergence between zero-field cooled and field cooled data indicates a weak ferromagnetism below 140 K. In temperature range of 140 K to 285 K, there is still a small mismatch between zero-field cooled and field cooled data, which can be ascribed to the presence of small amount of $LaCrO_3$ 'inherited' from the parent oxide $La_2SrCr_2O_7$ as discussed in Section 4.3.3 ($LaCrO_3$ has an antiferromagnetic ordering temperature of 285 K[71]).

The magnetization-field isotherm data collected at 5 K shows spin-glass behaviour as the centre of the hysteresis loop shifts away from the origin (Figure 4.7).

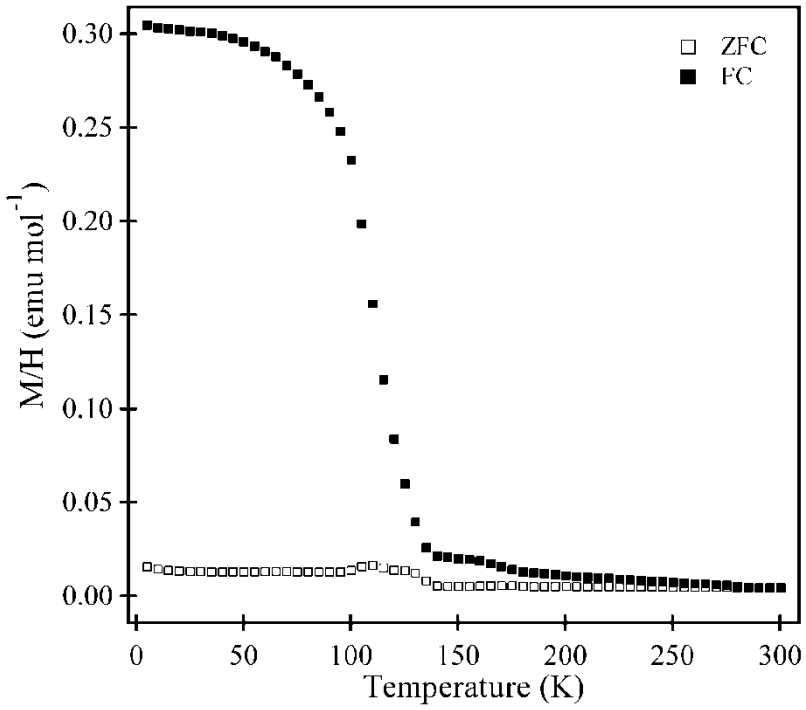


Figure 4.6. Plots of zero-field cooled and field cooled magnetization collected as a function of temperature from $La_2SrCr_2O_7F_2$.

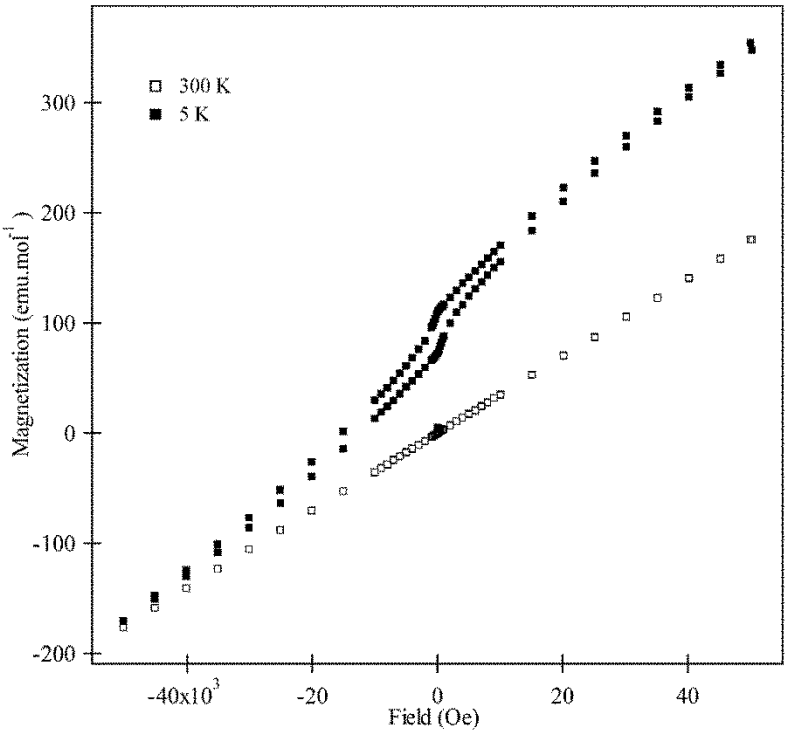


Figure 4.7. The magnetization-field isotherms collected at 300 K and 5 K from $La_2SrCr_2O_7F_2$.

4.3.4.2 Neutron powder diffraction data (5 K)

Neutron powder diffraction data collected at 5 K from $La_2SrCr_2O_7F_2$ show additional peaks with respect to the analogous data collected at 300 K as shown in Figure 4.8. Given the magnetic ordering behaviour shown in the magnetization data as discussed in 4.3.4.1, these additional diffraction features were considered to be magnetic scattering peaks. A magnetic symmetry analysis using the SARAh code[72] was performed for $La_2SrCr_2O_7F_2$ using its crystallographic unit cell in space group *A2/a* (magnetic ordering vector **k** = 0). This analysis yielded 4 irreducible representations each consisting of 3 basis vectors (as listed in Appendix, Table A4.1). These four symmetry compatible magnetic models were constructed and refined against the neutron powder diffraction data collected at 5 K. The best fit to the data was achieved by using a G-type antiferromagnetic ordered model with spins aligned parallel to crystallographic *c*-axis (Irreducible Representation 1) as shown in Figure 4.9. This irreducible allows weak ferromagnetism along the crystallographic *b*-axis, consistent with the magnetization data as discussed in Section 4.3.4.1. This weak ferromagnetic component was very small, and thus

neglected when the above magnetic models were constructed and refined against the low-temperature neutron diffraction data. The refined nuclear and magnetic structural parameters are detailed in Table A4.2 in Appendix. The ordered magnetic moment was refined to be 1.32(2) μ_B per chromium centre at 5 K, which is smaller than would be expected for a spin-only, S = 1 centre, suggesting an unquenched orbital contribution to the moment.

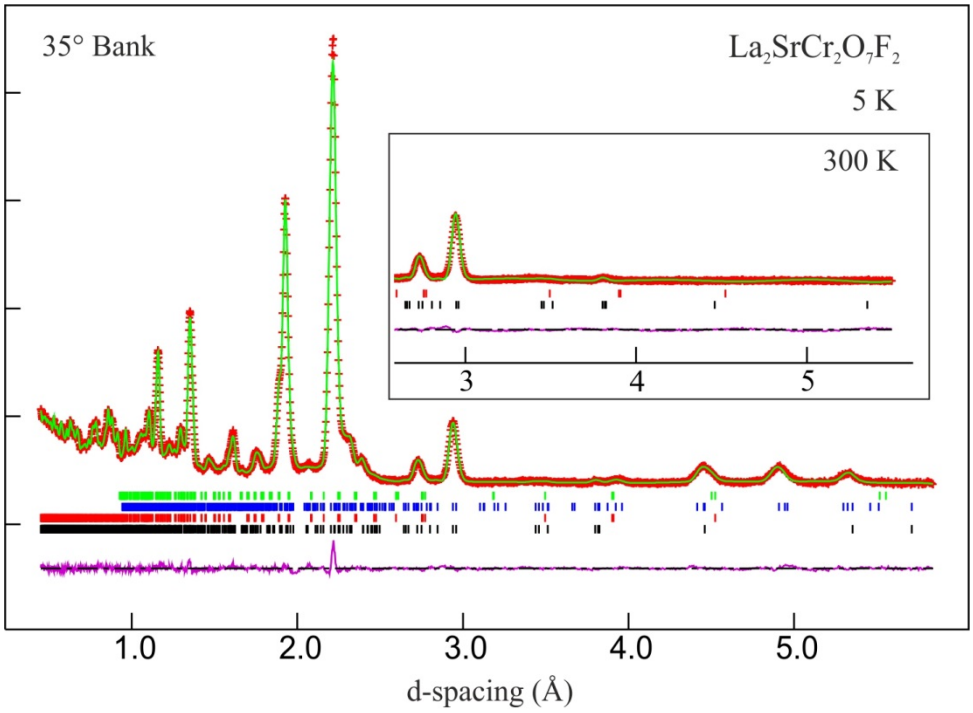


Figure 4.8. Observed, calculated and difference plots from the structural refinement of $La_2SrCr_2O_7F_2$ against neutron powder diffraction data collected at 5 K by using GEM diffractometer (ISIS, UK). Tick marks indicate peak positions of magnetic model of $La_2SrCr_2O_7F_2$ (blue) and $LaCrO_3$ magnetic model (green), $LaCrO_3$ impurities nuclear model (red), $La_2SrCr_2O_7F_2$ nuclear model (black). Insert: neutron diffraction data collected from $La_2SrCr_2O_7F_2$ at 300 K.

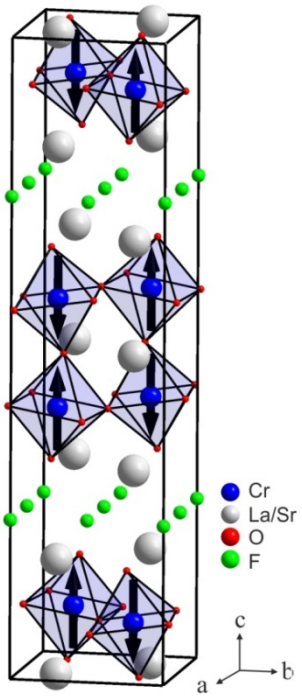


Figure 4.9. The magnetic structure of $La_2SrCr_2O_7F_2$ refined from neutron powder diffraction collected at 5K. Ordered moment = 1.32(2) μ_B per chromium centre at 5 K.

4.3.4.3 Variable temperature neutron powder diffraction data

Neutron powder diffraction data were collected from $La_2SrCr_2O_7F_2$ in the temperature range 5 < T/K < 160. All these diffraction patterns are similar to each other apart from a decrease in values of the refined ordered magnetic moment, indicating no obvious phase transition. The ordered moment was refined to zero at 140 K (Figure 4.10), in good agreement with the magnetization data shown in Figure 4.6.

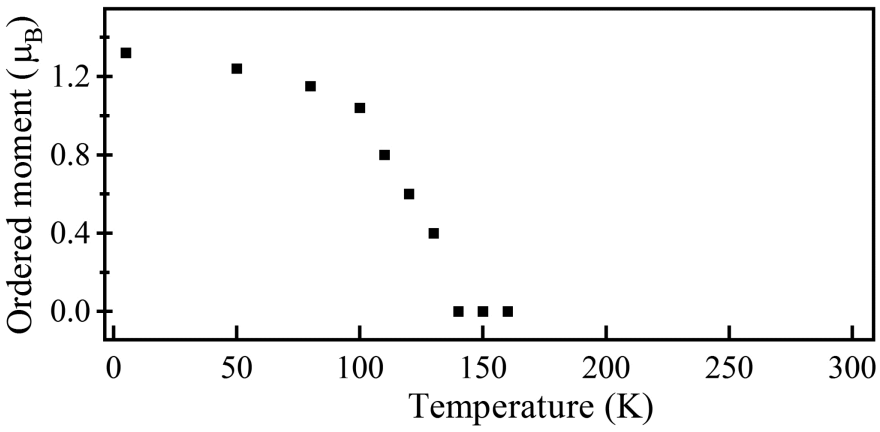


Figure 4.10. Ordered magnetic moment extracted from fits to neutron powder diffraction data.

4.3.3.4 Zero-field μ^+SR data

Zero-field μ^+SR data were collected from $La_2SrCr_2O_7F_2$ as a function of temperature. As shown in Figure 4.11 and Figure 4.12, strong persistent oscillations were observed in data collected at 5 K, consistent with long range antiferromagnetic order. These oscillations declined in frequency with increasing temperature and ultimately disappeared from the signal at T ~ 140 K, in agreement with the antiferromagnetic ordering temperatures observed in the magnetization and neutron diffraction data.

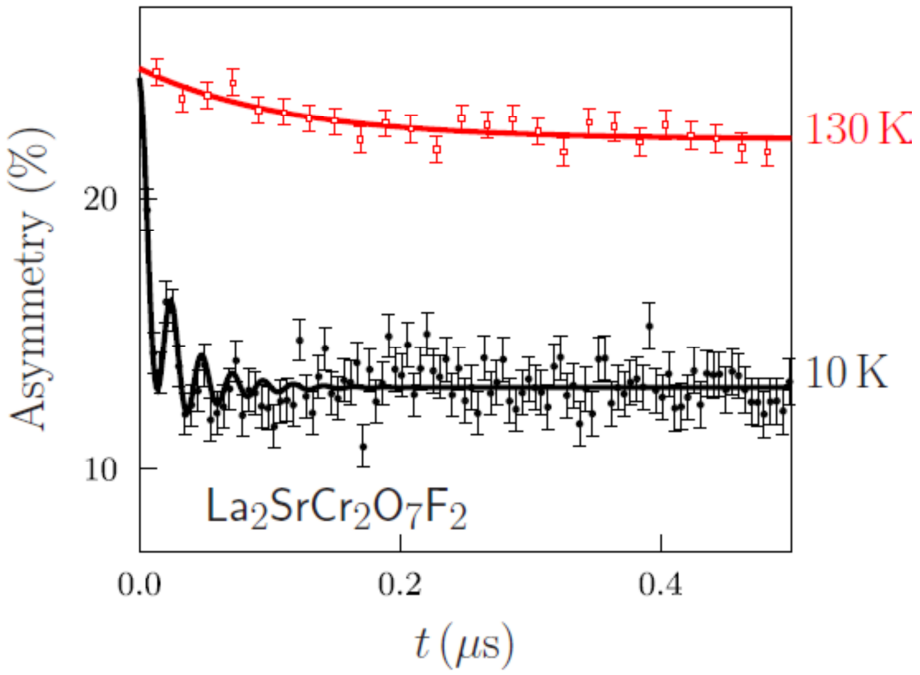


Figure 4.11. Oscillations in the asymmetry of μ^+SR data collected from $La_2SrCr_2O_7F_2$ at low temperature indicate long range magnetic order, consistent with the observation of antiferromagnetic order in the phase via neutron powder diffraction.

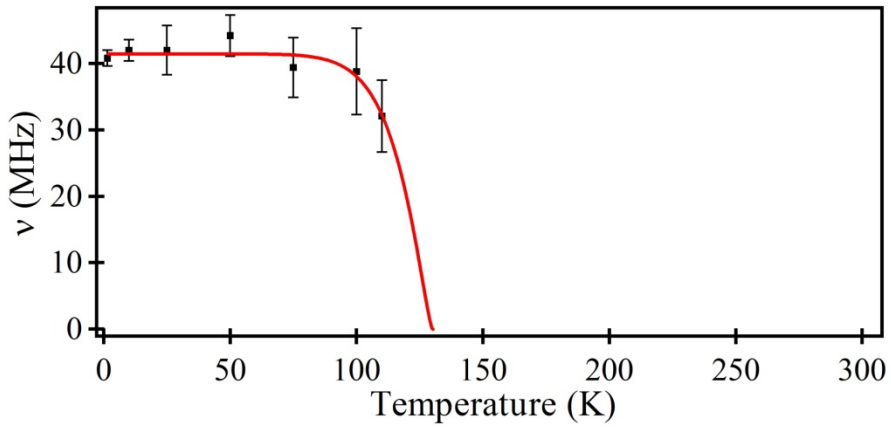


Figure 4.12. The muon oscillation frequency data collected as a function of temperature from $La_2SrCr_2O_7F_2$.

4.4 Discussion

4.4.1 Anion distribution of $La_2SrCr_2O_7F_2$

It is difficult to distinguish the oxide and fluoride anions from X-ray or neutron diffraction data as their scattering lengths are very similar as mentioned earlier.[46] However it is possible to deduce the oxide/fluoride distributions in some oxide-fluoride phases by detailed examination of the local bonding at anion sites using bond valence sums (BVS), as detailed in Chapter 2 Section 2.9.[83] The BVS of the anion sites in the structure of $La_2SrCr_2O_7$ and $La_2SrCr_2O_7F_2$ were calculated by supposing the sites were exclusively occupied by either oxide or fluoride anions (Table 4.3). To simplify the calculation, all A-cations were assumed to be La^{3+}, resulting in slightly overestimated BVS values compared to a La^{3+}/Sr^{2+} mixture.

These BVS data in Table 4.3 reveal that the tetrahedral interstitial anion site X(5) has the smallest BVS value, and thus should be considered to be occupied by fluorine instead of oxygen. Meanwhile the La/Sr(2)-X(5) bond lengths in $La_2SrCr_2O_7F_2$ were observed to range from 2.48 – 2.56 Å (Table 4.2), comparable to those Sr-F bond lengths observed for SrF_2 (2.511 Å)[84] and the range of M-F bond lengths seen in other fluorine intercalated Ruddlesden-Popper phases.[85,86] Furthermore the La/Sr(2)-F(1) bond lengths are much shorter than would be expected for an La/Sr-O bond. This supports our assertion that the X(5) site should be occupied by fluorine not oxygen. The X(1) anion site also has a relatively small BVS value. This is however consistent with the analogous BVS value of O(1) site in the parent oxide, $La_2SrCr_2O_7$. Given all the anion sites are known to be fully occupied from Rietveld refinement against neutron powder diffraction data, and the composition of the fluorinated sample calculated from TGA data is $La_2SrCr_2O_7F_2$, the X(5) site should be occupied exclusively by fluorine while X(1) by oxygen.

In conclusion, the BVS analysis indicates that the fluorination of $La_2SrCr_2O_7$ occurs via the simple insertion of fluoride ions into the tetrahedral interstitial anion site without any anion

exchange. This insertion-only behaviour was also observed in the topochemical fluorination of Sr_3RuMO_7 (M = Ru, Mn, Ti) and $Ln_{1.2}Sr_{1.8}Mn_2O_7$ phases. [22,23]

$La_2SrCr_2O_7$		**$La_2SrCr_2O_7F_2$**		
Anion	**BVS(O)**	**Anion**	**BVS(O)**	**BVS(F)**
O(1)	1.756	X(1)/O(1)	1.677	1.275
O(2)	1.890	X(2)/O(2)	2.105	1.615
O(3)	2.208	X(3)/O(3)	1.911	1.470
O(4)	2.180	X(4)/O(4)	1.989	1.528
		X(5)/F(1)	1.588	1.164

Table 4.3. Anion bond valence sums from $La_2SrCr_2O_7$ and $La_2SrCr_2O_7F_2$. Labelling scheme is shown in Figure 4.1.

4.4.2 Compression of the perovskite layers by fluorine insertion

The topochemical fluorine insertion into $La_2SrCr_2O_7$ leads to two structural effects: 1) a significant increase in *c*-lattice parameter, and 2) a dramatic compression of the perovskite layers within the phase. The *c*-lattice parameter increases from 20.182 Å in $La_2SrCr_2O_7$ to 22.682 Å in $La_2SrCr_2O_7F_2$. This expansion along *z*-axis is required to accommodate the inserted fluoride anions in the rock salt layer.

Although the *c*-lattice parameter increases on fluorination, the double perovskite blocks are heavily compressed along the *z*-axis. As shown in Figure 4.13, the *c*-dimension of the double perovskite blocks was measured as the distance parallel to the *z*-axis between the apical O(1) anions. This value decreases from 7.99 Å in $La_2SrCr_2O_7$ to 7.50 Å in $La_2SrCr_2O_7F_2$. This means the *c*-dimension of the double perovskite blocks of the fluorinated phase is ~0.5 Å shorter compared to that of its parent oxide phase, which is much greater than that would be expected from the contraction of the axial Cr-O bonds on oxidation. This compression, combined with a small contraction in the *ab*-plane area observed on fluorination, results in tighter Cr-O-Cr bond angles. As listed in Table 4.3 in this chapter, the Cr-O-Cr bond angles contract from 170.8º, 175.0º and 173.6º in $La_2SrCr_2O_7$ to 167.2º, 162.1º and 163.0º in $La_2SrCr_2O_7F_2$.

However, this contraction of the Cr-O-Cr bond angles appears to contradict what would be expected from a simple analysis on the tolerance factor. On oxidation of Cr^{3+} to smaller sized

Cr^{4+}, the tolerance factor, t, (t = <A-O>/(√2<B-O>)) should increase, and thus the bond angles approach to 180°. One explanation is that the insertion of fluoride ions into the rock salt layers of the host phase leads to a contraction of the La/Sr-F sheets, which when combined with the increase in anion-anion repulsion on fluoride insertion, overcomes the change in the tolerance factor, leading to a tightening of the bond angles.

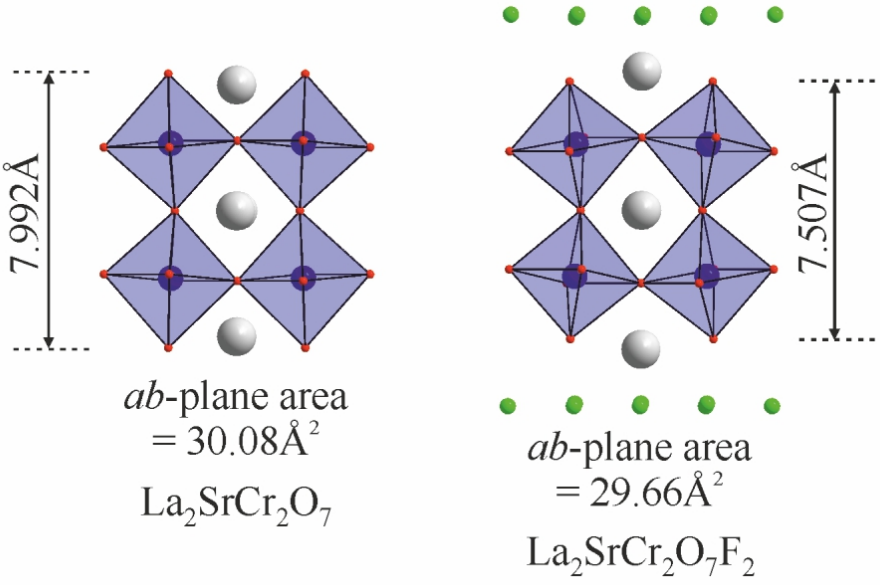


Figure 4.13. Fluorination of $La_2SrCr_2O_7$ leads to a compression of the perovskite blocks, both parallel to the *c*-axis and in the *ab*-plane, leading to a tightening of all Cr-O-Cr bond angles.

4.4.3 The cooperative tilting distortion in $La_2SrCr_2O_7F_2$

The $La_2SrCr_2O_7F_2$ adopts an *A2/a* tilting distortion, ($a^-a^-c^-$ / $a^-a^-c^-$) in Glazer notation as discussed in Chapter 1 Section 1.4. For ($a^-a^-c^-$ / $a^-a^-c^-$) tilting distortion, the adjacent octahedra rotate to the opposite directions along the *x*-, *y*- and *z*-axes, but with different rotational magnitudes along the *z*-axis. This tilting distortion is also adopted by its parent oxide, $La_2SrCr_2O_7$. The insertion of the fluorine anions results in a significant compression of the double perovskite blocks and thus tighter Cr-O-Cr bond angles as discussed in this chapter, Section 4.4.2. This suggests an increase in the size of the tilting and twisting distortions of the apex-linked CrO_6 octahedra on fluorination. This increase can be seen clearly if the rotation along *z*-axis is parameterized by the "in-plane" angle as discussed in Chapter 3 (Section 3.4.3.3), while the

rotation along *x*, *y*-axis is parametrized by the 'torsion angle' between adjacent O_{apical}-O_{axial} bonds. These angles are defined in Figure 4.14. On fluorination the rotations about *a*, *b* and *c*-axes increase from 2.61(5)°, 2.61(5)° and 2.77(3)° in $La_2SrCr_2O_7$ to 5.1(1)°, 5.1(1)° and 11.9(3)° in $La_2SrCr_2O_7F_2$ respectively. These values imply that the fluorination process enhances the tilting distortions about all Cartesian axes from $La_2SrCr_2O_7$ to $La_2SrCr_2O_7F_2$, especially the octahedral rotations about *c*-axis which increased by 9.2(3)°.

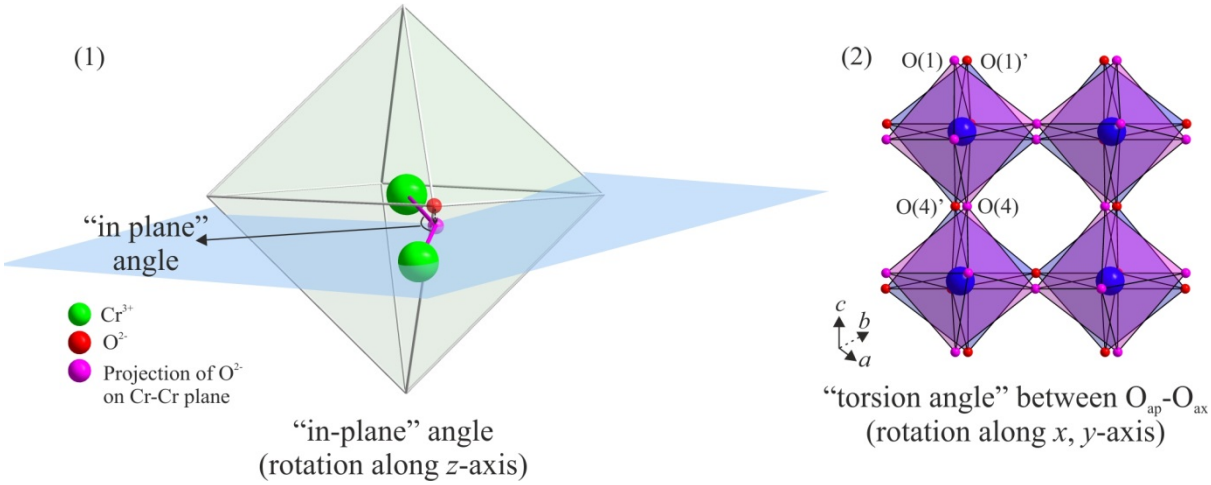


Figure 4.14. (1) The Cr-O-Cr "in-plane" angle: defined as the Cr-O-Cr angle assuming the three ions lie in the same plane. This angle emphasizes octahedral rotations about *c* rather than the in plane axes that dominate the Cr-O-Cr; The rotation about *z*-axis is thus defined as "180° - δ" where δ is the "in-plane" angle; (2) The 'torsion angle' between adjacent O_{apical}-O_{axial} bonds (between O(1)-O(2) and O(1)'-O(2)'). This angle is directly influenced by octahedral rotations about *a*, *b*-axis. The rotations about *a*, *b*-axis are not distinguishable, thus mean value was taken for analysis (that is, half value of the 'torsion angle' was taken as the rotation about *a*-axis).

4.4.4 Magnetism

4.4.4.1 Magnetism of $La_2SrCr_2O_7F_2$

The neutron diffraction data reveal that $La_2SrCr_2O_7F_2$ adopts a canted G-type antiferromagnetic state below 140 K with spins aligned parallel to crystallographic *c*-axis, which allows a weak ferromagnetism along the crystallographic b-axis. This is consistent with the results of magnetization and μ^+SR data. Its spin glass behaviour is inherited from its parent oxide, $La_2SrCr_2O_7$. As discussed in detail earlier in Chapter 3, the spin glass behaviour of $La_2SrCr_2O_7$

arises from the intergrowth of single layer into the n = 2 Ruddlesden Popper structure (Chapter 3, Figure 3.17). The arrangement of n = 2 Ruddlesden Popper structure could be interrupted by the intergrowth of single layers. This intergrowth was confirmed by the weak *hkl* dependent peak broadening in the diffraction data as mentioned in Section 4.3.2. This intergrowth interrupts the antiferromagnetic order, resulting in the small spin glassy behaviour.

Another explanation of this spin glass behaviour could be that a small portion of Cr^{3+} in the parent structure wasn't fully oxidized to Cr^{4+} during the fluorination, leading to magnetic frustration within the mixed valence Cr centres. However, as discussed in section 4.3.2, the composition of the fluorinated phase was confirmed to be $La_2SrCr_2O_7$ by TGA data, indicating the portion of Cr^{3+}, if it existed, should be too tiny to take account for the spin glass behaviour. Moreover, the magnetization-field isotherms collected at different temperatures (Figure 4.14) show that this spin glass behaviour is not observed at 120 K, a lower temperature than the magnetic ordering temperature (140 K). This observation combined with the strong persistent oscillations from the μ^+SR data indicates that this spin glass behaviour is not a bulk effect, but resulting from the intergrowth of the single layer.

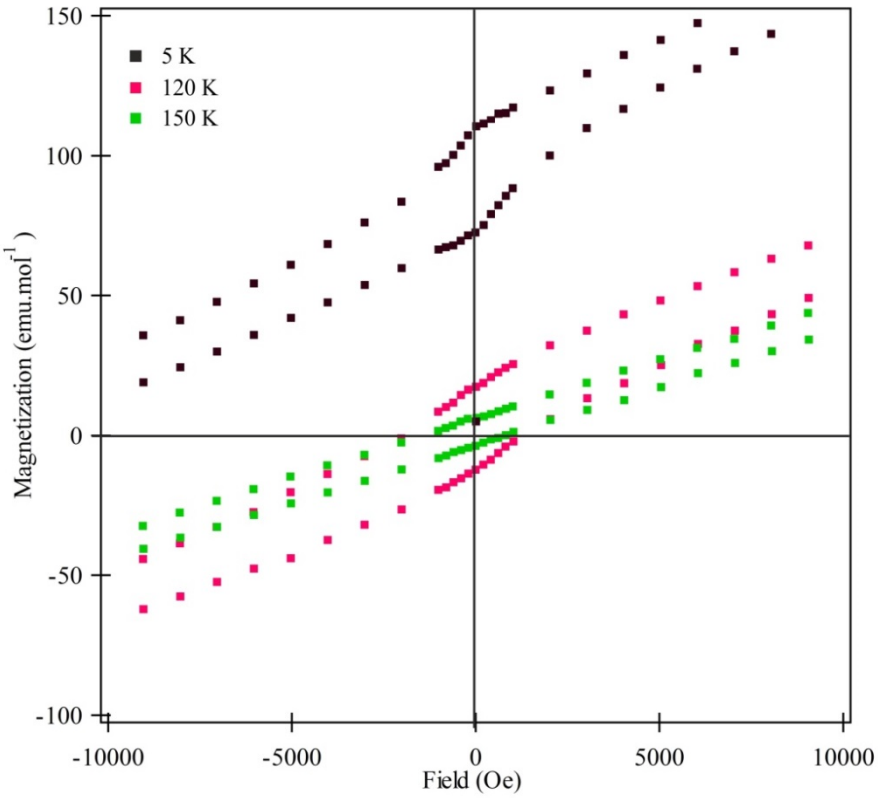


Figure 4.14. The magnetization-field isotherms collected at 5 K, 120 K and 150 K from $La_2SrCr_2O_7F_2$.

4.4.4. Magnetism of $La_2SrCr_2O_7$ and $La_2SrCr_2O_7F_2$

The $La_2SrCr_2O_7$ and $La_2SrCr_2O_7F_2$ are both antiferromagnetic below T_N ~ 260 K and 140 K respectively. The decline in the magnetic ordering temperature on fluorination could be ascribed to the oxidation of Cr^{3+} $La_2SrCr_2O_7$ in to Cr^{4+} in $La_2SrCr_2O_7F_2$ on fluorination, and thus fewer electrons contributing the magnetic interactions. In addition, the tightening of the Cr-O-Cr bond angles on fluorination leads to a poorer overlapping of chromium *d*-orbitals, thus weakening the superexchange interaction between adjacent chromium centres, resulting in a lower ordering temperature in $La_2SrCr_2O_7F_2$. Moreover, the fluoride anions inserted in between the rock salt layers further separate the adjacent interlayer chromium cations, weakening the superexchange interaction and thus a lower T_N for $La_2SrCr_2O_7F_2$.

4.4.5 Comparison to other phases containing Cr^{4+} centre

During the fluorination, the local coordination geometry of Cr cations remained largely

unchanged, while their oxidation state is raised from Cr^{3+} in $La_2SrCr_2O_7$ to Cr^{4+} in $La_2SrCr_2O_7F_2$. An n = 2 Ruddlesden-popper phase containing octahedrally coordinated Cr^{4+} centre, $La_2SrCr_2O_7F_2$, was therefore successfully made at ambient pressure by topochemical fluorination. The $La_2SrCr_2^{4+}O_7F_2$ made in this way adopts a monoclinic symmetry with a space group of *A2/a*. It shows a canted antiferromagnetic behaviour below $T_N \approx 140$ K. A cold pressed pellet of $LaSr_2Cr_2O_7F_2$ had a resistivity at room temperature which was greater than could be measured with our apparatus ($\rho > 100$ KΩ cm @ 300 K), indicating insulating behaviour.

Three phases prepared under high pressure processes were found to be suitable for comparison. These phases are $Sr_3Cr_2O_7$, $CaCrO_3$ and $SrCrO_3$. The $Sr_3Cr_2O_7$ phase has been reported[70] as a structurally undistorted n = 2 Ruddlesden-Popper phase, which could be indexed using a tetragonal unit cell in space group *I4/mmm* (Cr-O-Cr = 180º). It shows a semiconducting behaviour with antiferromagnetic order observed below 220K. The $CaCrO_3$ phase has been reported as a structurally distorted perovskite phase in space group *Pnma* (Cr-O-Cr = 158.9º, 157.7º) which exhibits antiferromagnetic order below 90 K[87]. The $SrCrO_3$ phase has been reported as an undistorted perovskite phase in space group *Pm-3m* (Cr-O-Cr = 180º). It has been described by different authors as either a paramagnetic phase with no sign of magnetic order down to 2 K[88], or as a phase which undergoes an orbital ordering transition and exhibiting antiferromagnetic order below $T_N \sim 40$ K[89]. This ambiguity in the behaviour of $SrCrO_3$ presumably arises from the difficulty in preparing phase-pure, oxygen-stoichiometric samples using high pressure processes.

At first sight the structure-property relations of these phases appear contradictory: structurally distorted $CaCrO_3$ has a higher magnetic ordering temperature than undistorted $SrCrO_3$, yet structurally undistorted $Sr_3Cr_2O_7$ has a higher magnetic ordering temperature than distorted $La_2SrCr_2O_7F_2$. These apparently contradictory structure-property relationships can be rationalized by considering the analysis previously described by Goodenough which relates the

magnetic ordering temperature of a phase to strength of interaction between metal centres, quantified by the transfer integral, *b*.[90,91] Figure 4.15 shows a schematic phase diagram for the expected evolution of the magnetic ordering temperature (T_N) of a phase as a function of interaction strength. When the interaction between metal centres is low (small *b*), phases are highly insulating with low magnetic ordering temperatures. As *b* increases super-exchange interactions strengthen and T_N rises. However when the interaction between metals reaches a critical value, b_c, inter-metallic interactions are strong enough to allow some of the valence electrons to become itinerant, screening the magnetic couplings between neighbouring metal centres, weakening the super-exchange interactions and leading to a decline in T_N with increasing *b*, until metallic behaviour and Pauli paramagnetism are observed at b_m.

The perovskite phases $CaCrO_3$ and $SrCrO_3$ are thought to lie close to metallic behaviour in the range $b_c < b < b_m$. in this region the structural distortion observed for $CaCrO_3$ would result in a weakening of the intermetallic interaction (smaller *b*) compared to undistorted $SrCrO_3$, consistent with the larger T_N observed for the calcium phase, as shown in Figure 4.15. In contrast the layered phases, $Sr_3Cr_2O_7$ and $La_2SrCr_2O_7F_2$ appear to lie in the region $b < b_c$ as this would be consistent with the observation that T_N declines with decreasing Cr-O-Cr bond angle. The small transfer integral, *b*, observed for the layered Ruddlesden-Popper phases compared to the perovskite materials can be rationalized by observing that the addition of rock salt layers into the extended perovskite lattice lowers the dimensionality of the system decreasing the average Cr-Cr inter-cation interaction and thus reduces *b*. Analogous band narrowing has been observed in the $Sr_{n+1}Ir_nO_{3n+1}$ series, in which '3-dimensional' $SrIrO_3$ is a correlated metal, but '2-dimensional' Sr_2IrO_4 is a Mott insulator[92].

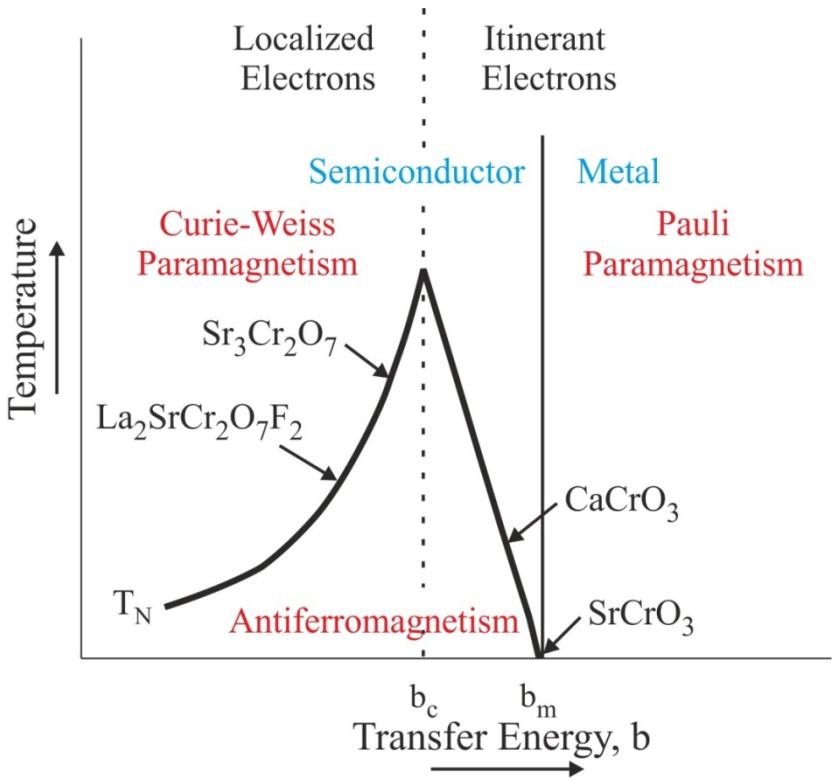


Figure 4.15. Schematic plot of temperature-transfer integral phase diagram for one electron per orbital. Arrows indicate apparent positions of Cr^{4+} phases.

4.5 Conclusion

The n = 2 Ruddlesden-popper phase containing octahedrally coordinated Cr^{4+} centres was successfully made at ambient pressure by topochemical fluorination of $La_2SrCr_2O_7$ to $La_2SrCr_2O_7F_2$. The fluorinated phase adopts a monoclinic symmetry in space group *A2/a* with robust antiferromagnetic order below T_N ~ 140 K. A great compression of the perovskite layer within the Ruddlesden-Popper structure is observed on fluorination, which leads to a tightening of the Cr-O-Cr bond angle and hence weakens the interaction between adjacent Cr cations. As a result the oxyfluoride phase lies further from the crossover for insulating to metallic behaviour than many other Cr^{4+} oxide phases.

Chapter 5: $La_{2-x}Sr_{1+x}Cr_2O_7$, $La_2Sr_{0.5}Ca_{0.5}Cr_2O_7$ and $La_{2-x}Sr_{1+x}Cr_2O_7F_2$

5.1 Introduction

In this chapter, the substitution of La with Sr, and Sr with Ca cations in $La_2SrCr_2O_7$ will be investigated to study how changing the average size and charge of the A-cations modifies the structure and physical properties in this system. The analogous $La_{2-x}Sr_{1+x}Cr_2O_7F_2$ were also synthesised and characterized in this chapter.

5.2 Experimental

Samples of $La_{2-x}Sr_{1+x}Cr_2O_7$ (x = 0.2, 0.3, 0.4) and $La_2Sr_{0.5}Ca_{0.5}Cr_2O_7$ were prepared in a similar way as $La_2SrCr_2O_7$. Suitable quantities of La_2O_3 (99.999%, dried at 900 °C), $SrCO_3$ (99.99%), $CaCO_3$ (99.99%), Cr_2O_3 (99.97%) were ground together and then the mixtures were heated in air at 1000 °C for 20 h to decompose the carbonate. The resulting material was then pressed into 13 mm diameter pellets and heated for 4 periods of 55 h at 1460 °C under flowing argon. However considerable amounts of impurities such as La_2O_3 and $LaCrO_3$ still remained in the $La_{1.6}Sr_{1.4}Cr_2O_7$ product after several periods of heating at 1550 °C, thus $La_{1.6}Sr_{1.4}Cr_2O_7$ was not included in the following discussion.

Fluorination reactions of $La_{2-x}Sr_{1+x}Cr_2O_7$ (x = 0.2, 0.3) were carried out using CuF_2 as a fluorination agent as described in the fluorination of $La_2SrCr_2O_7$ in Chapter 4. To avoid contamination of the samples with CuO which occurs when mixing the CuF_2 with mixed directly into the sample, the CuF_2 was heated separately from the sample as described in Chapter 4. The CuF_2 was heated at 500 °C under flowing oxygen to liberate fluorine. The resulted O_2/F_2 gas mixture was then passed over a sample of $La_{2-x}Sr_{1+x}Cr_2O_7$ (x = 0.2, 0.3) powder, held at 310 °C in adjacent furnace. Samples were then treated at this temperature for two periods of 48 h, with the CuF_2 reagent being replaced between heating periods. Samples of $La_{1.8}Sr_{1.2}Cr_2O_7F_2$ and

$La_{1.7}Sr_{1.3}Cr_2O_7F_2$ were thus obtained.

Similar Thermogravimetric analysis (TGA) as discussed in Chapter 4 (4.3.2) was carried out on the fluorinated samples from $La_{1.8}Sr_{1.2}Cr_2O_7$ and $La_{1.7}Sr_{1.3}Cr_2O_7$. The samples were fully converted to SrF_2 and $La_{1-x}Sr_xCrO_3$, and there is no sign of the formation of LaF_3. The compositions were thus confirmed to be $La_{1.8}Sr_{1.2}Cr_2O_7F_2$ and $La_{1.7}Sr_{1.3}Cr_2O_7F_2$.

5.3 Results

5.3.1 $La_{1.8}Sr_{1.2}Cr_2O_7$ and $La_{1.8}Sr_{1.2}Cr_2O_7F_2$

5.3.1.1 X-ray powder diffraction data

The X-ray patterns of $La_{1.8}Sr_{1.2}Cr_2O_7$ are similar to that of $La_2SrCr_2O_7$, thus the *A2/a* model adopted by $La_2SrCr_2O_7$ was constructed with the La:Sr ratio being adjusted for a composition of $La_{1.8}Sr_{1.2}Cr_2O_7$. As a result $La_{1.8}Sr_{1.2}Cr_2O_7$ could be readily indexed into the *A2/a* symmetry with lattice parameters of a = 5.477 Å, b = 5.469 Å, c = 20.20 Å and β = 90.11°.

The X-ray patterns of $La_{1.8}Sr_{1.2}Cr_2O_7F_2$ are similar to that of its analogous $La_2SrCr_2O_7F_2$. A similar shifting and splitting of (115) peak as shown in Chapter 4 (Figure 4.3) were also observed for $La_{1.8}Sr_{1.2}Cr_2O_7F_2$, which indicates a successful topochemical fluorination reaction. $La_{1.8}Sr_{1.2}Cr_2O_7F_2$ could be indexed into an *A2/a* symmetry with lattice parameters of a = 5.444(1) Å, b = 5.488(1) Å, c = 22.59 (1) Å, β = 90.42 (1)º.

5.3.1.2 Neutron powder diffraction data (300 K)

$La_{1.8}Sr_{1.2}Cr_2O_7$: A similar symmetry analysis discussed in Chapter 3 (section 3.3.1.2) was carried out on $La_{1.8}Sr_{1.2}Cr_2O_7$. Crystallographic models listed in Chapter 3 (Table 3.1) were constructed and refined against the neutron powder diffraction data collected from $La_{1.8}Sr_{1.2}Cr_2O_7$ at 300 K. During the refinement, all atomic positional and displacement parameters were allowed to refine freely, and the Sr/La distribution over the 9-cordinate and 12-cordinate A-cation sites was allowed to refine within the constraints of the total sample composition and that each cation site must remain fully occupied. A tiny amount of $LaCrO_3$ was observed in the diffraction pattern,

and thus this was added to the model as a second phase. A weak *hkl* dependent peak broadening were observed in $La_{1.8}Sr_{1.2}Cr_2O_7$ as in $La_2SrCr_2O_7$, hence an anisotropic broadening axis (001) was added to the peak shape description to allow crystal microstrain perpendicular and parallel to this axis to be refined independently.

In common with $La_2SrCr_2O_7$, the *Amam*, the $A2_1am$ and $A2/a$ models gave relatively good statistical fits. Similarly, the SHG inactivity of $La_{1.8}Sr_{1.2}Cr_2O_7$ rules out the polar $A2_1am$ model. The *Amam* symmetry is incompatible with the canted antiferromagnetism (Section 5.3.1.3) observed from $La_{1.8}Sr_{1.2}Cr_2O_7$, and thus eliminated from consideration. As a result the *A2/a* model is the only reasonable candidate structure for $La_{1.8}Sr_{1.2}Cr_2O_7$. Plots of the observed and calculated data from the 35° bank are shown in Figure 5.1, and that of other banks are in Figure A5.1 in Appendix. The detailed structural parameters of the refined model are given in Table 5.1.

$La_{1.8}Sr_{1.2}Cr_2O_7F_2$: An *A2/a* model based on $La_2SrCr_2O_7F_2$ (see Chapter 4) was constructed and refined against the neutron diffraction data collected from $La_{1.8}Sr_{1.2}Cr_2O_7F_2$. The La/Sr A-cation distribution was fixed at the values observed for the $La_{1.8}Sr_{1.2}Cr_2O_7$ parent phase with all other atomic positional and displacement parameters allowed to refine freely. The refinement converged steadily to give a good statistical fit. Plots of the observed and calculated data from the 35° bank are shown in Figure 5.1, and that of other banks are in Figure A5.2 in Appendix. The detailed structural parameters of the refined model are given in Table 5.2.

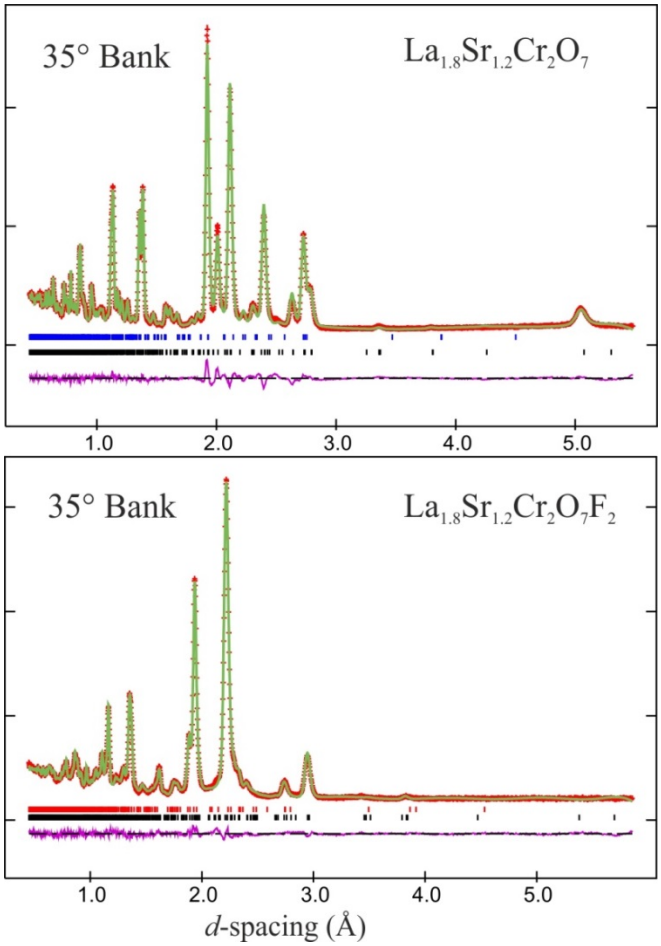


Figure 5.1. Observed, calculated and difference plots from the structural refinement of $La_{1.8}Sr_{1.2}Cr_2O_7$ and $La_{1.8}Sr_{1.2}Cr_2O_7F_2$ against neutron powder diffraction data collected at 300 K. Lower tick marks indicate peak positions of the majority phase, upper tick marks of a $LaCrO_3$ secondary phase.

Atom	site	*x*	*y*	*z*	Fraction	U_{iso} (Å^2)
La/Sr(1)	4e	¼	0.7434(10)	0	84(2)/15(2)	0.0070(1)
La/Sr(2)	8f	0.2479(8)	0.7529(7)	0.1825(1)	47(1)/52(1)	0.0050(2)
Cr(1)	8f	0.2519(16)	0.2445(13)	0.0986 (1)	1	0.0005(1)
O(1)	8f	0.2538(13)	0.2539(9)	0.1978(1)	1	0.0137(2)
O(2)	8f	0.0018(19)	-0.0008(33)	0.1008(1)	1	0.0098(1)
O(3)	8f	0.4988(22)	0.5017(41)	0.0924(1)	1	0.0124(1)
O(4)	4e	¼	0.2316(11)	0	1	0.0131(3)
$La_{1.8}Sr_{1.2}Cr_2O_7$ – space group: *A*2/*a* *a* = 5.4773(3) Å, *b* = 5.4691(3) Å, *c* = 20.206(1) Å, β = 90.11(1)º volume = 605.31(8)Å^3 phase fraction = 96.8 (1) weight percent						
$LaCrO_3$ – space group: *Pnma* *a* = 5.451(2) Å, *b* = 7.739(5) Å, *c* = 5.509(2) Å phase fraction = 3.2(1) weight percent						

χ^2 =, wRp = 4.54%, Rp = 3.93%

Table 5.1. Structural parameters refined against neutron powder diffraction data collected at 300 K from $La_{1.8}Sr_{1.2}Cr_2O_7$.

Atom	site	*x*	*y*	*z*	Fraction	U_{iso} (Å^2)
La/Sr(1)	4e	¼	0.7500(8)	0	84/15	0.0050 (6)
La/Sr(2)	8f	0.2507(9)	0. 7486(7)	0.1788(1)	47/52	0.0097(2)
Cr(1)	8f	0.2506(21)	0. 2455(16)	0.0860(1)	1	0.0037(5)
O(1)	8f	0.2602(9)	0.2896(8)	0.1662(1)	1	0.0081(2)
O(2)	8f	-0.0227(8)	0.0205(12)	0.0959(1)	1	0.0087(8)
O(3)	8f	0.5228(10)	0.4803(14)	0.0758 (1)	1	0.0110(8)
O(4)	4e	¼	0. 1972(11)	0	1	0.0119(12)
F(1)	8f	0.5055(6)	0.4998(13)	0.2536(1)	1	0.0054(5)
$La_{1.8}Sr_{1.2}Cr_2O_7F_2$ – space group: *A*2/*a* *a* = 5.4481(10) Å, *b* = 5.4946(10) Å, *c* = 22.615(4) Å, β = 90.41(1)º volume = 676.9(3)Å^3 phase fraction = 94.7(1) weight percent						
$LaCrO_3$ – space group: *Pnma* *a* = 5.458(2) Å, *b* = 7.681(3) Å, *c* = 5.553(2) Å phase fraction = 5.3(1) weight percent						
χ^2 =, wRp = 3.81%, Rp = 3.16%						

Table 5.2. Structural parameters refined against neutron powder diffraction data collected at 300 K from $La_{1.8}Sr_{1.2}Cr_2O_7F_2$. The A-cation fractions in the table were fixed at the values observed for the $La_{1.8}Sr_{1.2}Cr_2O_7$ parent phase, and thus listed without errors.

5.3.1.3 Magnetization data

The magnetization data collected from $La_{1.8}Sr_{1.2}Cr_2O_7$ in an applied field of 100 Oe show similar features to that of $La_2SrCr_2O_7$ as shown in Figure 5.2. The divergence between zero-field cooled and field cooled data indicates a weak ferromagnetism below 240 K. In the temperature range 240 < T/K < 285, there is still a small mismatch between zero-field cooled and field cooled data, which could be ascribed to the existence of small amount of $LaCrO_3$ impurities ($LaCrO_3$ has a antiferromagnetic ordering temperature of 285 K[71]). The magnetization-field isotherm data collected at 5 K shows weak spin-glass behaviour resulting from the intergrowth of the single layer into Ruddlesden-Popper structure as explained in Chapter 3, Section 3.4.5.

$La_{1.8}Sr_{1.2}Cr_2O_7F_2$ adopts a weak ferromagnetic behaviour similar to that of $La_2SrCr_2O_7F_2$ but with a lower magnetic ordering temperature (120 K).

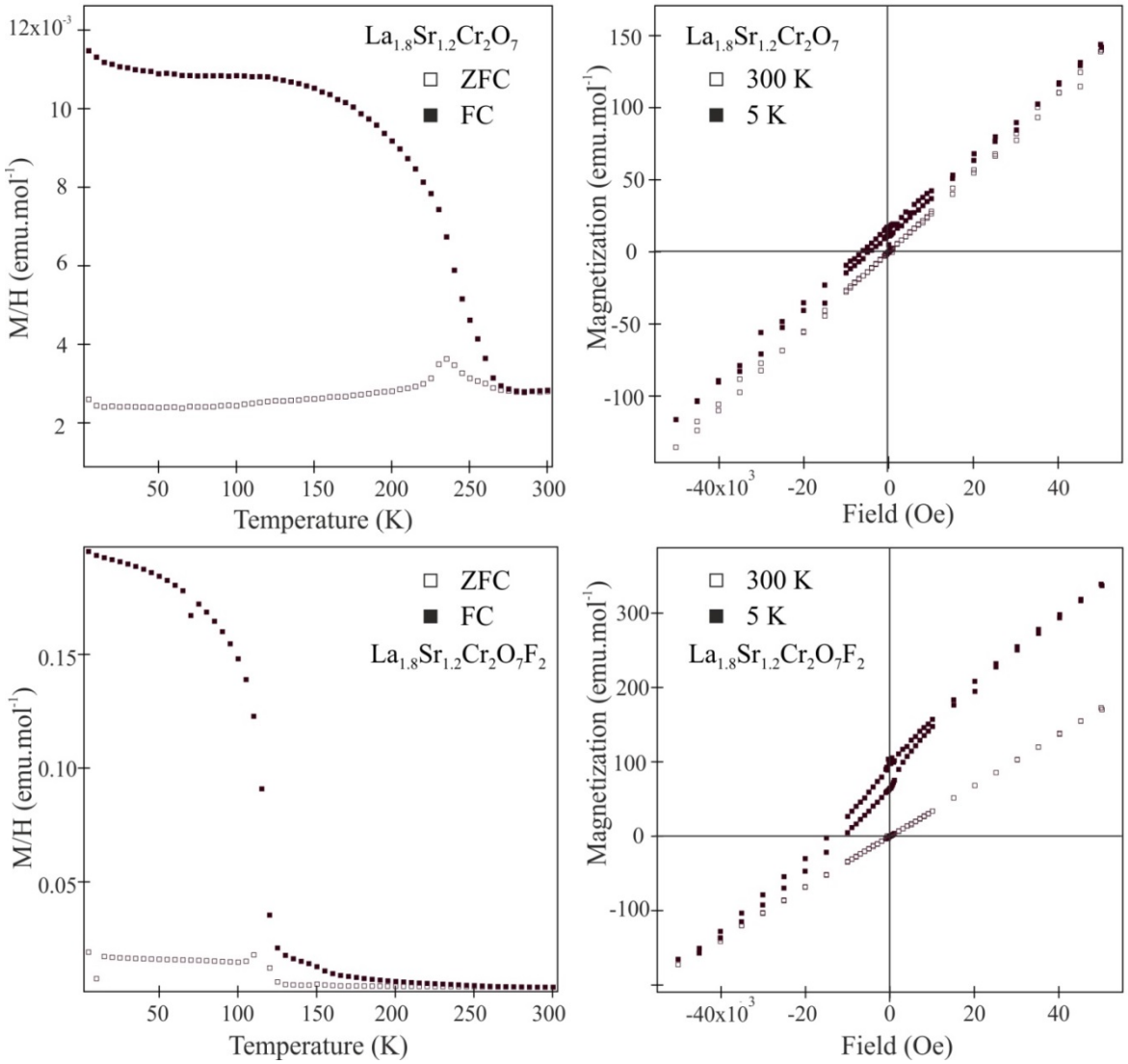


Figure 5.2. Plots of zero-field cooled and field cooled magnetization collected as a function of temperature, and the magnetization-field isotherms collected at 300 K and 5 K from $La_{1.8}Sr_{1.2}Cr_2O_7$ and $La_{1.8}Sr_{1.2}Cr_2O_7F_2$.

5.3.1.4 Neutron powder diffraction data (5K)

Neutron powder diffraction data collected from $La_{1.8}Sr_{1.2}Cr_2O_7$ and $La_{1.8}Sr_{1.2}Cr_2O_7F_2$ at 5 K both show additional diffraction features compared to analogous data collected at 300 K (Figure 5.3). These addition features, in common with those observed in $La_2SrCr_2O_7$ and $La_2SrCr_2O_7F_2$, were considered to be magnetic scattering peaks. These additional diffraction features can be indexed using the crystallographic unit cell indicating a magnetic ordering vector

k = 0. A similar magnetic symmetry analysis using the Sarah code[72] as discussed in Chapter 3 (Section 3.3.2.2) and Chapter 4 (Section 4.3.4.2) was performed on both $La_{1.8}Sr_{1.2}Cr_2O_7$ and $La_{1.8}Sr_{1.2}Cr_2O_7F_2$. The results show that, like $La_2SrCr_2O_7$, $La_{1.8}Sr_{1.2}Cr_2O_7$ adopts a G-type antiferromagnetic model with spins aligned parallel to the crystallographic *b*-axis, and with a weak ferromagnetic component along both the crystallographic *a*- and *c*-axes (see Chapter 3, Figure 3.6). $La_{1.8}Sr_{1.2}Cr_2O_7F_2$, similar to $La_2SrCr_2O_7F_2$, adopts a G-type antiferromagnetic model with spins aligned parallel to the crystallographic *c*-axis, and with a weak ferromagnetic component along the crystallographic *b*-axis (see Chapter 4, Figure 4.9). These components of the magnetic lattice were too small to extract from the diffraction data, so were set to zero during the refinement. These weak ferromagnetism features are consistent with the canted antiferromagnetism observed from their magnetization data.

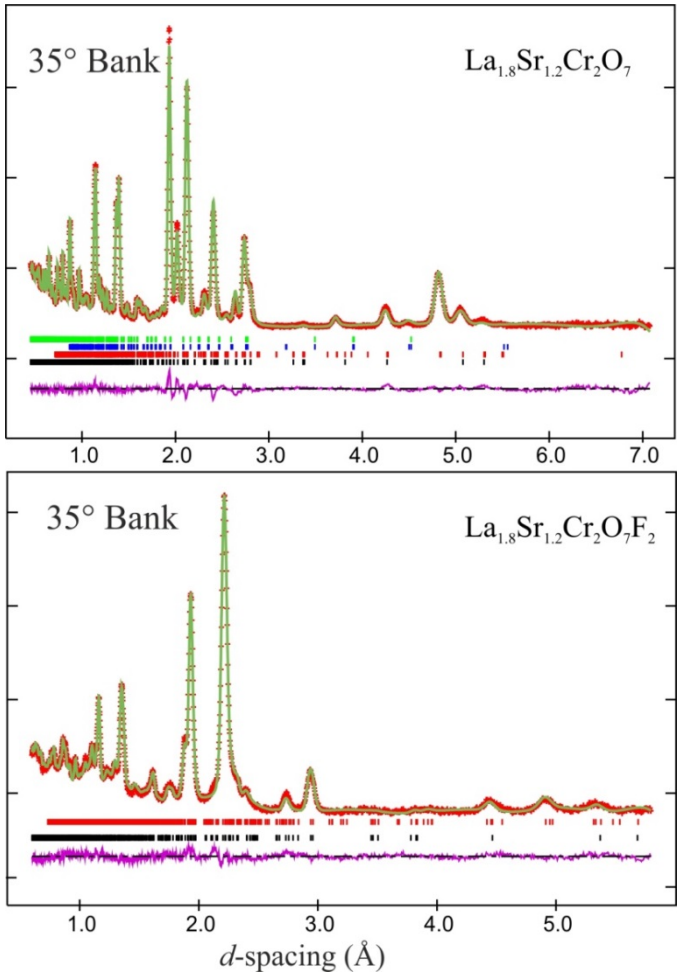


Figure 5.3. Observed, calculated and difference plots from the structural refinement of $La_{1.8}Sr_{1.2}Cr_2O_7$ against neutron powder diffraction data collected at 5 K. Black tick marks indicate nuclear peak positions for the majority phase, green tick marks for the $LaCrO_3$ secondary phase, red tick marks magnetic peak positions for the majority phase, and blue tick marks magnetic peak positions for the $LaCrO_3$ secondary phase.

Plots of the observed and calculated data of all the banks collected from $La_{1.8}Sr_{1.2}Cr_2O_7$ and $La_{1.8}Sr_{1.2}Cr_2O_7F_2$ are shown in Figure A5.3 and Figure A5.4 in Appendix. The refined nuclear and magnetic structural parameters of $La_{1.8}Sr_{1.2}Cr_2O_7$ and $La_{1.8}Sr_{1.2}Cr_2O_7F_2$ are shown in Table A5.1 and Table A5.2 in Appendix.

5.3.2 $La_{1.7}Sr_{1.3}Cr_2O_7$ and $La_{1.7}Sr_{1.3}Cr_2O_7F_2$

5.3.2.1 X-ray powder diffraction data

No neutron data were collected from $La_{1.7}Sr_{1.3}Cr_2O_7$ and $La_{1.7}Sr_{1.3}Cr_2O_7F_2$, hence x-ray diffraction data were used to determine their lattice parameters.

The X-ray patterns of $La_{1.7}Sr_{1.3}Cr_2O_7$ are similar to that of $La_2SrCr_2O_7$, thus the *A2/a* model adopted by $La_2SrCr_2O_7$ was constructed with the La:Sr ratio being adjusted for a composition of $La_{1.7}Sr_{1.3}Cr_2O_7$. As a result $La_{1.7}Sr_{1.3}Cr_2O_7$ could be readily indexed into the *A2/a* symmetry with lattice parameters of a = 5.463(1) Å, b = 5.460(1) Å, c = 20.19(1) Å and β = 90.0(1)°. The X-ray patterns of $La_{1.7}Sr_{1.3}Cr_2O_7F_2$ are similar to that of its analogous $La_2SrCr_2O_7F_2$. A similar shifting and splitting of (115) peak as shown in Chapter 4 (Figure 4.3) were also observed for $La_{1.7}Sr_{1.3}Cr_2O_7F_2$, which indicates a successful topochemical fluorination reaction. $La_{1.7}Sr_{1.3}Cr_2O_7F_2$ could be indexed into an *A2/a* symmetry with lattice parameters of a = 5.465(1) Å, b = 5.509(1) Å, c = 22.57 (1) Å, β = 90.2 (1)º.

5.3.2.2 Magnetization data

The magnetization data of $La_{1.7}Sr_{1.3}Cr_2O_7$ and $La_{1.7}Sr_{1.3}Cr_2O_7F_2$ are shown in Figure 5.4. These data reveal an antiferromagnetic behaviour alike to that of $La_2SrCr_2O_7$ and $La_2SrCr_2O_7F_2$ respectively, but with a lower magnetic ordering temperature (210 K for $La_{1.7}Sr_{1.3}Cr_2O_7$ and 100 K for $La_{1.7}Sr_{1.3}Cr_2O_7F_2$). Similarly the small divergence between zero-field cooled and field

cooled data above the magnetic ordering temperature arises from a small amount of $LaCrO_3$ impurities existed in these two samples. The spin glass behaviour was also observed in $La_{1.7}Sr_{1.3}Cr_2O_7$ and $La_{1.7}Sr_{1.3}Cr_2O_7F_2$, which could be ascribed to the intergrowth of the single layer into Ruddlesden-Popper structure as explained in Chapter 3 (Section 3.4.4).

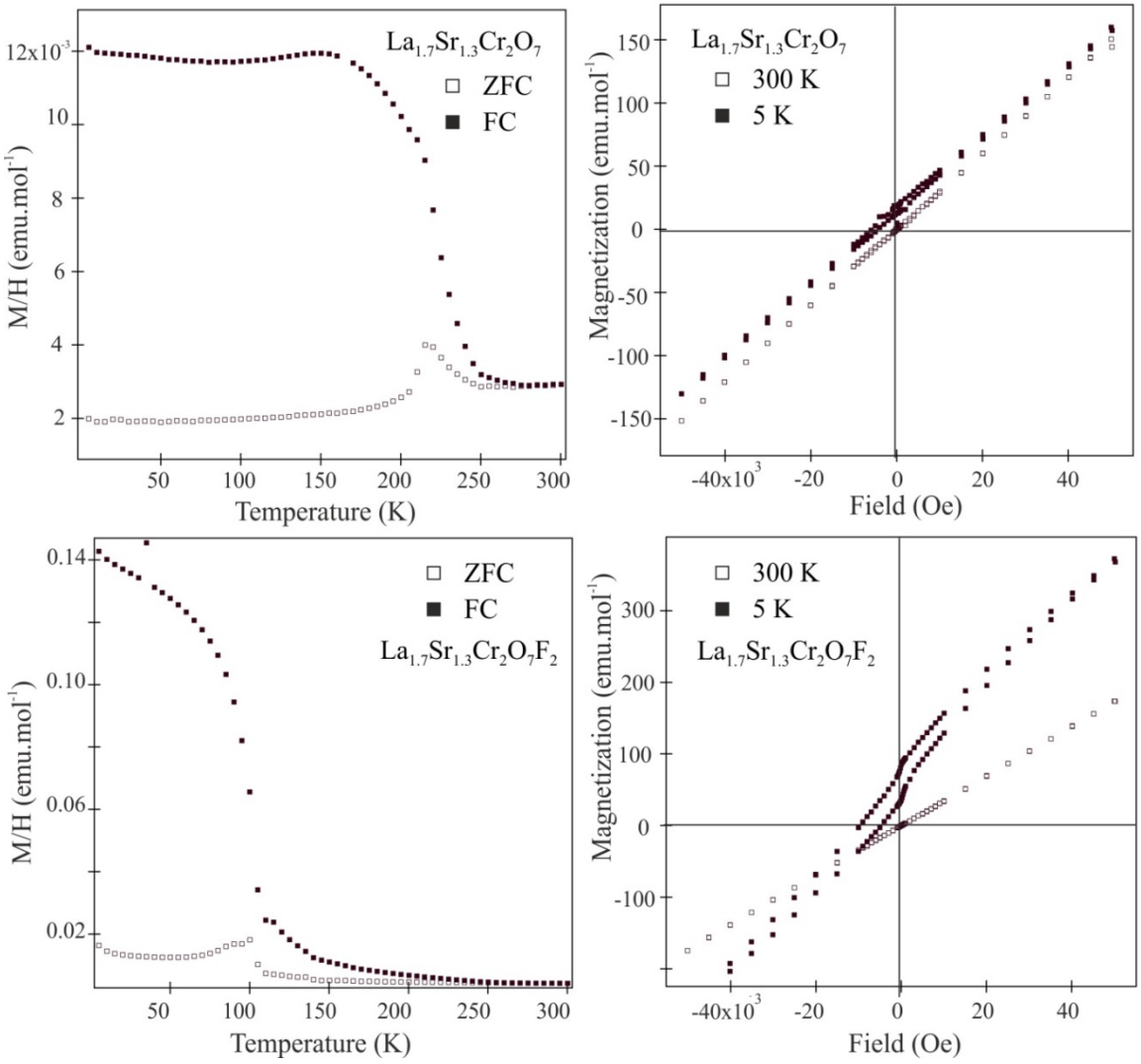


Figure 5.4. Plots of zero-field cooled and field cooled magnetization collected as a function of temperature, and the magnetization-field isotherms collected at 300 K and 5 K from $La_{1.7}Sr_{1.3}Cr_2O_7$ and $La_{1.7}Sr_{1.3}Cr_2O_7F_2$.

5.3.3 $La_2Sr_{0.5}Ca_{0.5}Cr_2O_7$

5.3.3.1 X-ray powder diffraction data

The X-ray patterns of $La_2Sr_{0.5}Ca_{0.5}Cr_2O_7$ are similar to that of $La_2SrCr_2O_7$, indicating that the substitution of Sr^{2+} to Ca^{2+} didn't induce a phase change. The X-ray pattern of

$La_2Sr_{0.5}Ca_{0.5}Cr_2O_7$ could be readily indexed into the *A2/a* symmetry (adopted by $La_2SrCr_2O_7$) with lattice parameters of a = 5.460(1) Å, b = 5.490(1) Å, c = 19.9(1) Å and β = 90.0(1)°.

5.3.3.2 Neutron diffraction data (300 K)

The *A2/a* models were constructed and refined against the neutron diffraction data from $La_2Sr_{0.5}Ca_{0.5}Cr_2O_7$ by using the D2B diffractometer (ILL, Grenoble). As the atomic position of doped Ca^{2+} cations are uncertain, two models are constructed to evaluate the distribution of Ca^{2+} cations over the two A-cation sites in Ruddlesden-Popper structure. That is, in one model, the Ca^{2+} cations sit exclusively on the perovskite 12-coordinate site while in the other model, the Ca^{2+} cations sit exclusively on the 9-coordinate site residing in the rock salt layer. At the early stage of the refinement, the A-cation distributions over the two A-sites were not refined. As a result, the second model in which the Ca^{2+} cations sit exclusively on the perovskite 9-coordinate site gave better statistical fit and reasonable A-site thermal factors (the first model gave unrealistic negative A-site thermal factors). Then the Sr/La distribution over the A-cation sites was allowed to refine within the constraints of the total sample composition and that each cation site must remain fully occupied, while the occupancy of the Ca^{2+} cations stayed unrefined. It turned out that the first model still gave unrealistic A-site distributions and thermal factors, while the second model gave a reasonable fit the data. Therefore, the Ca^{2+} cations are proposed to reside preferentially on the smaller 9-coordinate site. This is consistent with a slight shortening of the c-lattice parameter in $La_2Sr_{0.5}Ca_{0.5}Cr_2O_7$ (c = 19.980(1) Å compared to c = 20.181(1) Å in $La_2SrCr_2O_7$), resulting from a smaller Ca^{2+} cation replacing bigger Sr^{2+} in rock salt layers.

Plots of the observed and calculated data are shown in Figure 5.5, and the detailed structural parameters of the refined model are given in Table 5.3.

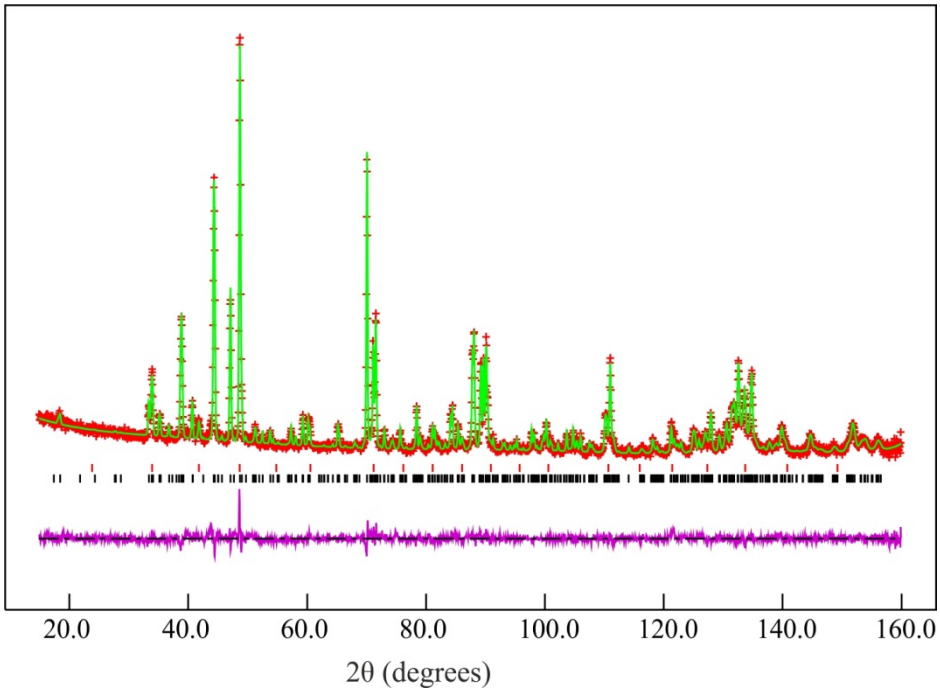


Figure 5.5. Observed, calculated and difference plots from the structural refinement of $La_2Sr_{0.5}Ca_{0.5}Cr_2O_7$ against neutron powder diffraction data collected at 300 K by using the D2B diffractometer (ILL, Grenoble). Lower tick marks indicate nuclear peak positions for the majority phase, upper tick marks for the $LaCrO_3$ secondary phase.

Atom	site	*x*	*y*	*z*	Fraction	U_{iso} (Å^2)
La/Sr(1)	4e	¼	0.7452(11)	0	78(2)/22(2)	0.005(1)
La/Sr(2)/Ca(1)	8f	0.2468(20)	0.7400(9)	0.1825(1)	61(1)/14(1)/25	0.004(1)
Cr(1)	8f	0.2544(28)	0.2561(21)	0.0990(2)	1	0.0005(1)
O(1)	8f	0.2432(28)	0.2808(11)	0.1994(1)	1	0.013(1)
O(2)	8f	-0.0030(27)	0.0001(35)	0.1041(2)	1	0.004(1)
O(3)	8f	0.4908(20)	0.5101(23)	0.0902(2)	1	0.008(1)
O(4)	4e	¼	0.2076(13)	0	1	0.007(1)
$La_2Sr_{0.5}Ca_{0.5}Cr_2O_7$ – space group: *A*2/*a* *a* = 5.4617(1) Å, *b* = 5.4913(1) Å, *c* = 19.980(1) Å, β = 89.96(1)º volume = 599.26(3) Å^3 phase fraction = 95.8 (1) weight percent						
$LaCrO_3$ – space group: *Pnma* *a* = 5.469(2) Å, *b* = 7.762(5) Å, *c* = 5.512(2) Å phase fraction = 4.1(1) weight percent						
χ^2 = 2.13, wRp = 3.97%, Rp = 3.14%						

Table 5.3. Structural parameters refined against neutron powder diffraction data collected at 300 K from $La_2Sr_{0.5}Ca_{0.5}Cr_2O_7$.

5.3.3.3 Magnetization

The magnetization data of $La_2Sr_{0.5}Ca_{0.5}Cr_2O_7$ are shown in Figure 5.6, suggesting antiferromagnetic behaviour similar to that of $La_2SrCr_2O_7$ but with a higher magnetic ordering

temperature $T_N \approx 295$ K.

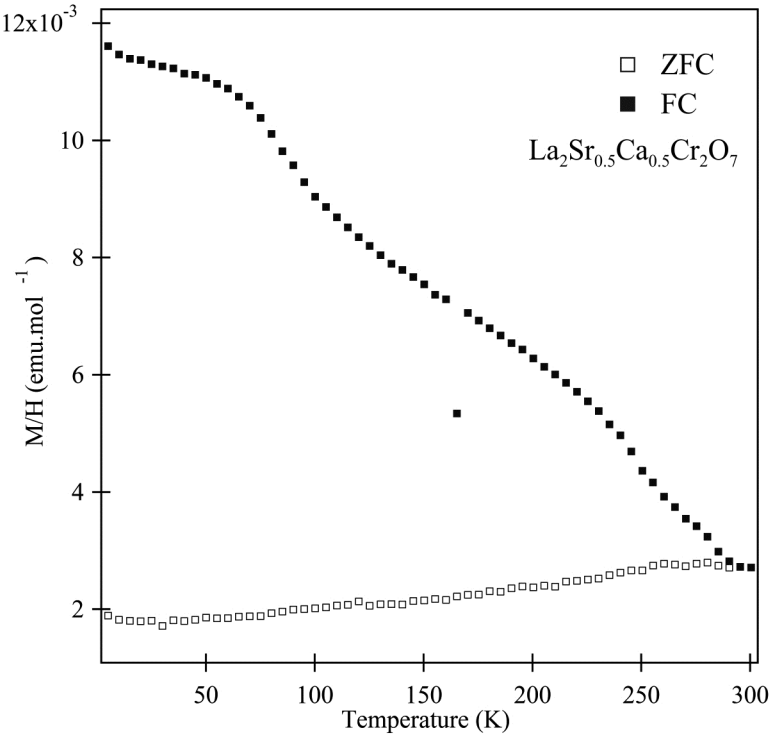


Figure 5.6. Plots of zero-field cooled and field cooled magnetization collected from $La_2Sr_{0.5}Ca_{0.5}Cr_2O_7$.

5.4 Discussion

5.4.1 Structural comparison in $La_2SrCr_2O_7$, $La_{1.8}Sr_{1.2}Cr_2O_7$ and $La_2Sr_{0.5}Ca_{0.5}Cr_2O_7$

Both $La_{1.8}Sr_{1.2}Cr_2O_7$ and $La_2Sr_{0.5}Ca_{0.5}Cr_2O_7$ adopt a monoclinic symmetry in space group *A2/a* with an unusual A-cation distribution (La^{3+} in 12-coordinate sites), similar to that of $La_2SrCr_2O_7$. As discussed in Chapter 3, the principal driver for the unusual distribution of the La and Sr cations is the desire to lower the charge difference between the La-O rock salt and Sr-O perovskite layers (discussed in Section 3.4.3.1), and thus make the CrO_6 units more symmetric. This unusual distribution of the La and Sr cations could be stabilized by the cooperative tilting distortion of the CrO_6, and thus $La_2SrCr_2O_7$ *A2/a* ($\Phi\Phi\Phi_z$ /$\Phi\Phi\Phi_z$) structure. This hypothesis is further tested by the distribution of Ca^{2+} in $La_2Sr_{0.5}Ca_{0.5}Cr_2O_7$. As the ionic radius of Ca^{2+} is comparable to that of La^{3+} ($r_{Ca}{}^{2+}$ =1.18; $r_{La}{}^{3+}$ =1.22), one would have thought that Ca^{2+} would behave similar to La^{3+} which means locating itself to the bigger 12-coordinate sites. However the

fact is that Ca^{2+} preferentially occupies the smaller 9-coordinate sites residing in the rock salt layer in $La_2Sr_{0.5}Ca_{0.5}Cr_2O_7$ as discussed in this chapter (Section 5.3.3.2). This supports the hypothesis that it is the charge difference that drives La^{3+} to sit in the bigger 12-coordinate site, otherwise La^{3+} would behave as 'normal' as Ca^{2+}.

The substitution of the A-cations in $La_2SrCr_2O_7$ modifies the Cr-O-Cr bond angles as shown in Table 5.4. This modification can be explained by the change of the tolerance factor t = <A-O>/$\sqrt{2}$×<B-O>. Substitution of a bigger A-cation (Sr^{2+} to La^{3+}) as well as a slight oxidation of B-cation gives $La_{1.8}Sr_{1.2}Cr_2O_7$ a bigger tolerance factor than $La_2SrCr_2O_7$, while substitution of a smaller A-cation (Ca^{2+}) gives $La_2Sr_{0.5}Ca_{0.5}Cr_2O_7$ a smaller tolerance factor than $La_2SrCr_2O_7$. Thus, the Cr-O-Cr angels are generally straightened in $La_{1.8}Sr_{1.2}Cr_2O_7$, while tightened in $La_2Sr_{0.5}Ca_{0.5}Cr_2O_7$.

$La_2SrCr_2O_7$	**Bond length (Å)**	**$La_2SrCr_2O_7$**	**Bond Angles (°)**
Cr-O(1)	2.037(3)	Cr(1)-O(2)-Cr(1)	173.6(5)
Cr-O(4)	1.972(2)	Cr(1)-O(3)-Cr(1)	175.0(6)
Cr-O(2)	1.919(12)	Cr(1)-O(4)-Cr(1)	170.8(8)
Cr-O(2)	1.973(12)		
Cr-O(3)	1.876(13)		
Cr-O(3)	2.000(13)		
$La_{1.8}Sr_{1.2}Cr_2O_7$	**Bond length (Å)**	**$La_{1.8}Sr_{1.2}Cr_2O_7$**	**Bond Angles (°)**
Cr-O(1)	2.005(3)	Cr(1)-O(2)-Cr(1)	172.5(9)
Cr-O(4)	1.994(2)	Cr(1)-O(3)-Cr(1)	179.8(8)
Cr-O(2)	1.955(20)	Cr(1)-O(4)-Cr(1)	175.9(3)
Cr-O(2)	1.966(20)		
Cr-O(3)	1.911(17)		
Cr-O(3)	1.917(17)		
$La_2Sr_{0.5}Ca_{0.5}Cr_2O_7$	**Bond length (Å)**	**$La_2Sr_{0.5}Ca_{0.5}Cr_2O_7$**	**Bond Angles (°)**
Cr-O(1)	2.011(5)	Cr(1)-O(2)-Cr(1)	173.8(11)
Cr-O(4)	1.996(4)	Cr(1)-O(3)-Cr(1)	168.1(8)
Cr-O(2)	1.991(22)	Cr(1)-O(4)-Cr(1)	164.6(5)
Cr-O(2)	1.935(22)		
Cr-O(3)	1.909(18)		
Cr-O(3)	1.937(18)		

Table 5.4. Selected bond lengths, angles and bond valence sums from the refined structure at 300 K. Labelling scheme is shown in Figure 5.7.

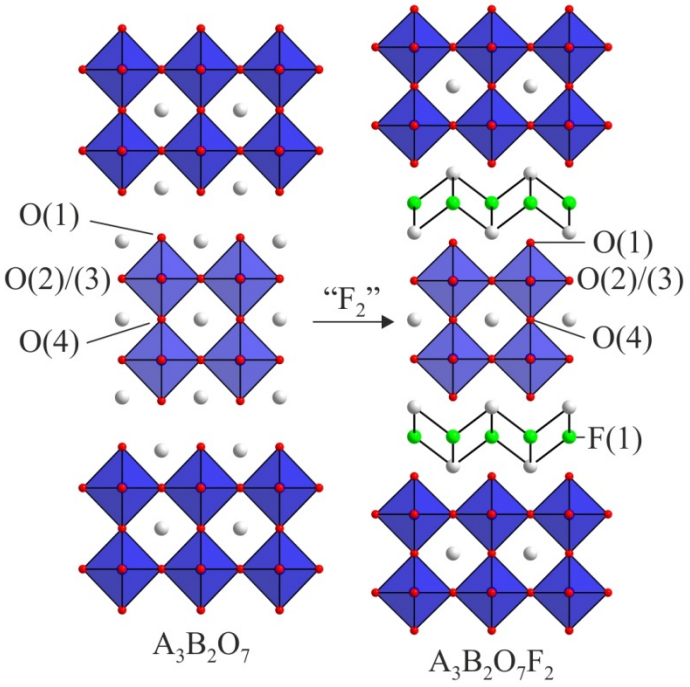


Figure 5.7. Labelling scheme of Ruddlesden-Popper phases containing Cr.

5.4.2 Magnetic comparison in $La_{2-x}Sr_{1+x}Cr_2O_7$ and $La_2Sr_{0.5}Ca_{0.5}Cr_2O_7$

$La_{2-x}Sr_{1+x}Cr_2O_7$ (x = 0, 0.2, 0.3) and $La_2Sr_{0.5}Ca_{0.5}Cr_2O_7$ all adopt a G-type antiferromagnetic model with spins aligned parallel to the crystallographic *b*-axis, but with different magnetic ordering temperature (T_N). Figure 5.8 shows the trend of magnetic ordering temperature with respect to the tolerance factor in $LnCrO_3$ (Ln is a lanthanide), as well as the trend of that of the Ruddlesden-Popper phases discussed in this chapter. It can be observed that a smaller A-site cation in $LnCrO_3$, which results in a smaller tolerance factor, leads to a lower T_N as a smaller t < 1 weakens the Cr-O-Cr superexchange interactions. The tolerance factors of the Cr Ruddlesden-Popper phases (calculated by t = <A-O>/√2×<B-O>) rank as flowing: $La_2Sr_{0.5}Ca_{0.5}Cr_2O_7$ < $La_2SrCr_2O_7$ < $La_{1.8}Sr_{1.2}Cr_2O_7$ < $La_{1.7}Sr_{1.3}Cr_2O_7$. This is consistent with the structural analysis earlier in this chapter (Section 5.4.1.1) that the Cr-O-Cr bond angles increase from $La_2Sr_{0.5}Ca_{0.5}Cr_2O_7$ to $La_2SrCr_2O_7$ to $La_{1.8}Sr_{1.2}Cr_2O_7$. One would thus expect that the magnetic ordering temperature would increase by the same order. However, an opposite trend was observed that a smaller t < 1 gives a higher T_N as shown in Figure 5.8. In $La_{2-x}Sr_{1+x}Cr_2O_7$ (x = 0, 0.2, 0.3) series, this could be explained by a slight increase in Cr oxidation state when

replacing La with Sr. This increase in Cr oxidation state reduces the number of electrons contributing to the magnetic moment, and thus leads to a lower T_N. This effect dominates the magnetic trend of $La_{2-x}Sr_{1+x}Cr_2O_7$ (x = 0, 0.2, 0.3). For $La_2Sr_{0.5}Ca_{0.5}Cr_2O_7$, its abnormal high T_N with respect to its low t might be explained by Ca^{2+} replacing Sr^{2+} in the rock salt layer. This replacement leads to a smaller c-lattice parameters in $La_2Sr_{0.5}Ca_{0.5}Cr_2O_7$ compared to $La_2SrCr_2O_7$ as mentioned in this chapter (Section 5.3.3.2). As result, the mean distance between adjacent unlinked interlayer Cr cations decreases (Cr cations are closer) from 6.741(12) Å in $La_2SrCr_2O_7$ to 6.628(18) Å in $La_2Sr_{0.5}Ca_{0.5}Cr_2O_7$, while the mean distance between adjacent intralayer Cr cations stays almost the same, 3.908(5) Å in $La_2SrCr_2O_7$ to 3.933(20) Å in $La_2Sr_{0.5}Ca_{0.5}Cr_2O_7$. In Ruddlesden-Popper phases, the magnetic interaction between the interlayer B-cation centres is weaker since the superexchange interaction weakens by distance. This weak interaction thus defines the magnetic ordering temperature. The closer distance in two adjacent unlinked interlayer Cr cations in $La_2Sr_{0.5}Ca_{0.5}Cr_2O_7$ strengthens the magnetic interaction, thus improves T_N greatly.

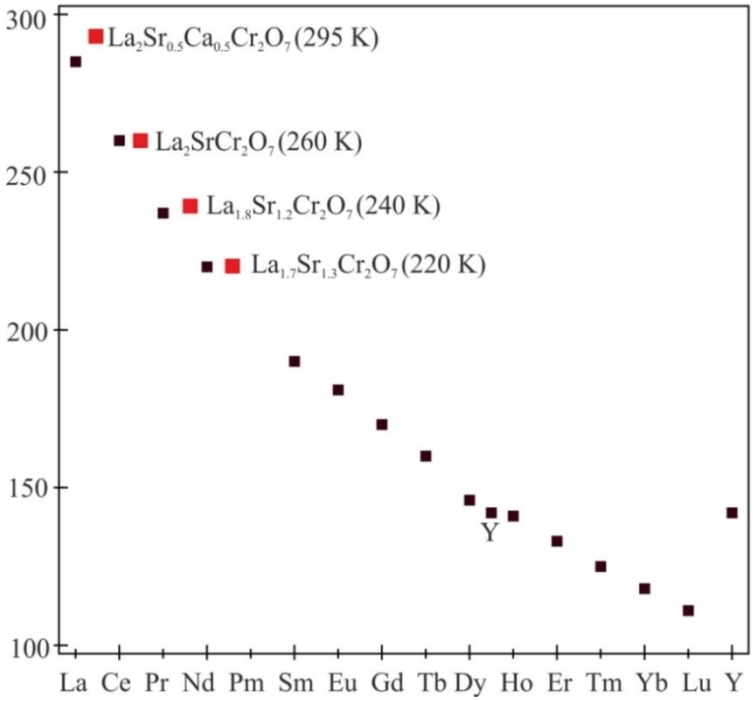


Figure 5.8. Variation of the T_N with lanthanide ion for $LnCrO_3$,[93-105] and $La_{2-x}Sr_{1+x}Cr_2O_7$ (x = 0, 0.2, 0.3) and $La_2Sr_{0.5}Ca_{0.5}Cr_2O_7$.

5.4.3 $La_{1.8}Sr_{1.2}Cr_2O_7$ and $La_{1.8}Sr_{1.2}Cr_2O_7F_2$

On topochemical fluorination of $La_{1.8}Sr_{1.2}Cr_2O_7$, the *c*-lattice parameter increases from 20.206(1) in $La_{1.8}Sr_{1.2}Cr_2O_7$ to 22.615(4) Å in $La_{1.8}Sr_{1.2}Cr_2O_7F_2$. This expansion along *z*-axis, in common with topochemical fluorination of other Ruddlesden-Popper phases, is required to accommodate the inserted fluoride anions in the rock salt layer. A similar compression of the perovskite layers within the phase as observed during the fluorination of $La_2SrCr_2O_7$ was also observed during that of $La_{1.8}Sr_{1.2}Cr_2O_7$. As shown in Figure 5.9, the *c*-dimension of the double perovskite (defined in Chapter 4, Section 4.4.2) decreases from 7.99 Å in $La_{1.8}Sr_{1.2}Cr_2O_7$ to 7.53 Å in $La_{1.8}Sr_{1.2}Cr_2O_7F_2$, while the *ab*-plane area remain largely unchanged. This compression leads to tighter Cr-O-Cr bond angles; as listed in Table 5.1 and Table 5.2, the Cr-O-Cr bond angles contract from 172.5, 179.8º and 175.9º in $La_{1.8}Sr_{1.2}Cr_2O_7$ to 163.2º, 163.5º and 164.4º in $La_{1.8}Sr_{1.2}Cr_2O_7F_2$.

A similar bond valence sum (BVS) analysis as discussed in Chapter 4 (Section 4.4.1) was carried out on $La_{1.8}Sr_{1.2}Cr_2O_7$ and $La_{1.8}Sr_{1.2}Cr_2O_7F_2$. These BVS data in Table 5.5 reveal that the tetragonal interstitial anion site X(5) has the smallest BVS value, and thus should be considered to be occupied by fluorine instead of oxygen. All the other anion sites should be considered to be occupied exclusively by oxygen. Similar to $La_2SrCr_2O_7F_2$, the X(1) anion site in $La_{1.8}Sr_{1.2}Cr_2O_7F_2$ also has a relatively small BVS value. As explained in Chapter 4 (Section 4.4.1), this is consistent with the analogous BVS value of O(1) site in the parent oxide, $La_{1.8}Sr_{1.2}Cr_2O_7$, and thus this X(1) should be occupied by oxygen.

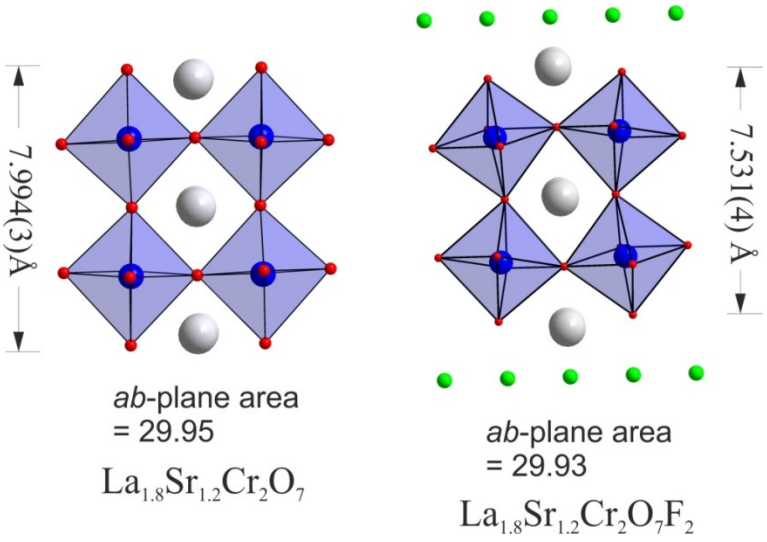


Figure 5.9. Fluorination of $La_{1.8}Sr_{1.2}Cr_2O_7$ leads to a compression of the perovskite blocks, both parallel to the *c*-axis and in the *ab*-plane, leading to a tightening of all Cr-O-Cr bond angles.

$La_{1.8}Sr_{1.2}Cr_2O_7$		**$La_{1.8}Sr_{1.2}Cr_2O_7F_2$**		
Anion	**BVS(O)**	**Anion**	**BVS(O)**	**BVS(F)**
O(1)	1.811	X(1)/O(1)	1.814	1.448
O(2)	2.261	X(2)/O(2)	2.147	1.752
O(3)	2.102	X(3)/O(3)	2.126	1.720
O(4)	1.837	X(4)/O(4)	2.258	1.821
		X(5)/F(1)	1.586	1.163

Table 5.5. Anion bond valence sums from $La_{1.8}Sr_{1.2}Cr_2O_7$ and $La_{1.8}Sr_{1.2}Cr_2O_7F_2$. Labelling scheme is shown in Figure 5.7.

5.4.3 $La_2SrCr_2O_7F_2$ and $La_{1.8}Sr_{1.2}Cr_2O_7F_2$

As discussed earlier (Section 5.4.1), $La_{1.8}Sr_{1.2}Cr_2O_7$ has a bigger tolerance factor and thus straightened Cr-O-Cr bond angles compared to that of $La_2SrCr_2O_7$. However, after fluorination, though the equatorial Cr-O-Cr bond angles in $La_{1.8}Sr_{1.2}Cr_2O_7F_2$ are slightly straighter than that of $La_2SrCr_2O_7F_2$, the axial Cr-O-Cr bond angles are much tighter in $La_{1.8}Sr_{1.2}Cr_2O_7F_2$ as shown in Table 5.6 (Cr(1)-O(4)-Cr(1)). This might be explained by the observation that the extra Sr cations in $La_{1.8}Sr_{1.2}Cr_2O_7F_2$ replace La in the 9-coordinate A-sites, resulting in more Sr cations in the rock salt layer (La/Sr = 0.47/0.52 in $La_{1.8}Sr_{1.2}Cr_2O_7F_2$, 0.58/0.42 in $La_2SrCr_2O_7F_2$). On fluorination, the CrO_6 octahedra were forced to twist further to accommodate not only the fluorine ions that were inserted into the rock salt layer, but also those extra Sr cations that have a

larger ionic radius. Therefore, the Cr-O-Cr angles in $La_{1.8}Sr_{1.2}Cr_2O_7F_2$ are tighter than that of $La_2SrCr_2O_7F_2$. This tightening in Cr-O-Cr angles leads to a weakening of the superexchange interaction between adjacent Cr centres, leading to a lower magnetic ordering temperature (T_N) in $La_{1.8}Sr_{1.2}Cr_2O_7F_2$ ($T_N \approx 120$ K) than that of $La_2SrCr_2O_7F_2$ ($T_N \approx 140$ K).

$La_2SrCr_2O_7F_2$	**Bond length (Å)**	**$La_2SrCr_2O_7F_2$**	**Bond Angles (°)**
Cr-O(1)	1.845(5)	Cr(1)-O(2)-Cr(1)	162.1(4)
Cr-O(4)	1.936(5)	Cr(1)-O(3)-Cr(1)	163.0(4)
Cr-O(2)	1.932(10)	Cr(1)-O(4)-Cr(1)	167.2(1)
Cr-O(2)	1.962(11)		
Cr-O(3)	1.943(10)		
Cr-O(3)	1.956(10)		
$La_{1.8}Sr_{1.2}Cr_2O_7F_2$	**Bond length (Å)**	**$La_{1.8}Sr_{1.2}Cr_2O_7F_2$**	**Bond Angles (°)**
Cr-O(1)	1.840(5)	Cr(1)-O(2)-Cr(1)	163.2(6)
Cr-O(4)	1.961(5)	Cr(1)-O(3)-Cr(1)	163.5(5)
Cr-O(2)	1.948(12)	Cr(1)-O(4)-Cr(1)	164.4(6)
Cr-O(2)	1.961(12)		
Cr-O(3)	1.948(12)		
Cr-O(3)	1.961(12)		

Table 5.6. Selected bond lengths, angles and bond valence sums from the refined structure of $La_{1.8}Sr_{1.2}Cr_2O_7F_2$ at 300 K. Labelling scheme is shown in Figure 5.7.

5.5 Conclusion

The A-site doping in $La_2SrCr_2O_7$ for the preparation of $La_{2-x}Sr_{1+x}Cr_2O_7$ (x = 0.2, 0.3) and $La_2Sr_{0.5}Ca_{0.5}Cr_2O_7$ leads to no obvious change in structural framework and the antiferromagnetic behaviour. These non-stoichiometric phases adopt a similar distorted *A2/a* structure with the unusual A-site distribution over the 12- and 9-coordinate A-sites (a smaller La cation prefers bigger 12-coordinate sites). In $La_2Sr_{0.5}Ca_{0.5}Cr_2O_7$, the doped Ca^{2+} cations prefer the smaller 9-coordinate A-sites, which further proves that the principal driver for the unusual distribution of the La and Sr cations is the desire to lower the charge difference between the La-O rock salt and Sr-O perovskite layers. $La_{2-x}Sr_{1+x}Cr_2O_7F_2$ (x = 0.2, 0.3) behaves in a similar manner to $La_2SrCr_2O_7F_2$. Their magnetic ordering temperatures are $T_N \sim 120$ K and 100 K respectively.

Chapter 6: Topochemical fluorination of $La_3Ni_2O_7$ to $La_3Ni_2O_{5.5}F_{3.5}$

6.1 Introduction

As discussed earlier, only a few materials have been reported as multiferroic, despite that this type of multifunctional materials can find application in a wide range of technologies. The difficulties and strategies in preparing multiferroic materials were discussed in detail in Chapter 1, Section 1.6. Those strategies include utilizing the cooperative tilting distortions of BO_6 octahedra in $n = 2$ Ruddlesden-Popper phases. However, a significant challenge in implementing this idea is the great difficulty in stabilizing the desired $A2_1am$ ($a^-a^-c^+$/ $a^-a^-c^+$) polar structure which has an extremely small tolerance factor.

Given this challenge, we then have sought to use the topochemical manipulation to stabilize polar twisting distortions of Ruddlesden-Popper phases, specifically the extensive fluorine insertion chemistry of double-layered Ruddlesden-Popper oxide phases.[26,106-111] During the fluorination of $La_2SrCr_2O_7$, it is observed that the insertion of fluoride ions modifies the host structure, enhancing the cooperative twisting and distortion of apex-linked CrO_6 octahedra. As discussed earlier in Chapter 4, fluoride anions can be inserted into tetrahedral interstitial sites within the rock salt layers of the framework, which in the simplest cases converts an $A_3B_2O_7$ oxide phase into an $A_3B_2O_7F_2$ oxide-fluoride. In addition to oxidizing the transition metal B-cations, fluorine insertion can have a dramatic influence on the twisting distortions of the host Ruddlesden-Popper lattice. In particular, fluorination appears to modify the twisting of octahedra around the crystallographic *z*-axis. During the fluorination of $La_2SrCr_2O_7$, for example, the fluorination process enhance the tilting distortion about *z*-axis by 9.2(3)° (parameterized by the "in-plane" angle). This structural modification during topochemical fluorination can also be found in previous reports. For example, the fluorination of $Sr_3(Mn_{0.5}Ru_{0.5})_2O_7$ to $Sr_3(Mn_{0.5}Ru_{0.5})_2O_7F_2$ drives a change from the aristotype $a^0a^0c^0$/ $a^0a^0c^0$, *I4/mmm* framework to a $a^0a^0c^-$/ $a^0a^0c^-$, *Acaa* distorted lattice, as shown in Figure 6.1.[106] Similarly fluorination of $Sr_3Ru_2O_7$

drives a disordered twisting of the RuO_6 octahedra around the *z*-axis to yield an $a^0a^0c^{+/-}$ $a^0a^0c^{+/-}$ distorted structure for $Sr_3Ru_2O_7F_2$.[26] This suggests that topochemical fluorination could be used to introduce a '*z*-twist' to other *n* = 2 Ruddlesden-Popper oxide phases and drive a phase with an $a^-a^-c^0/a^-a^-c^0$, *Amam* distortion to adopt an $a^-a^-c^+/ a^-a^-c^+$, $A2_1am$ polar structure. This chapter describes the topochemical fluorination of $La_3Ni_2O_7$, an *n* = 2 Ruddlesden-Popper phase which adopts an *Amam* distorted structure,[112] and contains oxidizable transition metal cations, making it an ideal host phase to test this idea. The bulk of this work has been published in *Chemistry of Materials*.[113]

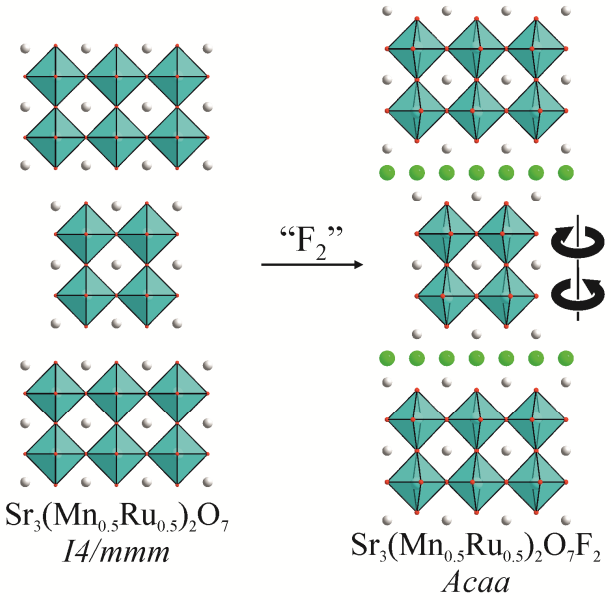


Figure 6.1. Topochemical fluorination of $Sr_3(Mn_{0.5}Ru_{0.5})_2O_7$ to $Sr_3(Mn_{0.5}Ru_{0.5})_2O_7F_2$ induces a 'z-twist' into the *n* = 2 Ruddlesden-Popper network.

6.2 Experimental

$La_3Ni_2O_7$ was synthesized via the citrate gel method.[112] Suitable stoichiometric ratios of La_2O_3 (99.99%, dried at 900 °C) and Ni powder (99.99%) were dissolved in a minimal quantity of 6 M nitric acid. Citric acid and ethylene glycol were then added, and the solution was heated with constant stirring. A blue gel thus formed and was heated to 350 °C until a loose black powder was obtained. The powder was ground and then heated to 1000 °C in air at a rate of 1 °C/min to remove the remaining organic components. The resulting powder was then pressed

into pellets before 2 further 48 hour heating cycles at 1250 °C under flowing oxygen. X-ray powder diffraction data confirmed the formation of single phase samples, with lattice parameters in good agreement with previous reported values (a = 5.392(1) Å, b = 5.447(1) Å, c = 20.517(1) Å).[112]

Fluorination of $La_3Ni_2O_7$ was carried out using CuF_2 as a fluorination agent as described in the fluorination of $La_2SrCr_2O_7$ in Chapter 4. To avoid contamination of the samples with CuO which occurs when mixing the CuF_2 with mixed directly into the sample, the CuF_2 was heated separately from the sample as described in Chapter 4. The CuF_2 was heated at 500 °C under flowing oxygen to liberate fluorine. The resulted O_2/F_2 gas mixture was then passed over a sample of $La_3Ni_2O_7$ powder, held at temperature ranging from 150 to 340 °C in an adjacent furnace (See Chapter 2 Figure 2.1). No obvious reaction was observed until heating the $La_3Ni_2O_7$ powder at 220 °C. The reaction temperature was optimized to 270 °C after a series of small scale tests. Samples were then treated at this temperature for two periods of 48 h, with the CuF_2 reagent being replaced between heating periods. To improve the crystallinity of the fluorinated products, samples were heated in sealed silica ampules at 350 °C for 48 hours.

6.3 Results

6.3.1 X-ray powder diffraction data of $La_3Ni_2O_xF_y$

The X-ray powder diffraction data collected from the fluorinated sample at different reaction stage during the fluorination process revealed a new phase forming with a larger c-lattice parameter relative to the starting material as the (115) peak shifted to higher d-spacing, similar to the fluorination of $La_2SrCr_2O_7$. This fluorinated phase can be indexed into an orthorhombic unit cell with a lattice of a = 5.431(1) Å, b = 5.507 (1) Å, c = 22.48 (1) Å, consistent with the formation of a topochemical fluorinated compound of composition of $La_3Ni_2O_xF_y$.

During the fluorination process, extra peaks were observed in the powder X-ray diffraction data that couldn't be indexed to either $La_3Ni_2O_7$ or the fluorinated phase $La_3Ni_2O_xF_y$.

This unidentified phase (marked by a blue circle in Figure 6.2) was considered as an intermediate phase, a staged structure in which the fluorine ions are inserted into alternative layers as adopted by $LaSrMnO_4F$. This staging behaviour was discussed earlier in Chapter 1 (Section 1.5.1), and the structure of $LaSrMnO_4F$ can be found in Chapter 1 Figure 1.7. The peak at $2\theta \approx 31°$ (marked by a blue circle in Figure 6.2) was considered as the (115) diffraction peak from this intermediate phase. The rest of the diffraction peaks overlapped with that from $La_3Ni_2O_7$ and $La_3Ni_2O_xF_y$, and thus are not distinguishable.

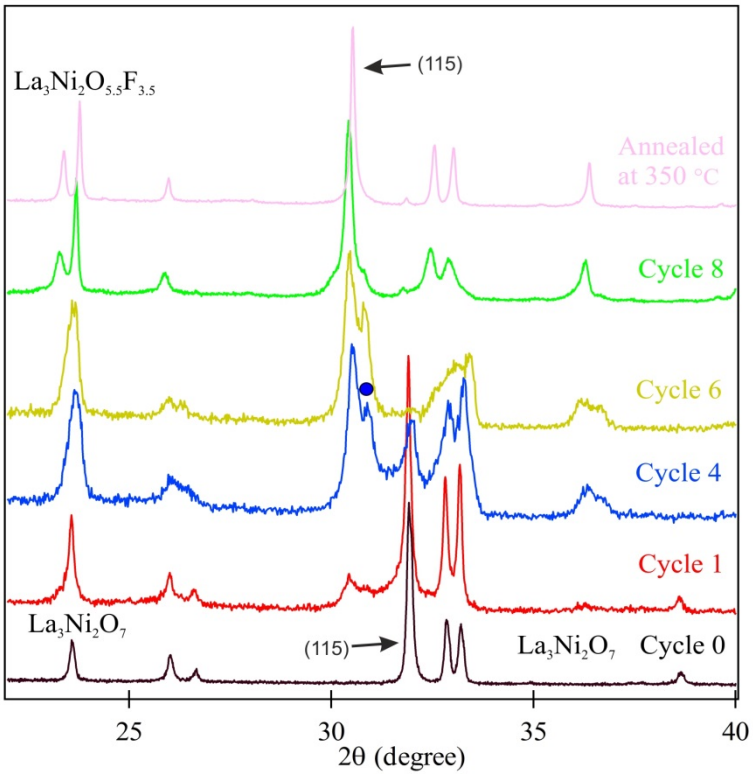


Figure 6.2. The evolution of the sample at different reaction stages during the fluorination process. Each cycle indicates a heating cycle of 2 days under the condition described in 6.2. The blue circle denotes the peak that might belong to an intermediate phase with low fluorine content in the rock salt layer.

It is worth noting that a clear change of the X-ray pattern was observed before and after annealing. As shown in Figure 6.2, before annealing, the peaks are broader and asymmetric. Meanwhile an obvious diffraction peak from an intermediate phase with lower fluorine content in the rock salt layer can also be observed at $2\theta \approx 31°$. This is because an uneven amount of fluoride ions was inserted into each rock salt layer during the fluorination. The low anion mobility at the

reaction temperature (270 °C) is not sufficient to overcome the energy barrier to form a 'regular' stacking of fluoride layers. Therefore, the anisotropic peak broadening resulting from this 'irregular' stacking of fluoride layers is observed in the X-ray pattern. The scattering peaks from a phase with lower fluorine content in the rock salt layer are also observed (marked in Figure 6.2). When annealing at a higher temperature (350 °C), the fluoride ions were able to rearrange through the whole lattice, and thus the diffraction peaks become sharper, more defined, and symmetric.

6.3.2 Compositional characterization of $La_3Ni_2O_xF_y$

6.3.2.1 Iodometric titration

Iodometric titrations were carried out to determine the oxidation state of the nickel in prepared samples. The detailed procedure was described in Chapter 2 (Section 2.6). In this series of titrations, a 1:1 (v/v) ratio of hydrochloric acid to distilled water was used to dissolve the samples. Titrations on $La_3Ni_2O_7$ were also carried out as a reference. The reaction during the titration could be described as following scheme S1 and S2:

$$\mathbf{Ni(2+x) + H^+ + xI^- \rightarrow Ni(2) + \frac{x}{2}I_2} \qquad \mathbf{S1}$$

$$\mathbf{\frac{x}{2}I_2 + xS_2O_3^{2-} \rightarrow xI^- + \frac{x}{2}S_4O_6^{2-}} \qquad \mathbf{S2}$$

Thus the overall reaction could be described as S3:

$$\mathbf{Ni(2+x) + xS_2O_3^{2-} \rightarrow Ni(2) + \frac{x}{2}S_4O_6^{2-}} \qquad \mathbf{S3}$$

The oxidation state of Ni in $La_3Ni_2O_xF_y$ was determined as +2.75(2). Crystallographic characterization of the $La_3Ni_2O_xF_y$ phase, described below in Section 6.3.3, indicated that all anion sites were fully occupied and thus $x + y = 9$, as observed for other fluorinated $n = 2$ Ruddlesden-Popper phases.[26,106,109,110] Thus the composition of $La_3Ni_2O_xF_y$ was determined to be $La_3Ni_2O_{5.5}F_{3.5}$.

Sample	Mass (mg)	$c_{Na_2S_2O_4}$ (10^{-3} mol/L)	$V_{Na_2S_2O_4}$(mL)	Oxidation state of Ni^{n+}	Mean Ni^{n+}
$La_3Ni_2O_7$	43.8	2.1217	34.6	2.533	2.52(2)
$La_3Ni_2O_7$	41.4		31.3	2.518	
$La_3Ni_2O_7$	40.2		30.1	2.513	
$La_3Ni_2O_xF_y$	41.1		42.0	2.766	2.75(2)
$La_3Ni_2O_xF_y$	39.1		39.3	2.753	
$La_3Ni_2O_xF_y$	36.9		36.8	2.748	

Table 6.1. Results of titrations on $La_3Ni_2O_7$ and $La_3Ni_2O_xF_y$.

6.3.2.2 Thermogravimetric data

Thermogravimetric analysis (TGA) was carried out by heating the fluorinated sample to 900 °C under flowing 10 % H_2/N_2 gas. The fluorinated sample was completely converted into LaOF, LaF_3, and Ni, confirmed by X-ray powder diffraction (Figure 6.3).

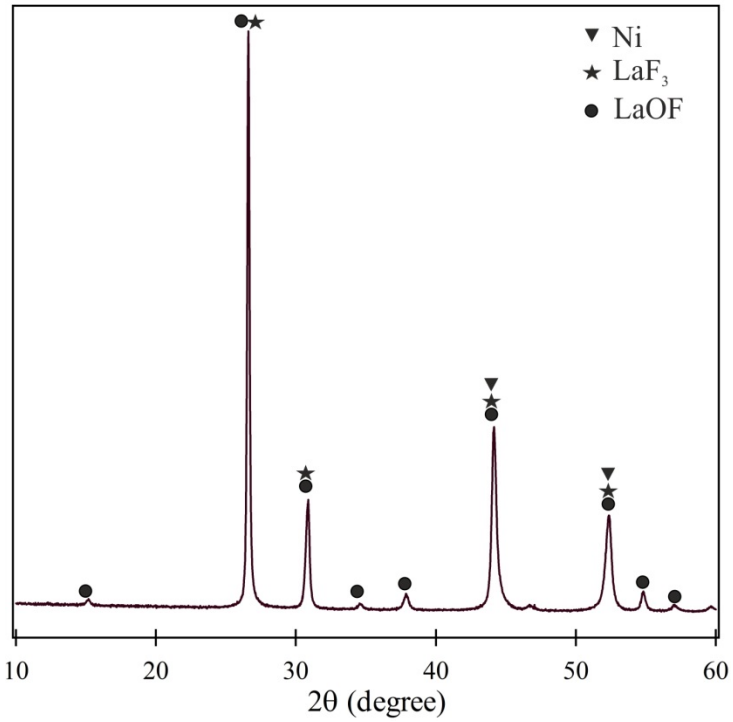


Figure 6.3. X-ray powder diffraction pattern collected from sample of $La_3Ni_2O_{5.5}F_{3.5}$ after heating under 10% H_2 in N_2 on TGA.

A mass loss of 6.40 % was observed (Figure 6.4). The expected mass loss of a $La_3Ni_2O_{5.5}F_{3.5}$ is calculated to be 6.39 % according to scheme S4:

$$\mathbf{La_3Ni_2O_{5.5}F_{3.5} \xrightarrow{H_2} 2.75LaOF + 0.25LaF_3 + 2Ni + 1.375O_2} \qquad \mathbf{S4}$$

The observed mass loss is in good agreement with that of the expected value. This confirmed a composition of $La_3Ni_2O_{5.5}F_{3.5}$ for the fluorinated sample, consistent with the results of the iodometric analysis in Section 6.3.2.2.

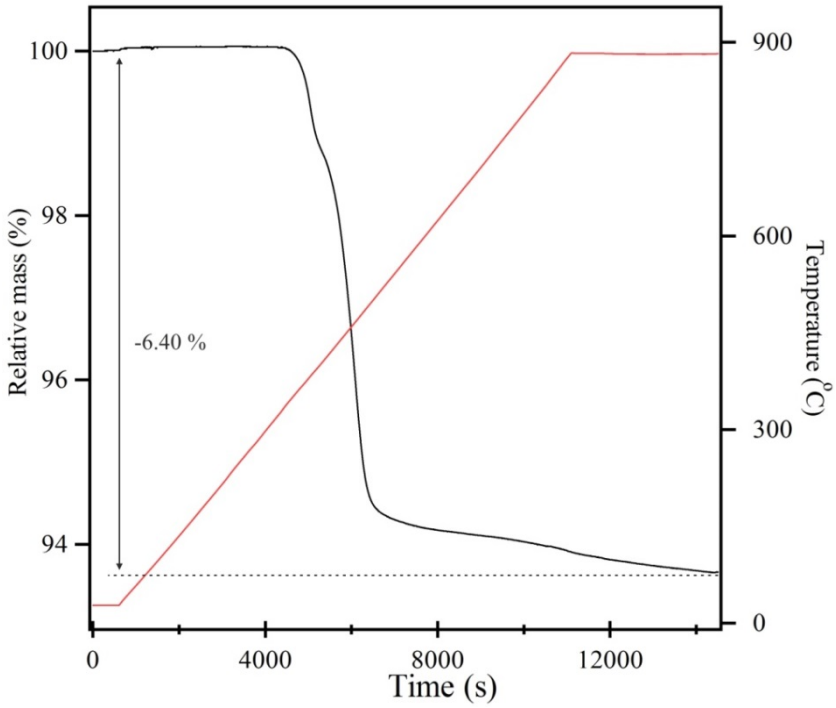


Figure 6.4. Thermogravimetric data collected by heating $La_3Ni_2O_{5.5}F_{3.5}$ under 10% H_2 in N_2. Sample mass (black, left axis), sample temperature (red, right axis). Expected mass loss of $La_3Ni_2O_{5.5}F_{3.5}$ when converted to LaOF + Ni + LaF_3 = 6.39%.

6.3.3 Structural refinement of $La_3Ni_2O_{5.5}F_{3.5}$

Neutron powder diffraction data collected from $La_3Ni_2O_{5.5}F_{3.5}$ can be indexed using an orthorhombic unit cell with lattice parameters similar to that observed from X-ray diffraction data. On initial inspection, the fluorinated sample appeared to have extinction conditions consistent with A-centring, the centring extinction adopted by the parent oxide $La_3Ni_2O_7$. Thus three models with A-centring extinction were constructed based on twisting distortion schemes of n = 2 Ruddlesden-popper phase as detailed in Table 3.1 in Chapter 3. These three models are *Amam* with ($a^-a^-c^0/a^-a^-c^0$) rotation distortion, $A2_1am$ with ($a^-a^-c^+/ a^-a^-c^+$), and *A2/a* with ($a^-a^-c^-/a^-a^-c^-$).

During the refinement, all atomic positional and displacement parameters were set to refine freely. Given the very similar neutron scattering length of oxide and fluoride (O = 5.80 fm;

F = 5.65 fm), no attempt was made to differentiate between the two anions at this stage; that is, all anion sites treated as if they were occupied by oxide. The distribution of O^{2-}/F^{-} anions will be discussed in detail in Section 6.4.2.

Refinement of these three models against the neutron powder diffraction data proceeded smoothly. Fitting statistics (Table 6.2) show that the *Amam* ($a^{-}a^{-}c^{0}/a^{-}a^{-}c^{0}$) model gave a fit to the data worse than the other two models, thus was eliminated from consideration. The two remaining models, *A2₁am* ($a^{-}a^{-}c^{+}/ a^{-}a^{-}c^{+}$) and *A2/a* ($a^{-}a^{-}c^{-}/a^{-}a^{-}c^{-}$), are strikingly different with each other according to the rotation distortion scheme; *A2₁am* adopts an c^{+} "in-phase" tilting rotation while *A2/a* adopts an c^{-} "out-of-phase" tilting rotation along the *z*-axis (see Chapter 1 Section 1.4.1). However, despite this significant structural difference between them, these two models gave almost identical fitting statistics. This suggests either the tilting rotation along *z*-axis is too small to distinguish between the c^{+} and c^{-} rotations or neither of the *A2₁am* and *A2/a* models describe the structure of $La_3Ni_2O_{5.5}F_{3.5}$ correctly. If the former argument is true, the *Amam* ($a^{-}a^{-}c^{0}/a^{-}a^{-}c^{0}$) model with no tilting rotation along *z*-axis should fit to the data as well as the *A2₁am* and *A2/a* models. This contradicts to the poor fitting statistics from *Amam* model, which suggests the latter argument might be more persuasive.

Close inspection of the fits of the *A2₁am* and *A2/a* models to the neutron diffraction data results in a critical observation of a few weak diffraction peaks that are not compatible with the A-centring extinction conditions, especially in the d-spacing range from 2.2 to 2.5 Å as shown in Figure 6.5. A model was thus required with a lifting on the A-centring as well as a different c-tilt with the *A2₁am* and *A2/a* models. The symmetry analysis by Aleksandrov and Bartolome suggests a suitable model in a primitive unit cell with *Pnam* ($a^{-}a^{-}c^{+}/ a^{-}a^{-}(-c^{+})$) space group. As discussed in Chapter 1 Section 1.4.1, this *Pnam* model contains two contra-rotatory in-phase tilting modes about *z*-axis, which could be thought of as a hybrid of the *A2/a* and *A2₁am* distortions. Refinement of this primitive model proceeded smoothly, giving a much improved fit

to the data both statistically (Table 6.2) and visually (Figure 6.5). Plots of the observed and calculated data of 35° bank are shown in Figure 6.5, and that of other banks are in Figure A6.1 in Appendix. The detailed structural parameters of the refined model are given in Table 6.3. Selected bond lengths and angles from refined structures of $La_3Ni_2O_{5.5}F_{3.5}$ and $La_3Ni_2O_7$ at 298 K are shown in Table 6.4.

Space Group	Tilt System	Glazer Tilt	Number of refined Variables	χ^2	wRp (%)	Rp (%)
Amam	ΦΦ0/ΦΦ0	$a^-a^-c^0$/ $a^-a^-c^0$	91	5.002	4.60	6.05
A2/a	$\Phi\Phi\Phi_z$ /$\Phi\Phi\Phi_z$	$a^-a^-c^-$/ $a^-a^-c^-$	101	4.096	4.16	5.75
A2$_1$am	$\Phi\Phi\Psi_z$ /$\Phi\Phi\Psi_z$	$a^-a^-c^+$/ $a^-a^-c^+$	101	3.965	4.11	5.89
Pnam	$\Phi\Phi\Psi_z$ /$\Phi\Phi(-\Psi_z)$	$a^-a^-c^+$/ $a^-a^-(-c^+)$	102	2.918	3.53	4.16

Table 6.2. Fitting statistics from the structural refinement of $La_3Ni_2O_{5.5}F_{3.5}$ using different models. Φ indicates an out of phase rotation; Ψ indicates an in-phase rotation.

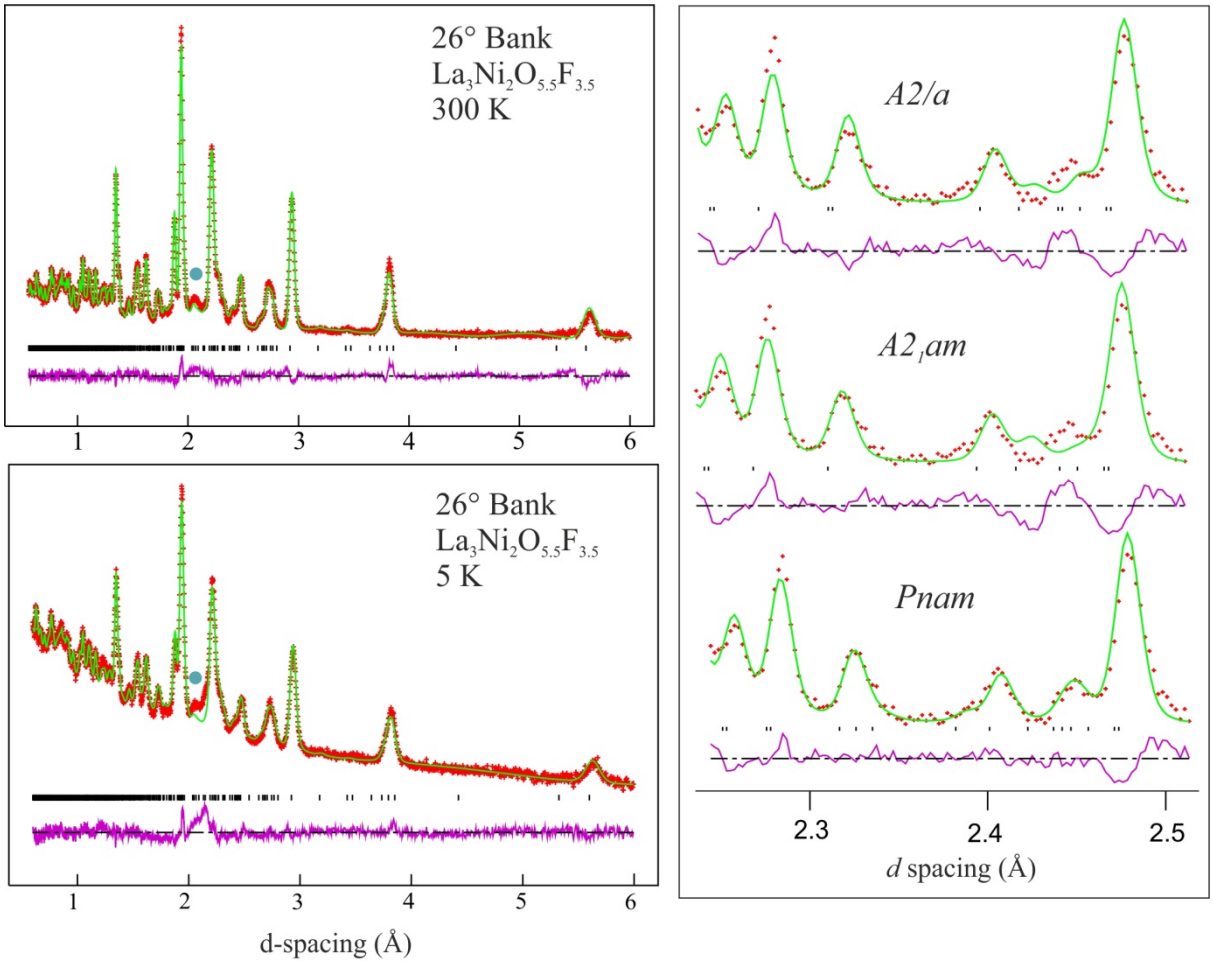


Figure 6.5. Observed, calculated and difference plots from the structural refinement of $La_3Ni_2O_{5.5}F_{3.5}$ against neutron powder diffraction data collected at 300 K and 5 K by using POLARIS diffractometer (ISIS, UK). The blue circles in the diffraction pattern mark a tiny amount of LaF_3 impurities in the sample.

Atom	site	*x*	*y*	*z*	$U_{iso}(Å^2)$
La(1)	4e	0.7148(7)	0.0017(9)	1/4	0.0059(6)
La(2)	8f	0.7564(6)	-0.0044(6)	0.0758(1)	0.0060(4)
Ni(1)	8f	0.7615(5)	0.0036(5)	0.8353(1)	0.0030(2)
O(1)	4e	0.7335(11)	0.5687(7)	1/4	0.0034(7)
O(2)	8f	0.7727(8)	-0.0554(6)	0.9198(1)	0.0072(6)
O(3)	8f	-0.0132(8)	0.2755(7)	0.8524(1)	0.0057(5)
O(4)	8f	0.4501(8)	0.2816(8)	0.3278(1)	0.0107(7)
F(1)	8f	-0.0082(8)	0.2557(9)	-0.0075(1)	0.0075(6)
$La_3Ni_2O_{5.5}F_{3.5}$ space group: *Pnam* *a* = 5.4312(10) Å *b* = 5.5074(10) Å *c* = 22.483(4) Å Volume = 672.5(4) $Å^3$ χ^2 = 2.918; *wRp*= 3.53%; *Rp* = 4.16%.					

Table 6.3. Structural parameters refined against neutron powder diffraction data collected at 300 K from $La_3Ni_2O_{5.5}F_{3.5}$

	$La_3Ni_2O_7$ **Bond length (Å)**	**$La_3Ni_2O_{5.5}F_{3.5}$** **Bond length (Å)**
Ni-O1	1.975(2)	1.951(2)
Ni-O2	2.227(5)	1.928(3)
Ni-O3	1.906(2)	1.963(5)
		1.972(5)
Ni-O4	1.941(2)	1.954(5)
		1.994(5)
	Bond angle (°)	**Bond angle (°)**
Ni-O1-Ni	167.64(8)	158.76(26)
Ni-O3-Ni	169.21(1)	154.71(26)
Ni-O4-Ni	171.14(1)	161.39(27)
	Octahedron rotation angle (º)	**Octahedron rotation angle (º)**
x-axis	4.91(7)	8.10(10)
y-axis	4.91(7)	8.10(10)
z-axis	0	6.85(7)

Table 6.4. Selected bond lengths and angles from refined structures of $La_3Ni_2O_{5.5}F_{3.5}$ and $La_3Ni_2O_7$ at 298 K.

6.3.4 Magnetic Characterization of $La_3Ni_2O_{5.5}F_{3.5}$

6.3.4.1 Magnetization data

Magnetization data collected from $La_3Ni_2O_{5.5}F_{3.5}$ in an applied field of 100 Oe show a weak divergence between zero-field cooled and field cooled data below T ~ 50 K as shown in Figure 6.6. Despite this feature, the zero-field cooled data can be approximately fitted to the Curie-Weiss law over the whole 5 < T/K < 300 temperature range to yields values of C = 0.142(3) cm^3 K mol^{-1}, = -14.4(2) K. The low value of the Curie constant, combined with the weak divergence between zero-field cooled and field cooled data suggest the localize spins on the nickel centres are not behaving as simple paramagnetic moments.

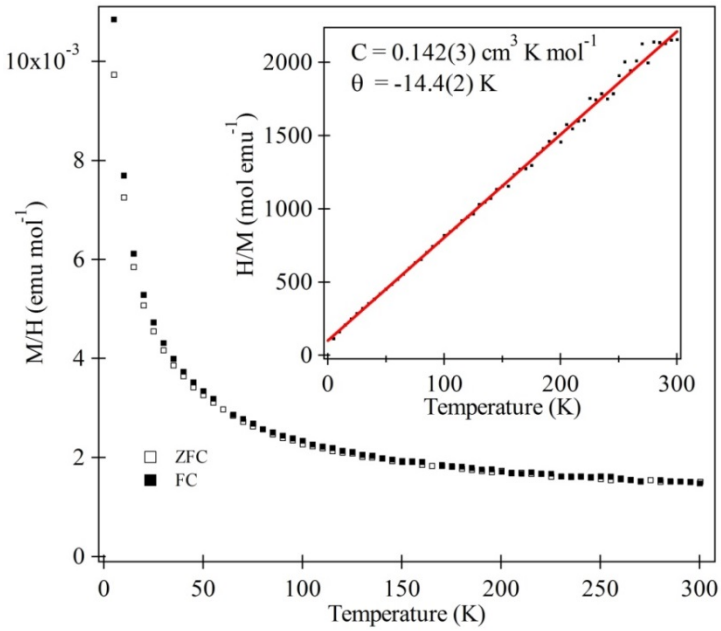


Figure 6.6. Zero-field cooled and field-cooled magnetization data collected as a function of temperature from $La_3Ni_2O_{5.5}F_{3.5}$ in an applied filed of 100 Oe.

6.3.4.2 Neutron powder diffraction data (5 K)

As shown in Figure 6.5, neutron powder diffraction data collected at 5 K from $La_3Ni_2O_{5.5}F_{3.5}$ can be readily fitted by the same structural model as used for the 300 K data. No obvious magnetic scattering peak was observed, suggesting no sign of magnetic order. The detailed structural parameters of the refined model are given in Table 6.5.

Atom	site	*x*	*y*	*z*	U_{iso}(Å^2)
La(1)	4e	0.7093(7)	0.0051(11)	1/4	0.0019(6)
La(2)	8f	0.7579(5)	-0.0043(7)	0.0756(1)	0.0015(4)
Ni(1)	8f	0.7657(5)	0.0030(5)	0.8354(1)	0.0013(2)
O(1)	4e	0.7358(13)	0.5703(9)	1/4	0.0010(7)
O(2)	8f	0.7697(10)	-0.0535(6)	0.9199(1)	0.0053(6)
O(3)	8f	-0.0119(8)	0.2790(7)	0.8526(1)	0.0039(5)
O(4)	8f	0.4502(8)	0.2866(9)	0.3281(1)	0.0049(6)
F(1)	8f	-0.0094(10)	0.2574(9)	-0.0076(1)	0.0052(6)
$La_3Ni_2O_{5.5}F_{3.5}$ space group: *Pnam* *a* = 5.4315(10) Å*b* = 5.4991(10) Å*c* = 22.461(4) Å Volume = 669.6(4) Å^3 χ^2 = 1.736; *wRp*= 1.54%; *Rp* = 2.65%.					

Table 6.5. Structural parameters refined against neutron powder diffraction data collected at 5 K from $La_3Ni_2O_{5.5}F_{3.5}$ by using POLARIS diffractometer (ISIS, UK).

6.4 Discussion

6.4.1 The fluorination chemistry

Heating $La_3Ni_2O_7$ under an F_2/O_2 flow leads to the formation of a fluorinated phase, whose composition was confirmed to be $La_3Ni_2O_{5.5}F_{3.5}$ by Iodimetric titration and Thermogravimetric (TGA) data as discussed in 6.3.2. In contrast to the fluorination of $La_2SrCr_2O_7$ where the average chromium oxidation state rises up one unit to Cr^{4+} from Cr^{3+}, the average nickel oxidation state only slightly rises up to $Ni^{+2.75}$ in $La_3Ni_2O_{5.5}F_{3.5}$ from $Ni^{+2.5}$ in $La_3Ni_2O_7$. This indicates a high level of fluoride-oxide anion exchange on fluorination of $La_3Ni_2O_7$. As discussed in Chapter 1 Section 1.5, on topochemical fluorination, fluoride ions could go into the parent framework by the following two processes: (1) a pure fluoride insertion process by inserting fluoride ions into the tetrahedral interstitial sites between the rock salt layer, or/and (2) an anion exchange process by replacing the existing oxide in the parent framework to fluoride ions.

On the fluorination $La_3Ni_2O_7$, both of these two processes were observed. This is not unique; similar high levels of anion exchange combined with fluoride insertion have been

reported on the fluorination of $Sr_3(Fe_{0.5}Ru_{0.5})_2O_7$ to $Sr_3(Fe_{0.5}Ru_{0.5})_2O_{5.5}F_{3.5}$, or $La_3BaFe_2O_7$ to $La_2BaFe_2O_5F_4$.[106,110] In this instance the high level of anion substitution during the fluorination of $La_3Ni_2O_7$ can be attributed to the difficulty of stabilizing the Ni^{3+} oxidation state.

6.4.2 The anion distribution of $La_3Ni_2O_{5.5}F_{3.5}$

As noted in 6.3.3, it is difficult to distinguish the oxide/fluoride anion from X-ray or neutron diffraction data as their scattering lengths are similar. However, as discussed in Chapter 2 Section 2.9 as well as Chapter 4 Section 4.4.1, the bond valence sums (BVS) sometimes offer a clue of the anion distribution in some fluorinated phases.

Table 6.6 lists the bond valence sums (BVS) of the anions sites for the 5 crystallographically distinct anion sites in the structure of $La_3Ni_2O_{5.5}F_{3.5}$. These BVS were calculated by supposing the sites were exclusively occupied by either oxide or fluoride anions The BVS of corresponding anion sites in the structure of $La_3Ni_2O_7$ were also calculated for comparison. The anion site labelling scheme is shown in Figure 6.7.

These data reveal that the tetragonal interstitial anion site X(5), which resides in the rock salt layers of the extended structure, has the smallest BVS value, consistent with the occupation of fluoride ions. Occupation of these 'interstitial' anion sites exclusively by fluoride ions has been observed widely in other topochemically fluorinated $n = 2$ Ruddlesden-popper phases, such as in the $La_2SrCr_2O_7F_2$ phase discussed in Chapter 4.

The anion stoichiometry of $La_3Ni_2O_{5.5}F_{3.5}$ indicates that fluoride ions must reside on other anion sites, in addition to the X(5) site. Table 6.6 shows that the apical anion site X(2) has a BVS value significantly lower than that of the rest of the anion sites, almost comparable with that of X(5). It is thus reasonable to conclude that the remaining fluoride ions are located in the apical X(2) anion sites, resulting in a 75% F^-:25% O^{2-} occupation. This preferred occupation of the apical anion site on fluoride-oxide anion exchange is not uncommon and has been reported for $Sr_3(Fe_{0.5}Ru_{0.5})_2O_{5.5}F_{3.5}$ previously.[60]

$La_3Ni_2O_7$		$La_3Ni_2O_{5.5}F_{3.5}$		
Anion	**BVS (O)**	**Anion**	**BVS (O)**	**BVS (F)**
O(1)	1.840	X(1)/O(1)	1.974	1.563
O(2)	1.706	X (2)/25% O^{2-}/75% F^-	1.481	1.147
O(3)	2.107	X(3)/O(3)	1.918	1.516
O(4)	2.017	X(4)/O(4)	1.811	1.436
		X(5)/F(1)	1.404	1.029

Table 6.6. Anion bond valence sums from $La_3Ni_2O_7$ and $La_3Ni_2O_{5.5}F_{3.5}$; the labelling scheme is shown below in Figure 6.7.

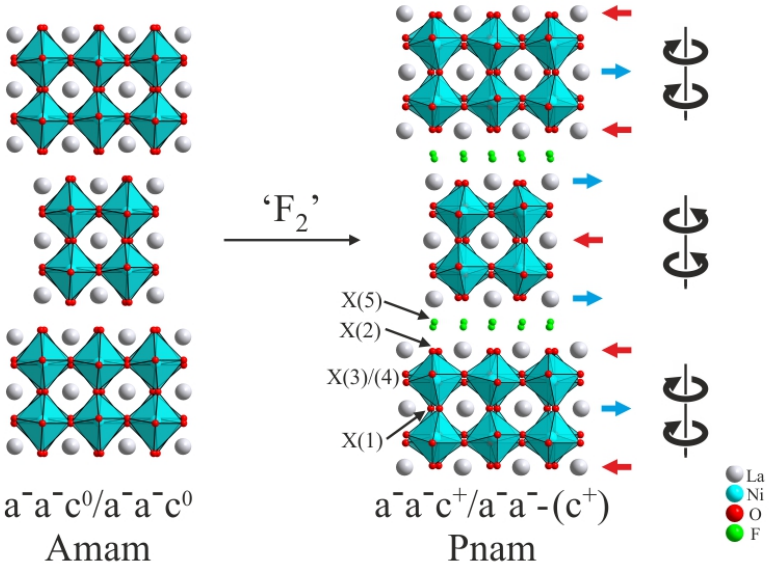


Figure 6.7. The fluorination $La_3Ni_2O_7$ (*Amam*) to $La_3Ni_2O_{5.5}F_{3.5}$ (*Pnam*).

6.4.3 Structural modification by topochemical fluorination

6.4.3.1 Compression of the perovskite layers by fluorine insertion

The insertion/exchange of fluorine into $La_3Ni_2O_7$ to form $La_3Ni_2O_{5.5}F_{3.5}$ leads to a tightening of all the Ni-X-Ni bond angles as shown in Table 6.6. The "in-plane" angle and 'torsion angle' between adjacent O_{apical}-O_{axial} bonds defined in Chapter 4 (Section 4.4.3) are used to parametrize the componential rotations of the NiX_6 octahedra around each Cartesian axis. The degree of rotations about each axis is also listed in Table 6.4. It reveals that, on fluorination, the rotational distortions around all three axes increase, from 4.91(7)º to 8.1(1)º around the *x*- and *y*-axes, and from zero to 6.85(7)º around the *z*-axis.

The tightening of all the Ni-X-Ni bond angles on fluorination can be attributed to a

compression of the perovskite double layers along the *z*-axis. As shown in Figure 6.8, the *c*-dimension of the double perovskite (defined in Chapter 4, Section 4.4.2) decreases from 8.36 Å in $La_3Ni_2O_7$ to 7.67 Å in $La_3Ni_2O_{5.5}F_{3.5}$. It is worth noting that the *ab*-plane area slightly expands from 29.38 $Å^2$ to 29.91 $Å^2$ during fluorination. In $La_3Ni_2O_7$, the NiO_6 octahedra present in $La_3Ni_2O_7$ have a large axial distortion, such that the ratio of $Ni\text{-}O_{axial}/Ni\text{-}O_{equatorial}$ = 1.09. Insertion of fluoride leads to a compression of the perovskite layers along the *z*-axis, presumably due to enhanced anion-anion repulsions, resulting in the $Ni(O/F)_6$ octahedra in $La_3Ni_2O_{5.5}F_{3.5}$ being axially compressed ($Ni\text{-}X_{axial}/Ni\text{-}X_{equatorial}$ = 0.98). This transformation from 'tall-thin' NiO_6 to 'short-fat' $Ni(O/F)_6$ naturally leads to an expansion of the Ni-X equatorial bonds, and introduces a rotation around the *z*-axis to accommodate these longer bonds within the perovskite framework (despite a slight expansion in the *a* and *b* lattice parameters).

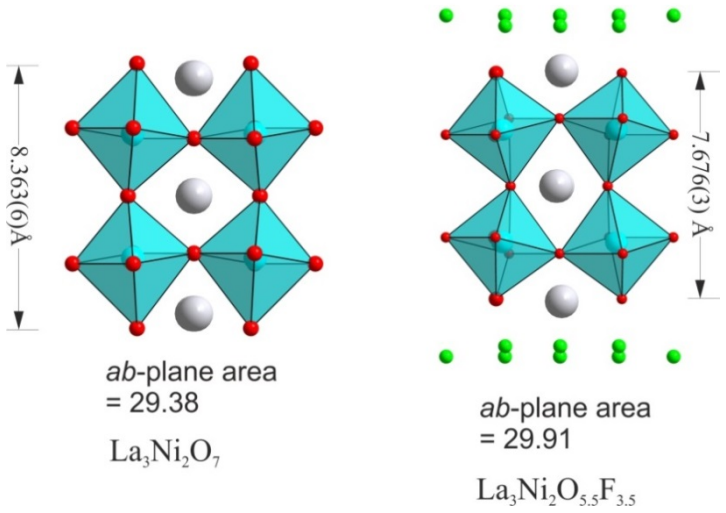


Figure 6.8. Fluorination of $La_3Ni_2O_{5.5}F_{3.5}$ leads to a compression of the perovskite blocks, both parallel to the *c*-axis and in the *ab*-plane, leading to a tightening of all Ni-X-Ni bond angles.

6.4.3.2 Introduction of an in-phase *c*-tilt to the network of octahedral and the lifting of local inversion symmetry in $La_3Ni_2O_{5.5}F_{3.5}$

The introduction of an in-phase *z*-twist to the network of octahedra results in each perovskite double layer adopting an $a^-a^-c^+$ distortion pattern, which lifts the inversion symmetry of each layer via the coupled displacements of the lanthanum A-cations. However despite breaking the inversion symmetry of the Ruddlesden-Popper framework locally, this distortion

does not break the inversion symmetry globally because the 'sense' of the in-phase *z*-axis rotation inverts between adjacent perovskite layers, and as a result the direction of the A-cation displacements is also inverted between adjacent perovskite layers. Thus the framework is described in the centrosymmetric space group *Pnam*, not the polar space group $A2_1am$. The comparison between these two models is shown in Figure 6.9. In polar $A2_1am$ structure, the two sets of double-perovskite blocks (marked in blue) are related by translation, while they are related by inversion symmetry in *Pnam* model.

The recovery of global inversion symmetry via the anti-alignment of locally acentric units (in this instance the polar perovskite double-layers) is an issue which has long hampered the design and synthesis of NCS phases. This has been particularly apparent when a basic building unit (BBU) approach has been adopted to prepare NCS phases. The BBU approach involves crystalizing acentric units, such as metal oxide-fluoride complex anions ($NbOF_5^{2-}$, VOF_5^{2-}, $MoO_2F_4^{2-}$, etc)[114-116] into extended networks with the intention of forming NCS lattices. However it has been widely observed that centrosymmetric structures in which the BBUs anti-align or adopt orientationally disordered arrangements tend to be favoured unless specific steps are taken to oppose this. In the oxide-fluoride case, the use of particular bridging ligands[117,118] or specific structure directing interactions between the oxide-fluoride anions and charge balancing cations[119] can be used to suppress the adoption of centrosymmetric lattices and direct the formation of NCS phases. This provides some hope that similar interactions can be employed within topochemically fluorinated Ruddlesden-Popper phases to suppress the formation of anti-ferroelectric structures and allow the formation of ferroelectric materials and by extension multiferroic materials.

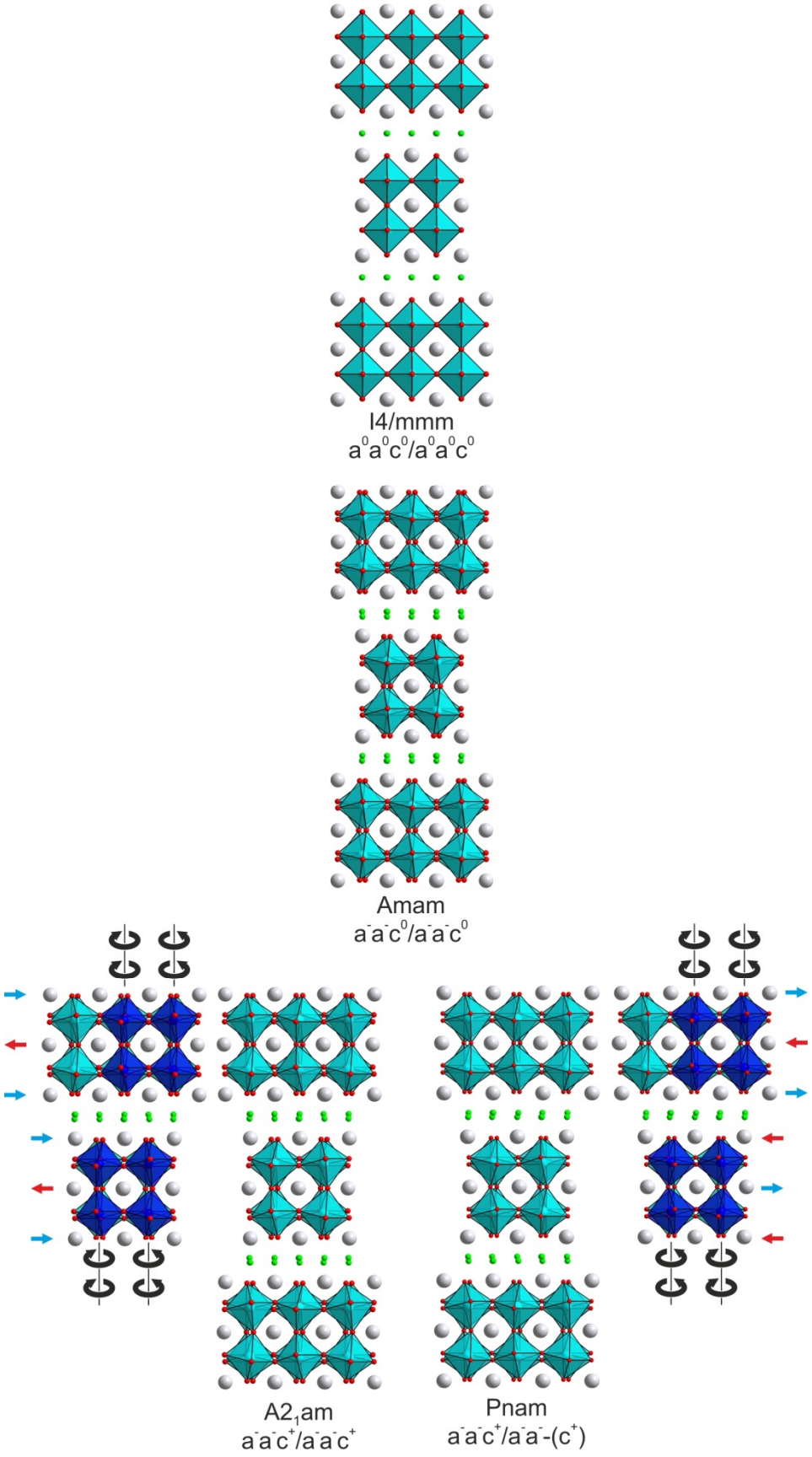


Figure 6.9. Comparison of octahedral rotations and A-cation displacements of *Amam*, *A2₁am* and *Pnam* distorted $A_3B_2O_7F_2$.

6.5 Conclusion

Topochemical fluorination of the n = 2 Ruddlesden-Popper oxide $La_3Ni_2O_7$ yields the oxide-fluoride $La_3Ni_2O_{5.5}F_{3.5}$. Insertion/exchange of fluoride ions leads to an enhancement of the structural distortion exhibited by the oxide starting material, driving a change from an *Amam*, $a^-a^-c^0/a^-a^-c^0$ lattice distortion to a *Pnam* $a^-a^-c^+/a^-a^-(c^+)$ lattice distortion in the oxide-fluoride phase. The introduction of a cooperative octahedral tilt around the crystallographic *z*-axis leads to a local breaking of the inversion symmetry of the host lattice on fluorination, although the global inversion symmetry of the lattice is retained due to an alternation in the *z*-tilt direction in adjacent perovskite sheets.

In a wider context this study reaffirms previous observations that topochemical fluorination acts to enhance the titling distortions of n = 2 Ruddlesden-Popper phases,[26,106,109] and as a result offers an alternative route, in addition to adjusting the tolerance factor by cation substitution, to tune the cooperative structural distortions of materials with this structure type. If appropriate methods can be found to suppress the formation of anti-ferroelectric phases, this facility to modify the structural distortions of layered perovskites will be particularly valuable in the directed search for magnetoelectric multiferroic materials, where the requirement to have paramagnetic centres necessitates the inclusion of transition metal B-cations with small ionic radii, which limits the minimum value the structural tolerance factor can take, and effectively precludes the stabilization of the highly-distorted frameworks required to break structural inversion symmetry.

Chapter 7: Characterization of $YSr_{2-x}Ca_xMn_2O_7$

7.1 Introduction

As discussed in Chapter 6, the insertion/exchange of fluoride ions into n = 2 Ruddlesden-Popper phases leads to an enhancement of the structural distortion exhibited by the oxide starting material ($La_3Ni_2O_7$), driving a change from an *Amam*, $a^-a^-c^0/a^-a^-c^0$ lattice distortion in $La_3Ni_2O_7$ phase to a *Pnam* $a^-a^-c^+/a^-a^-(c^+)$ lattice distortion in the $La_3Ni_2O_{5.5}F_{3.5}$ oxide-fluoride phase. The introduction of a cooperative octahedral tilt around the crystallographic *z*-axis leads to a local breaking of the inversion symmetry of the host lattice on fluorination, although the global inversion symmetry of the lattice is retained due to an alternation in the *z*-tilt direction in adjacent perovskite sheets to form an antiferroelectric structure. Topochemical fluorination still offers a potential route to tune the cooperative structural distortions of materials with an n = 2 Ruddlesden-Popper structure into a ferroelectric $A2_1am$ ($a^-a^-c^+/ a^-a^-c^+$) phase. Our attention was thus moved onto other n = 2 Ruddlesden-Popper phases with *Amam* ($a^-a^-c^0/a^-a^-c^0$) structures that could potentially act as a suitable host for topochemical fluorination.

One of the few compounds with an n = 2 Ruddlesden-Popper structure that has been reported to adopt *Amam* symmetry is $LaCa_2Mn_2O_7$, thus the fluorination of $LaCa_2Mn_2O_7$ was attempted. The structural analysis of the resulting fluorinated phase $LaCa_2Mn_2O_xF_y$, however, is hindered by the presence of considerable amount of impurities such as (La,Ca)MnO_3 and CaF_2. The X-ray pattern of $LaCa_2Mn_2O_xF_y$ is shown in Figure 7.1. The diffraction peaks from the (La,Ca)MnO_3 impurity phase overlap with those from the majority $LaCa_2Mn_2O_xF_y$ phase, which makes structural analysis on the subtle tilting distortions of the Ruddlesden-Popper phase unreliable.

Given the difficulties in finding suitable, previously reported n = 2 Ruddlesden-Popper structures with *Amam* symmetry, we then have sought to prepare new *Amam* ($a^-a^-c^0/a^-a^-c^0$) distorted phases by lowering the structural tolerance factor of existing n = 2 Ruddlesden-Popper

phases. As discussed in the Chapter 1, substitution of smaller cations onto the A-cation site could drive the framework to adopt increasingly distorted structure (tolerance factor *t* becomes smaller), as shown in Figure 7.2. Hence this chapter describes the structural change on the substitution of Sr^{2+} with Ca^{2+} cations in the *P4₂/mnm* distorted *n* = 2 Ruddlesden-Popper phase $YSr_2Mn_2O_7$.

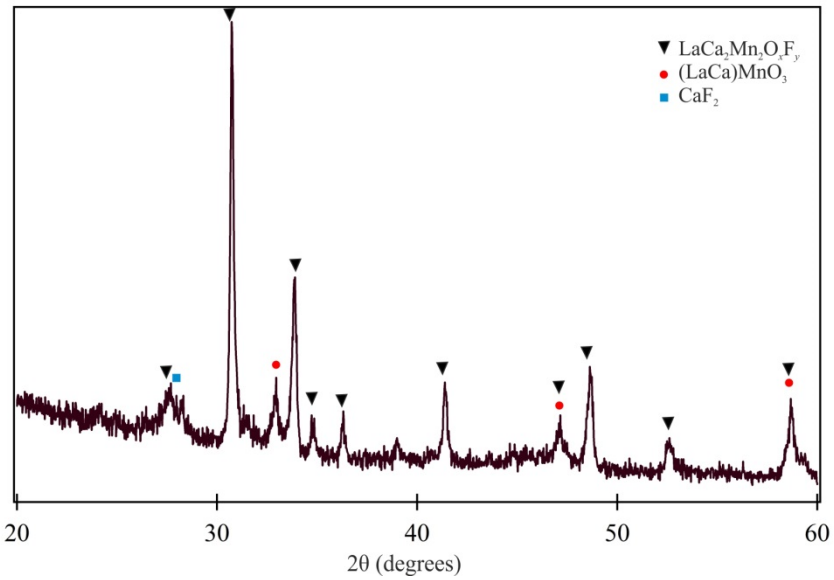


Figure 7.1. X-ray diffraction pattern of $LaCa_2Mn_2O_xF_y$.

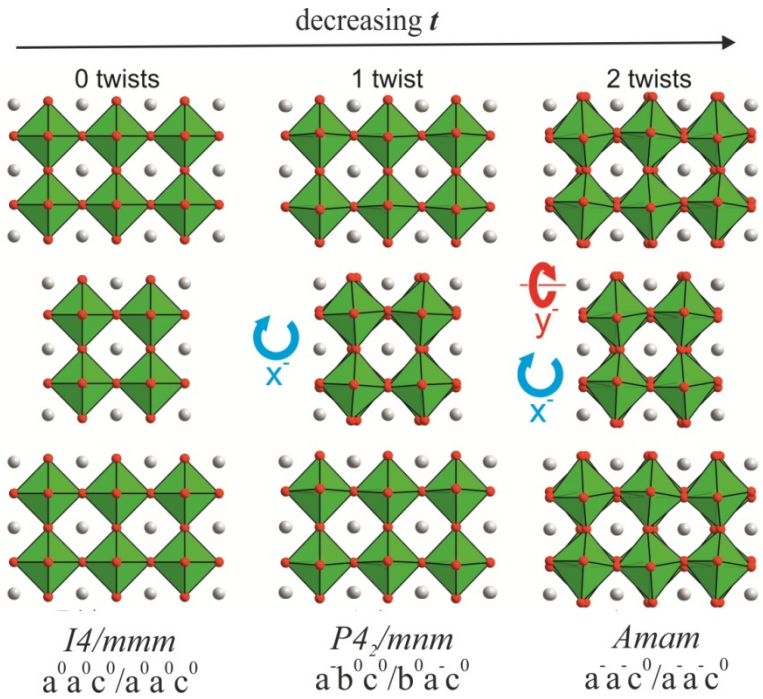


Figure 7.2. Scheme of tuning the tilting distortion in *n* = 2 Ruddlesden-Popper phases by lowering the tolerance factor.

7.2 Experimental

Samples in $YSr_{2-x}Ca_xMn_2O_7$ series (x = 0, 0.25, 0.5, 1.0 and 1.5) were prepared via a citrate gel method. Suitable stoichiometric ratios of Y_2O_3 (99.99%, dried at 900 °C), $SrCO_3$ (99.99%), $CaCO_3$ (99.99%) and MnO_2 (99.9%) were dissolved in a minimal quantity of 6 M nitric acid. Citric acid and ethylene glycol were then added, and the solution was heated with constant stirring. The gels thus formed and were heated to 350 °C until a loose black powder was obtained. The powders were ground and then heated to 1000 °C in air at a rate of 1 °C/min to remove the remaining organic components. The resulting powders were then pressed into pellets before further heat treatments. For the preparation of $YSr_2Mn_2O_7$ and $YSr_{1.75}Ca_{0.25}Mn_2O_7$, the sample pellets were heated for 3 periods of 48 h at 1350 °C in air and 2 further periods of 48 h at 1450 °C. For $YSrCaMn_2O_7$, the pellets were heated for 3 periods of 48 h at 1350 °C in air and 2 further periods of 48 h at 1400 °C. For $YSr_{0.5}Ca_{1.5}Mn_2O_7$, the pellets were heated for 3 periods of 48 h at 1350 °C in air and 2 further periods of 48 h at 1350 °C. Lower synthesis temperatures were employed for the Ca substituted samples to avoid melting.

The preparation of $YCa_2Mn_2O_7$ was also attempted, but the $YCa_2Mn_2O_7$ phase failed to form after 4 heating cycles of 48 hours at 1300 °C and the sample melts at 1325 °C.

7.3 Results

7.3.1 X-ray powder diffraction data of $YSr_{2-x}Ca_xMn_2O_7$

X-ray powder diffraction data collected from samples in the $YSr_{2-x}Ca_xMn_2O_7$ series (x = 0, 0.25, 0.5, 1.0 and 1.5) are shown in Figure 7.3. Clear changes in the X-ray diffraction data could be observed when increasing amounts of Ca^{2+} cations are doped into $YSr_2Mn_2O_7$. The shifting of the (115) and (0,0,10) diffraction peaks to a higher 2θ indicates a decrease of the c-lattice parameters, consistent with the occupation of smaller Ca^{2+} cations in the A-sites.

During the preparation of $YSr_{1.75}Ca_{0.25}Mn_2O_7$, the X-ray diffraction data reveal an anomalous peak shape and width from the (00l) ($l \neq 0$) diffraction, as shown in Figure 7.3. This

asymmetric and broad peak shape of (00*l*), such as the (0,0,10), could not be described satisfactorily by a single phase. This indicates that during the preparation of $YSr_{1.75}Ca_{0.25}Mn_2O_7$, the product separates into two similar n = 2 Ruddlesden-Popper phases.[120] This phase separation was commonly observed in the preparation of members of the $LnSr_2Mn_2O_7$ series (Ln is lanthanide)[74,81,120] as can be described by two possible schemes:

$$\mathbf{LnSr_2Mn_2O_7 \rightarrow Ln_{1+x}Sr_{2-x}Mn_2O_7 + Ln_{1-x}Sr_{2+x}Mn_2O_7} \quad (x \neq 0) \quad \mathbf{S1}$$

$$\mathbf{LnSr_2Mn_2O_7 \rightarrow LnSr_2Mn_2O_7\ (I) + LnSr_2Mn_2O_7\ (II)} \quad \mathbf{S2}$$

In scheme S1, the two similar Ruddlesden-Popper phases differ in A-cation composition, while in scheme S2, they share the same composition but different A-cation distributions between the 9- and 12-coordinate A-sites. This phase separation was also observed during the preparation of $YSr_{1.5}Ca_{0.5}Mn_2O_7$. A single phase failed to be obtained for $YSr_{1.75}Ca_{0.25}Mn_2O_7$ as well as $YSr_{1.5}Ca_{0.5}Mn_2O_7$ after several heating cycles at a higher reaction temperature near the melting point (T ≈ 1450 °C). These two phases were thus not considered for detailed structural analysis.

X-ray diffraction data collected from $YSrCaMn_2O_7$ and $YSr_{0.5}Ca_{1.5}Mn_2O_7$ can be fitted relatively well to a single phase model, and thus were discussed in detail in this Chapter. The splitting of the (200) diffraction peak to (200) and (020) in the X-ray diffraction data collected from $YSr_{0.5}Ca_{1.5}Mn_2O_7$ suggests a clear lowering of the symmetry from tetragonal to orthorhombic, while peak splitting in $YSrCaMn_2O_7$ is not obvious. It is therefore easier to characterize the structure of $YSr_{0.5}Ca_{1.5}Mn_2O_7$ first.

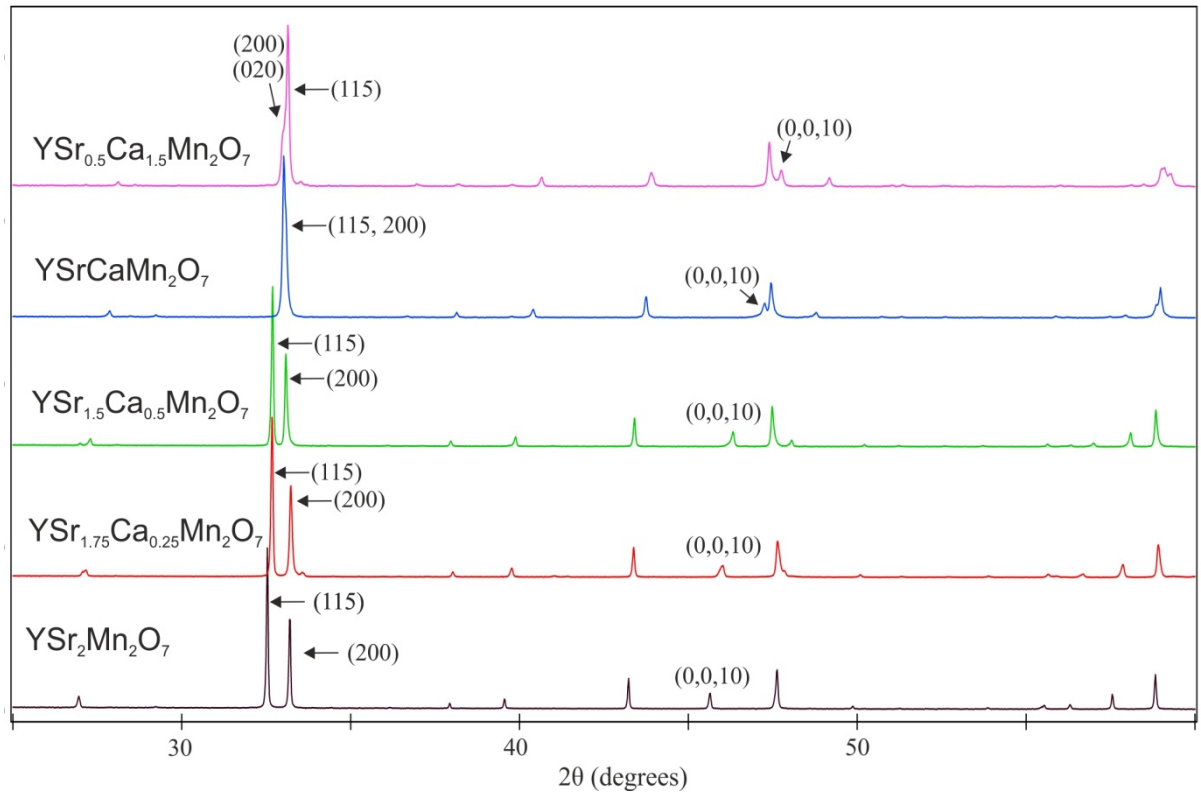


Figure 7.3. The X-ray diffraction data of samples in $YSr_{2-x}Ca_xMn_2O_7$ series (x = 0, 0.25, 0.5, 1.0 and 1.5).

7.3.2 Structural refinement of $YSr_{0.5}Ca_{1.5}Mn_2O_7$

The Rietveld refinements were carried out against X-ray powder diffraction data collected from $YSr_{0.5}Ca_{1.5}Mn_2O_7$ by using the *P4₂/mnm* ($a^-b^0c^0/b^0a^-c^0$) model reported for $YSr_2Mn_2O_7$ with Sr/Ca ratios modified for a composition of $YSr_{0.5}Ca_{1.5}Mn_2O_7$. The *P4₂/mnm* model gave a poor fit to the X-ray diffraction data collected from $YSr_{0.5}Ca_{1.5}Mn_2O_7$ (χ^2 = 15.35). Close inspection of the X-ray diffraction data reveals some diffraction peaks observed cannot be indexed by a tetragonal unit cell. Therefore an orthorhombic model in space group *Amam* ($a^-a^-c^0/a^-a^-c^0$) was constructed and refined against the X-ray diffraction data. Significant improvement on the fit (χ^2 = 1.930) was achieved, giving lattice parameters of a = 5.414(1), b = 5.428(1), and c = 19.035(1). Therefore, the *Amam* model with stated lattice parameters was used to refine against the neutron diffraction data collected using the HRPD diffractometer (ISIS, UK).

During the refinement against the neutron diffraction data, the Y^{3+} cations were fixed in the 9-coordinate site, while a mix of Sr^{2+} and Ca^{2+} cations distributed evenly over the two A-

cation sites. At first, occupancies of the A-cation sites were not refined. The refinement proceeded smoothly. However, close inspection of the refinement reveals that the *Amam* model cannot satisfactorily model all the neutron diffraction peaks, and poor fitting statistics are obtained (χ^2 = 17.18; *wRp*= 7.16 %; *Rp* = 6.31 %). Varying the A-cation distributions over the two A-sites without changing the *Amam* model fails to improve the fit to the data. This suggests that neither *$P4_2/mnm$* nor *Amam* models are suitable to describe the structure of $YSr_{0.5}Ca_{1.5}Mn_2O_7$.

Other suitable models with an orthorhombic symmetry were thus investigated for the refinement of the neutron diffraction data collected from $YSr_{0.5}Ca_{1.5}Mn_2O_7$. This investigation of suitable models is based on a symmetry analysis performed by Aleksandrov and Bartolome (A&B), in which the possible cooperative twisting distortions of the BO_6 octahedra in $A_3B_2O_7$ *n* = 2 Ruddlesden-Popper phases were discussed (as detailed in Chapter 1). Starting from *$P4_2/mnm$* ($a^-b^0c^0/b^0a^-c^0$) distortion adopted by $YSr_2Mn_2O_7$, substitution of smaller cations (Ca^{2+}) into A-cation site would possibly induce a further distortion to the framework. Thus one suitable model adopted by $YSr_{0.5}Ca_{1.5}Mn_2O_7$ could be the *Amam* model with ($a^-a^-c^0/a^-a^-c^0$) distortion, in which a rotation about *y*-axis with the same magnitude as that about *x*-axis is introduced into the framework. However, it is reasonable to argue that the magnitude of the induced rotations about *y*-axis by cation substitution is not necessary to be the same as that about *x*-axis. In this case, the structure adopts a ($a^-b^-c^0/b^-a^-c^0$, $a \neq b$) distortion rather than ($a^-a^-c^0/a^-a^-c^0$). The orthorhombic *Pnnm* model with the ($a^-b^-c^0/b^-a^-c^0$, $a \neq b$) distortion, in which the two rotations about the *x*- and *y*-axis differ in magnitude, was thus constructed and refined against the neutron diffraction data collected from $YSr_{0.5}Ca_{1.5}Mn_2O_7$.

At first, the occupancies of the A-cation sites were not refined, and the Y^{3+} cations were fixed in the 9-coordinate site, while a mix of Sr^{2+} and Ca^{2+} cations distributed evenly over the two A-cation sites. The refinement proceeded smoothly. A much better fit to the data was achieved by using the *Pnnm* than *Amam* model as shown in Table 7.1. The distribution of Sr^{2+} and Ca^{2+}

cations were then set to refine within the constraints of the total sample composition, while the Y^{3+} cations remained fixed in the 9-coordinate site. It was observed that the occupancy of Sr^{2+} cations at the 9-coordinate site was quickly refined to zero. The occupancy of Y^{3+} cations was then set to vary freely. Only a small deviation from the fixed value of the occupancy was observed, indicating the Y^{3+} cations sit preferably in the 9-coordinated site. Therefore, the A-cation distribution was modified as following: the Sr^{2+} cations were set exclusively in the 12-coordinate site, the Y^{3+} cations exclusively in the 9-coordinate site and Ca^{2+} occupies the rest of the A-cation sites. The *Pnnm* and *Amam* model with adjusted A-site distribution were refined against the neutron diffraction data collected from $YSr_{0.5}Ca_{1.5}Mn_2O_7$. It turned out that $YSr_{0.5}Ca_{1.5}Mn_2O_7$ can still be modelled significantly better in *Pnnm* space group, instead of *Amam*, as shown in Table 7.1.

Reasonable '3-tilt' models, such as *Pnam* and *$A2_1am$* models described in Chapter 6, were also constructed and refined against the neutron diffraction data collected from $YSr_{0.5}Ca_{1.5}Mn_2O_7$. These models gave a fit statistically worse than that of *Amam* model (χ^2 = 32.36 for *$A2_1am$*, 32.06 for *Pnma*), and thus not discussed.

Plots of the observed and calculated data of 90° bank are shown in Figure 7.4, and that of other banks are in Figure A7.3 in Appendix. The detailed structural parameters of the refined model are given in Table 7.2.

Space Group	Tilt System	Glazer Tilt	χ^2	wRp (%)	Rp (%)
$P4_2/mnm$	Φ00/0Φ0	$a^-b^0c^0$/ $b^0a^-c^0$	-	-	-
Pnnm	$\Phi_1\Phi_2 0/\Phi_2\Phi_1 0$	$a^-(a^-)'c^0$/ $(a^-)'a^-c^0$	10.62	5.63	5.43
Amam	ΦΦ0/ΦΦ0	$a^-a^-c^0$/ $a^-a^-c^0$	17.18	7.16	6.31

Table 7.1. Fitting statistics from the structural refinement of $YSr_{0.5}Ca_{1.5}Mn_2O_7$ using models based on the distortions of n = 2 Ruddlesden-Popper phases. Φ indicates an out of phase rotation; Ψ indicates an in-phase rotation.

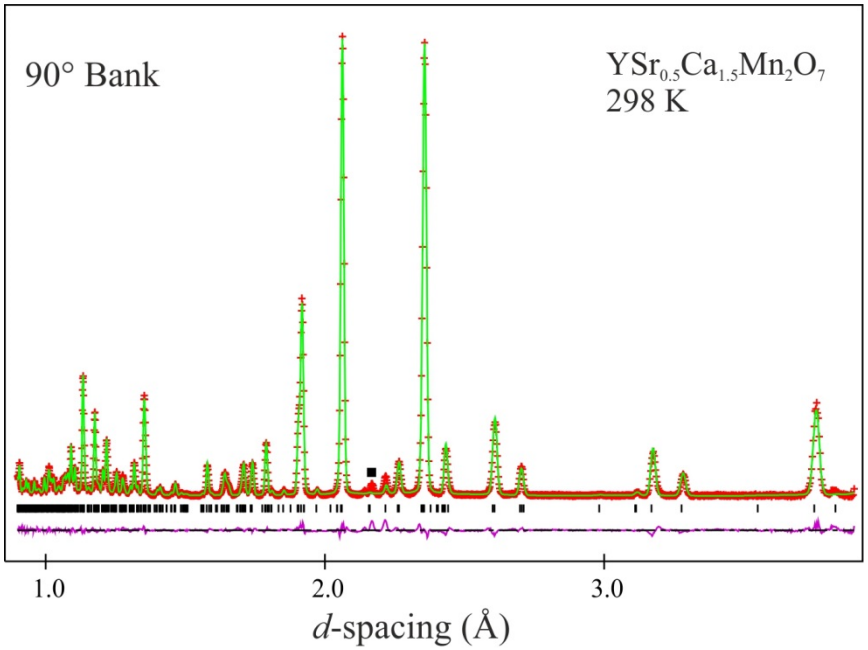


Figure 7.4. Observed, calculated and difference plots from the structural refinement of $YSr_{0.5}Ca_{1.5}Mn_2O_7$ by using *Pnnm* model against neutron powder diffraction data collected at room temperature by using HRPD diffractometer (ISIS, UK). The black square marks the diffraction peak from vanadium sample can ($d \approx 2.15$ Å).

Atom	**site**	***x***	***y***	***z***	**Fraction**	**U_{iso}(Å^2)**
Sr(1)/Ca(1)	4g	0.7534(11)	0.2506(9)	0	0.5/0.5	0.0032(2)
Y(1)/Ca(2)	8h	0.7625(6)	0.2332(4)	0.8176(1)	0.5/0.5	0.0032(2)
Mn(1)	8h	0.7475(16)	0.7507(12)	0.0998(1)	1	0.0010(4)
O(1)	8h	0.7844(7)	0.7991(6)	0.2017(1)	1	0.0112(5)
O(2)	4f	0	1/2	0.8953(3)	1	0.0094(15)
O(3)	4e	0	0	0.3815(1)	1	0.0083(8)
O(4)	4e	0	0	0.0878(1)	1	0.0095(8)
O(5)	4f	0	1/2	0.5985(3)	1	0.0094(16)
O(6)	4g	0.7159(10)	0.7052(8)	0	1	0.0116(6)
$YSr_{0.5}Ca_{1.5}Mn_2O_7$ space group: *Pnnm* *a* = 5.4143(1) Å *b* = 5.4291(1) Å *c* = 19.041(1) Å Volume = 559.74(3) Å^3 χ^2 = 10.62; *wRp*= 5.63 %; *Rp* = 5.43 %.						

Table 7.2. Structural parameters refined against neutron powder diffraction data collected at 300 K from $YSr_{0.5}Ca_{1.5}Mn_2O_7$.

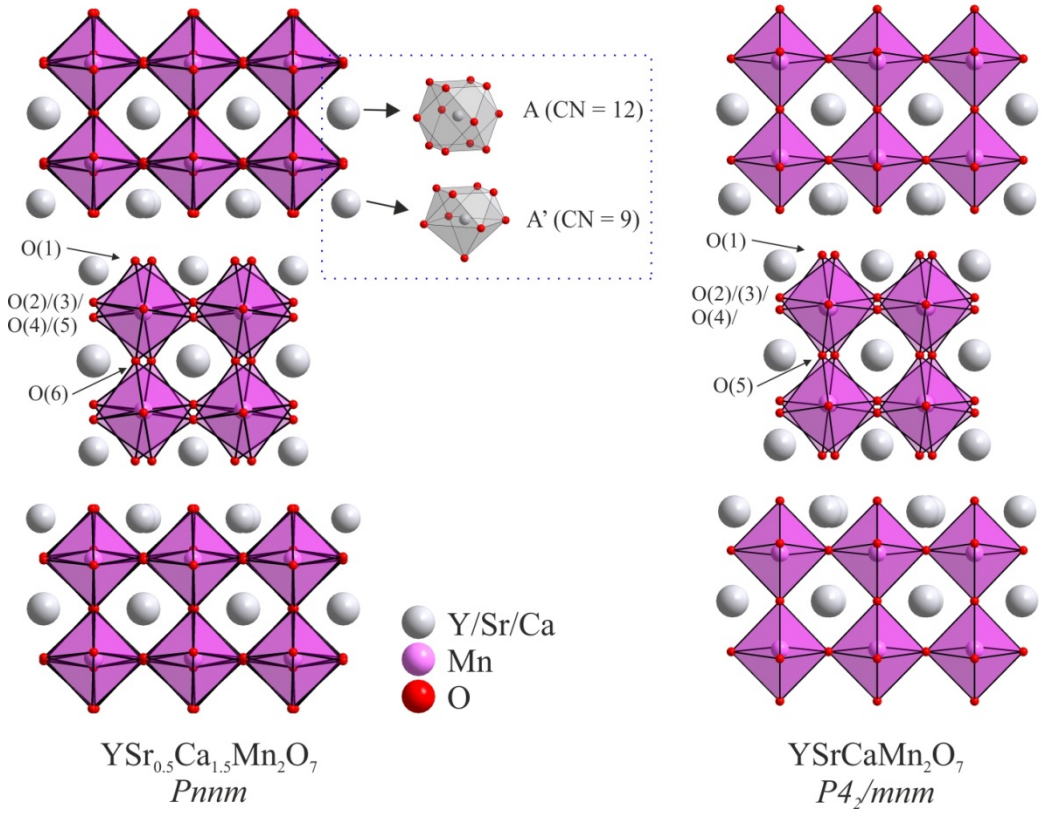


Figure 7.5. The labelling scheme for $YSrCaMn_2O_7$ (as well as $YSr_2Mn_2O_7$) and $YSr_{0.5}Ca_{1.5}Mn_2O_7$.

7.3.3 Structural refinement of $YSrCaMn_2O_7$

The tetragonal *P4₂/mnm* model adopted by $YSr_2Mn_2O_7$ was constructed and refined against neutron diffraction data collected from $YSrCaMn_2O_7$. The refinement proceeded smoothly and relatively good fitting statistics were obtained (χ^2 =16.50, wRp = 6.60 % and Rp = 6.40 %) as shown in Table 7.3. However, close inspection into the neutron diffraction data from the high resolution 168° bank reveals some diffraction peaks cannot be modelled satisfactorily due to their asymmetric peak shapes (Figure 7.6). This asymmetric peak shape cannot be accounted by (00*l*) dependent microstrain broadening. The (0,0,10) peak, particularly, cannot be modelled correctly by using any single phase model. This anomalous peak shape is also observed in other $LnSr_2Mn_2O_7$ series (Ln is lanthanide), as discussed in 7.2. A two-phase model within *P4₂/mnm* space group was thus constructed and refined against the neutron diffraction data. Significant improvement on the fit to the data was achieved (χ^2 = 5.686; *wRp*= 3.87%; *Rp* = 4.39%), compared to a single *P4₂/mnm* phase model (χ^2 = 16.50; *wRp*= 6.60%; *Rp* = 6.40%).

Moreover, the peak shapes were more satisfactorily modelled in a two-phase refinement as can be seen in Figure 7.6. Therefore, two phases are considered to coexist in $YSrCaMn_2O_7$.

As discussed in 7.2, this type of phase separation into two similar Ruddlesden-Popper phases could be found in $LnSr_2Mn_2O_7$ series (Ln is lanthanide) and might be described by scheme S1 or S2:

$$\mathbf{LnSr_2Mn_2O_7 \rightarrow Ln_{1+x}Sr_{2-x}Mn_2O_7 + Ln_{1-x}Sr_{2+x}Mn_2O_7 \quad (x \neq 0)} \quad \mathbf{S1}$$

$$\mathbf{LnSr_2Mn_2O_7 \rightarrow LnSr_2Mn_2O_7\ (I) + LnSr_2Mn_2O_7\ (II)} \quad \mathbf{S2}$$

In scheme S1, the two similar Ruddlesden-Popper phases differ in A-cation composition, while in scheme S2, they share the same composition but different A-cation distribution between the 9- and 12-coordinate A-sites. Two independent refinements were carried out to test which scheme to describe the $YSrCaMn_2O_7$ case.

Before any refinement, two assumptions were made: (1) Both phases were assumed to have a composition of $YSrCaMn_2O_7$; (2) All the A-cation sites were assumed to be occupied by strontium, meanwhile the occupancy of each A-cation site was set to the value of the mean scattering length scaled to that of Sr cation, as described by equation (1);

$$\frac{\overline{L}}{L_{Sr}} = \frac{L_{Sr}\times 1 + L_{Ca}\times 1 + L_Y \times 1}{3L_{Sr}} \qquad (1)$$

Where L_{Sr}, L_{Ca} and L_Y represent the neutron scattering lengths of Sr^{2+}, Ca^{2+} and Y^{3+} cations, the values of which are listed in Chapter 2, Table 2.1.

In one refinement (Refinement I), the occupancy of A-sites was allowed to refine freely from the original value ($\frac{\overline{L}}{L_{Sr}}$). In the other refinement (Refinement II), the occupancy of A-sites was refined conserving the original total scattering length. That is, in the latter case, the A-cations were only allowed to distribute over the two A-cation sites within the constraint of a composition of $YSrCaMn_2O_7$, while in Refinement I, no constraint was set such that compositions were allowed to vary. As a result, the A-site occupancies in both phases are the same (within error)

after Refinement I as those after Refinement II, as shown in Table 7.4. This indicates that the two phases have nearly the same composition of $YSrCaMn_2O_7$, but different A-site distributions, as could be described by scheme S2. The observation that the volumes of the two phases are almost identical (566.11(3) $Å^3$ and 566.79(1) $Å^3$) further supports the idea that this two phases have nearly the same composition. It is worth noting that during the refinement, the thermal factors of all the atoms in Phase I are constrained to be the same as the corresponding atoms in Phase II.

If all the Y^{3+} remain in the 9-coordination during the substitution of Sr^{2+} to Ca^{2+}, the Sr/Ca distribution over the two A-sites can be refined conserving the composition to be $YSrCaMn_2O_7$. The results as well as the refined lattice parameters of these two phases are shown in Table 7.5.

The orthorhombic *Pnnm* (adopted by $YSr_{0.5}Ca_{1.5}Mn_2O_7$) and *Amam* model were also constructed and refined against the neutron diffraction data collected from $YSrCaMn_2O_7$. The fitting statistics (Table 7.3) reveal that neither the *Pnnm* nor *Amam* model give better fitting statistics compared to the 2-phase *$P4_2/mnm$* model. Moreover, no obvious peak splitting was observed due to a lowering of the symmetry from tetragonal to orthorhombic space group, confirmin the tetragonal structure in space group *$P4_2/mnm$* adopted by $YSrCaMn_2O_7$.

Space Group	Tilt System	Glazer Tilt	χ^2	wRp (%)	Rp (%)
$P4_2/mnm$	Φ00/0Φ0	$a^-b^0c^0/\ b^0a^-c^0$	16.50	6.60	6.40
Pnnm	$\Phi_1\Phi_20/\Phi_2\Phi_10$	$a^-b^-c^0/\ b^-a^-c^0$	18.41	6.97	6.78
Amam	ΦΦ0/ΦΦ0	$a^-a^-c^0/\ a^-a^-c^0$	20.99	7.45	7.07
$P4_2/mnm$ (2-phase model)	Φ00/0Φ0	$a^-a^0c^0/\ a^0a^-c^0$	5.686	3.87	4.39

Table 7.3. Fitting statistics from the structural refinement of $YSrCaMn_2O_7$ using models based on the distortions of *n* = 2 Ruddlesden-Popper phases. Φ indicates an out of phase rotation; Ψ indicates an in-phase rotation.

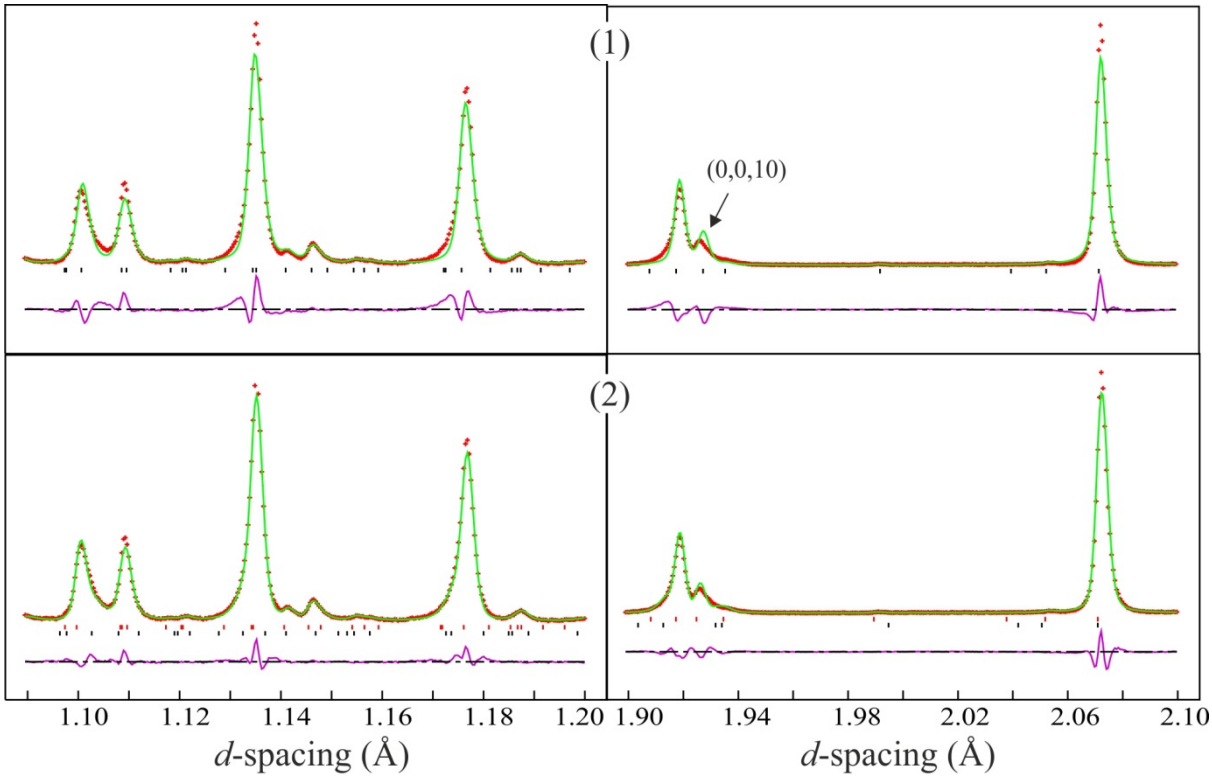


Figure 7.6. Observed, calculated and difference plots from the structural refinement of $YSrCaMn_2O_7$ by using *P4₂/mnm* model against neutron powder diffraction data (Bank 168°) collected at room temperature with HRPD diffractometer (ISIS, UK). The figures on the top are from refinement using a single phase model, while those on the bottom from refinement using two *P4₂/mnm* phases.

	Coordinate Sites	**Original value ($\frac{\bar{L}}{L_{Sr}}$) / %**	**Refinement I / %**	**Refinement II / %**
Phase I	12-	0.9245	0.923(11)	0.925(9)
	9-	0.9245	0.921(9)	0.924(4)
Phase II	12-	0.9245	0.965(6)	0.971(4)
	9-	0.9245	0.897(5)	0.901(2)

Table 7.4. The original value of the A-site occupancies and corresponding values after Refinement I and II in both phases.

Phase I						
Atom	**site**	***x***	***y***	***z***	**Fraction**	**U_{iso}(Å^2)**
Sr(1)/Ca(1)	4f	0.2542(8)	0.2542(8)	0	0.79(2)/0.20(2)	0.0062(4)
Y(1)/Sr(2)/ Ca(2)	8j	0.2654(5)	0.2654(5)	0.1823(2)	0.5/0.10(1)/ 0.39(1)	0.0039(3)
Mn(1)	8j	0.2568(12)	0.2568(12)	0.4018(3)	1	0.0012(2)
O(1)	8j	0.2168(8)	0.2168(8)	0.2966(2)	1	0.0145(3)
O(2)	8h	0	1/2	0.1029(3)	1	0.0101(3)
O(3)	4e	0	0	0.1168(4)	1	0.0082(4)
O(4)	4e	0	0	0.4075(4)	1	0.0081(4)
O(5)	4g	0.2216(9)	0.7783(9)	0	1	0.0093(4)
$YSrCaMn_2O_7$ space group: *$P4_2/mnm$* Phase Fraction: 34.1 % *a* = 5.4123(1) Å *b* = 5.4123(1) Å *c* = 19.325(1) Å Volume = 566.11(3) Å^3						
Phase II						
Atom	**site**	***x***	***y***	***z***	**Fraction**	**U_{iso}(Å^2)**
Sr(1)/Ca(1)	4f	0.2517(4)	0.2517(4)	0	0.91(1)/0.09(1)	0.0062(4)
Y(1)/Sr(2)/ Ca(2)	8j	0.2632(2)	0.2632(2)	0.1831(1)	0.5/0.04(1)/ 0.46(1)	0.0039(3)
Mn(1)	8j	0.2520(5)	0.2520(5)	0.3998(1)	1	0.0012(2)
O(1)	8j	0.2126(3)	0.2126(3)	0.2987(1)	1	0.0145(3)
O(2)	8h	0	1/2	0.1024(2)	1	0.0101(3)
O(3)	4e	0	0	0.1159(1)	1	0.0082(4)
O(4)	4e	0	0	0.4083(2)	1	0.0081(4)
O(5)	4g	0.2216(3)	0.7783 (4)	0	1	0.0093(4)
$YSrCaMn_2O_7$ space group: *$P4_2/mnm$* Phase Fraction: 65.8(1) % *a* = 5.4254(1) Å *b* = 5.4254(1) Å *c* = 19.255(1) Å Volume = 566.79(1) Å^3 χ^2 = 5.794; *wRp*= 3.91 %; *Rp* = 4.38 %.						

Table 7.5. Structural parameters refined against neutron powder diffraction data collected at 300 K from $YSrCaMn_2O_7$.

7.4 Discussion

7.4.1 A-cation substitution

An increasing amount of Ca^{2+} was doped into $YSr_2Mn_2O_7$, driving a change in the crystallographic structure from tetragonal symmetry in space group *$P4_2/mnm$* to orthorhombic

symmetry in space group *Pnnm*. The doped Ca^{2+} cations prefer to replace the Sr^{2+} residing in the smaller 9-coordinate sites. In $YSr_{0.5}Ca_{1.5}Mn_2O_7$, nearly all the Sr^{2+} cations in the 9-coordinate sites were replaced by Ca^{2+} as discussed previously in Section 7.3.2. In $YSrCaMn_2O_7$, the majority of the Ca^{2+} cations in Phase I and nearly all the Ca^{2+} cations in Phase II were located in 9-coordinate sites, as discussed in Section 7.3.3. The increasing amount of smaller A-cations in the rock salt layer (Ca^{2+} in this case) drives closer the adjacent manganese along the *c*-direction (both the interlayer and intralayer Mn-Mn distances are shorter compared to that of $YSr_2Mn_2O_7$). As a result, the *c*-lattice parameters of $YSr_{2-x}Ca_xMn_2O_7$ decrease significantly as the concentration of Ca^{2+} increases as shown in Figure 7.2. This significant decrease in c-lattice parameters led to a structural effect similar to that caused by the topochemical fluorination. That is, the dimension of the perovskite block (as defined in Chapter 4 Section 4.4.3) is noticeably compressed as shown in Figure 7.7. This compression resulted in a tightening of the Mn-O-Mn bond angles, especially the Mn-O_{axial}-Mn bond angles along the *c*-axis (Mn-O5-Mn in $YSr_2Mn_2O_7$ and $YSrCaMn_2O_7$, while the Mn-O6-Mn in $YSr_{0.5}Ca_{1.5}Mn_2O_7$) as listed in Table 7.6. The degree of the octahedron rotations about each axis, parameterized by the "in-plane" angle and 'torsion angle' between adjacent O_{apical}-O_{axial} bonds defined in Chapter 4 (Section 4.4.3), is also listed in Table 7.6. It reveals that the rotational distortions around *x*- and *y*-axes increase when Sr^{2+} are replaced by Ca^{2+} cations, from 3.6(1)º in $YSr_2Mn_2O_7$ to an average of 7.0(1)º in $YSrCaMn_2O_7$ and to 8.9(1)º in $YSr_{0.5}Ca_{1.5}Mn_2O_7$ around the *x*-axis, and from zero to 1.7(1)º in $YSr_{0.5}Ca_{1.5}Mn_2O_7$ around the *y*-axis.

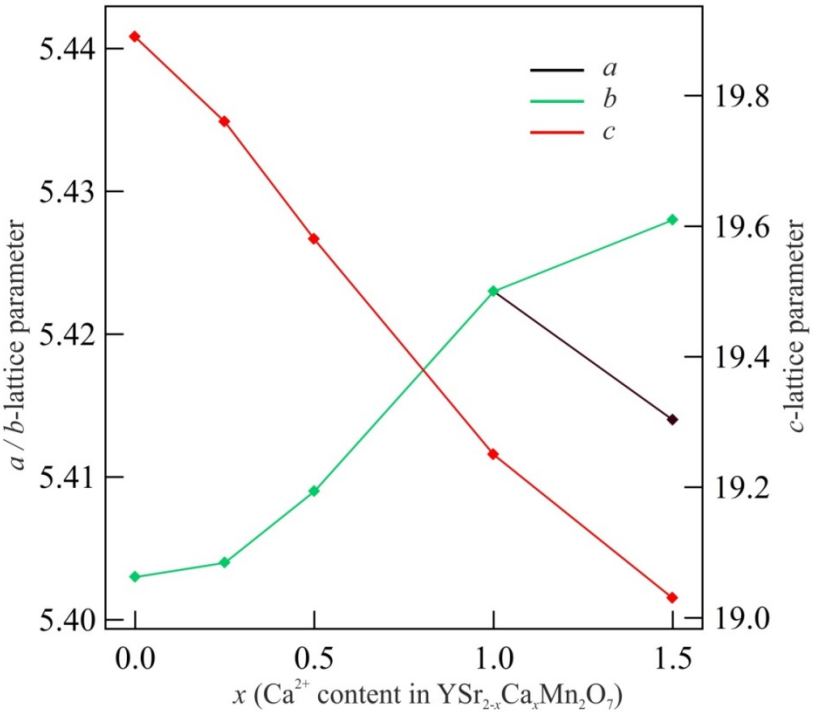


Figure 7.3. The change of lattice parameters in $YSr_{2-x}Ca_xMn_2O_7$ series (x = 0, 0.25, 0.5, 1.0 and 1.5).

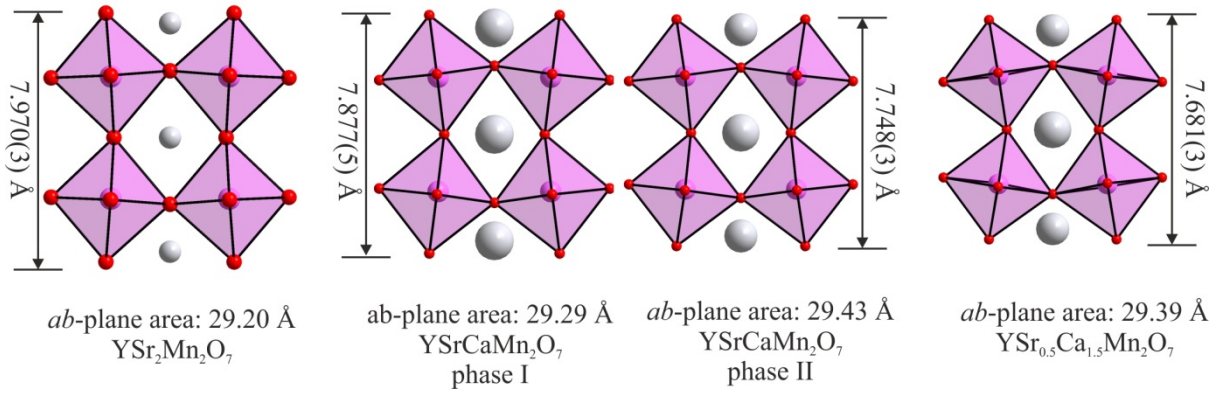


Figure 7.7. The dimensions of the perovskite block in $YSr_2Mn_2O_7$, $YSrCaMn_2O_7$ and $YSr_{0.5}Ca_{1.5}Mn_2O_7$.

	$YSr_2Mn_2O_7$ Bond length (Å)	$YSrCaMn_2O_7$ Bond length (Å)		$YSr_{0.5}Ca_{1.5}Mn_2O_7$ Bond length (Å)
		Phase I	**Phase II**	
Mn-O1	2.032(3)	2.056(7)	1.970(3)	1.968(3)
Mn-O2	1.911(5)	1.916(7)	1.919(3)	1.931(8)
Mn-O3	1.912(5)	1.896(7)	1.927(3)	1.943(8)
Mn-O4	1.919(5)	1.969(7)	1.940(3)	1.937(8)
Mn-O5	1.961(2)	1.905(6)	1.940(2)	1.905(8)
Mn-O6				1.924(2)
	Mn-Mn Distance (Å)	**Mn-Mn Distance (Å)**	**Mn-Mn Distance (Å)**	**Mn-Mn Distance (Å)**
Interlayer Mn-Mn	6.613(4)	6.462(8)	6.375(3)	6.328(6)
Intralayer Mn-Mn along *c*-axis	3.917(3)	3.795(8)	3.859(3)	3.801(3)
Average Intralayer Mn-Mn along *ab*-plane	3.814(8)	3.827(9)	3.836(3)	3.842(11)
	Bond angle (°)	**Bond angle (°)**	**Bond angle (°)**	**Bond angle (°)**
Mn-O2-Mn	177.97(23)	174.57(33)	177.70(18)	174.46(33)
Mn-O3-Mn	169.24(23)	158.14(38)	161.95(12)	158.88(27)
Mn-O4-Mn	177.27(23)	173.58(37)	170.32(17)	166.45(27)
Mn-O5-Mn	174.15(8)	170.06(36)	168.04(14)	178.51(34)
Mn-O6-Mn				162.03(36)
	Octahedron rotation angle (º)	**Octahedron rotation angle (º)**	**Octahedron rotation angle (º)**	**Octahedron rotation angle (º)**
x-axis	3.6(1)	6.7(1)	7.3(1)	8.9 (1)
y-axis	0	0	0	1.7(1)
z-axis	0	0	0	0

Table 7.6. Selected bond lengths and angles from refined structures of $YSr_2Mn_2O_7$, $YSrCaMn_2O_7$ and $YSr_{0.5}Ca_{1.5}Mn_2O_7$ at 298 K.

7.4.2 The *Pnnm* distortion

As stated at the beginning, substitution of smaller cations onto the A-cation site should drive the framework to adopt increasingly distorted arrangements (tolerance factor *t* becomes

smaller). This statement is proved by the observation that the substitution of Sr^{2+} to Ca^{2+} cations led to an increase in the magnitude of rotational distortions around the *x*-axis, and induced a rotational distortion around the *y*-axis in $YSr_{0.5}Ca_{1.5}Mn_2O_7$. It is observed that lowering the symmetry from *P4₂/mnm* ($a^-b^0c^0/b^0a^-c^0$) by A-cation substitution does not result into the *Amam* ($a^-a^-c^0/a^-a^-c^0$) symmetry. Instead, a phase with *Pnnm* ($a^-b^-c^0/b^-a^-c^0$, $a \neq b$) symmetry was obtained. This suggests that the rotational distortion around the *y*-axis increases in magnitude continually, from no distortion ('b^0') in *P4₂/mnm* to a magnitude of non-zero ('b^-', $a \neq b$) distortion in *Pnnm*, and then hypothetically to a magnitude of ('a^-', $a = b$) in *Amam*, as shown in Figure 7.8.

The A-cation substitution in $YSr_{2-x}Ca_xMn_2O_7$ induces a rotational distortion about the *y*-axis with a magnitude of 1.7(1)º in $YSr_{0.5}Ca_{1.5}Mn_2O_7$, while increasing the existing rotational distortion about the *x*-axis from a magnitude of 3.6(1)º in $YSr_2Mn_2O_7$ to 8.9(1)º in $YSr_{0.5}Ca_{1.5}Mn_2O_7$, as shown in Table 7.6. If taking the $La_3Ni_2O_7$ with an *Amam* distortion as a comparison, one could observe that the octahedron ration angle about *x*- and *y*-axes in $La_3Ni_2O_7$ has an average magnitude of 4.9(1)º as shown in Chapter 6, Table 6.5. It is reasonable to propose that it would be more and more difficult to stabilize that *Pnnm* distortion if the rotational angle about *y*-axis keeps increasing, which eventually would leads to the *Amam* distortion. This novel *Pnnm* distortion ($a^-b^-c^0/b^-a^-c^0$, $a \neq b$) could thus be seen as an intermediate in structural change from *P4₂/mnm* to *Amam*.

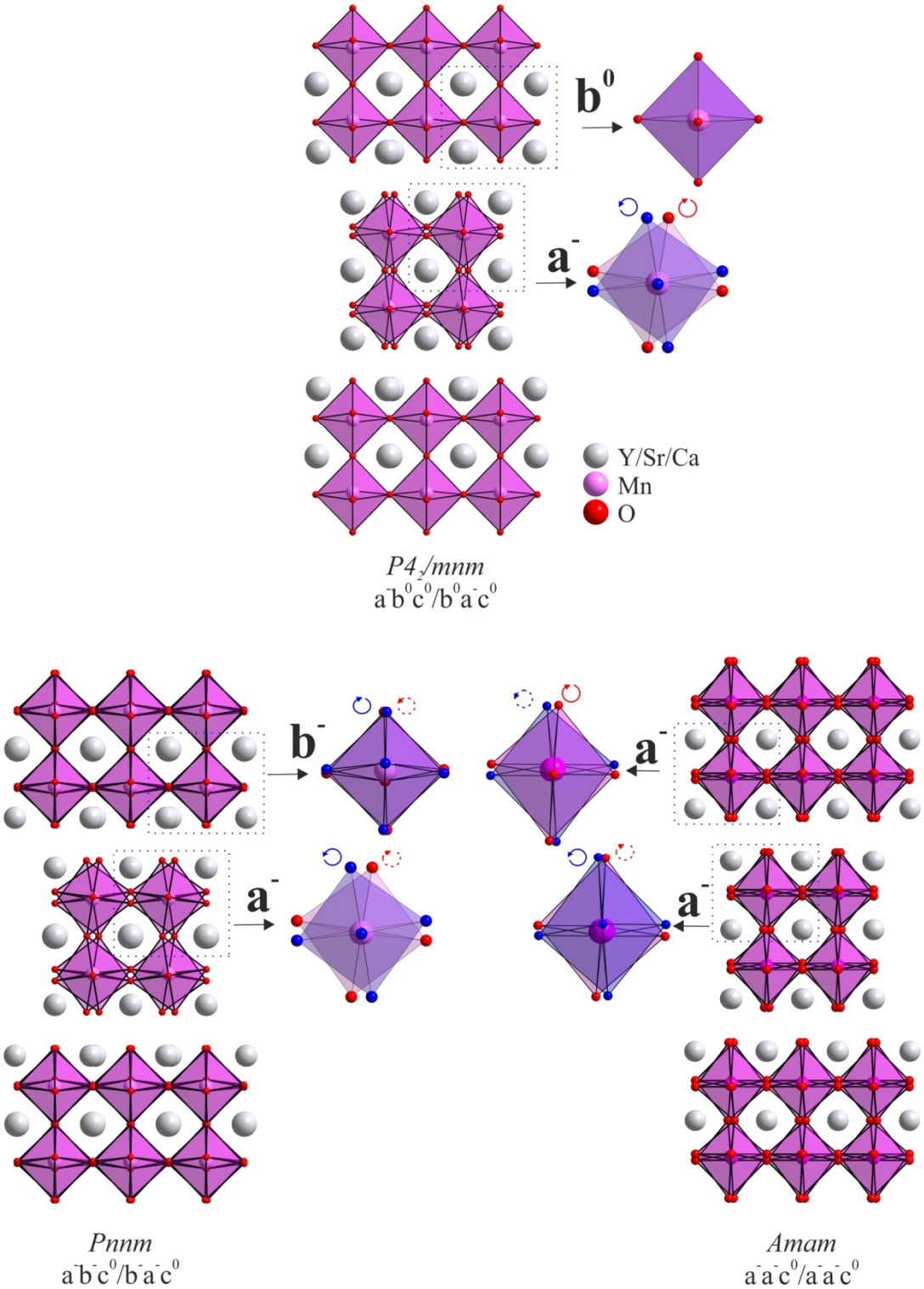


Figure 7.8. The *P4₂/mnm*, *Pnnm* and *Amam* structures.

7.5 Magnetization data of $YSr_{2-x}Ca_xMn_2O_7$

Magnetization data collected from $YSr_{2-x}Ca_xMn_2O_7$ (x = 0, 1 and 1.5) in an applied field of 100 Oe are shown in Figure 7.9. The divergence between zero-field cooled and field cooled data suggests a canted antiferromagnetic behaviour below $T_N \approx 15$ K for $YSr_2Mn_2O_7$, below $T_N \approx 35$ K for $YSr_{0.5}Ca_{1.5}Mn_2O_7$. For $YSrCaMn_2O_7$, two magnetic features could be observe at temperature range of $10 < T_N/K < 50$ and $50 < T_N/K < 100$, consistent with the discussion that there are two phases in $YSrCaMn_2O_7$.

The substitution of Sr^{2+} with smaller Ca^{2+} cations in A-sites results in a smaller overall tolerance factor in $YSr_{0.5}Ca_{1.5}Mn_2O_7$ compared to that of $YSr_2Mn_2O_7$, which is further supported by the tighter Mn-O-Mn bond angles in $YSr_{0.5}Ca_{1.5}Mn_2O_7$ compared to that of $YSr_2Mn_2O_7$. A poorer overlapping of the transition metal *d*-orbitals, resulting from a tighter Mn-O-Mn bond angle, weakens the superexchange interaction and hence gives a lower T_N. One would thus expect that the magnetic ordering temperature (T_N) of $YSr_{0.5}Ca_{1.5}Mn_2O_7$ would be lower than that of $YSr_2Mn_2O_7$. However, an unexpected higher T_N was observed in $YSr_{0.5}Ca_{1.5}Mn_2O_7$ as shown in Figure 7.9. This opposite t-T_N trend (a smaller $t < 1$ results in a higher T_N) is also observed in $La_{2-x}Sr_{1+x}Cr_2O_7$ (x = 0, 0.2, 0.3) and $La_2Sr_{0.5}Ca_{0.5}Cr_2O_7$ as discussed in Chapter 5, Section 5.4.2. One reasonable explanation is that the mean distance between adjacent Mn cations is shortened in $YSr_{0.5}Ca_{1.5}Mn_2O_7$ than that in $YSr_2Mn_2O_7$, especially the distances between adjacent interlayer Mn cations. In Ruddlesden-Popper phases, the magnetic interaction between the interlayer B-cation centres is weaker since the superexchange interaction weakens by distance. This weak interaction thus defines the magnetic ordering temperature. The closer distance in two adjacent unlinked interlayer Mn cations in $La_2Sr_{0.5}Ca_{0.5}Cr_2O_7$ strengthens the magnetic interaction, thus improves T_N greatly.

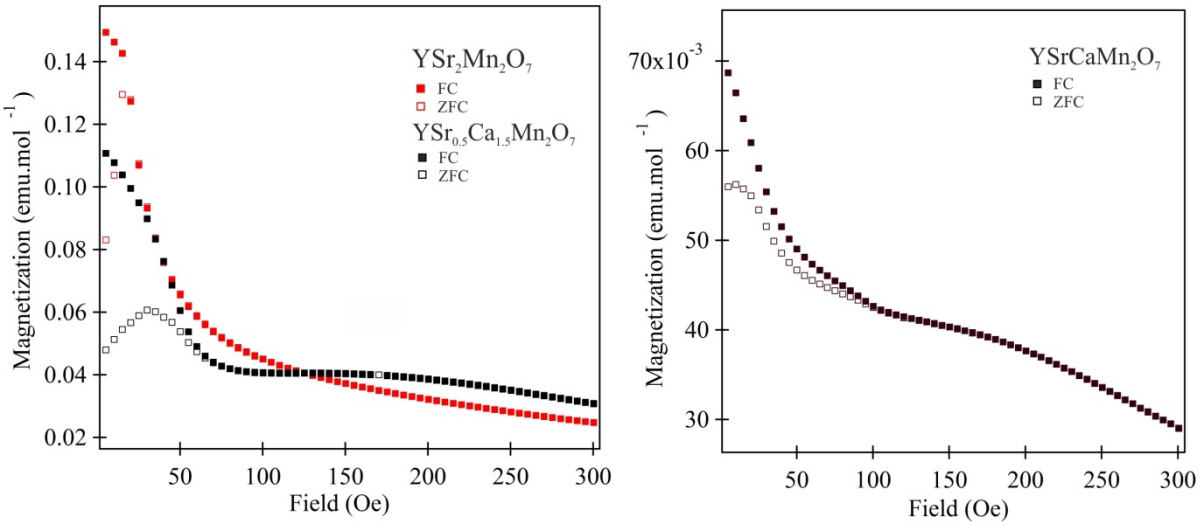


Figure 7.9. Zero-field cooled and field-cooled magnetization data collected as a function of temperature from $YSr_{2-x}Ca_xMn_2O_7$ (x = 0, 1 and 1.5) in an applied filed of 100 Oe.

7.6 Conclusion

The substitution of Sr^{2+} with Ca^{2+} cations in $YSr_2Mn_2O_7$ led to an increasing distortion of the metal-oxide framework, resulting in the formation of an orthorhombic symmetry in space group *Pnnm* adopted by $YSr_{0.5}Ca_{1.5}Mn_2O_7$. This novel *Pnnm* distortion ($a^-b^-c^0/b^-a^-c^0$, $a \neq b$) can be seen as an intermediate in structural change from *P4₂/mnm* ($a^-b^0c^0/b^0a^-c^0$) to *Amam* ($a^-a^-c^0/a^-a^-c^0$).

Chapter 8: Topochemical fluorination of $YSr_2Mn_2O_7$ to $YSr_2Mn_2O_{5.5}F_{3.5}$ and $YSr_2Mn_2O_{6.4}F_{1.5}$

8.1 Introduction

As discussed in Chapter 6, the fluorination of $La_3Ni_2O_7$ introduces a cooperative octahedral tilt around the crystallographic *z*-axis, driving a structural change from an *Amam*, $a^-a^-c^0/a^-a^-c^0$ lattice distortion in $La_3Ni_2O_7$ to a *Pnam* $a^-a^-c^+/a^-a^-(c^+)$ lattice distortion in the $La_3Ni_2O_{5.5}F_{3.5}$ oxide-fluoride phase. In this chapter, the fluorination of $YSr_2Mn_2O_7$ with the *P4₂/mnm* $(a^-b^0c^0/b^0a^-c^0)$ distortion is investigated. If a cooperative octahedral tilt around the crystallographic *z*-axis is induced in $YSr_2Mn_2O_7$ with the *P4₂/mnm* $(a^-b^0c^0/b^0a^-c^0)$ distortion on fluorination, the fluorinated phase can potentially adopt a polar phase in space group *P2₁nm* with the $(a^-b^0c^+/b^0a^-c^+)$ distortion.

In addition, the novel $YSr_{0.5}Ca_{1.5}Mn_2O_7$ phase with the *Pnnm* $(a^-b^-c^0/b^-a^-c^0)$ as discussed in Chapter 7 is also discussed in this chapter.

8.2 Experimental

$YSr_2Mn_2O_7$ and $YSr_{0.5}Ca_{1.5}Mn_2O_7$ were prepared via the citrate gel method as described in Chapter 7. Fluorination of $YSr_2Mn_2O_7$ and $YSr_{0.5}Ca_{1.5}Mn_2O_7$ was performed using CuF_2 as a fluorination agent as described in the fluorination of $La_2SrCr_2O_7$ in Chapter 4. To avoid contamination of the samples with CuO which occurs when mixing the CuF_2 with mixed directly into the sample, the CuF_2 was heated separately from the sample as described in Chapter 4. The CuF_2 was heated at 500 °C under flowing oxygen to liberate fluorine. The resulting O_2/F_2 gas mixture was then passed over a sample of $YSr_2Mn_2O_7$ or $YSr_{0.5}Ca_{1.5}Mn_2O_7$ powder, held at 400 °C in an adjacent furnace (see Chapter 2, Figure 2.1). Samples were then treated at this temperature for four periods of 48 h, with the CuF_2 reagent being replaced between heating periods. For the fluorination of $YSr_2Mn_2O_7$, a single phase was obtained after the above treatment.

For the fluorination of $YSr_{0.5}Ca_{1.5}Mn_2O_7$, a mixture of $YSr_{0.5}Ca_{1.5}Mn_2O_7$ and $YSr_{0.5}Ca_{1.5}Mn_2O_xF_y$ was obtained. Significant amounts of $YSr_{0.5}Ca_{1.5}Mn_2O_7$ remained in the product after another three periods of 48 h at 400 °C. Raising the reaction temperature led to a decomposition of the product into binary fluorides.

The intermediate $YSr_2Mn_2O_{6.4}F_{1.5}$ was prepared by grinding together suitable amount of $YSr_2Mn_2O_7$ and $YSr_2Mn_2O_xF_y$.The resulting powder was heated in sealed silica ampules at 400 °C for 7 periods of 3 days. Suitable amounts of $YSr_2Mn_2O_7$ were added in between each heating cycle, until a relatively phase pure sample was obtained.

8.3 Results

8.3.1 X-ray powder diffraction data of $YSr_2Mn_2O_{5.5}F_{3.5}$, $YSr_2Mn_2O_{6.4}F_{1.5}$ and $YSr_{0.5}Ca_{1.5}Mn_2O_xF_y$

8.3.1.1 X-ray diffraction data of $YSr_2Mn_2O_{5.5}F_{3.5}$ and $YSr_2Mn_2O_{6.4}F_{1.5}$

The X-ray powder diffraction data collected from fluorinated samples at different reaction stages during the fluorination process revealed a new phase forming with a larger *c*-lattice parameter relative to the starting material as the (115) peak shifted to larger *d*-spacing, similar to the fluorination of $La_2SrCr_2O_7$. This fluorinated phase can be indexed by using a tetragonal unit cell with lattice parameters of a = 5.325(1) Å, c = 22.63 (1) Å, consistent with the formation of a topochemical fluorinated compound, $YSr_2Mn_2O_{5.5}F_{3.5}$.

During the fluorination of $YSr_2Mn_2O_7$, extra peaks were observed in the powder x-ray diffraction data that couldn't be indexed to either $YSr_2Mn_2O_7$ or the fluorinated phase $YSr_2Mn_2O_{5.5}F_{3.5}$. This unidentified phase (marked in Figure 8.1) was considered as an intermediate phase with lower fluorine content in the rock salt layer compared to $YSr_2Mn_2O_{5.5}F_{3.5}$. The average composition of the intermediate phase was later confirmed to be $YSr_2Mn_2O_{6.4}F_{1.5}$ as discussed in Section 8.3.4. The observation of an intermediate phase with low fluorine content is

not unprecedented, and was observed in the fluorination of $LaSrMnO_4$ (Chapter 1 Section 1.5) and $La_3Ni_2O_7$ (Chapter 6 Section 6.3.1).

The intermediate phase, $YSr_2Mn_2O_{6.4}F_{1.5}$, was obtained by annealing a mixture of suitable amount of the $YSr_2Mn_2O_7$ and fully fluorinated $YSr_2Mn_2O_{5.5}F_{3.5}$, as described in Section 8.2. The X-ray powder diffraction data collected from the annealed product revealed a new phase forming with a tetragonal unit cell with lattice parameters of a = 5.398(1) Å, c = 20.80(1) Å. The c-lattice parameter of this intermediate phase falls right in between that of $YSr_2Mn_2O_7$ (c = 19.89(1) Å) and fully fluorinated $YSr_2Mn_2O_xF_y$ (c = 22.63(1) Å).

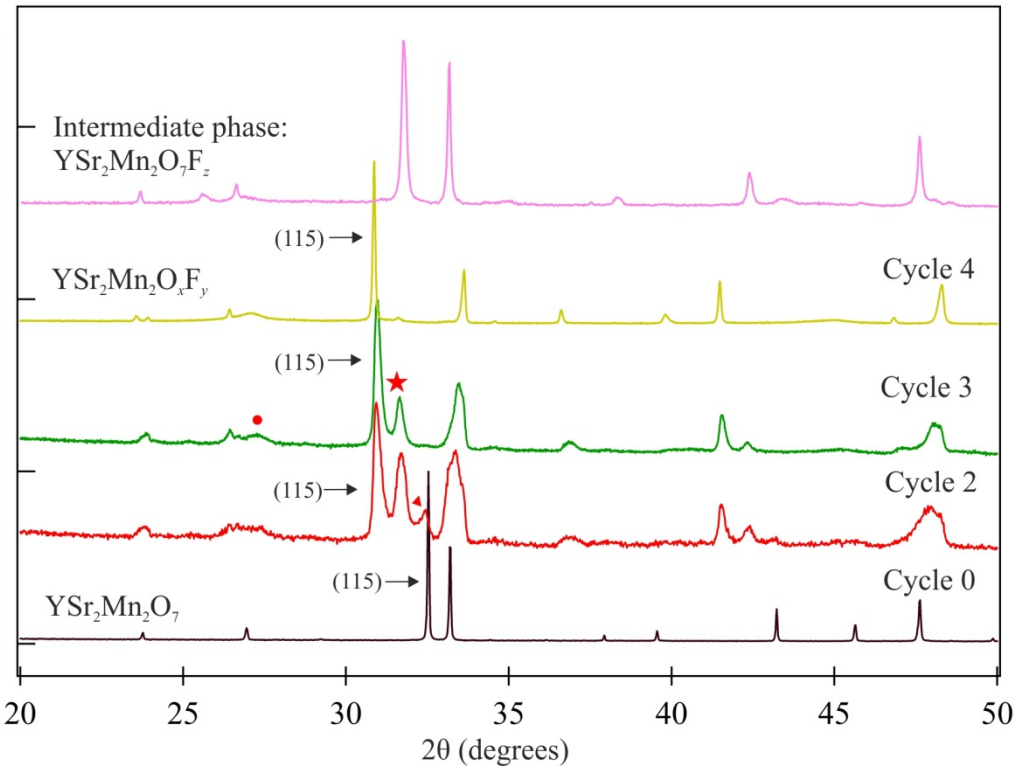


Figure 8.1. The evolution of the sample at different reaction stages during the fluorination of $YSr_2Mn_2O_7$. Each cycle indicates a heating cycle of 2 days under conditions described in 8.2. The red star denotes the peak that belongs to an intermediate phase; the red triangle denotes the peak of starting oxide $YSr_2Mn_2O_7$; the red circle denotes the binary fluorides (CaF_2 or SrF_2).

8.3.1.2 X-ray diffraction data of $YSr_{0.5}Ca_{1.5}Mn_2O_xF_y$

The fluorination of $YSr_{0.5}Ca_{1.5}Mn_2O_7$ with *Pnnm* structure (as discussed in Chapter 7) was carried out. However, a single fluorinated phase failed to be obtained. A considerable

amount of starting material $YSr_{0.5}Ca_{1.5}Mn_2O_7$ remains in the product, as can be seen in Figure 8.2. The reason for this incomplete of the reaction is still not known.

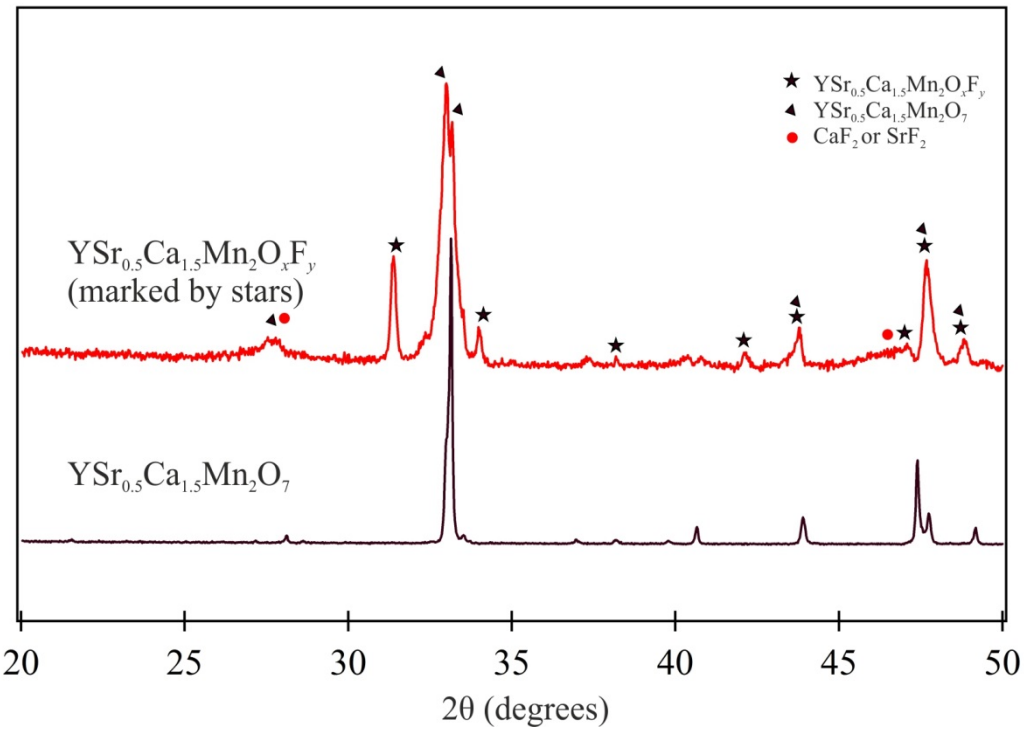


Figure 8.2. The fluorination of $YSr_{0.5}Ca_{1.5}Mn_2O_7$.

8.3.2 Compositional characterization of fully fluorinated product $YSr_2Mn_2O_xF_y$ ($YSr_2Mn_2O_{5.5}F_{3.5}$) by iodometric titration

Iodometric titrations were carried out to determine the oxidation state of the manganese in the fully fluorinated product $YSr_2Mn_2O_xF_y$. The detailed procedure is described in Chapter 2 (Section 1.2). In this series of titrations, a 1:2 (v/v) ratio of hydrochloric acid to distilled water was used to dissolve the samples. Titrations on $YSr_2Mn_2O_7$ were also carried out as a reference. The reaction during the titration could be described as following scheme:

$$\mathbf{Mn(2+x) + H^+ + xI^- \rightarrow Mn(2) + \frac{x}{2}I_2} \qquad \mathbf{S1}$$

$$\mathbf{\frac{x}{2}I_2 + xS_2O_3^{2-} \rightarrow xI^- + \frac{x}{2}S_4O_6^{2-}} \qquad \mathbf{S2}$$

Thus the overall reaction could be described as:

$$\mathbf{Mn(2+x) + xS_2O_3^{2-} \rightarrow Mn(2) + \frac{x}{2}S_4O_6^{2-}} \qquad \mathbf{S3}$$

The oxidation state of Mn in $YSr_2Mn_2O_xF_y$ was determined as +3.75(3). Crystallographic characterization of the $YSr_2Mn_2O_xF_y$ phase, described below in Section 8.3.3, indicated that all anion sites were fully occupied and thus $x + y = 9$, as observed for other fluorinated $n = 2$ Ruddlesden-Popper phases.[26,106,109,110] Thus the composition of $YSr_2Mn_2O_xF_y$ was determined to be $YSr_2Mn_2O_{5.5}F_{3.5}$.

Sample	Mass (mg)	$c_{Na_2S_2O_4}$ (10^{-3} mol/L)	$V_{Na_2S_2O_4}$(mL)	Oxidation state of Mn^{n+}	Mean Mn^{n+}
$YSr_2Mn_2O_7$	35.2	4.519	48.5	3.515	3.50(1)
$YSr_2Mn_2O_7$	30.5		41.8	3.507	
$YSr_2Mn_2O_7$	27.6		37.7	3.501	
$YSr_2Mn_2O_xF_y$	28.6		41.7	3.741	3.75(3)
$YSr_2Mn_2O_xF_y$	29.7		43.5	3.774	
$YSr_2Mn_2O_xF_y$	32.5		47.1	3.730	

Table 8.1. Results of titrations on $YSr_2Mn_2O_7$ and $YSr_2Mn_2O_xF_y$.

8.3.3 Structural refinement of $YSr_2Mn_2O_{5.5}F_{3.5}$

Neutron powder diffraction data collected from $YSr_2Mn_2O_{5.5}F_{3.5}$ can be indexed using a tetragonal unit cell with lattice parameters similar to that observed from X-ray diffraction data. The *P4₂/mnm* model constructed based on the structure of the parent oxide $YSr_2Mn_2O_7$ was refined against the neutron diffraction data collected from $YSr_2Mn_2O_{5.5}F_{3.5}$ at room temperature by using HRPD diffractometer. During the refinement, the Y/Sr distributions over the 9- and 12-coordinate A-sites were fixed at the values observed for the cation-ordered $YSr_2Mn_2O_7$ parent phase with all other atomic positional and displacement parameters allowed to refine freely. The oxygen/fluorine anion distributions were not considered in this stage since their neutron scattering lengths are strikingly similar (O = 5.80 fm, F = 5.65 fm), and all the anion sites were considered to be fully occupied.

Other models with orthorhombic symmetry such as *Pnnm* and *Amam* were also constructed and refined against the neutron diffraction data collected from $YSr_2Mn_2O_{5.5}F_{3.5}$, though no obvious peak splitting was observed due to a lowering of the symmetry from tetragonal to orthorhombic space group. As shown in Table 8.3, the tetragonal *P4₂/mnm* model

gives the best statistical fit to the data. Moreover, the *a*-lattice parameter was refined to the same value as *b*-lattice parameter within error (a = 5.3274(10) Å ≈ b = 5.3272(10) Å) confirming a tetragonal symmetry adopted by $YSr_2Mn_2O_{5.5}F_{3.5}$. It is thus reasonable to conclude that the tetragonal *P4₂/mnm* model best describes $YSr_2Mn_2O_{5.5}F_{3.5}$.

Plots of the observed and calculated data are shown in Figure 8.3. The detailed structural parameters of the refined model are given in Table 8.2. In the end of the refinement, the occupancy of each anion site was set to be refined freely. It turned out that all the anion sites were fully occupied within error.

Atom	**site**	***x***	***y***	***z***	**Fraction**	**U_{iso}(Å^2)**
Sr(1)	4f	0.2521(20)	0.2521(20)	0	1	0.0139(8)
Y(1)/Sr(2)	8j	0.2439(13)	0.2439(13)	0.1813(1)	0.5/0.5	0.0139(8)
Mn(1)	8j	0.2528(22)	0.2528(22)	0.4143(3)	1	0.010(10)
O(1)	8j	0.2252(18)	0.2252(18)	0.3321(2)	1	0.054(29)
O(2)	8h	0	1/2	0.0827(4)	1	0.012(1)
O(3)	4e	0	0	0.0823(6)	1	0.034(4)
O(4)	4e	0	0	0.4002(6)	1	0.037(5)
O(5)	4g	0.2466(20)	0.7533(20)	0	1	0.004(1)
F(1)	4e	1/2	1/2	0.2482(10)	1	0.069(7)
F(2)	4d	0	1/2	1/4	1	0.041(4)
$YSr_2Mn_2O_{5.5}F_{3.5}$ space group: *P4₂/mnm* *a* = 5.3266(1) Å *c* = 22.634(1) Å Volume = 642.19(6) Å^3 χ^2 = 5.438; *wRp* = 4.95 %; *Rp* = 4.53 %.						

Table 8.2. Structural parameters refined against neutron powder diffraction data collected at 300 K from $YSr_2Mn_2O_{5.5}F_{3.5}$ by using HRPD diffractometer (UK, ISIS).

Space Group	Tilt System	Glazer Tilt	χ^2	wRp (%)	Rp (%)
P4₂/mnm	Φ00/0Φ0	$a^-b^0c^0/b^0a^-c^0$	5.43	4.95	4.53
Pnnm	$\Phi_1\Phi_2 0/\Phi_2\Phi_1 0$	$a^-b^-c^0/b^-a^-c^0$	7.54	5.83	5.13
Amam	ΦΦ0/ΦΦ0	$a^-a^-c^0/a^-a^-c^0$	5.99	5.2	5.07

Table 8.3. Fitting statistics from the structural refinement of $YSr_2Mn_2O_{5.5}F_{3.5}$ using models based on the distortions of n = 2 Ruddlesden-Popper phases. Φ indicates an out of phase rotation; Ψ indicates an in-phase rotation.

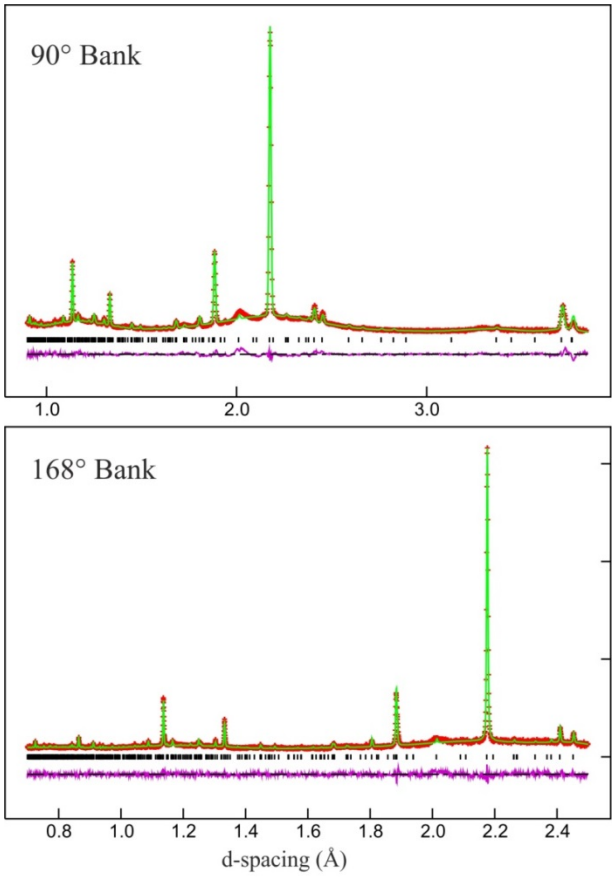


Figure 8.3. Observed, calculated and difference plots from the structural refinement of $YSr_{0.5}Ca_{1.5}Mn_2O_7$ by using *Pnnm* model against neutron powder diffraction data collected at room temperature by using HRPD diffractometer (ISIS, UK). The broad diffraction peak at $d \approx 2.15$ Å is from vanadium sample can.

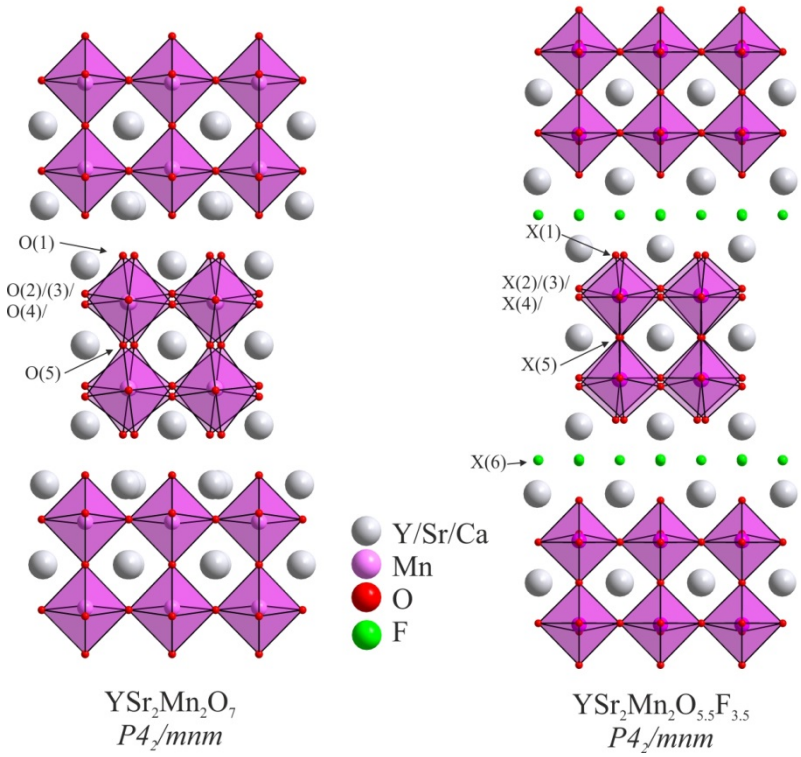


Figure 8.5. The labelling scheme of phases discussed in this chapter.

8.3.4 Compositional characterization of staged phase $YSr_2Mn_2O_{7-\delta}F_z$ ($YSr_2Mn_2O_{6.4}F_{1.5}$).

Iodometric titrations were carried out to determine the oxidation state of the manganese in the staged fluorinated product $YSr_2Mn_2O_{7-\delta}F_z$. The detailed titration procedure was described in Chapter 2 (Section 2.6). In this series of titrations, a 1:2 (v/v) ratio of hydrochloric acid to distilled water was used to dissolve the samples. The reaction during the titration could be described as scheme S1, S2 and S3 as stated earlier in Section 8.3.2. The average oxidation state of Mn in $YSr_2Mn_2O_{7-\delta}F_z$ was determined as +3.66(3). However, crystallographic characterization of the $YSr_2Mn_2O_{7-\delta}F_z$ phase, described below in Section 8.3.5, suggests the presence of anion vacancies. Thus the composition of $YSr_2Mn_2O_{7-\delta}F_z$ is still ambiguous as it could not be deduced from the oxidation state of Mn alone.

During the preparation, a 1:1.22 mass ratio of $YSr_2Mn_2O_7$ to $YSr_2Mn_2O_{5.5}F_{3.5}$ was used to prepare the staged phase $YSr_2Mn_2O_{7-\delta}F_z$. As this reaction was carried out in sealed silica ampules, the law of conservation of mass and stoichiometry should apply. This combined with the oxidation state of Mn (+3.66(3)) by iodometric titration gives a composition of $YSr_2Mn_2O_{6.4}F_{1.5}$.

Sample	Mass (mg)	$c_{Na_2S_2O_4}$ (10^{-3} mol/L)	$V_{Na_2S_2O_4}$(mL)	Oxidation state of Mn^{n+}	Mean Mn^{n+}
$YSr_2Mn_2O_{7-\delta}F_z$	25.7	4.519	36.9	3.674	3.66(3)
$YSr_2Mn_2O_{7-\delta}F_z$	20.0		28.4	3.635	
$YSr_2Mn_2O_{7-\delta}F_z$	25.4		36.6	3.687	

Table 8.4. Results of titrations on $YSr_2Mn_2O_{7-\delta}F_z$.

8.3.5 Structural refinement of $YSr_2Mn_2O_{6.4}F_{1.5}$

As discussed in Section 8.3.1.1, the X-ray powder diffraction data collected from the intermediate phase, $YSr_2Mn_2O_{6.4}F_{1.5}$, can be indexed into a tetragonal unit cell with lattice of a = 5.398(1) Å, c = 20.80(1) Å. The $P\bar{4}2_1m$ model with tetragonal symmetry was constructed based on lowering the symmetry of the *P4₂/mnm* model adopted by $YSr_2Mn_2O_7$ as well as $YSr_2Mn_2O_{5.5}F_{3.5}$. During the refinement, the Y/Sr A-cation distributions were fixed at the values observed for the cation-ordered $YSr_2Mn_2O_7$ parent phase with all other atomic positional and

displacement parameters allowed to refine freely. The oxygen/fluorine anion distribution was not considered since their neutron scattering lengths are strikingly similar. The refinement using $P\bar{4}2_1m$ proceeds smoothly, giving relatively good fitting statistics with χ^2 = 7.826, *wRp* = 5.71 % and *Rp* = 5.68 %.

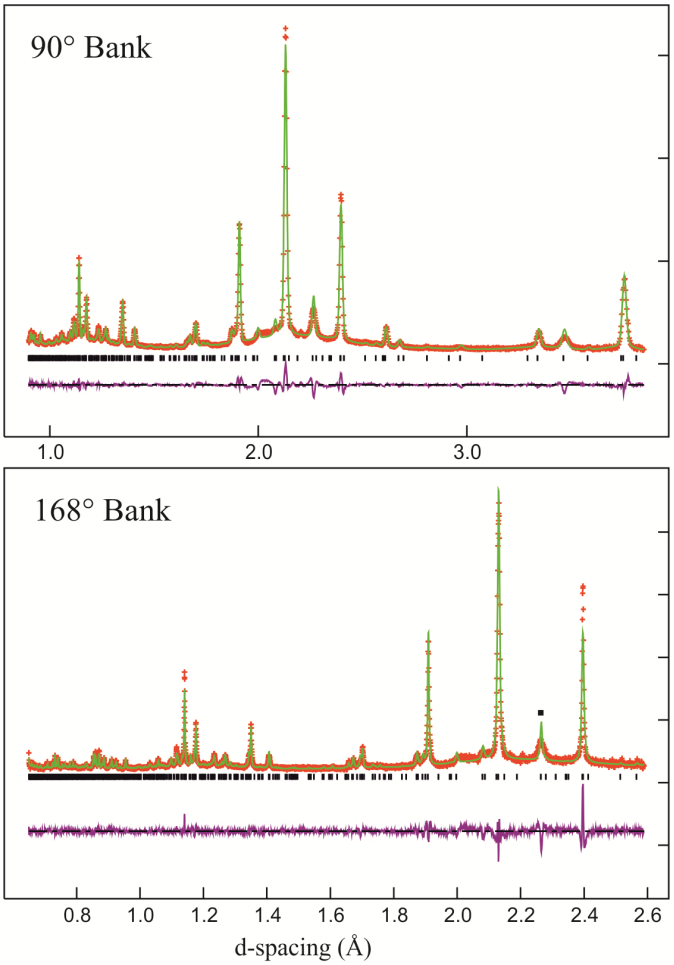


Figure 8.6. Observed, calculated and difference plots from the structural refinement of $YSr_2Mn_2O_{6.4}F_{1.5}$ by using $P\bar{4}2_1m$ model against neutron powder diffraction data collected at room temperature by using HRPD diffractometer (ISIS, UK).

However, close inspection of the neutron diffraction data of $YSr_2Mn_2O_{6.4}F_{1.5}$, especially data from high angle banks, reveals some broad peaks that cannot be described correctly by using the $P\bar{4}2_1m$ model. High resolution synchrotron X-ray diffraction data were thus collected from $YSr_2Mn_2O_{6.4}F_{1.5}$. As shown in Figure 8.7, an unexpected splitting of the (00*l*) diffraction peaks were observed, suggesting that these data cannot be modelled satisfactory by a single phase. The

presence of more than one phase in combination with the nonstoichiometric feature of $YSr_2Mn_2O_{6.4}F_{1.5}$ makes a detailed analysis of the crystal structure of $YSr_2Mn_2O_{6.4}F_{1.5}$ very challenging. The structure of this intermediate phase (or these intermediate phases) remains unclear.

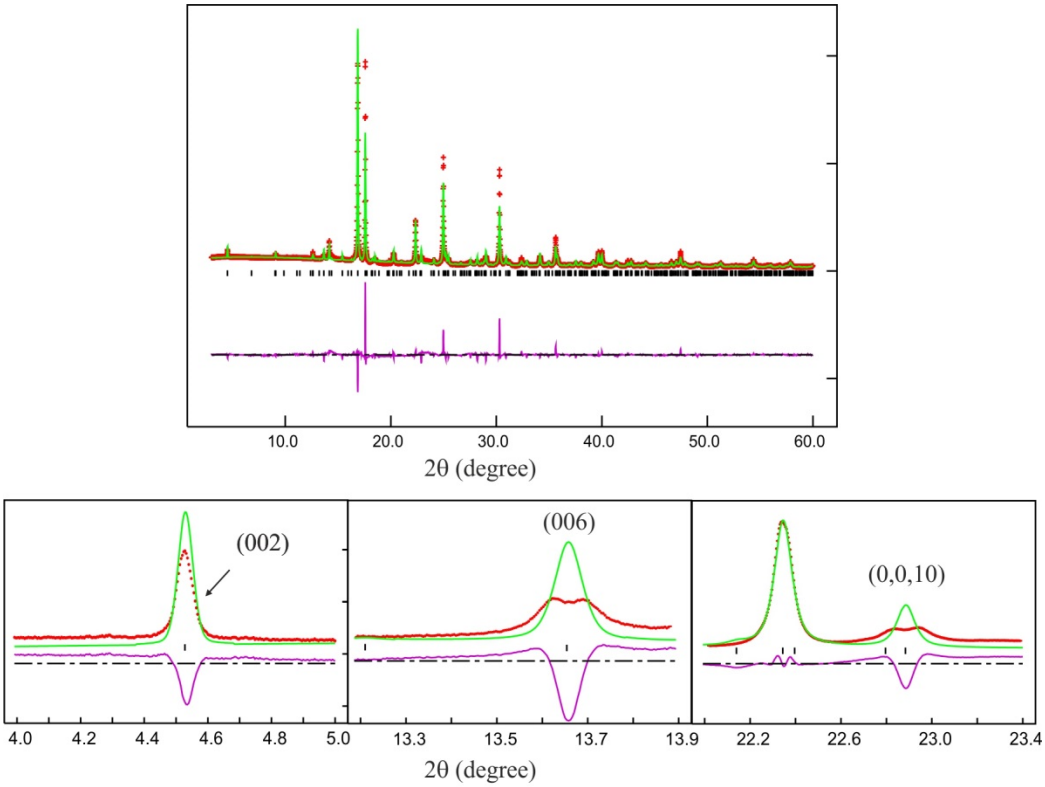


Figure 8.7. Observed, calculated and difference plots from the structural refinement of $YSr_2Mn_2O_{6.4}F_{1.5}$ by using $P\bar{4}2_1m$ model against the synchrotron X-ray diffraction data collected at room temperature at I11 (Diamond, UK).

8.4 Discussion

8.4.1 The fluorination chemistry and the anion distribution in $YSr_2Mn_2O_{5.5}F_{3.5}$

Heating $YSr_2Mn_2O_7$ under an F_2/O_2 flow leads to the formation of a fully fluorinated phase, whose composition was confirmed to be $YSr_2Mn_2O_{5.5}F_{3.5}$ by the iodometric titration as discussed in 8.3.2. Similar to the fluorination of $La_3Ni_2O_7$ as discussed in Chapter 6, the average manganese oxidation state only rises slightly up to $Mn^{+3.75}$ in $YSr_2Mn_2O_{5.5}F_{3.5}$ from $Mn^{+3.5}$ in $YSr_2Mn_2O_7$, indicating a high level of fluoride-oxide anion exchange on fluorination of $YSr_2Mn_2O_7$. As X-ray and neutron diffraction scattering lengths of fluoride anions both differ

only slightly with that of oxide anions, the anion distribution in fluorinated phases cannot be determined by the diffraction data alone. Thus the bond valence sums (BVS) discussed earlier in Chapter 2 Section 2.9 as well as Chapter 4 and 6 were used for examining locations of the fluoride anions.

$YSr_2Mn_2O_7$		**$YSr_2Mn_2O_{5.5}F_{3.5}$**		
Anion	**BVS (O)**	**Anion**	**BVS (O)**	**BVS (F)**
O(1)	1.893	X (1)/25% O^{2-}/75% F^-	1.659	1.443
O(2)	2.329	X(2)/O(1)	2.125	1.962
O(3)	2.346	X(3)/O(3)	2.213	2.048
O(4)	2.335	X(4)/O(4)	1.932	1.938
O(5)	1.852	X(5)/O(5)	2.153	1.937
		X(6)/F(1)	1.669	1.277

Table 8.5. Anion bond valence sums from $YSr_2Mn_2O_7$ and $YSr_2Mn_2O_{5.5}F_{3.5}$; the labelling scheme is shown below in Figure 8.5.

Table 8.5 lists the bond valence sums (BVS) of the anions sites for the 6 crystallographically distinct anion sites in the structure of $YSr_2Mn_2O_{5.5}F_{3.5}$. These BVS were calculated by supposing the sites were exclusively occupied by either oxide or fluoride anions The BVS of corresponding anion sites in the structure of $YSr_2Mn_2O_7$ were also calculated for comparison. The anion site labeling scheme is shown in Figure 8.5. These data reveal that the two smallest BVS values were calculated from the tetragonal interstitial anion site X(6) and the apical anion site X(1), consistent with the occupation of fluoride ions. Occupation of the tetragonal interstitial anion site exclusively by fluoride ions is commonly observed in other topochemically fluorinated n = 2 Ruddlesden-popper phases, including the $La_2SrCr_2O_7F_2$ and $La_3Ni_2O_{5.5}F_{3.5}$ phases discussed in this thesis in Chapter 4 and Chapter 6 respectively. The small value of BVS from anion site X(1) suggests that fluoride anions exchange preferentially with the apical oxide anions in the existing parent framework, resulting in an anion distribution of 75% F^-:25% O^{2-} in this X(1) site. Partial occupation of the apical anion site X(1) by fluoride anions is also not

uncommon. It has been reported previously for $Sr_3(Fe_{0.5}Ru_{0.5})_2O_{5.5}F_{3.5}$ and was discussed in this thesis in Chapter 6.

8.4.2 Structural modification by topochemical fluorination from $YSr_2Mn_2O_7$ to $YSr_2Mn_2O_{5.5}F_{3.5}$

Similar to the fluorination of $La_2SrCr_2O_7$ and $La_3Ni_2O_7$ discussed in Chapter 4 and 6 respectively, the fluorination of $YSr_2Mn_2O_7$ causes two structural effects: 1) a significant increase in the *c*-lattice parameter and 2) a dramatic compression of the perovskite layers within the phase. On fluorination, the *c*-lattice parameter increases from 19.905(1) Å in $YSr_2Mn_2O_7$ to 22.634(1) Å in $YSr_2Mn_2O_{5.5}F_{3.5}$. Despite this increase, the *c*-dimension of the double perovskite (defined in Chapter 4, Section 4.4.2) decreases from 7.970(3) Å in $YSr_2Mn_2O_7$ to 7.601(6) Å in $YSr_2Mn_2O_{5.5}F_{3.5}$, as shown in Figure 8.8. This compression of the perovskite layers along the *z*-axis is presumably caused by enhanced anion-anion repulsions resulting from the insertion of fluoride ions.

As discussed earlier in Chapter 6, the fluorination of $La_3Ni_2O_7$ leads to an enhancement of the structural distortion exhibited by the oxide starting material ($La_3Ni_2O_7$), introducing a cooperative octahedral tilt around the crystallographic *z*-axis, driving a structural change from an *Amam*, $a^-a^-c^0/a^-a^-c^0$ lattice distortion in $La_3Ni_2O_7$ to a *Pnam* $a^-a^-c^+/a^-a^-(c^+)$ lattice distortion in the $La_3Ni_2O_{5.5}F_{3.5}$ oxide-fluoride phase. Similarly fluorination of $Sr_3(Mn_{0.5}Ru_{0.5})_2O_7$ to $Sr_3(Mn_{0.5}Ru_{0.5})_2O_7F_2$ drives a change from the aristotype $a^0a^0c^0/\ a^0a^0c^0$, *I4/mmm* framework to a $a^0a^0c^-/\ a^0a^0c^-$, *Acaa* distorted lattice.[106] Fluorination of $Sr_3Ru_2O_7$ also drives a disordered twisting of the RuO_6 octahedra around the *z*-axis to yield an $a^0a^0c^{+/-}\ a^0a^0c^{+/-}$ distorted structure for $Sr_3Ru_2O_7F_2$. Therefore, it is reasonable to expect that a cooperative octahedral tilt around the crystallographic *z*-axis should be induced on fluorination of $YSr_2Mn_2O_7$ (space group: *P4₂/mnm*). However, Rietveld refinements discussed in Section 8.3.3 suggest that the fluorinated phase, $YSr_2Mn_2O_{5.5}F_{3.5}$, retains *P4₂/mnm* ($a^-b^0c^0/b^0a^-c^0$) symmetry with no octahedral tilt around the *z*-

axis. This is probably because unlike $La_3Ni_2O_7$, $Sr_3(Mn_{0.5}Ru_{0.5})_2O_7$ and $Sr_3Ru_2O_7$, the presence of two A-cations differing greatly in radius in $YSr_2Mn_2O_7$ gives rise to A-cation ordering over the 9- and 12-coordinate A-sites within the Ruddlesden-Popper structure. As reported, the bigger 12-coordinate A-sites in $YSr_2Mn_2O_7$ are exclusively occupied by Sr^{2+}. This A-cation ordering is not likely to be disrupted at low temperatures for fluorination reactions. Thus the A-cations in $YSr_2Mn_2O_{5.5}F_{3.5}$ should remain ordered over the 9- and 12-coordinate A-sites. As discussed in Chapter 3 Section 3.4.3 and 3.4.4, n = 2 Ruddlesden-Popper phases with 'normal' A-cation ordering (placing larger A-cations on the larger 12-coordinate perovskite A-site) favour crystal structures with high symmetry. For example, $La_2SrFe_2O_7$ with a 53:47 Sr:La ratio on the perovskite A-site adopts an undistorted *I*4/*mmm* structure.[5] Likewise $La_2BaFe_2O_7$ with a 73:37 Ba:La ratio on the perovskite A-site also adopts an undistorted *I*4/*mmm* structure.[5] Neither of these two phases exhibits any collective rotations of their FeO_6 octahedra. In contrast, as discussed in Chapter 3, $La_2SrCr_2O_7$ with unusual A-cation distributions by placing smaller La^{3+} on the larger perovskite A-site adopts a monoclinic, highly distorted *A2/a* structure. Therefore, 2-tilt ($a^-b^0c^+/b^0a^-c^+$) or ($a^-b^0c^-/b^0a^-c^-$) symmetry, that contains extra distortions around the crystallographic *z*-axis than 1-tilt *P4₂/mnm* ($a^-b^0c^0/b^0a^-c^0$) symmetry, is not favoured by the A-cation ordered $YSr_2Mn_2O_{5.5}F_{3.5}$ phase. As a result, unlike fluorination of $La_3Ni_2O_7$, $Sr_3(Mn_{0.5}Ru_{0.5})_2O_7$ and $Sr_3Ru_2O_7$, in which a cooperative octahedral tilt around the crystallographic *z*-axis was induced in their fluorinated phases, the fluorinated phase of $YSr_2Mn_2O_7$, $YSr_2Mn_2O_{5.5}F_{3.5}$, remains 1-tilt *P4₂/mnm* ($a^-b^0c^0/b^0a^-c^0$) symmetry with no octahedral tilt around the *z*-axis.

As discussed earlier, the fluorination of $YSr_2Mn_2O_7$ leads to a dramatic compression of the perovskite layer along the *z*-axis. Lattice strains caused by this compression would be released if cooperative tilting and twisting distortions were introduced to the apex-linked MnO_6 octahedra. However, as discussed above, the cation ordered $YSr_2Mn_2O_{5.5}F_{3.5}$ phase favours to

adopt a 1-tilt *P4₂/mnm* structure. This tendency of remaining in relatively high symmetry resulting from the A-cation ordering in $YSr_2Mn_2O_{5.5}F_{3.5}$ leads to a poor Mn-O bonding environment in each MnO_6 unit. Fortunately, in $YSr_2Mn_2O_{5.5}F_{3.5}$ with mixed valences of Mn^{3+} and Mn^{4+}, the occupation of e_g antibonding orbitals in Mn^{3+} with $t_{2g}^3e_g^1$ electronic configuration lowers the ligand-field stabilization energy (LFSE), which helps stabilize the uneven M-O bonding in $YSr_2Mn_2O_{5.5}F_{3.5}$ when adopting the 1-tilt *P4₂/mnm* symmetry. In contrast, as discussed in Chapter 3 Section 3.4.4, $La_2SrCr_2O_7$ with Cr^{3+} ($t_{2g}^3e_g^0$) favours locating Cr^{3+} in an even, highly symmetric bonding environment. This combined with the unusual A-cation distribution leads to the adoption of a highly distorted 3-tilt structure observed for $La_2SrCr_2O_7$.

A similar case can be found in the fluorination of cation-ordered $La_2BaFe_2O_7$ with a 73:37 Ba:La ratio on the perovskite A-site, which adopts an undistorted *I*4/*mmm* structure[5]. This undistorted *I*4/*mmm* symmetry remains in the fluorinated phase, $La_2BaFe_2O_5F_4$.[24] This provides further support to the hypothesis that high symmetry is preferred by A-cation ordered phases and stabilized by the lowering of LFSE when e_g antibonding orbitals are occupied (Fe^{3+}, $t_{2g}^3e_g^2$).

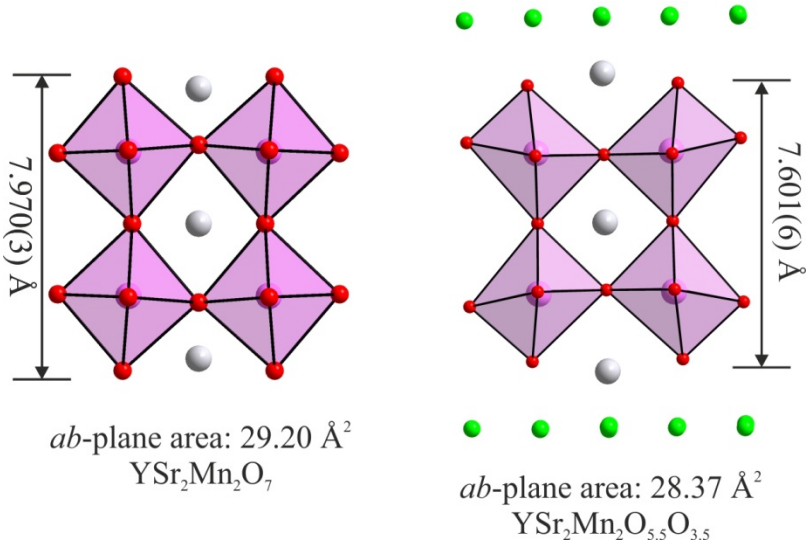


Figure 8.8. The dimensions of the perovskite block in $YSr_2Mn_2O_7$, and $YSr_2Mn_2O_{5.5}F_{3.5}$.

Selected bond lengths and angles from the refined structure of $YSr_2Mn_2O_7$ and $YSr_2Mn_2O_{5.5}F_{3.5}$ are listed in Table 8.4 and the labelling scheme is shown in Figure 8.5. From Table 8.4, it can be observed that Mn shifts away from the centre of an octahedron in

$YSr_2Mn_2O_{5.5}F_{3.5}$, since the Mn-O5-Mn and Mn-O3-Mn bond angles differ greatly from the corresponding O1-O5-O1 and O4-O3-O4 angles. If taking these O1-O5-O1 and O4-O3-O4 bond angles into account, it can be observed from Table 8.4 that, in common with the fluorination of other fluorinated phases discussed in this thesis, the fluorination of $YSr_2Mn_2O_7$ leads to more distorted MO_6 octahedra in $YSr_2Mn_2O_{5.5}F_{3.5}$.

	$YSr_2Mn_2O_7$ Bond length (Å)	**$YSr_2Mn_2O_{5.5}F_{3.5}$ Bond length (Å)**
Mn-O1	2.032(3)	1.872(8)
Mn-O2	1.911(5)	1.885(12)
Mn-O3	1.912(5)	1.864(12)
Mn-O4	1.919(5)	1.931(12)
Mn-O5	1.961(2)	1.940(7)
	Bond angle (°)	**Bond angle (°)**
Mn-O2-Mn	177.97(23)	175.87(55)
Mn-O3-Mn	169.24(23)	175.27(66)
O4-O3-O4	173.26(23)	167.99(29)
Mn-O4-Mn	177.27(23)	160.97(63)
Mn-O5-Mn	174.15(8)	179.75(67)
O1-O5-O1	172.60(8)	173.61(32)

Table 8.4. Selected bond lengths and angles from the refined structure of $YSr_2Mn_2O_7$ and $YSr_2Mn_2O_{5.5}F_{3.5}$. Labelling scheme is shown in Figure 8.5.

8.5 Conclusion

The fluorination of $YSr_2Mn_2O_7$ leads to the formation of a fully fluorinated phase, $YSr_2Mn_2O_{5.5}F_{3.5,}$ as well as staged phases with an average composition of $YSr_2Mn_2O_{6.4}F_{1.5}$. The fluorination of $YSr_2Mn_2O_7$ to $YSr_2Mn_2O_{5.5}F_{3.5}$ leads to a dramatic compression of the perovskite layer along the *z*-axis. However, unlike the fluorination of $La_3Ni_2O_7$ which introduces a cooperative octahedral tilt around the crystallographic *z*-axis, the fluorinated phase $YSr_2Mn_2O_{5.5}F_{3.5}$ remains $P4_2/mnm$ with the ($a^-b^0c^0/b^0a^-c^0$) distortion as adopted by the parent oxide $YSr_2Mn_2O_7$. This preference of relatively high symmetry is driven by the A-cation ordering over the 9- and 12-coordinate A-sites in $YSr_2Mn_2O_{5.5}F_{3.5}$.

Chapter 9: Conclusion

This thesis describes the characterization of some n = 2 Ruddlesden-Popper oxide phases ($A_3B_2O_7$; A = La, Y, Sr or Ca; B = Cr, Ni or Mn) and their topochemically fluorinated phases.

$La_2SrCr_2O_7$ was initially prepared to act as a substrate for a topochemical fluorination study focused on synthesizing phases containing Cr^{4+}, as described in Chapter 4. However, detailed analysis of the structure of $La_2SrCr_2O_7$ revealed a novel interaction which couples the A-site La/Sr cation distribution to the ordered twisting distortions of the CrO_6 octahedra. As discussed in Chapter 3, $La_2SrCr_2O_7$ adopts an *A2/a* ($a^-a^-c^-/a^-a^-c^-$) distorted structure with an unusual Sr/La distribution (the 12-coordinate A-sites of $La_2SrCr_2O_7$ are occupied by 82(2)% La^{3+} and 18(2)% Sr^{2+}). DFT calculations performed on $La_2SrCr_2O_7$ suggest that this unusual Sr/La distribution is driven by the desire to reduce the charge difference between the La-O rock salt and Sr-O perovskite layers. Meanwhile, this unusual Sr/La distribution locally breaks symmetry about the equatorial oxygens, allowing them to displace and the CrO_6 units to rotate. This promotes the O_{eq} and Cr bonding environments to be optimized. The energy gain from the charge equalization and the improvement of bonding environments drives $La_2SrCr_2O_7$ to adopt the *A2/a* ($a^-a^-c^-/a^-a^-c^-$) distorted structure with unusual Sr/La distributions.

As discussed in Chapter 4, topochemical fluorination of $La_2SrCr_2O_7$ yields $La_2SrCr_2O_7F_2$ with octahedrally coordinated Cr^{4+} centres. The insertion of the fluorine anions results in a significant compression of the perovskite block along the *z*-axis within the structure, leading to enhanced $a^-a^-c^-/a^-a^-c^-$ distortion as adopted by $La_2SrCr_2O_7F_2$. The tighter Cr-O-Cr bond angles in $La_2SrCr_2O_7F_2$ suggest weakened interactions between adjacent Cr cations, and therefore a lower antiferromagnetic ordering temperature. As a result $La_2SrCr_2O_7F_2$ lies further from the crossover for insulating to metallic behaviour than many other Cr^{4+} oxide phases.

The A-site doping in $La_2SrCr_2O_7$ for the preparation of $La_{2-x}Sr_{1+x}Cr_2O_7$ (x = 0.2, 0.3) and $La_2Sr_{0.5}Ca_{0.5}Cr_2O_7$ is discussed in Chapter 4. These non-stoichiometric phases adopt a similar

distorted *A2/a* ($a^-a^-c^-/a^-a^-c^-$) structure with the unusual A-site distribution over the 12- and 9-coordinate A-sites as described for $La_2SrCr_2O_7$. In $La_2Sr_{0.5}Ca_{0.5}Cr_2O_7$, the doped Ca^{2+} cations prefer the smaller 9-coordinate A-sites, which further proves that the principal driver for the unusual distribution of the La and Sr cations is the desire to lower the charge difference between the La-O rock salt and Sr-O perovskite layers. $La_{2-x}Sr_{1+x}Cr_2O_7F_2$ (x = 0.2, 0.3) behaves in a similar manner to $La_2SrCr_2O_7F_2$. Their magnetic ordering temperatures are T_N ~ 120 K and 100 K respectively.

The topochemical fluorination of $La_2SrCr_2O_7$ where the fluorination enhances the tilting magnitude of the $a^-a^-c^-/a^-a^-c^-$ distortion, together with the previous report on the fluorination of $Sr_3(Mn_{0.5}Ru_{0.5})_2O_7$ where the fluorination drives a structural change from *I4/mmm* ($a^0a^0c^0/ a^0a^0c^0$) to Acaa ($a^0a^0c^-/ a^0a^0c^-$), inspires us to investigate the fluorination of $La_3Ni_2O_7$ to examine if this could drive a structural change from *Amam* ($a^-a^-c^+/ a^-a^-c^+$) to the highly desired ferroelectric $A2_1am$ ($a^-a^-c^+/ a^-a^-c^+$) structure. As discussed in Chapter 6, topochemical fluorination of $La_3Ni_2O_7$ yields $La_3Ni_2O_{5.5}F_{3.5}$. The fluorination enhances the structural distortion exhibited by $La_3Ni_2O_7$, driving a structural change from an *Amam* lattice distortion to an antiferroelectric *Pnam* ($a^-a^-c^+/a^-a^-(c^+)$) lattice distortion in $La_3Ni_2O_{5.5}F_{3.5}$, rather than the polar $A2_1am$ ($a^-a^-c^+/ a^-a^-c^+$) distortion. The introduction of a cooperative octahedral tilt around the crystallographic *z*-axis leads to a local breaking of the inversion symmetry of the host lattice on fluorination. The global inversion symmetry of the lattice is retained in $La_3Ni_2O_{5.5}F_{3.5}$ due to an alternation in the *z*-tilt direction in adjacent perovskite sheets.

The research on the structural change driven by topochemical fluorination of phases with *Amam* ($a^-a^-c^0/a^-a^-c^0$) lattice distortion is hindered by the difficulties in finding other suitable, previously reported n = 2 Ruddlesden-Popper structures with *Amam* symmetry. Therefore, Chapter 7 investigates if a new n = 2 Ruddlesden-Popper phase with *Amam* ($a^-a^-c^0/a^-a^-c^0$) lattice distortion could be prepared by lowering the tolerance factor of the existing phase, $YSr_2Mn_2O_7$,

with *P4₂/mnm* ($a^-b^0c^0/b^0a^-c^0$) lattice distortion. As a result, the substitution of Sr^{2+} with Ca^{2+} cations in $YSr_2Mn_2O_7$ drives an increasing distortion of the metal-oxide framework, leading to the formation of an orthorhombic symmetry in space group *Pnnm* adopted by $YSr_{0.5}Ca_{1.5}Mn_2O_7$. This novel *Pnnm* ($a^-b^-c^0/b^-a^-c^0$, $a \neq b$) lattice distortion can be seen as an intermediate in structural change from *P4₂/mnm* ($a^-b^0c^0/b^0a^-c^0$) to *Amam* ($a^-a^-c^0/a^-a^-c^0$). However, as noted in Chapter 8, fluorination of $YSr_{0.5}Ca_{1.5}Mn_2O_7$ with *Pnnm* structure has not been studied as a single fluorinated phase cannot be obtained.

The introduction of a cooperative octahedral tilt around the crystallographic *z*-axis in the fluorinated phase $La_3Ni_2O_{5.5}F_{3.5}$ inspires us to investigate if the fluorination of $YSr_2Mn_2O_7$ could drive a structural change from *P4₂/mnm* ($a^-b^0c^0/b^0a^-c^0$) lattice distortion to the ferroelectric *P2₁nm* ($a^-b^0c^+/b^0a^-c^+$) lattice distortion. As concluded from Chapter 8, however, no structural change on fluorination was observed and the fluorinated phase $YSr_2Mn_2O_{5.5}F_{3.5}$ still adopts the *P4₂/mnm* ($a^-b^0c^0/b^0a^-c^0$) lattice distortion. This preference of retaining relatively high symmetry is driven by the A-cation ordering over the 9- and 12-coordinate A-sites in $YSr_2Mn_2O_{5.5}F_{3.5}$. The poor Mn-O bonding in each MnO_6 unit in $YSr_2Mn_2O_{5.5}F_{3.5}$ resulting from the adoption of the 1-tilt *P4₂/mnm* symmetry is compensated by the lowering of the ligand-field stabilization energy (LFSE) when the e_g antibonding orbitals are occupied (Mn^{3+}, $t_{2g}^3e_g^1$).

In conclusion, this whole course of investigation suggests that 1) topochemical fluorination is an attractive method to modify the rotational distortion of the CrO_6 octahedra in Ruddlesden-Popper phases by introducing a cooperative octahedral tilt around the crystallographic *z*-axis to the existing lattice framework; 2) the cooperative, symmetry-lowering distortions of $n = 2$ Ruddlesden-Popper phases are not solely directed by the structural tolerance factor, but determined by a combination of different parameters including the A-cation distribution over two different A-sites within the structure.

Appendix

Chapter 3

A3.1 Structural Models

All the structural models refined against the neutron powder diffraction data were based on the symmetry analysis by Aleksandrov and Bartolome (see Chapter 1 Section 1.4). All models were constructed as a' = √2×a, b' = √2×b, c' = c expansions on the highest symmetry I4/mmm description of the undistorted $A_3B_2O_7$ structure. The lattice vector orientation was conserved between different symmetry descriptions, necessitating the use of non-standard space group settings as detailed below. Outline descriptions of each of the models are described below.

***Acam* #64 ($00\Psi_z/00\Psi_z$)**

Atom	Wycoff	x	y	z
La/Sr	4b	½	0	0
La/Sr	8d	½	0	~ 0.18
Cr	8d	0	0	~ 0.09
O	4a	0	0	0
O	8d	0	0	~0.19
O	16g	¼ + x	¼ + y	~0.1

***Acaa* #68 ($00\Phi_z/00\Phi_z$)**

Atom	Wycoff	x	y	z
La/Sr	4b	¾	¼	0
La/Sr	8e	¾	¼	~ 0.18
Cr	8e	¾	¾	~ 0.09
O	4a	¾	¾	0
O	16i	½ + x	½ + y	~ 0.09
O	8e	¾	¾	~ 0.19

***Acmm* #67 (ΦΦ0/-Φ-Φ0)**

Atom	Wycoff	x	y	z
La/Sr	4g	¼ +x	¾	0
La/Sr	8n	¼ + x	¼	~ 0.31
Cr	8n	¾ + x	¼	~ 0.4
O	8n	¼ + x	¾	~ 0.7
O	4g	¾ + x	¼	½
O	8i	½	½	~ 0.1
O	8h	0	½	~ 0.1

***Amam* #63 (ΦΦ0/ΦΦ0)**

Atom	Wycoff	x	y	z
La/Sr	4c	¼	¼ + y	½
La/Sr	8g	¾	¼ + y	~ 0.18

Cr	8g	¼	¼ + y	~ 0.09
O	8g	¼	¼ + y	~ 0.20
O	4c	¼	¼ + y	0
O	8e	½	0	~ 0.09
O	8e	0	½	~ 0.09

***Amam disordered* #63 (ΦΦ0/ΦΦ0)** (* occupancy = ½)

Atom	Wycoff	X	y	z
La/Sr	4c	¼	¼ + y	½
La/Sr	8g	¾	¼ + y	~ 0.18
Cr	8g	¼	¼ + y	~ 0.09
O	8g	¼	¼ + y	~ 0.20
O	4c	¼	¼ + y	0
O*	16h	½ + x	y	~ 0.09
O*	16h	x	½ + y	~ 0.09

***A2$_1$am* #36 (ΦΦΨ_z /ΦΦΨ_z)**

Atom	Wycoff	X	y	z
La/Sr	4a	¼ + x	¾ + y	0
La/Sr	8b	¼ + x	¼ + y	~ 0.31
Cr	8b	¾ + x	¼ + y	~ 0.4
O	8b	¼ + x	¾ + y	~ 0.7
O	4a	¾ + x	¼ + y	½
O	8b	x	½ + y	~ 0.1
O	8b	x	y	~ 0.1

***Pnam* #62 (ΦΦΨ_z /ΦΦ-Ψ_z)**

Atom	Wycoff	x	y	z
La/Sr	4c	¾ + x	y	¼
La/Sr	8d	¾ + x	y	~ 0.05
Cr	8d	¾ + x	y	~ 0.85
O	4c	¾ + x	½ + y	¼
O	8d	¾ + x	y	~ 0.95
O	8d	x	¼ + y	~ 0.85
O	8d	½ + x	¼ + y	~ 0.35

***A2/a* #15 (ΦΦΦ$_z$ /ΦΦΦ$_z$)**

Atom	Wycoff	x	y	z
La/Sr	4e	¼	¼ + y	0
La/Sr	8f	¼ + x	¾ + y	~ 0.18
Cr	8f	¼ + x	¼ + y	~ 0.09
O	4e	¼	¼ + y	0
O	8f	x	y	~ 0.09
O	8f	½ + x	½ + y	~ 0.09
O	8f	¼ + x	¼ + y	~ 0.19

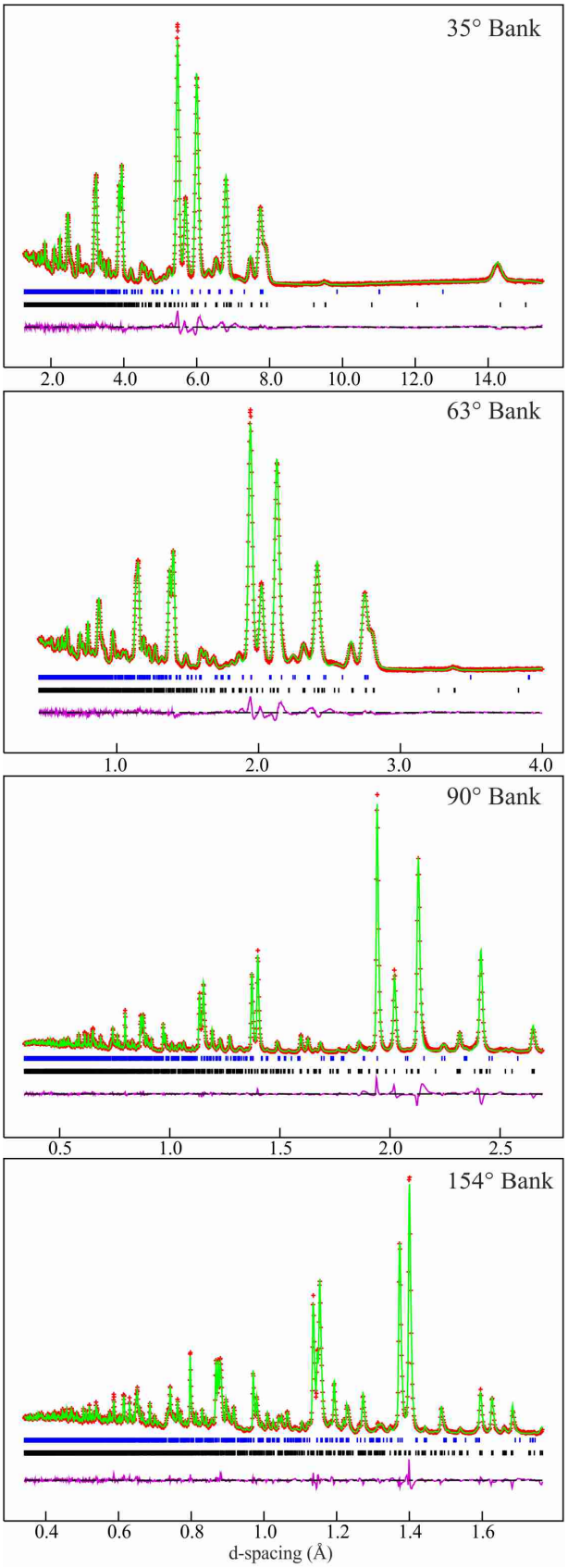


Figure A3.1. Observed, calculated and difference plots from the structural refinement of $La_2SrCr_2O_7$ against neutron powder diffraction data collected at room temperature. Lower tick marks indicate peak positions for the majority phase, upper tick marks for the $LaCrO_3$ secondary phase.

A3.2 Magnetic Symmetry Analysis

Irreducible				**Irreducible**				**Irreducible**				**Irreducible**			
Basis Vector 1				**Basis Vector 1**				**Basis Vector 1**				**Basis Vector 1**			
Atom	x	y	z	Atom	x	y	z	Atom	x	y	z	Atom	x	y	z
Cr(1)	0	0	1	Cr(1)	0	0	1	Cr(1)	0	0	1	Cr(1)	0	0	1
Cr(2)	0	0	-1	Cr(2)	0	0	-1	Cr(2)	0	0	1	Cr(2)	0	0	1
Cr(3)	0	0	1	Cr(3)	0	0	-1	Cr(3)	0	0	1	Cr(3)	0	0	-1
Cr(4)	0	0	-1	Cr(4)	0	0	1	Cr(4)	0	0	1	Cr(4)	0	0	-1
Basis Vector 2				**Basis Vector 2**				**Basis Vector 2**				**Basis Vector 2**			
Atom	x	y	z	Atom	x	y	z	Atom	x	y	z	Atom	x	y	z
Cr(1)	0	1	0	Cr(1)	0	1	0	Cr(1)	0	1	0	Cr(1)	0	1	0
Cr(2)	0	1	0	Cr(2)	0	1	0	Cr(2)	0	-1	0	Cr(2)	0	-1	0
Cr(3)	0	1	0	Cr(3)	0	-1	0	Cr(3)	0	1	0	Cr(3)	0	-1	0
Cr(4)	0	1	0	Cr(4)	0	-1	0	Cr(4)	0	-1	0	Cr(4)	0	1	0
Basis Vector 3				**Basis Vector 3**				**Basis Vector 3**				**Basis Vector 3**			
Atom	x	y	z	Atom	x	y	z	Atom	x	y	z	Atom	x	y	z
Cr(1)	1	0	0	Cr(1)	1	0	0	Cr(1)	1	0	0	Cr(1)	1	0	0
Cr(2)	-1	0	0	Cr(2)	-1	0	0	Cr(2)	1	0	0	Cr(2)	1	0	0
Cr(3)	1	0	0	Cr(3)	-1	0	0	Cr(3)	1	0	0	Cr(3)	-1	0	0
Cr(4)	-1	0	0	Cr(4)	1	0	0	Cr(4)	1	0	0	Cr(4)	-1	0	0

Table A3.1. The 4 irreducible representations yielded from analysis of the magnetic symmetry of $La_2SrCr_2O_7$ in space group *A2/a* using the SARAh code. $La_2SrCr_2O_7$ adopts the arrangement noted by the Irreducible Representation 4. The labelling scheme is shown in Figure A3.2.

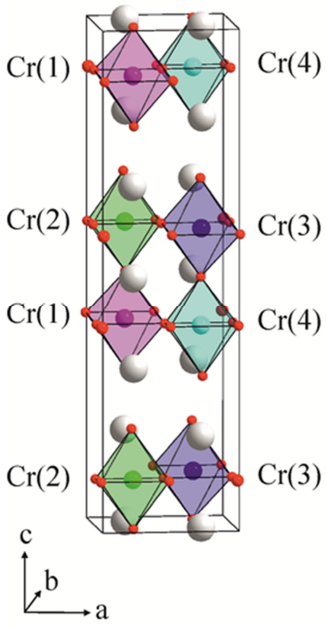


Figure A3.2. Labelling scheme for magnetic analysis in Table A3.1.

A3.3 Magnetic refinement details

Atom	site	*x*	*y*	*z*	Fraction	U_{iso} (Å^2)
La/Sr(1)	4e	¼	0.7437(8)	0	82/17	0.0063(1)
La/Sr(2)	8f	0.2444(8)	0.7465(5)	0.1817(1)	58/42	0.0051(2)
Cr(1)	8f	0.2516(15)	0.2490(14)	0.0978(1)	1	0.0011(2)
O(1)	4e	¼	0.2298(12)	0	1	0.0086(3)
O(2)	8f	0.9868(10)	0.9985(25)	0.1012(1)	1	0.0084(2)
O(3)	8f	0.5045(9)	0.5025(22)	0.0919(1)	1	0.0093(1)
O(4)	8f	0.2419(13)	0.2655(8)	0.1984(1)	1	0.0088(3)
$La_2SrCr_2O_7$ – space group: *A*2/*a* *a* = 5.4892(3) Å, *b* = 5.4765(3) Å, *c* = 20.157(1) Å, β = 89.88(1)º volume = 605.9(1)Å^3 phase fraction = 96.3 weight percent						
Atom	*x*	*y*	*z*	M_y (μ_B)		
Cr(1)	0.251	0.249	0.097	-2.51(3)		
Cr(2)	0.251	0.749	0.597	-2.51(3)		
Cr(3)	0.248	0.249	0.902	2.51(3)		
Cr(4)	0.248	0.749	0.402	2.51(3)		
Cr(5)	0.748	0.751	0.902	-2.51(3)		
Cr(6)	0.748	0.251	0.402	-2.51(3)		
Cr(7)	0.751	0.751	0.097	2.51(3)		
Cr(8)	0.751	0.251	0.597	2.51(3)		
$LaCrO_3$ – space group: Pnma *a* = 5.467(2) Å, *b* = 7.760(5) Å, *c* = 5.508(2) Å phase fraction = 3.7 weight percent						
χ^2 = 4.69, wRp = 4.24%, Rp = 3.11%						

Table A3.2 Nuclear and magnetic structural parameters refined against neutron powder diffraction data collected at 5 K from $La_2SrCr_2O_7$by using GEM diffractometer (ISIS, UK).

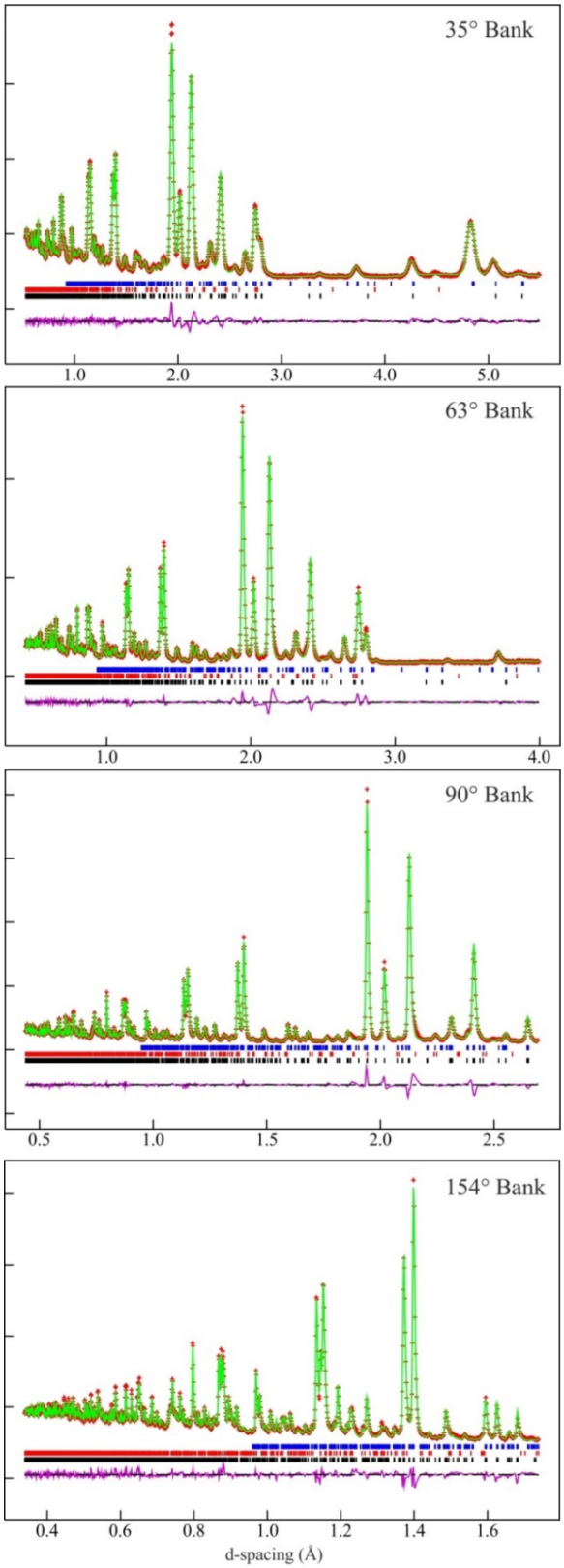


Figure A3.3 Observed, calculated and difference plots from the structural refinement of $La_2SrCr_2O_7$ against neutron powder diffraction data collected at 5K by using GEM diffractometer (ISIS, UK). Lower tick marks indicate nuclear peak positions for the majority phase, middle tick marks for the $LaCrO_3$ secondary phase, upper tick marks magnetic peak positions for the majority phase.

A3.4. First principles structures

Table A3.3 enumerates the symmetry of each structure we considered. The La/Sr sites columns denote which La and Sr ions were swapped from their expected positions as shown in Figure A3.4. As an example the ninth row of Table A3.3 means that La4 and La8 sites were swapped with the Sr1 and Sr2 sites. The energies of these structures after relaxation is shown in Figure A3.5 as a function of the mean Sr-Sr distance in the relaxed *Amam* structure after swapping La/Sr for each A-site distribution.

Structure Number	La sites	Sr sites	*A2/a* like structure	*Pnam* like structure	$A2_1am$ like structure
1	1	4	*P1*	*P1*	*P1*
2	1	3	*P1*	*P1*	*P1*
3	1	2	*P1*	*P1*	*P1*
4	1	1	*P1*	*P1*	*P1*
5	1, 2	3, 4	*P-1*	$P2_1$	*P1*
6	1, 7	1, 2	*P1*	*P1*	*P1*
7	1, 6	1, 2	*P1*	*P1*	*P1*
8	1, 4	1, 2	*Pc*	*Pc*	*Pc*
9	4, 8	1, 2	*P1*	*P1*	*P1*
10	1, 4	1, 3	*P1*	*P1*	*P1*
11	1, 3	1, 2	*P2*	*Pm*	*P1*
12	1, 7	1, 3	$P2_1$	$P2_1$	*Pc*
13	1, 2	1, 2	*P-1*	$P2_1$	*P1*
14	3, 4	1, 2	*P-1*	$P2_1$	*P1*
15	1, 2	1, 3	*P1*	*P1*	*P1*
16	1, 2	1, 4	*P1*	*P1*	*P1*
17	1, 3	1, 4	*P2*	*Pm*	*P1*
18	1, 3	1, 3	*P2*	*Pm*	*P1*
19	4, 8	2, 4	*P1*	*Pc*	*P1*
20	1, 4, 7	1, 2, 4	*P1*	*P1*	*P1*
21	1, 4, 7	1, 2, 3	*P1*	*P1*	*P1*
22	1, 7, 8	1, 2, 4	*P1*	*P1*	*P1*
23	1, 7, 8	1, 2, 3	*P1*	*P1*	*P1*
24	1, 7, 8	2, 3, 4	*P1*	*P1*	*P1*
25	3, 4, 8	1, 2, 3	*P1*	*P1*	*P1*
26	1, 4, 8	1, 3, 4	*P1*	*P1*	*P1*
27	1, 4, 8	2, 3, 4	*P1*	*P1*	*P1*
28	1, 7, 8	1, 3, 4	*P1*	*P1*	*P1*
29	3, 4, 8	1, 2, 4	*P1*	*P1*	*P1*
30	1, 4, 8	1, 2, 3	*P1*	*P1*	*P1*
31	1, 4, 8	1, 2, 4	*P1*	*P1*	*P1*
32	1, 4, 6, 7	1, 2, 3, 4	$P2_1/c$	$P2_1/c$	$Pca2_1$
33	1, 4, 7, 8	1, 2, 3, 4	*P1*	*P1*	*P1*

34	3, 4, 5, 6	1, 2, 3, 4	$P2_1/c$	$P2_12_12_1$	Pc
35	3, 4, 7, 8	1, 2, 3, 4	$P\text{-}1$	$P2_1/c$	$P2_1$
36	1, 4, 5, 8	1, 2, 3, 4	Cc	$Pna2_1$	Pc

Table A3.3 Symmetries of the structures we considered with alternate A-site orders. Refer to Figure A3.4 for labelling scheme of the La and Sr sites.

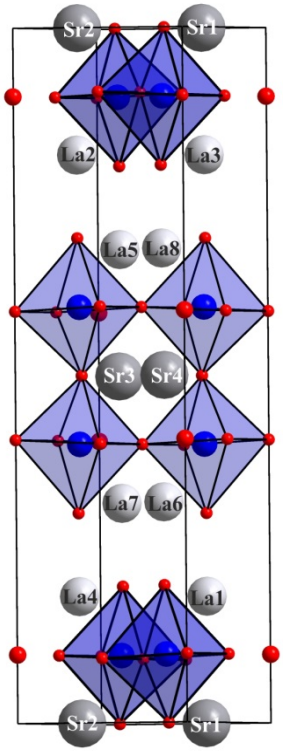


Figure A3.4. Schematic labelling the A-site positions.

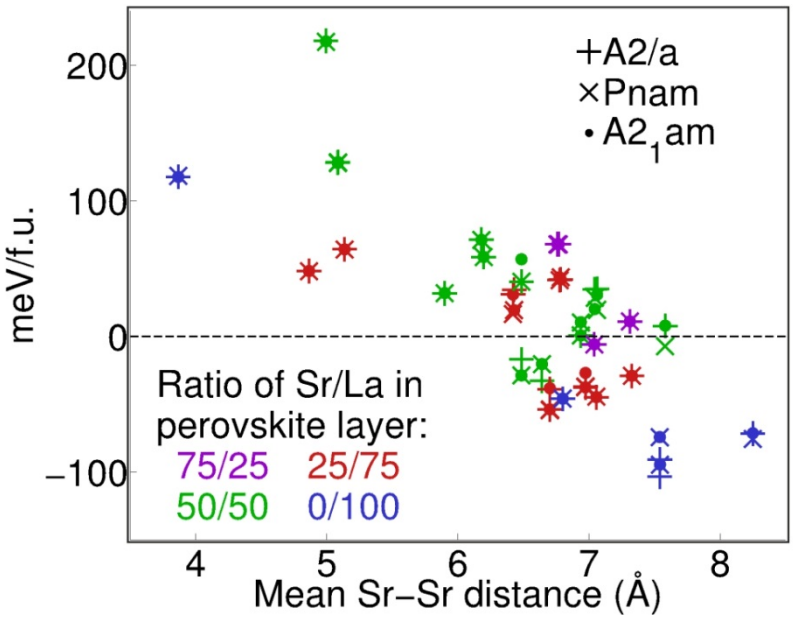


Figure A3.5. Relaxed energies per formula unit (f.u.) of our 108 structures with varying La/Sr distributions with respect to the energy of the *Amam* reference structure with La/Sr cations on their expected sites (we take the energy of this structure to be the zero of energy, indicated by the horizontal dashed line). Color and shape of points indicate

the ratio of Sr/La distribution and initial ionic positions respectively. The horizontal axis is the mean distance between Sr cations in our relaxed *Amam* structure after swapping Sr/La positions, but before any further relaxation.

A3.5. Linear correlation analysis of structural features

To guide our search for structural trends we calculated statistical quantities for a range of structural features for each of our relaxed structures, as listed in Table A3.4. Many of these features are based on the bond valence model. In many cases we averaged a particular feature over the entire structure, which was necessary because the low symmetry of many structures allowed, for instance, each CrO_6 octahedron in a particular structure to be unique. We also included variances, minima, and maxima of various structural features to help quantify structures with a large range of a particular structural feature.After calculating each of the features in Table A3.4, we calculated a pairwise linear correlation coefficient for each pair of features within each of the structures we considered. Figure A3.6 is a visualization of the results for structures relaxed starting from the *A2/a* ionic positions and constrained to the experimental unit cell. This allowed us to easily identify trends, such as the nearly perfect correlation between the average maximum Cr-O bond length and the average CrO_6 volume.

For comparison we also show the pairwise linear correlation coefficients for relaxations starting from the *A2/a* ionic positions but with an unconstrained unit cell in Figure A3.7. While the overall trends appear similar, the structural correlations after allowing cell relaxation tend to be weaker. This is especially apparent for features involving average discrepancy factors (features 28-36). We attribute this difference in part to the low symmetry of our structures, which allows the unit cell to relax in a different way for each structure. Further, the bond valence model is based on coefficients that are fit to experimental data. In our experience this seems to cause the model to become less reliable for interpreting DFT results that are not constrained to the experimental volume. For these reasons, we focused on results that were constrained to the experimental unit cell.

1	Calculated energy of structure
2	Average Cr-O-Cr in plane angle
3	Variance of Cr-O-Cr in plane angle
4	Average Cr-O-Cr angle
5	Variance of Cr-O-Cr angle
6	Bond valence global instability index
7	Average Cr-O bond length
8	Average CrO_6 volume
9	Average CrO_6 distortion index
10	Average CrO_6 quadratic elongation
11	Average CrO_6 bond angle variance

12	Variance of the average Cr-O bond length in each CrO_6
13	Variance of CrO_6 volumes
14	Variance of CrO_6 distortion indices
15	Variance of CrO_6 quadratic elongations
16	Variance of CrO_6 bond angle variance
17	Minimum of average Cr-O bond length in each CrO_6
18	Minimum CrO_6 volume
19	Minimum CrO_6 distortion index
20	Minimum CrO_6 quadratic elongation
21	Minimum CrO_6 bond angle variance
22	Maximum of average Cr-O bond length in each CrO_6
23	Maximum CrO_6 volume
24	Maximum CrO_6 distortion index
25	Maximum CrO_6 quadratic elongation
26	Maximum CrO_6 bond angle variance
27	Range of CrO_6 distortion indices
28	Average discrepancy factor of La
29	Average discrepancy factor of Sr
30	Average discrepancy factor of Cr
31	Average discrepancy factor of La in perovskite layer
32	Average discrepancy factor of La in rock salt layer
33	Average discrepancy factor of Sr in rock salt layer
34	Average discrepancy factor of apical oxygen in perovskite layer
35	Average discrepancy factor of apical oxygen in rock salt layer
36	Average discrepancy factor of equatorial oxygen
37	Variance of discrepancy factor of La
38	Variance of discrepancy factor of Sr
39	Variance of discrepancy factor of CR
40	Variance of discrepancy factor of La in perovskite layer
41	Variance of discrepancy factor of La in rock salt layer
42	Variance of discrepancy factor of Sr in rock salt layer
43	Variance of discrepancy factor of apical oxygen in perovskite layer
44	Variance of discrepancy factor of apical oxygen in rock salt layer
45	Variance of discrepancy factor of equatorial oxygen
46	Ratio of Sr in perovskite layer
47	Average minimum Cr-O bond length
48	Average maximum Cr-O bond length

Table A3.4 List of the structural features we calculated for each of our relaxed structures.

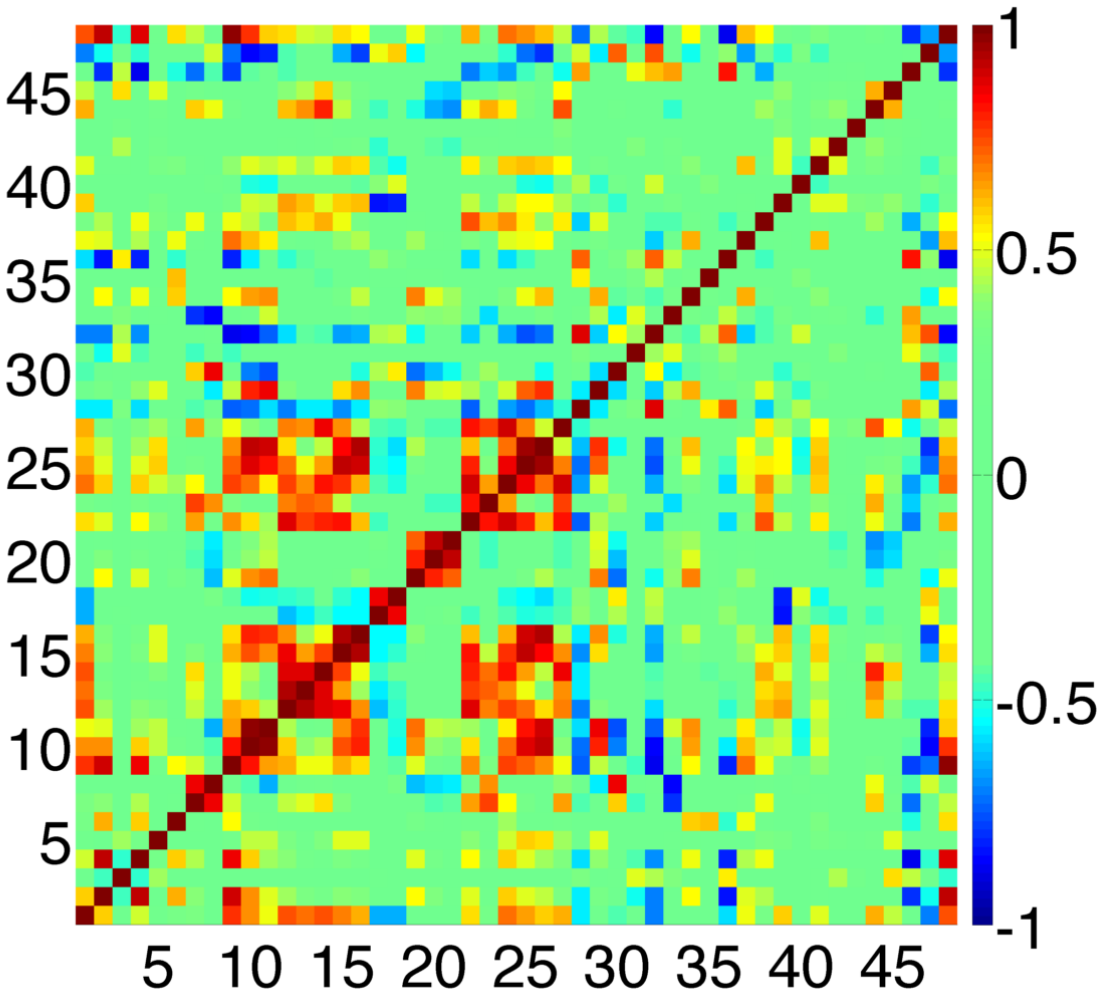


Figure A3.6. Linear correlation coefficients of the features listed in Table A3.4 for structures relaxed starting from *A2/a* ionic positions and constrained to the experimental unit cell.

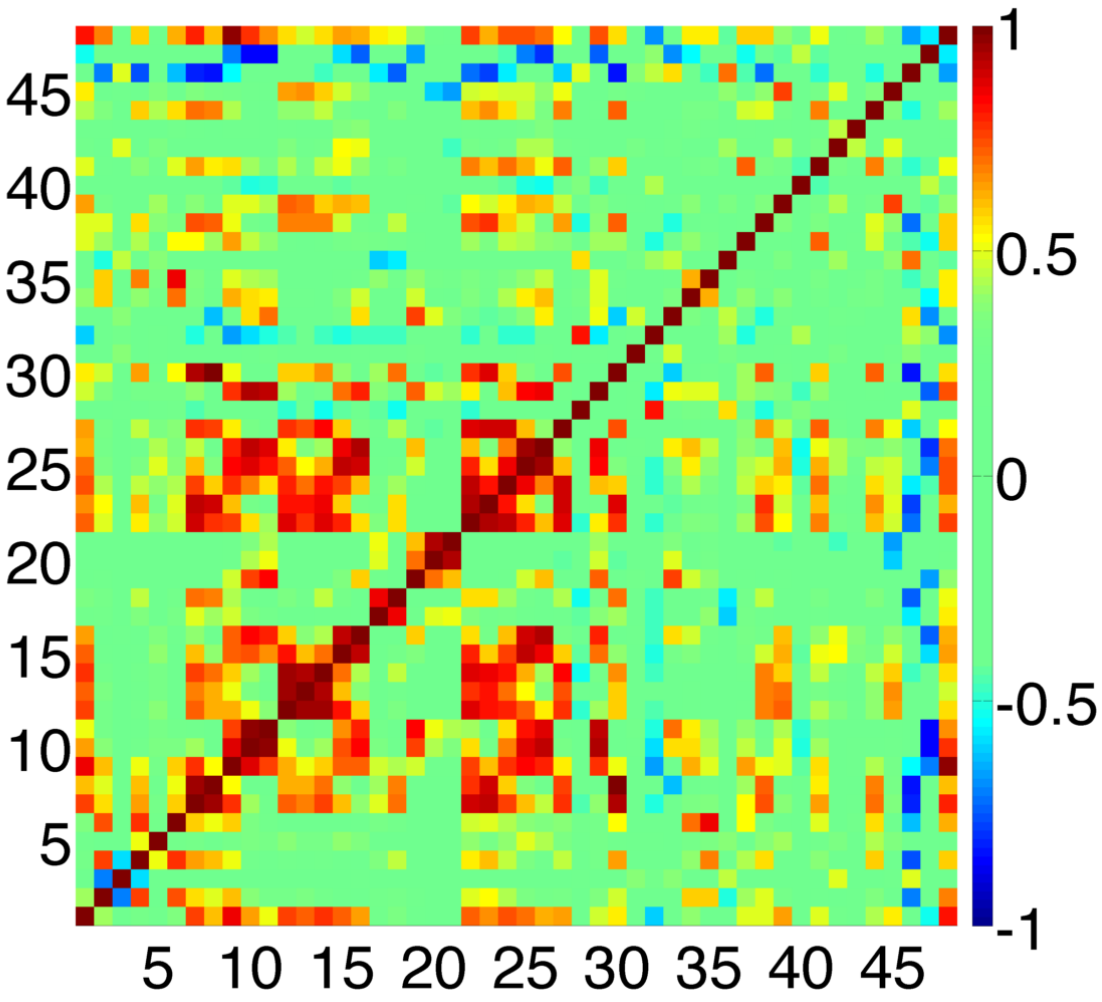


Figure A3.7. Linear correlation coefficients of the features listed in Table A3.4 for structures relaxed starting from *A2/a* ionic positions with the unit cell fully relaxed.

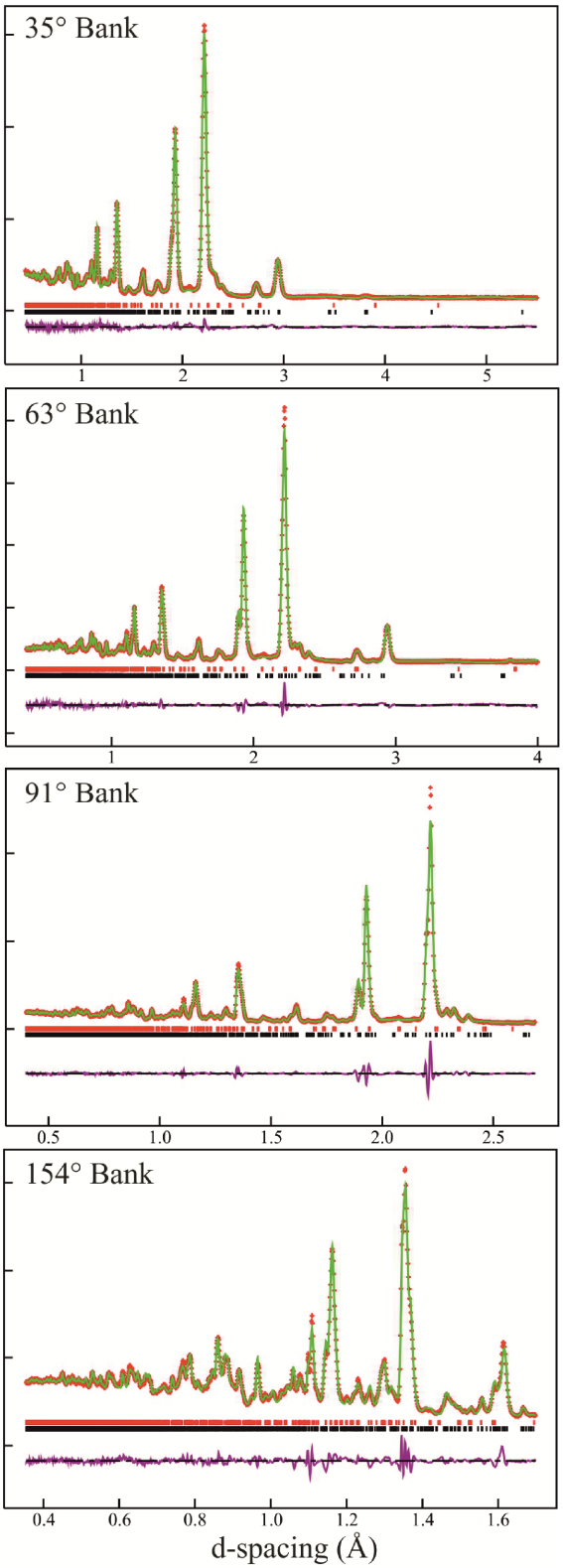


Figure A4.1. Observed, calculated and difference plots from the structural refinement of $La_2SrCr_2O_7F_2$ against neutron powder diffraction data collected at 300 K by using GEM diffractometer (ISIS, UK). Lower tick marks indicate peak positions of the majority phase, upper tick marks of a $LaCrO_3$ secondary phase.

Irreducible Representation 1				**Irreducible Representation 2**				**Irreducible Representation 3**				**Irreducible Representation 4**			
Basis Vector 1				**Basis Vector 1**				**Basis Vector 1**				**Basis Vector 1**			
Atom	x	y	z	Atom	x	y	z	Atom	x	y	z	Atom	x	y	z
Cr(1)	1	0	0	Cr(1)	1	0	0	Cr(1)	1	0	0	Cr(1)	1	0	0
Cr(2)	-1	0	0	Cr(2)	-1	0	0	Cr(2)	1	0	0	Cr(2)	1	0	0
Cr(3)	1	0	0	Cr(3)	-1	0	0	Cr(3)	1	0	0	Cr(3)	-1	0	0
Cr(4)	-1	0	0	Cr(4)	1	0	0	Cr(4)	1	0	0	Cr(4)	-1	0	0
Basis Vector 2				**Basis Vector 2**				**Basis Vector 2**				**Basis Vector 2**			
Atom	x	y	z	Atom	x	y	z	Atom	x	y	z	Atom	x	y	z
Cr(1)	0	1	0	Cr(1)	0	1	0	Cr(1)	0	1	0	Cr(1)	0	1	0
Cr(2)	0	1	0	Cr(2)	0	1	0	Cr(2)	0	-1	0	Cr(2)	0	-1	0
Cr(3)	0	1	0	Cr(3)	0	-1	0	Cr(3)	0	1	0	Cr(3)	0	-1	0
Cr(4)	0	1	0	Cr(4)	0	-1	0	Cr(4)	0	-1	0	Cr(4)	0	1	0
Basis Vector 3				**Basis Vector 3**				**Basis Vector 3**				**Basis Vector 3**			
Atom	x	y	z	Atom	x	y	z	Atom	x	y	z	Atom	x	y	z
Cr(1)	0	0	1	Cr(1)	0	0	1	Cr(1)	0	0	1	Cr(1)	0	0	1
Cr(2)	0	0	-1	Cr(2)	0	0	-1	Cr(2)	0	0	1	Cr(2)	0	0	1
Cr(3)	0	0	1	Cr(3)	0	0	-1	Cr(3)	0	0	1	Cr(3)	0	0	-1
Cr(4)	0	0	-1	Cr(4)	0	0	1	Cr(4)	0	0	1	Cr(4)	0	0	-1

Table A4.1. The 4 irreducible representations yielded from analysis of the magnetic symmetry of $La_2SrCr_2O_7F_2$ in space group A2/a using the SARAh code. The labelling scheme is shown in Figure A4.2.

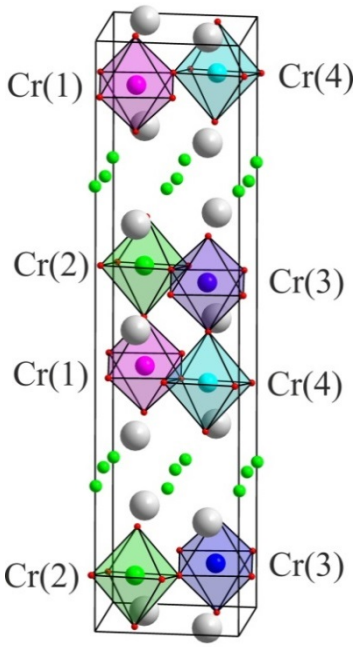


Figure A4.2. Labelling scheme for magnetic analysis in Table A4.1.

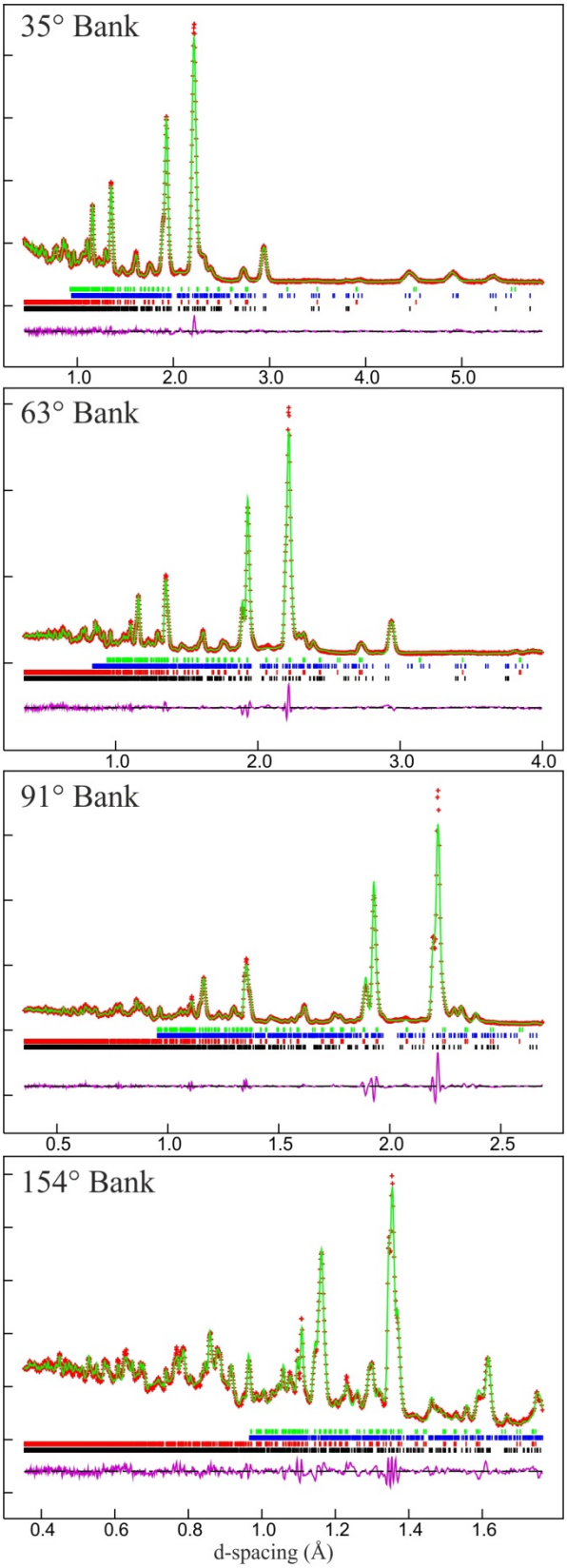


Figure A4.3. Observed, calculated and difference plots from the structural and magnetic refinement of $La_2SrCr_2O_7F_2$ against neutron powder diffraction data collected at 5 K by using GEM diffractometer (ISIS, UK). Lower tick marks (black) indicate nuclear peak positions of the majority phase, lower middle tick marks (red) nuclear peak positions of

a $LaCrO_3$ secondary phase, upper middle tick marks (purple) magnetic peak positions of the majority phase and upper tick marks (green) magnetic peak positions of a $LaCrO_3$ secondary phase.

	x	**y**	**z**	**Fraction**	**U_{iso} (Å^2)**
La/Sr(1)	¼	0.7529(9)	0	0.82/0.17	0.0045(6)
La/Sr(2)	0.2507(6)	0.7500(6)	0.1785(1)	0.58/0.42	0.0065(5)
Cr(1)	0.2462(16)	0.2498(12)	0.0841(3)	1	0.0016(5)
O(1)	0.2587(9)	0.2928(8)	0.1658(1)	1	0.0093(7)
O(2)	0.9681(9)	0.0304(11)	0.0942(1)	1	0.0062(8)
O(3)	0.5262(9)	0.4751(11)	0.0761(1)	1	0.0061(8)
O(4)	¼	0.2101(12)	0	1	0.0130(10)
F(1)	0.4963(7)	0.5006(11)	0.2523(1)	1	0.0082(5)
$La_2SrCr_2O_7F_2$ – space group: *A*2/*a* *a* = 5.4212(6) Å, *b* = 5.4695(7) Å, *c* = 22.664(2) Å, β = 90.54(1)º volume = 672.0(2)Å^3 phase fraction = 96.7 weight percent					
$LaCrO_3$ – space group: *Pnma* *a* = 5.467(2) Å, *b* = 7.764(5) Å, *c* = 5.513(2) Å phase fraction = 3.4 weight percent					
χ^2 = 4.24, wRp = 4.45%, Rp = 3.79%					

Table A4.2. Nuclear structural parameters refined against neutron powder diffraction data collected at 5 K from $La_2SrCr_2O_7F_2$.

Atom	*x*	*y*	*z*	M_z (μ_B)
Cr(1)	0.246	0.249	0.084	1.32(8)
Cr(2)	0.246	0.749	0.584	1.32(8)
Cr(3)	0.253	0.249	0.915	-1.32(8)
Cr(4)	0.253	0.749	0.415	-1.32(8)
Cr(5)	0.753	0.750	0.915	1.32(8)
Cr(6)	0.753	0.250	0.415	1.32(8)
Cr(7)	0.746	0.750	0.084	-1.32(8)
Cr(8)	0.746	0.250	0.584	-1.32(8)

Table A4.3. Magnetic structural parameters refined against neutron powder diffraction data collected at 5 K from $La_2SrCr_2O_7F_2$.

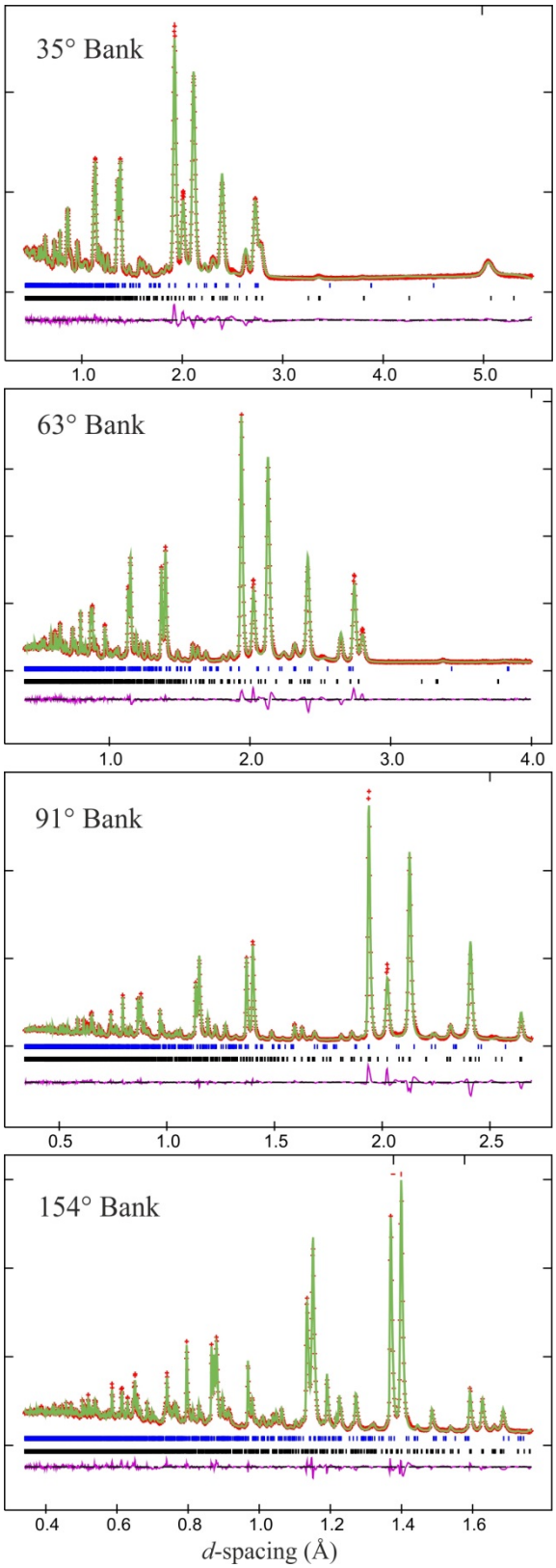


Figure A5.1. Observed, calculated and difference plots from the structural refinement of $La_{1.8}Sr_{1.2}Cr_2O_7$ against neutron powder diffraction data collected at 300 K by using GEM diffractometer (ISIS, UK). Lower tick marks indicate peak positions of the majority phase, upper tick marks of a $LaCrO_3$ secondary phase.

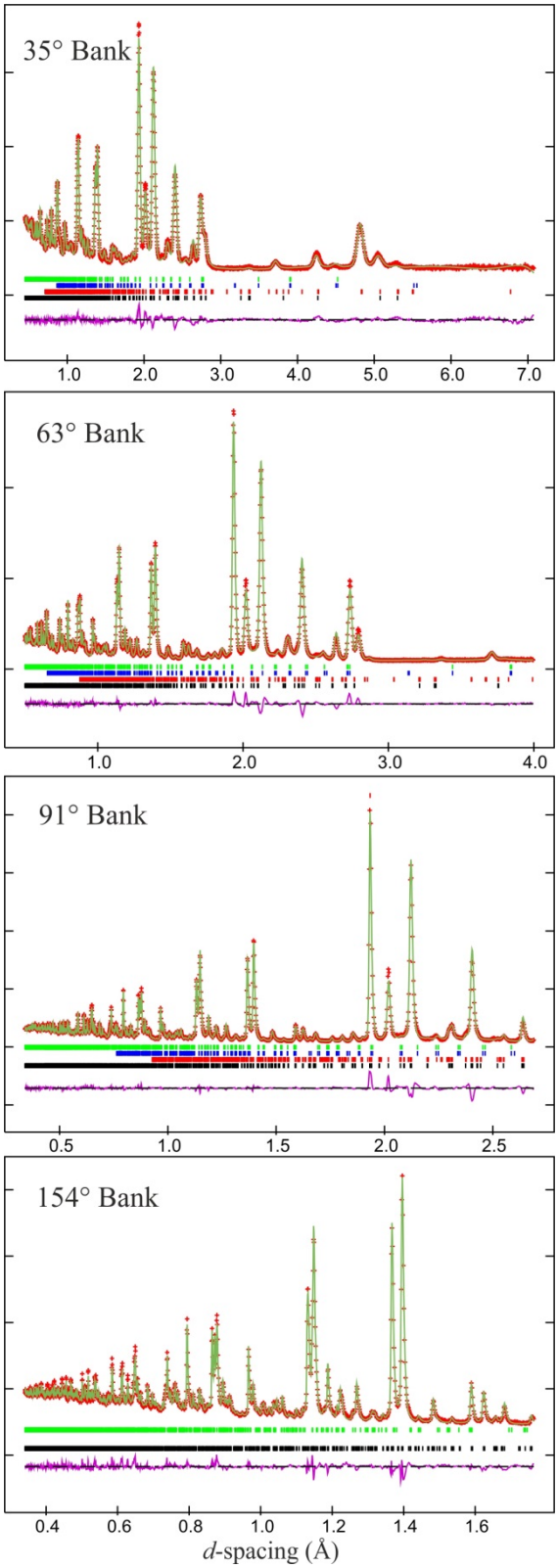


Figure A5.2. Observed, calculated and difference plots from the structural refinement of $La_{1.8}Sr_{1.2}Cr_2O_7$ against neutron powder diffraction data collected at 5 K by using GEM diffractometer (ISIS, UK). Black tick marks indicate nuclear peak positions for the majority phase, green tick marks for the $LaCrO_3$ secondary phase, red tick marks

magnetic peak positions for the majority phase, and blue tick marks magnetic peak positions for the $LaCrO_3$ secondary phase.

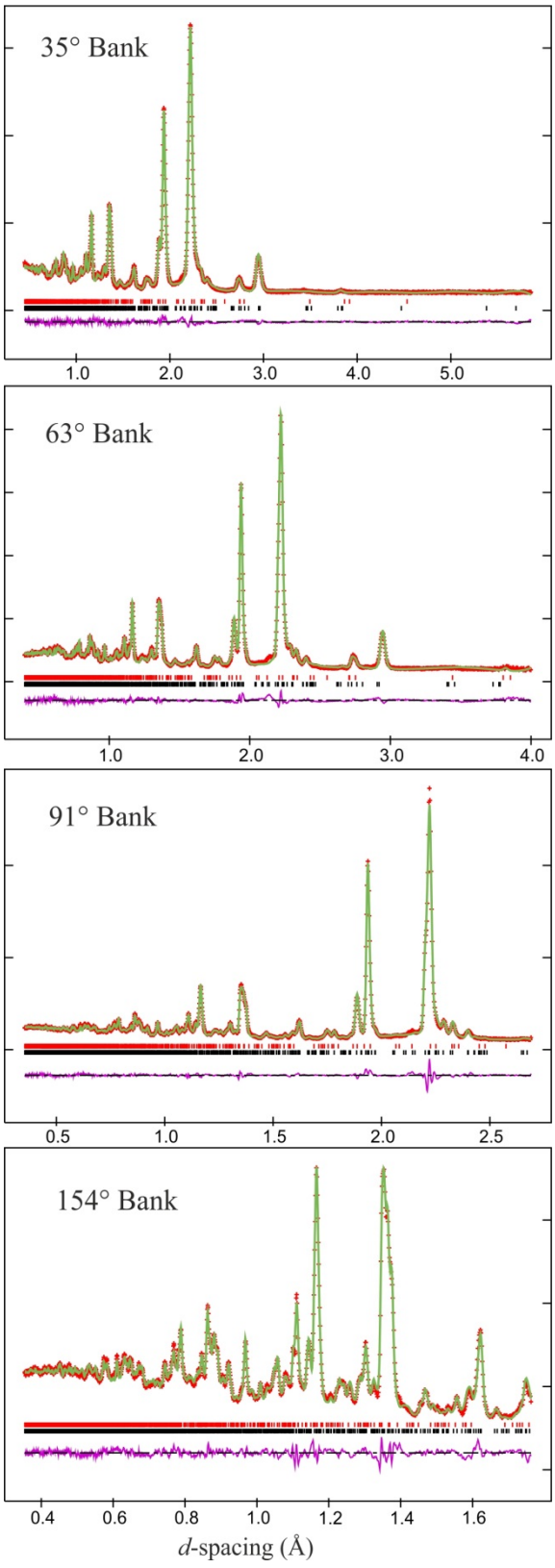


Figure A5.3. Observed, calculated and difference plots from the structural refinement of $La_{1.8}Sr_{1.2}Cr_2O_7F_2$ against neutron powder diffraction data collected at 300 K by using GEM diffractometer (ISIS, UK). Lower tick marks indicate peak positions of the majority phase, upper tick marks of a $LaCrO_3$ secondary phase.

Atom	site	*x*	*y*	*z*	Fraction	U_{iso} (Å^2)
La/Sr(1)	4e	¼	0.7475(9)	0	84/15	0.0037(2)
La/Sr(2)	8f	0.2465(7)	0.7473(7)	0.1793(1)	47/52	0.0020(2)
Cr(1)	8f	0.2522(16)	0.2478(13)	0.0985(1)	1	0.001(1)
O(1)	8f	0.2505(15)	0.2715(5)	0.1979(1)	1	0.0065(3)
O(2)	8f	0.0047(12)	-0.0026(21)	0.1003(1)	1	0.0040(3)
O(3)	8f	0.4944(12)	0.5044(19)	0.0910(1)	1	0.0049(3)
O(4)	4e	¼	0.2275(10)	0	1	0.0109(6)
$La_{1.8}Sr_{1.2}Cr_2O_7$ – space group: *A*2/*a* *a* = 5.4671(3) Å, *b* = 5.570(3) Å, *c* = 20.163(1) Å, β = 90.11(1)º volume = 601.54 Å^3						
Atom	*x*	*y*	*z*	M_y (μ_B)		
Cr(1)	0.250	0.250	0.902	-2.18(4)		
Cr(2)	0.750	0.750	0.901	2.18(4)		
Cr(3)	0.250	0.750	0.598	2.18(4)		
Cr(4)	0.750	0.250	0.598	-2.18(4)		
Cr(5)	0.250	0.750	0.402	-2.18(4)		
Cr(6)	0.750	0.250	0.402	2.18(4)		
Cr(7)	0.250	0.250	0.098	2.18(4)		
Cr(8)	0.750	0.750	0.098	-2.18(4)		
χ^2 = 4.41, wRp = 4.25%, Rp = 3.54%						

Table A5.1 Nuclear and magnetic structural parameters refined against neutron powder diffraction data collected at 5 K from $La_{1.8}Sr_{1.2}Cr_2O_7$.

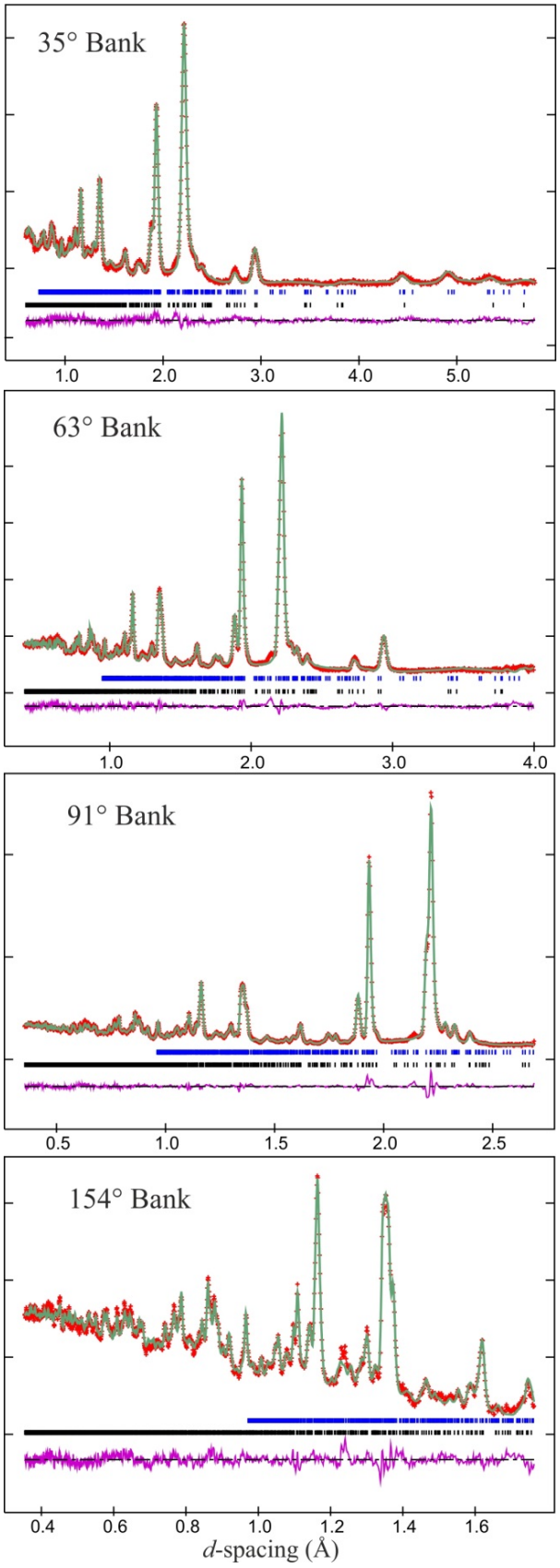


Figure A5.4. Observed, calculated and difference plots from the structural refinement of $La_{1.8}Sr_{1.2}Cr_2O_7F_2$ against neutron powder diffraction data collected at 5 K by using GEM diffractometer (ISIS, UK). Lower tick marks indicate nuclear peak positions for the majority phase; Upper tick marks magnetic peak positions for the majority phase.

Atom	site	*x*	*y*	*z*	Fraction	U_{iso} (Å^2)
La/Sr(1)	4e	¼	0.7497(11)	0	84/15	0.0028(2)
La/Sr(2)	8f	0.2465(7)	0.7473(7)	0.1793(1)	47/52	0.0028(2)
Cr(1)	8f	0.2511(17)	0.2472(18)	0.0841(1)	1	0.0011(2)
O(1)	8f	0.242(1)	0.2914(8)	0.1669(14)	1	0.0053(6)
O(2)	8f	0.0238(8)	-0.0224(12)	0.0957(1)	1	0.0061(8)
O(3)	8f	0.4766(9)	0.5186(12)	0.0751(1)	1	0.0035(6)
O(4)	4e	¼	0.1947(11)	0	1	0.0043(10)
F(1)	8f	0.4960(8)	0.5018(14)	0.2538(1)	1	0.0054(6)
$La_{1.8}Sr_{1.2}Cr_2O_7F_2$ – space group: *A*2/*a* *a* = 5.4353(13) Å, *b* = 5.4854(13) Å, *c* = 22.560(1) Å, β = 89.49(1)º volume = 672.6(1)Å^3						
Atom	*x*	*y*	*z*	M_y (μ_B)		
Cr(1)	0.252	0.242	0.914	-1.60(7)		
Cr(2)	0.752	0.758	0.914	1.60(7)		
Cr(3)	0.248	0.742	0.586	1.60(7)		
Cr(4)	0.748	0.258	0.586	-1.60(7)		
Cr(5)	0.252	0.742	0.414	-1.60(7)		
Cr(6)	0.752	0.258	0.414	1.60(7)		
Cr(7)	0.248	0.242	0.086	1.60(7)		
Cr(8)	0.748	0.758	0.086	-1.60(7)		
χ^2 = 3.93, wRp = 3.02%, Rp = 2.27%						

Table A5.2 Nuclear and magnetic structural parameters refined against neutron powder diffraction data collected at 5 K from $La_{1.8}Sr_{1.2}Cr_2O_7F_2$.

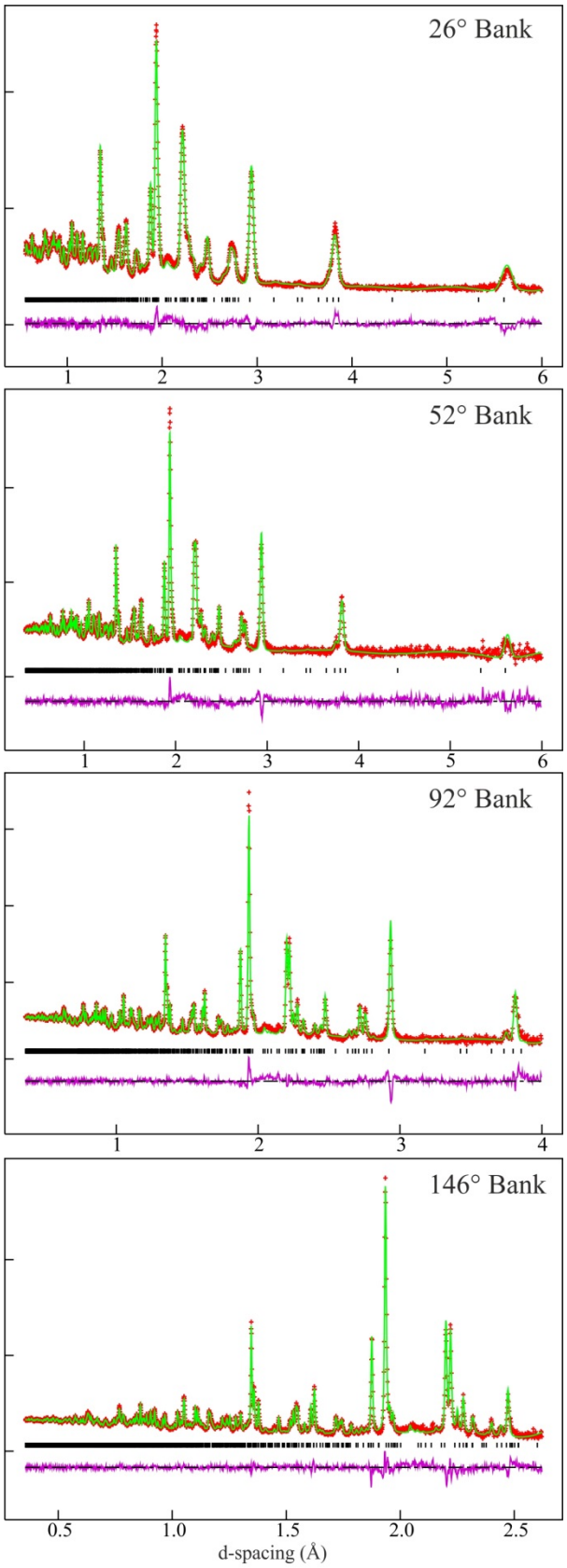


Figure A6.1. Observed, calculated and difference plots from the structural refinement of $La_3Ni_2O_{5.5}F_{3.5}$ against neutron powder diffraction data collected at 300 K by using POLARIS diffractometer (ISIS, UK).

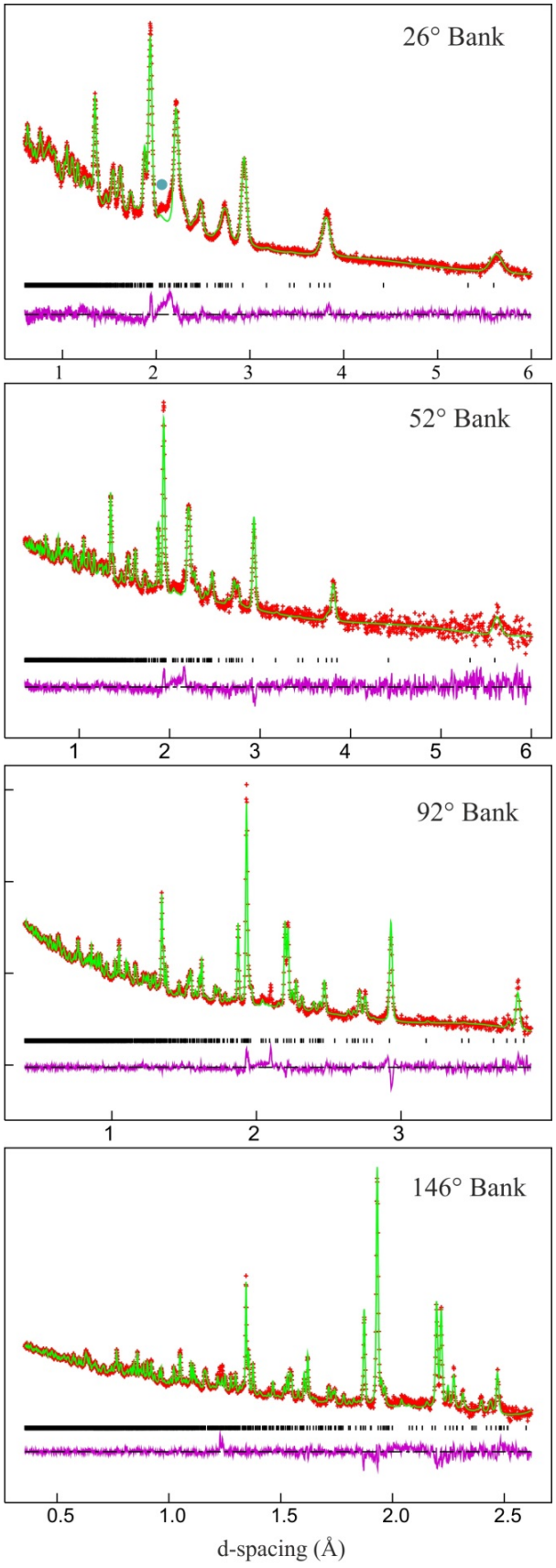


Figure A6.2. Observed, calculated and difference plots from the structural refinement of $La_3Ni_2O_{5.5}F_{3.5}$ against neutron powder diffraction data collected at 5 K by using POLARIS diffractometer (ISIS, UK).

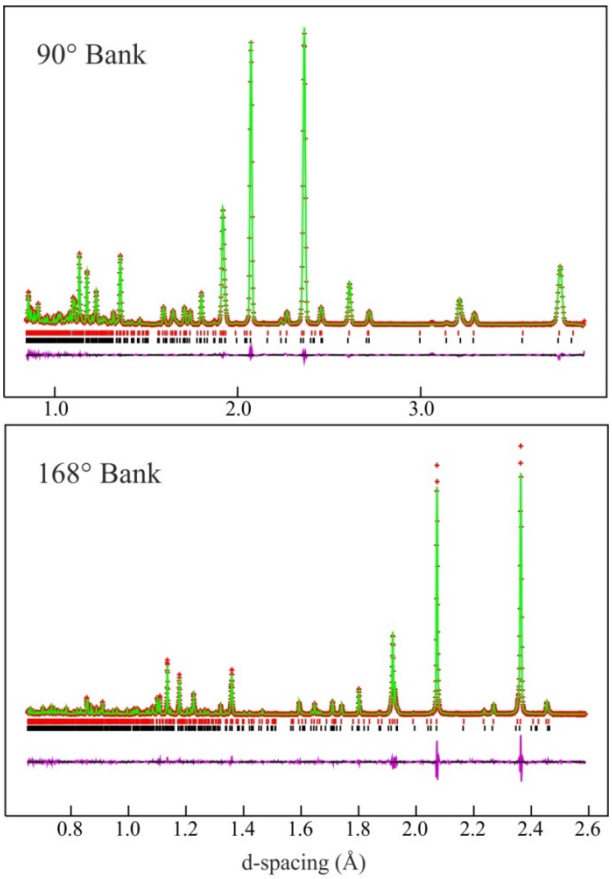


Figure A7.1. Observed, calculated and difference plots from the structural refinement of $YSrCaMn_2O_7$ by using two *P4₂/mnm* models against neutron powder diffraction data collected at 300 K by using HRPD diffractometer (ISIS, UK).

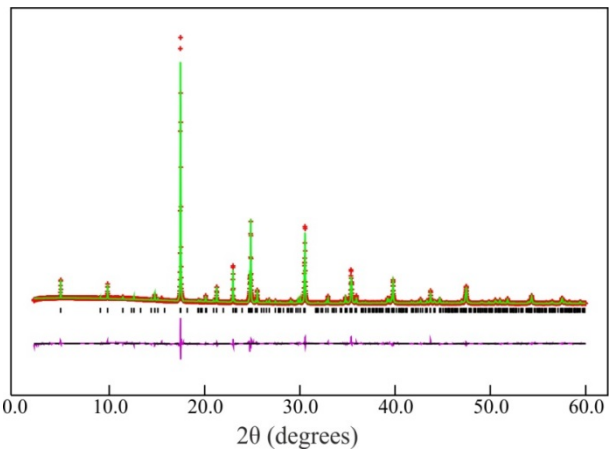


Figure A7.2. Observed, calculated and difference plots from the structural refinement of $YSrCaMn_2O_7$ by using *P4₂/mnm* model against the synchrotron X-ray diffraction data (I11, Diamond).

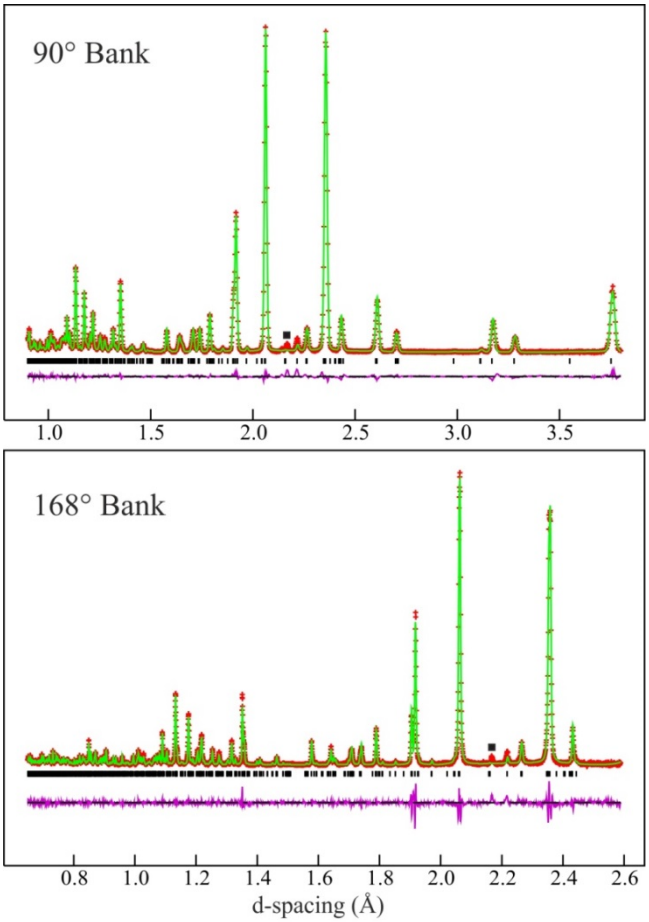
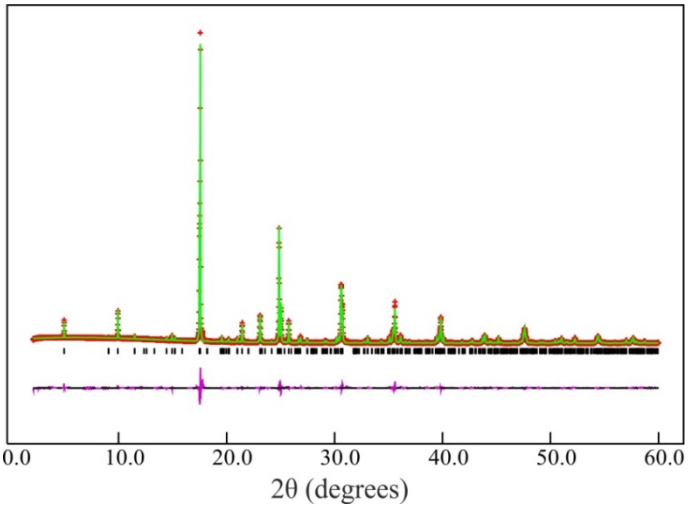


Figure A7.3. Observed, calculated and difference plots from the structural refinement of $YSr_{0.5}Ca_{1.5}Mn_2O_7$ by using *Pnnm* model against neutron powder diffraction data collected at room temperature by using HRPD diffractometer (ISIS, UK). The black square marks the diffraction peak from vanadium sample can ($d \approx 2.15$ Å).



.

Figure A7.3. Observed, calculated and difference plots from the structural refinement of $YSr_{0.5}Ca_{1.5}Mn_2O_7$ by using *Pnnm* model against the synchrotron X-ray diffraction data (I11, Diamond).

References

(1) Goodenough, J. B. *Localized to Itinerant Electronic Transition in Perovskite Oxides*, 2001.

(2) Peña, M. A.; Fierro, J. L. G. *Chemical Reviews* **2001**, *101*, 1981.

(3) Cohen, R. E. *Nature* **1992**, *358*, 136.

(4) Jin, C. Q.; Zhou, J. S.; Goodenough, J. B.; Liu, Q. Q.; Zhao, J. G.; Yang, L. X.; Yu, Y.; Yu, R. C.; Katsura, T.; Shatskiy, A.; Ito, E. *Proceedings of the National Academy of Sciences of the United States of America* **2008**, *105*, 7115.

(5) Gurusinghe, N. N. M.; de la Figuera, J.; Marco, J. F.; Thomas, M. F.; Berry, F. J.; Greaves, C. *Materials Research Bulletin* **2013**, *48*, 3537.

(6) David, W. I. F.; Harrison, W. T. A.; Gunn, J. M. F.; Moze, O.; Soper, A. K.; Day, P.; Jorgensen, J. D.; Hinks, D. G.; Beno, M. A.; Soderholm, L.; Capone Ii, D. W.; Schuller, I. K.; Segre, C. U.; Zhang, K.; Grace, J. D. *Nature* **1987**, *327*, 310.

(7) Schiffer, P.; Ramirez, A. P.; Bao, W.; Cheong, S. W. *Physical Review Letters* **1995**, *75*, 3336.

(8) Bonanos, N.; Knight, K. S.; Ellis, B. *Solid State Ionics* **1995**, *79*, 161.

(9) Goldschmidt, V. M. *Naturwissenschaften* **1926**, *14*, 477.

(10) Abramov, Y. A.; Tsirelson, V. G.; Zavodnik, V. E.; Ivanov, S. A.; Brown I. D. *Acta Crystallographica Section B* **1995**, *51*, 942.

(11) Torrance, J. B.; Lacorre, P.; Nazzal, A. I.; Ansaldo, E. J.; Niedermayer, C. *Phys. Rev. B* **1992**, *45*, 8209.

(12) Buttner, R. H.; Maslen, E. N. *Acta Crystallographica Section B* **1992**, *48*, 644.

(13) Cox, P. A. *The Electronic Structure and Chemistry of Solids* Oxford University Press: United States, 1987.

(14) Cheetham, A. K.; Day, P. *Solid State Chemistry Compounds*; Oxford University Press, 1992.

(15) Imada, M.; Fujimori, A.; Tokura, Y. *Reviews of Modern Physics* **1998**, *70*, 1039.

(16) Norman, M. R.; Pépin, C. *Reports on Progress in Physics* **2003**, *66*, 1547.

(17) Battle, P. D.; Millburn, J. E.; Rosseinsky, M. J.; Spring, L. E.; Vente, J. F. *Chem. Mater.* **1997**, *9*, 3136.

(18) Meng, J.; Satoh, H.; Ishida, M.; Kamegashira, N. *J. Alloys Compounds* **2006**, *408*, 1182.

(19) Glazer, A. *Acta Crystallographica Section B* **1972**, *28*, 3384.

(20) Aleksandrov, K. S.; Bartolome, J. *Journal of Physics: Condensed Matter* **1994**, *6*, 8219.

(21) Li, R. K.; Greaves, C. *Physical Review B* **2000**, *62*, 3811.

(22) Aikens, L. D.; Gillie, L. J.; Li, R. K.; Greaves, C. *Journal of Materials Chemistry* **2002**, *12*, 264.

(23) Romero, F. D.; Bingham, P. A.; Forder, S. D.; Hayward, M. A. *Inorganic Chemistry* **2013**, *52*, 3388.

(24) Gurusinghe, N. N. M.; Fones, J. C.; Marco, J. F.; Berry, F. J.; Greaves, C. *Dalton Transactions* **2014**, *43*, 2038.

(25) Aikens, L. D.; Li, R. K.; Greaves, C. *Chemical Communications* **2000**, 2129.

(26) Li, R. K.; Greaves, C. *Phys. Rev. B* **2000**, *62*, 3811.

(27) Ma, J.; Hu, J.; Li, Z.; Nan, C.-W. *Advanced Materials* **2011**, *23*, 1062.

(28) Hill, N. A. *The Journal of Physical Chemistry B* **2000**, *104*, 6694.

(29) Kunz, M.; Brown, I. D. *Journal of Solid State Chemistry* **1995**, *115*, 395.

(30) Spaldin, N. A. *Magnetic Materials Fundamentals and Applications*; Cambridge Unveristy Press, 2011.
(31) Ramesh, R.; Spaldin, N. A. *Nature Materials* **2007**, *6*, 21.
(32) Katsufuji, T.; Takagi, H. *Physical Review B* **2001**, *64*, 054415.
(33) Rondinelli, J. M.; Fennie, C. J. *Advanced Materials* **2012**, *24*, 1961.
(34) Mulder, A. T.; Benedek, N. A.; Rondinelli, J. M.; Fennie, C. J. *Advanced Functional Materials* **2013**, *23*, 4810.
(35) Bousquet, E.; Dawber, M.; Stucki, N.; Lichtensteiger, C.; Hermet, P.; Gariglio, S.; Triscone, J. M.; Ghosez, P. *Nature* **2008**, *452*, 732.
(36) Fukushima, T.; Stroppa, A.; Picozzi, S.; Perez-Mato, J. M. *Physical Chemistry Chemical Physics* **2011**, *13*, 12186.
(37) Benedek, N. A.; Rondinelli, J. M.; Djani, H.; Ghosez, P.; Lightfoot, P. *Dalton Transactions* **2015**, *44*, 10543.
(38) Pitcher, M. J.; Mandal, P.; Dyer, M. S.; Alaria, J.; Borisov, P.; Niu, H.; Claridge, J. B.; Rosseinsky, M. J. *Science* **2015**, *347*, 420.
(39) Pechini, M. P.; SPRAGUE ELECTRIC CO: United States, 1967; Vol. 3330697.
(40) Danks, A. E.; Hall, S. R.; Schnepp, Z. *Materials Horizons* **2016**, *3*, 91.
(41) Slater, P. R.; Hodges, J. P.; Francesconi, M. G.; Edwards, P. P.; Greaves, C.; Gameson, I.; Slaski, M. *Physica C: Superconductivity* **1995**, *253*, 16.
(42) West, A. R. *Soldi State Chemistry and Its Applications*, John Wiley & Sons Ltd., 1984.
(43) Barnes, P.; Cockcroft, J. K.; Jacques, S.; Vickers, M. http://pd.chem.ucl.ac.uk/pdnn/inst2/work.htm.
(44) http://www.diamond.ac.uk/Home/About/How-Diamond-Works.html.
(45) Thompson, S. P.; Parker, J. E.; Potter, J.; Hill, T. P.; Birt, A.; Cobb, T. M.; Yuan, F.; Tang, C. C. *Review of Scientific Instruments* **2009**, *80*, 075107.
(46) Sears, V. F. *Neutron News* **2006**, *3*, 26.
(47) Buras, B.; Gerward, L. *Acta Crystallographica Section A* **1975**, *31*, 372.
(48) http://pd.chem.ucl.ac.uk/pdnn/inst3/pulsed.htm.
(49) Caglioti, G.; Paoletti, A.; Ricci, F. P. *Nuclear Instruments* **1958**, *3*, 223.
(50) Williams, W. G.; Ibberson, R. M.; Day, P.; Enderby, J. E. *Physica B: Condensed Matter* **1997**, *241*, 234.
(51) http://wwwisis2.isis.rl.ac.uk/disordered/gem/gem_home.htm.
(52) Hannon, A. C. *Nuclear Instruments and Methods in Physics Research Section A: Accelerators, Spectrometers, Detectors and Associated Equipment* **2005**, *551*, 88.
(53) http://www.isis.stfc.ac.uk/instruments/gem/gem2467.html.
(54) http://www.isis.stfc.ac.uk/instruments/polaris/technical/polaris-technical-information7277.html.
(55) http://www.isis.stfc.ac.uk/instruments/hrpd/documents/hrpd-documents4439.html.
(56) https://www.ill.eu/instruments-support/instruments-groups/groups/dif/instruments/#.
(57) Toby, B. H. *Powder Diffraction* **2006**, *21*, 67.
(58) Rietveld, H. *Journal of Applied Crystallography* **1969**, *2*, 65.
(59) Brese, N. E.; O'Keeffe, M. *Acta Crystallographica Section B* **1991**, *47*, 192.
(60) Denis Romero, F.; Gianolio, D.; Cibin, G.; Bingham, P. A.; d'Hollander, J. C.; Forder, S. D.; Hayward, M. A. *Inorganic Chemistry* **2013**, *52*, 10920.
(61) Zhang, R.; Read, G.; Lang, F.; Lancaster, T.; Blundell, S. J.; Hayward, M. A. *Inorganic Chemistry* **2016**, *55*, 3169.
(62) Parameswaran, K. R.; Kurz, J. R.; Roussev, R. V.; Fejer, M. M. *Opt. Lett.* **2002**, *27*, 43.

(63) Kim, H. G.; Yoo, J. S.; Ok, K. M. *Journal of Materials Chemistry C* **2015**, *3*, 5625.
(64) Ok, K. M.; Chi, E. O.; Halasyamani, P. S. *Chemical Society Reviews* **2006**, *35*, 710.
(65) Knapp, M. C.; Woodward, P. M. *Journal of Solid State Chemistry* **2006**, *179*, 1076.
(66) King, G.; Woodward, P. M. *Journal of Materials Chemistry* **2010**, *20*, 5785.
(67) Benedek, N. A. *Inorganic Chemistry* **2014**, *53*, 3769.
(68) Benedek, N. A.; Rondinelli, J. M.; Djani, H.; Ghosez, P.; Lightfoot, P. *Dalton Transactions* **2015**, *44*, 10543.
(69) Zhang, R.; Abbett, B. M.; Read, G.; Lang, F.; Lancaster, T.; Tran, T. T.; Halasyamani, P. S.; Blundell, S. J.; Benedek, N. A.; Hayward, M. A. *Inorganic Chemistry* **2016**, *55*, 8951.
(70) Castillo-Martínez, E.; Alario-Franco, M. Á. *Solid State Sciences* **2007**, *9*, 564.
(71) Tezuka, K.; Hinatsu, Y.; Nakamura, A.; Inami, T.; Shimojo, Y.; Morii, Y. *Journal of Solid State Chemistry* **1998**, *141*, 404.
(72) Wills, A. S. *Physica B: Condensed Matter* **2000**, *276–278*, 680.
(73) Shannon, R. *Acta Crystallographica Section A* **1976**, *32*, 751.
(74) Battle, P. D.; Millburn, J. E.; Rosseinsky, M. J.; Spring, L. E.; Vente, J. F.; Radaelli, P. G. *Chemistry of Materials* **1997**, *9*, 3136.
(75) Meng, J.; Satoh, H.; Ishida, M.; Kamegashira, N. *Journal of Alloys and Compounds* **2006**, *408-412*, 1182.
(76) Rao, G. H.; Bärner, K.; Brown, I. D. *Journal of Physics: Condensed Matter* **1998**, *10*, L757.
(77) Baur, W. *Acta Crystallographica Section B* **1974**, *30*, 1195.
(78) Darie, C.; Goujon, C.; Bacia, M.; Klein, H.; Toulemonde, P.; Bordet, P.; Suard, E. *Solid State Sciences* **2010**, *12*, 660.
(79) Prado-Gonjal, J.; Schmidt, R.; Romero, J. J.; Avila, D.; Amador, U.; Moran, E. *Inorganic Chemistry* **2013**, *52*, 313.
(80) Belik, A. A.; Matsushita, Y.; Tanaka, M.; Takayama-Muromachi, E. *Chemistry of Materials* **2012**, *24*, 2197.
(81) Sloan, J.; Battle, P. D.; Green, M. A.; Rosseinsky, M. J.; Vente, J. F. *Journal of Solid State Chemistry* **1998**, *138*, 135.
(82) Castillo-Martínez, E.; Schönleber, A.; van Smaalen, S.; Arévalo-López, A. M.; Alario-Franco, M. A. *Journal of Solid State Chemistry* **2008**, *181*, 1840.
(83) Simon Case, G.; L. Hector, A.; Levason, W.; L. Needs, R.; F. Thomas, M.; T. Weller, M. *Journal of Materials Chemistry* **1999**, *9*, 2821.
(84) Greis, O.; Petzel, T. *Z. Anorg. Allg. Chem.* **1974**, *403*, 1.
(85) Denis Romero, F.; Bingham, P. A.; Forder, S. D.; Hayward, M. A. *Inorg. Chem.* **2013**, *52*, 3388.
(86) Li, R. K.; Greaves, C. *Physical Review B* **2000**, *62*, 3811.
(87) Castillo-Martínez, E.; Durán, A.; Alario-Franco, M. Á. *Journal of Solid State Chemistry* **2008**, *181*, 895.
(88) Zhou, J. S.; Jin, C. Q.; Long, Y. W.; Yang, L. X.; Goodenough, J. B. *Physical Review Letters* **2006**, *96*, 046408.
(89) Ortega-San-Martin, L.; Williams, A. J.; Rodgers, J.; Attfield, J. P.; Heymann, G.; Huppertz, H. *Physical Review Letters* **2007**, *99*, 255701.
(90) Goodenough, J. B.; Longo, J. M.; Kafalas, J. A. *Materials Research Bulletin* **1968**, *3*, 471.
(91) Battle, P. D.; Goodenough, J. B.; Price, R. *Journal of Solid State Chemistry* **1983**, *46*, 234.

(92) Moon, S. J.; Jin, H.; Kim, K. W.; Choi, W. S.; Lee, Y. S.; Yu, J.; Cao, G.; Sumi, A.; Funakubo, H.; Bernhard, C.; Noh, T. W. *Physical Review Letters* **2008**, *101*, 226402.

(93) Cao, Y.; Cao, S.; Ren, W.; Feng, Z.; Yuan, S.; Kang, B.; Lu, B.; Zhang, J. *Applied Physics Letters* **2014**, *104*, 232405.

(94) Gordon, J. D.; Hornreich, R. M.; Shtrikman, S.; Wanklyn, B. M. *Physical Review B* **1976**, *13*, 3012.

(95) Bartolomé, F.; Bartolomé, J.; Castro, M.; Melero, J. J. *Physical Review B* **2000**, *62*, 1058.

(96) Gupta, P.; Poddar, P. *RSC Advances* **2016**, *6*, 82014.

(97) Tsushima, K.; Takemura, I.; Osaka, S. *Solid State Communications* **1969**, *7*, 71.

(98) Yoshii, K. *Journal of Solid State Chemistry* **2001**, *159*, 204.

(99) McDannald, A.; Jain, M. *Journal of Applied Physics* **2015**, *118*, 043904.

(100) Su, Y.; Zhang, J.; Feng, Z.; Li, Z.; Shen, Y.; Cao, S. *Journal of Rare Earths* **2011**, *29*, 1060.

(101) Bertaut, E. F.; Mareschal, J. *Solid State Communications* **1967**, *5*, 93.

(102) Yoshii, K. *Materials Research Bulletin* **2012**, *47*, 3243.

(103) Motokawa, M.; Hori, H.; Nishimura, H.; Tsushima, K.; Date, M. *Journal of Magnetism and Magnetic Materials* **1986**, *59*, 243.

(104) Hornreich, R. M.; Shtrikman, S.; Wanklyn, B. M.; Yaeger, I. *Physical Review B* **1976**, *13*, 4046.

(105) Sharma, Y.; Sahoo, S.; Perez, W.; Mukherjee, S.; Gupta, R.; Garg, A.; Chatterjee, R.; Katiyar, R. S. *Journal of Applied Physics* **2014**, *115*, 183907.

(106) Denis Romero, F.; Bingham, P. A.; Forder, S. D.; Hayward, M. A. *Inorganic Chemistry* **2013**, *52*, 3388.

(107) Sivakumar, T.; Wiley, J. B. *Mater. Res. Bull.* **2009**, *44*, 74.

(108) Hayward, M. A. *Semiconductor Science and Technology* **2014**, *29*.

(109) Zhang, R.; Read, G.; Lang, F.; Lancaster, T.; Blundell, S. J.; Hayward, M. A. *Inorganic Chemistry* **2016**, *55*, 3169.

(110) Gurusinghe, N. N. M.; Fones, J. C.; Marco, J. F.; Berry, F. J.; Greaves, C. *Dalton Transactions.* **2014**, *43*, 2038.

(111) Hayward, M. A. In *Comprehensive Inorganic Chemistry II*; Reedijk, J., Poeppelmeier, K. R., Eds.; Elsevier: Oxford, 2013; Vol. 2, p 417.

(112) Ling, C. D.; Argyriou, D. N.; Wu, G. Q.; Neumeier, J. J. *J. Solid State Chem.* **2000**, *152*, 517.

(113) Zhang, R.; Senn, M. S.; Hayward, M. A. *Chemistry of Materials* **2016**, *28*, 8399.

(114) Izumi, H. K.; Kirsch, J. E.; Stern, C. L.; Poeppelmeier, K. R. *Inorganic Chemistry* **2005**, *44*, 884.

(115) Welk, M. E.; Norquist, A. J.; Stern, C. L.; Poeppelmeier, K. R. *Inorganic Chemistry* **2000**, *39*, 3946.

(116) Heier, K. R.; Norquist, A. J.; Halasyamani, P. S.; Duarte, A.; Stern, C. L.; Poeppelmeier, K. R. *Inorganic Chemistry* **1999**, *38*, 762.

(117) Donakowski, M. D.; Gautier, R.; Yeon, J. H.; Moore, D. T.; Nino, J. C.; Halasyamani, P. S.; Poeppelmeier, K. R. *J. Am. Chem. Soc.* **2012**, *134*, 7679.

(118) Gautier, R.; Gautier, R.; Chang, K. B.; Poeppelmeier, K. R. *Inorganic Chemistry* **2015**, *54*, 1712.

(119) Marvel, M. R.; Lesage, J.; Baek, J.; Halasyamani, P. S.; Stern, C. L.; Poeppelmeier, K. R. *J. Am. Chem. Soc.* **2007**, *129*, 13963.

(120) Battle, P. D.; Green, M. A.; Laskey, N. S.; Millburn, J. E.; Murphy, L.; Rosseinsky, M. J.; Sullivan, S. P.; Vente, J. F. *Chemistry of Materials* **1997**, *9*, 552.